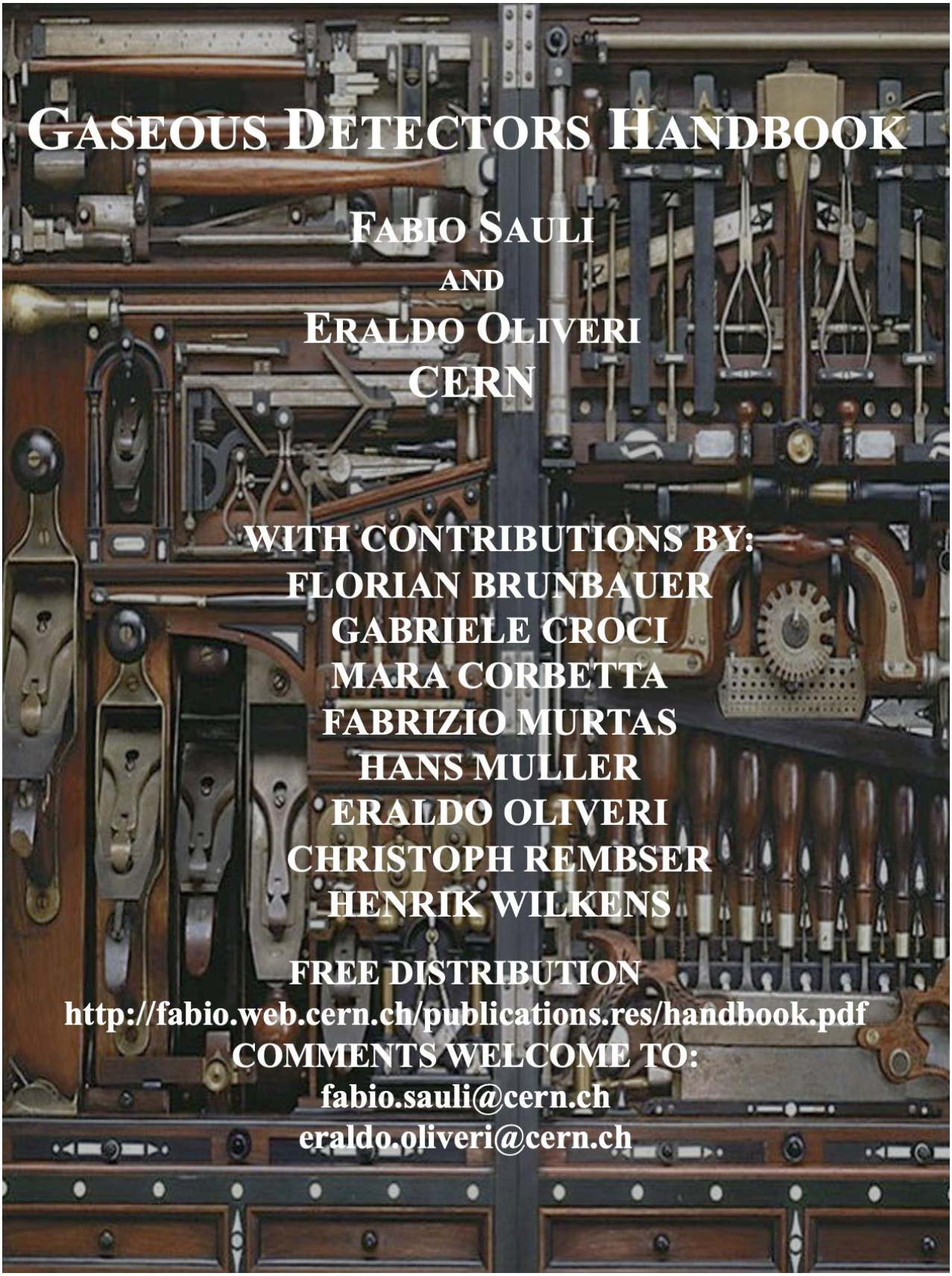

GASEOUS DETECTORS HANDBOOK

FABIO SAULI
AND
ERALDO OLIVERI
CERN

WITH CONTRIBUTIONS BY:
FLORIAN BRUNBAUER
GABRIELE CROCI
MARA CORBETTA
FABRIZIO MURTAS
HANS MULLER
ERALDO OLIVERI
CHRISTOPH REMBSER
HENRIK WILKENS

FREE DISTRIBUTION
http://fabio.web.cern.ch/publications.res/handbook.pdf
COMMENTS WELCOME TO:
fabio.sauli@cern.ch
eraldo.oliveri@cern.ch

FOREWORD

This document collects plots and tables useful to understand and operate gaseous counters, and in particular the recently developed micro-pattern devices. An extended bibliography provides references to relevant works on the subject, as well as links to numerous web-based software tools permitting to estimate gas properties as energy loss of charged and neutral radiation, drift and diffusion of electrons and ions.

Readers are encouraged to send to the author proposed additions and corrections that can be included in future upgrades of the writeup.

The aim of the authors Figure 1-1is to give to the Handbook the largest distribution to all interested scholars; it is available for free downloads and can be printed and circulated. Registration is not required, but will allow the users to receive future upgrades of the document; please send an e-mail to the author with the mention "Handbook" in the subject line, as well as any comment, suggestion and proposals for improvements. Short contributions on related subjects are welcome and will be included in future upgrades.

Some contributors are, or have been, members of the Gas Detectors Development (GDD) group at CERN led by Leszek Ropelewski; the group is associated to the international collaboration RD51 and DRD1, Development of Micro-Pattern Gas Detector Technologies.

Comments to: fabio.sauli@cern.ch or eraldo.oliveri@cern.ch

Gaseous Detectors Handbook downloads:
https://fabio.web.cern.ch/handbook.html

Fabio Sauli Home page:
https://fabio.web.cern.ch

CONTENTS

1 UNITS, CONVERSION FACTORS AND CONSTANTS

Metric prefixes:

yotta (Y)	zetta (Z)	exa E	peta (P)	tera (T)	giga (G)	mega (M)	kilo (K)
10^{24}	10^{21}	10^{18}	10^{15}	10^{12}	10^{9}	10^{6}	10^{3}
deci (d)	centi (c)	milli (m)	micro (μ)	nano (n)	pico (p)	femto (f)	atto (a)
10^{-1}	10^{-2}	10^{-3}	10^{-6}	10^{-9}	10^{-12}	10^{-15}	10^{-18}

Length

1 meter (m) = 39.3700 inches (in) = 3.2808 feet (ft)
1 mil = 0.001 in = 0.0254 mm = 25.4 μm
1 kilometer (km) = 1000 m = 0.62137 mile
1 centimeter (cm) = 10^{-2} m
1 micron (μm) = 10^{-6} m = 10^{-4} cm
1 nanometer (nm) = 10^{-9} m
1 ångström (Å) = 10^{-10} m = 10 nm
1 fermi = 10^{-15} m
1 light year = 9.4637 10^{15} m

Time

1 hour (hr) = 60 minutes (min) = 3600 seconds (s)
1 day (d) = 24 hr = 1440 min = 86400 s
1 year (y) = 365 d = 8760 hr = 5.265 10^{5} min = 3.1536 10^{7} s

Angles

1 radian = $360^{0}/2\pi$ = 57.2958 deg

Mass:

1 gram = 2.2046 10^{-3} lb
1 lb = 453.592 grams

Density

1 gram/cm^3 = 0.03613lb/cubic inch

Pressure

1 atmosphere (atm) = 1.0133 bars = 760 torr (mmHg) = 14.696 lb/square inch
1 dyne/cm^2 = 1.01971 10^{-3} g/cm^2

Temperature

1 centigrade (^{0}C) = 1 Kelvin (^{0}K) = 1.8 Fahrenheit (^{0}F)
0 ^{0}K = -273.14 ^{0}C = -459.72 ^{0}F

Force

1 newton (N) = 10^{5} dyne = 1kg-meter/s^2 = 0.2248 lb wt

Work and energy

1 joule (J) = 1 newton-meter = 10^{7} ergs = 10^{7} dyne-cm
1 gram-calory = 4.186 joules
1 electron-volt = 1.602176 10^{-19} joule
1/kT = 38.6817 eV (at 300 ^{0}K)

Power

1 watt (W) = 1 joule/s
1 horse power (hp) = 745.70 W

Electrical units

Charge: coulomb (C)
Current: ampere (coulomb/s) (A)
Voltage: volt (V)
Electric field E (V/cm))
Reduced electric field E/N: Townsend (Td) = 10^{-21}Vm^2
Capacitance: farad (F)

Resistance: ohm (Ω)
Bulk resistivity: Ω cm Surface resistivity; Ω/square
Magnetic field: gauss; 1 tesla (T) = 10 kgauss

Miscellaneous physical constants

Standard Temperature and Pressure (STP): 0^0C, 1 bar
Normal Temperature and Pressure (NTP): 20^0C, 1 bar
Density of air (STP): 1.29 10^{-3} g/cm^3
Density of water: 1 g/ml (0^0C); 0.9970 g/ml (25^0C)
Velocity of sound in air (STP): 331.7 m/s; in water (20^0C): 1470 m/s
Cross sections: 1 barn = 10^{-24} cm^2
π: 3.141593...
e: 2.7182818...
Planck constant h = 6.6260 10^{-34} J s
$E = h\,c/\lambda$
E (eV)=1.298/λ (μm) = 1298/λ (nm) (Figure 1-1)
E (keV) = 12.40/λ(Å)
Boltzmann constant (k): 1.3806 10^{-23} J/^{0}K = 8.617 10^{-5} eV/^{0}K
Avogadro number: N_0 = 6.02214 10^{23} molecules/g mole
= 2.6871 10^{19} molecules/cm^3 (ideal gas at STP)
Loschmidt constant N = 2.6867811(15)×10^{25} /m^3 (ideal gas at STP)
Velocity of light (c): 2.99792 10^{10} cm/s
Electron charge: 1.6027 10^{-19} C
Electron mass m_e: 9.1085 10^{-28} g = 0.51098 MeV
Specific electron charge e/m_e : 1.75888 10^{11} C/kg
Proton mass m_p: 1.67243 10^{-24} g = 938.232 MeV
Neutron mass m_n: 1.67474 10^{-24} g = 939.526 MeV
Alpha particle mass $m_{\alpha:}$ 6.6442 10^{-24} g = 3727.377 MeV
Free space permittivity ε_0 = 8.8542 10^{-12} farad/m
Free space impedance $Z_0 = 376.731\ \Omega$

Radioactivity, exposure and dose

Activity: becquerel (Bq) disintegrations/s; 1 curie (Ci) = 3.7 10^{10} becquerel (Bq)
1 röntgen (rem) = 2.58 10^{-4} C/kg-air = 10^{-2} sievert (Sv)
Absorbed dose: 1 gray (Gy) = 1 J/kg
1 rad = 10^{-2} Gy; 1 krad = 10 Gy

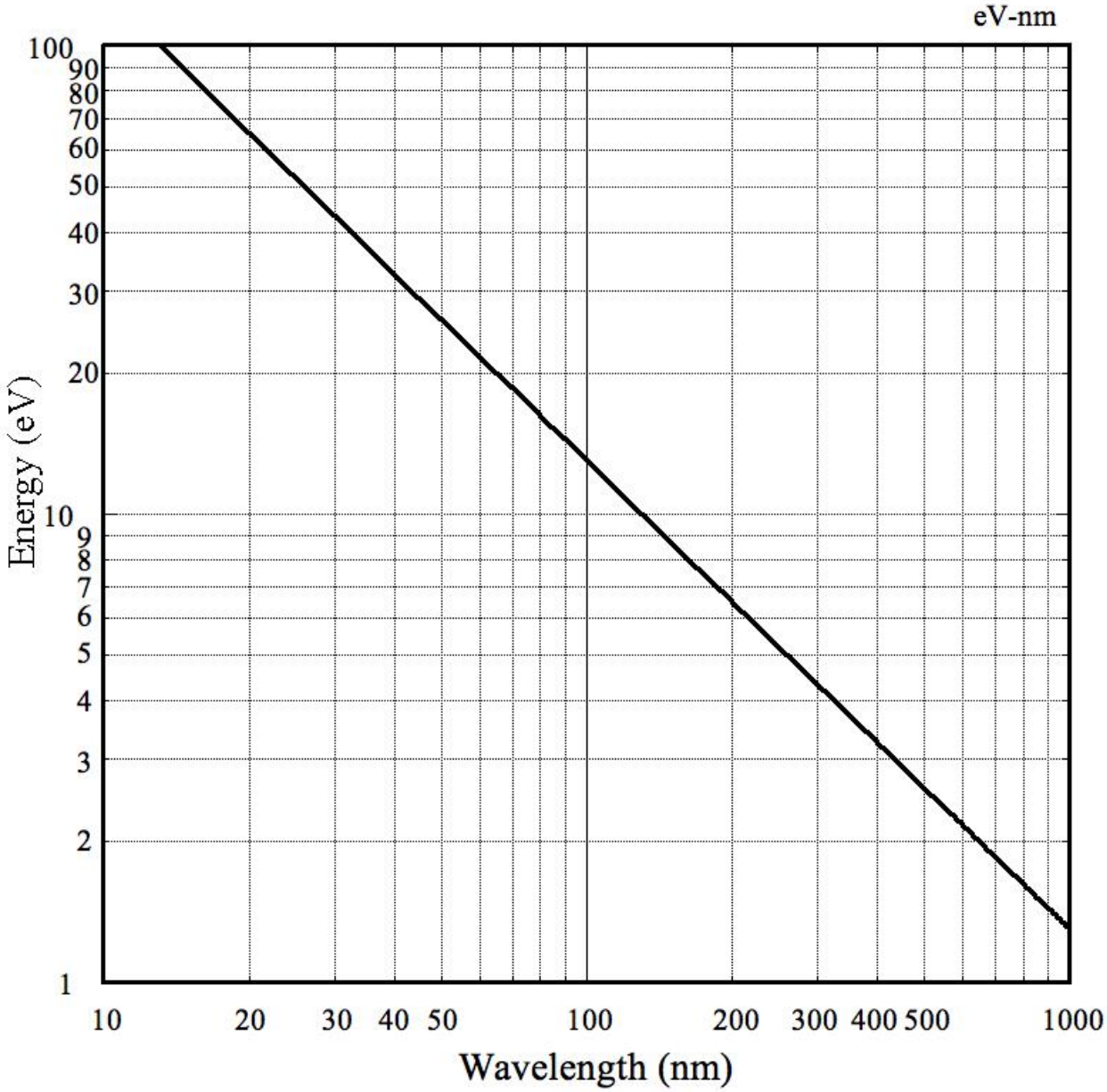

Figure 1-1: Photon's wavelength-energy correlation.

2 BASIC LABORATORY HARDWARE

Contributed by Florian Brunbauer (CERN)

Commissioning, operation and calibration of gaseous detectors in the lab makes use of a wide range of specialized instrumentation and optical and electronic readout devices. Equally important, various pieces of basic laboratory hardware are used in the development and study of gaseous detectors and in setting up laboratory test benches to characterize their performance. This section describes some basic equipment and give examples of useful hardware.

Specific instruments are indicated as examples and do not in any way represent a recommended choice; a variety of equivalent tools are available with alternative suppliers and should be considered as options to satisfy the requirements.

2.1 Low voltage power supplies

While detector powering typically requires HV supplies, described in more detail in a following chapter, many types of instrumentation and readout devices require low voltage power supplies. This can range from supply voltages of ±5V for some preamplifiers to providing low voltage power to advanced front end chips and readout hybrids. For laboratory test benches, low voltage supplies providing voltages of typically 5V, 12V or 24V may also be used to power motorized stages, environmental sensors, valves or cooling fans. Low voltage power supplies often feature multiple channels, which can be independently controlled. An example is the Gossen LSP 33K triple-channel DC power supply unit shown in Figure 2-1.

Figure 2-1: Triple channel power supply with independent channels and voltage or current controlled modes (Gossen LSP 33K).

Individual low voltage power supply channels have voltage and current control knobs or digital setting of voltage and current parameters. They can be operated in voltage or current controlled modes, where one parameter will be imposed and the other one will follow up to a defined limit. If a device needs to be supplied with a fixed voltage, the desired voltage can be set in voltage-controlled mode and the supply will try to keep the output stable at this voltage. Only when excessive current flows through the circuit (higher than the set current limit or capabilities of the device) will the voltage be decreased. In current controlled mode, the device will try to maintain a set output current while adjusting the voltage. Before switching on / enabling outputs, be sure to verify if the device is operating on voltage/current controlled mode and that voltage and current setpoints are correct.

Many low voltage power supplies feature + and - terminals for each channel so the polarity can be defined by the user. If a positive output voltage is needed, the - terminal can be connect to GND (e.g. a banana-plug cable to yellow-green port) and positive voltage will be available at the + terminal. Conversely, if a negative voltage is required, the + terminal can be shorted to GND and negative voltage is available at the - terminal. Thus, multi-channel power supplies can be easily used to provide positive and negative voltage for example to bipolar preamplifiers. For this, the - terminal of channel 1 and the + terminal of channel 2 can be shorted together to provide a common reference and then the + terminal of channel 1 and the - terminal of channel 2 can be used to provide positive / negative voltage, respectively.

2.2 Electrical measurements

Basic electrical measurements such as voltage, current, resistance and capacitance are useful for verification of connections, basic tests of detector integrality and troubleshooting. Most basic electrical measurements can be performed with digital multimeters and even basic devices provide high flexibility and many different measurement modes. An example is shown in Figure 2-2

Figure 2-2: Left: Digital multimeter for basic electrical measurements (Keysight U1241B). Right: High voltage probe for multimeter (Fluke 80K-6).

For debugging power and detector connections, multimeters can be used to measure the continuity of cables, verify that (low) applied voltages are correctly applied to detect a detector. When testing detectors such as GEMs, multimeters can be used to measure resistance between electrodes and verify that there are no electrical shorts. In addition, they can be used to get a coarse measurement of capacitance between electrodes to verify connections and confirm that capacitances are as expected.

To verify high voltages on the detector, high voltage probes can be used which feature voltage dividers to scale high voltage values down to values compatible with multimeters. For example, a 1000:1 high voltage probe can be used to verify that high voltage values are correct applied along a resistive voltage divider chain. Using such a device, e.g. 2kV applied on the cathode of a detector will be scaled to 2V recorded by the multimeter.

2.3 High-resolution ammeters

Monitoring the current on detector electrodes requires high resolution ammeters. During detector calibration but also during prolonged operation, recording currents on electrodes of a gaseous detector can be a valuable tool to measure and monitor gain and stability.

Picoammeters like the one shown in Figure 2-3 below offer high resolution and sensitivity and can be used to see even small current or variations in current on detector elements.

Figure 2-3: Example of a picoammeter with a range from 2fA to 20mA (Keithley 6487).

For measuring the gain and calibrating detector response, a wide dynamic range for current measurements is important. Depending on incident radiation type and flux, primary currents used in laboratory test setups can typically vary from below a pA to nA ranges. When measuring currents in a detector with high charge multiplication values of several µA can be reached.

To minimize noise and allow for high sensitivity current measurements, ammeters like the one shown above can use triax cables, where the inner conductor and the inner shield are used for the in-series current measurement and the outer shield to minimize noise. Ammeters will have a high-impedance input and a low-impedance output - in the device above, the inner conductor is the high-impedance input. This input should be connected to the detector electrode (current source) while the low-impedance output should be connected to the power supply or GND, depending on the power scheme of the detector. The outer conductor should be well grounded.

To protect the ammeter from possible discharges in the detector, a high value series resistor should be connected between the input terminal and the detector electrode.

Ammeters may also be able to provide a certain bias current, which can be used for resistance measurements across a wide range of values. This can be used e.g. to measure the insulation between detector electrodes: to this extent, the ammeter should be configured to provide a constant voltage and measure the current flowing with high precision for >GΩ resistance measurements.

Digital ammeters with connection interfaces can be remote controlled and read out with vendor-provided software. This may be used for averaging multiple measurement points for low currents.

2.4 Oscilloscopes

From basic operation of detectors and recording of first signals to detailed performance tests, oscilloscopes offer a versatile way to record and visualize electronic signals collected on detector electrodes. Basic oscilloscopes like the one shown in Figure 2-4 are useful for verifying detector operation, stability, minimizing noise and recording signals.

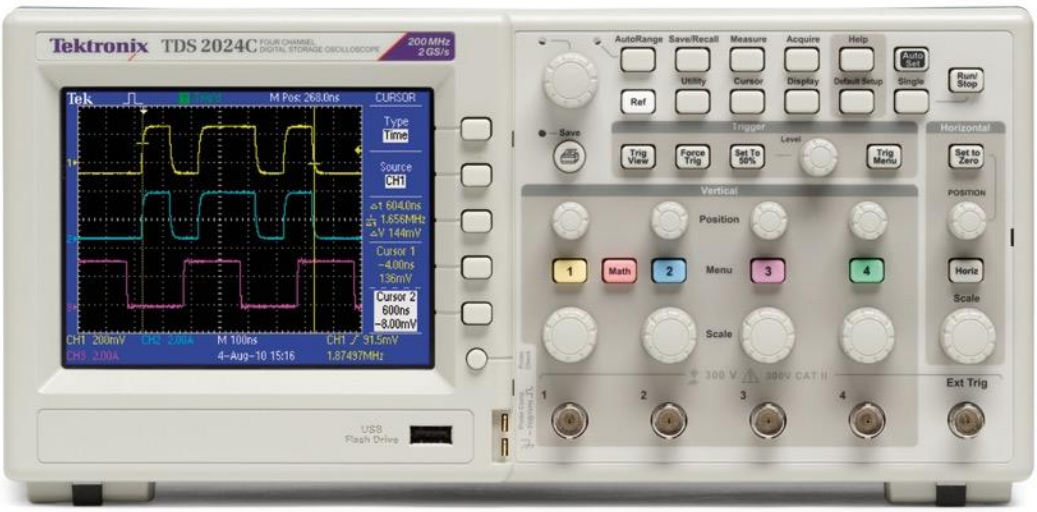

Figure 2-4: 4-channel digital storage oscilloscope (Tektronix TDS2024C).

Important characteristics of oscilloscopes are their bandwidth, their sampling frequency and memory, input termination options and their connectivity and signal acquisition options. For basic performance tests and verification of detector stability, sampling frequency and bandwidth are not of great concern and several hundred MHz bandwidth and close to GSample/s sampling are sufficient. When using shaping preamplifiers with long shaping times, lower end specifications of oscilloscopes are typically sufficient.

When using high-bandwidth preamplifiers to reproduce detector signal shapes, oscilloscopes also have to provide high bandwidth and sampling frequencies to accurately digitize signal shapes. Bandwidths of several GHz and sampling frequencies >10GS/s are available in medium to higher end oscilloscopes and can be used to accurately record fast signals from high-bandwidth preamplifier.

Modern oscilloscopes provide advanced signal processing and statistics functions and can be used to measure a wide range of quantities in real time. This can include monitoring the rate of signals as well as measurement and plotting the distribution of signal amplitudes or integrals which can be used for real-time monitoring of detector gain and stability.

2.5 Gas leak detectors

Verifying gas tightness of detector vessels is an important and regular task when assembling detector prototypes. This is true both for ensuring good gas quality and know gas composition in a detector but especially when working with flammable or otherwise harmful gases. A simple verification of tightness can be performed by comparing input and output gas flow. When using e.g. ball-flow meters like Vogtlin's *V-100* flowmeters, on both input and output gas lines of a detector, the fluxes can be readily compared. When flowing gas at rates of several l/h, an output flow value lower than the input flow hints at a leak of the detector vessel or gas connections.

To find the location of leaks in order to address the issue, several different tools are available. If the inside of the vessel is slightly above ambient pressure, which will be the case if there is a flowmeter or other flow restricting device on the output gas line, the gas leaking out of the vessel can be used to find the leak location. A basic method can be the use of soap-based sprays to apply soap on areas suspected of leaking and checking for bubble formation. Significant leaks will incur a formation and growth of soap bubbles and point at the leak location. It should be noted that this may leave residues of soap on the vessel which may not be acceptable or desired.

An alternative way is the use of electronic gas leak detectors such as the device shown in Figure 2-5:

Figure 2-5Figure 2-5: General purpose leak detector (**Qualichek 196**).

General purpose leak detectors emit audible or visual alarms when detecting certain gases and can typically be switched to be sensitive to different gases such as He, Ar, CO_2 to name but a few. Approaching the detector with the probe of a gas leak detector can be a selective way to test suspected leaks in different locations around the vessel. Care should be taken to allow for sufficient reaction time when the probe is pointed at a single location before moving on to another one.

If the detector vessel can withstand vacuum, an alternative gas leak search method could be used: pumping the vessel to below a few mbar level, monitoring the pressure with a vacuum gauge and spraying solvents like ethanol on areas with suspected leaks. In this case, a pressure increase indicated by a gauge can hint at a leak in the location on which the liquid was applied.

An advanced way to measure gas quality and verify detector tightness is the use of gas analyzers measuring the speed of sound in a gas mixture and comparing it to expected values like the device shown in Figure 2-6*:*

Figure 2-6: Binary Gas Analyzer (**SRS BGA244**).

This non-invasive device can be connected in the output line of a detector and can be set to detect either a single gas species and monitor its purity or detect a gas mixture and monitor the mixing ratio. Any contaminations such as air leaking into the detector will be reflected in a lower purity value or a mixing ratio deviating from the expected value for single gases or mixtures, respectively.

3 HIGH VOLTAGE POWER SUPPLIES AND DISTRIBUTION

Contributed by Fabrizio Murtas (INFN-LNF)

3.1 Voltage and current ranges required for gaseous detector

Gas detectors are typically supply with high voltages with the aim of creating charge drift and multiplication fields in order to create the electrical signals. The electric fields generally range between 0.1 and 5 V/cm for the drift fields and several hundred V/cm for the fields necessary for charge multiplication.

Depending on the geometry of the detector, the needed voltages can reach up to O(10 kV).This requires particular attention in the handling of detectors and the use of appropriate protections to avoid electrical discharges that may involve the researcher himself. Typical currents driven by detector are less than mA, depending also on the incident particle flux.

One of the most complex detectors to be powered is certainly the triple GEM, which needs seven power supply channels in cascade for a single detector. Depending on the type of detector you want to build also other high voltage channels can be added to the system. It is for this reason that we will focus on triple GEM detectors to describe the high voltage systems to be used for gas detectors. Typical layouts are shown in Figure 3-1.

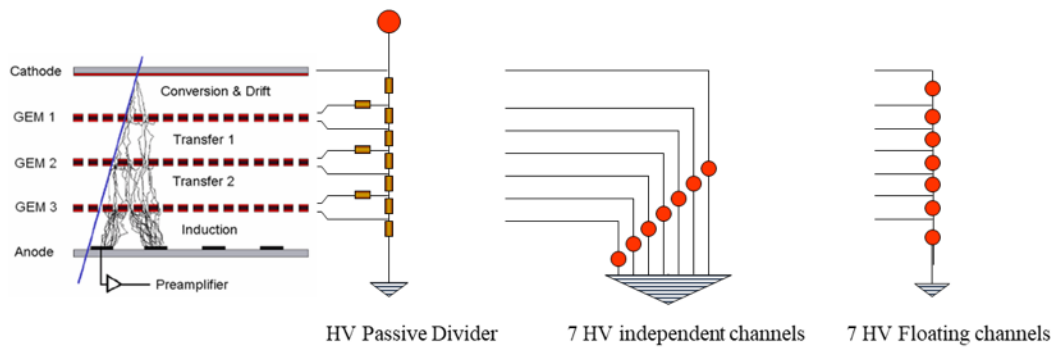

Figure 3-1: Voltage scheme typically used in a Triple GEM detector

Three possible solutions have been used to implement a triple GEM HV power supply:
1. A resistive divider which, where one HV channel supplies the 7 voltages;
2. Seven independent HV power supplies in cascade, all referred to ground;
3. Seven floating power supplies each referring to the previous stage.

Advantages and disadvantages of the individual solutions are:

1) The advantage lies in the use of only one power supply channel but suffers from a high partition current, preventing the monitoring of the currents drawn by the individual GEMs. In case of a continuous discharge on a GEM foil, it is difficult to detect it unless there are current monitors after the divider for each supply line. The electric fields and the GEM voltages are fixed by the values of the resistors used: when the detector gain is changed, all electric fields automatically change. To achieve a stable condition of the detector gain, the divider current is usually set two order of magnitude higher than that needed for the chamber operation.
2) The layout of seven independent power supplies referred to ground allow a precise control of the GEM's voltages and the drift fields, but with the major disadvantage that in the event of discharges and power rapid changes on the voltages can be applied to the single foil which can damage it. To overcome this problem, it is necessary to set the parameters of the power supply in such a way that the up and down ramps prevent exceeding 500 V for each single GEM. The HV power supply can monitor the individual currents with high precision (typically order of nA). Using this configuration, it is possible to set the gain of the detector independently from the drift fields.

3) Use of seven floating power supplies, each referring to the previous stage, allow maximum flexibility in the powering of the detector, with maximum protection even in case of discharge of individual GEMs. There are no needs of particular configuration and settings of the HV system.

3.2 Noise requirements, filtering

Triple-GEM technologies are used to detect particle fluxes up to MHz/cm^2 on active areas of hundreds of square centimeters. Fluctuations in energy loss or local defects may induce occasional discharges, with the energy of the charge stored in the capacitance between electrodes; for large areas and voltages this can result in permanent damage of the electrodes. An effective protection against damages is the reduction of the GEM area, dividing the electrode in sectors individually powered ,and an increase of the recharge time to prevent a continuous discharge. Sectors are separated foils with 200 μm separation lines typically on the side facing the drift electrode; it is preferred not to exceed 100 cm^2 of surface for each sector. Trying to avoid an increment of the HV channels, the sectors are decoupled through 1 Mohm SMD resistances soldered directly on the GEM foil (Bencivenni *et al.*, 2002).

HV filters (Figure 3-2) can be used to reduce noise and pickup; the use of resistive circuits for HV filtering and discharge protection can however reduce the rate capability to few tens of kHz/cm^2 or less; this effect has been recently reported on the X ray spectroscopy for Tokamak monitor systems. So while the choice of the C in the scheme of (Figure 3-2 is 2 or 3 nF (1/5 of the GEM sector capacitance), the resistors value has to be selected depending on the particle flux impinging on the detector during its operation.

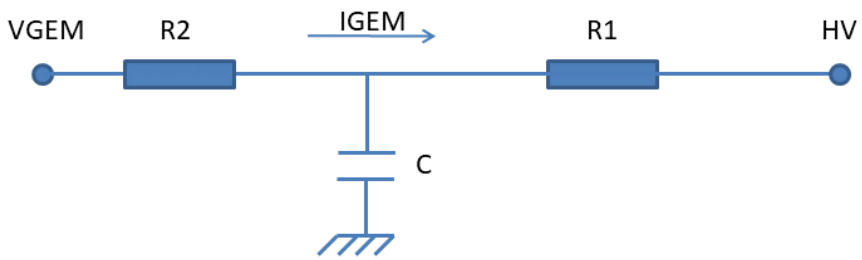

(Figure 3-2: Typical scheme of a High Voltage filter.

For medium rate detector, the choice is typically R2=1 MΩ, C=2.3 nF, R1=470 kΩ, optimal to protect the GEM but resulting in a moderate 1% drop of the operating with 3 μA of detector driven current.

For high-rate fluxes (20 μA currents) the previous choice could be problematic, as it results in the voltage drop of 7%. A better configuration in this case could be 100 kΩ-2.3 nF-47 kΩ, with a consequent reduction of voltage around 0.5%. Probably also a configuration 10 - 2.3 - 47 could be safe because the recharge time is about 25 μs allowing removal of the ions produced inside the holes during discharge. Choosing too low resistors values however can result in a deterioration of the GEM or a permanent short circuit.

One has to bear in mind that the filters are also used to decouple the detector from the power supply system: in the case of large distance between detectors and power supplies, the energy stored in the cables can very harmful in case of discharge of the detector.

Figure 3-3 shows two type of filters for triple GEM detector, adopted for the LHCb muon chamber and the GEMPix detector (Murtas, 2020).

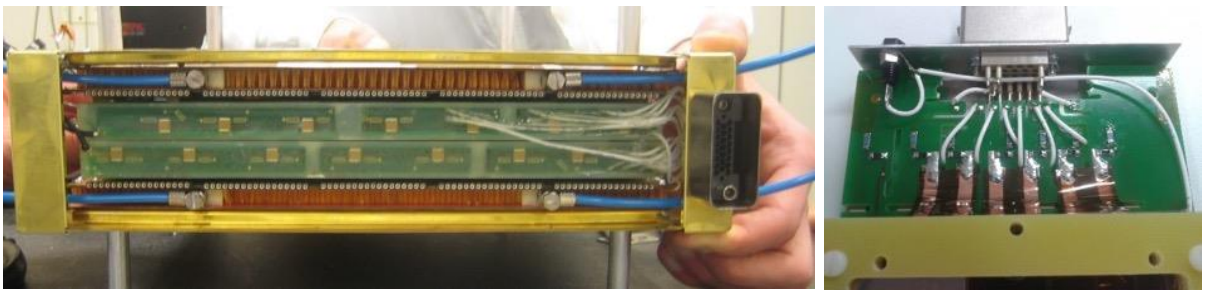

Figure 3-3: on the left the filter used for the LHCb chamber; on the right the GEMPix filter before the insulator bath with Ciba 2011.

3.3 Self-contained units (DC-DC converters)

Several models of commercial power supplies, shown in Figure 3-4, are very useful for detector development works. All of them have both negative and positive polarity**,** hardware-settable on the module, reaching voltages up to 8 kV. The output connector is always an SHV.

The N471A module is often used to control the currents drawn by the detector with nA sensitivity. It has been used very often for quality control and conditioning of GEMs before the final detector assembly. It is relatively old with manual settings, including maximum currents and ramps), but has the advantage of real time monitoring of the current on a small dial. It has two channels with a voltage resolution of 1V and ripple of 60 mV.

The N1471 module, an evolution of the previous**, t**he N1471A module has the possibility of remote control and **is** therefore also controllable by Labview programs with USB cable**s**. It was also used for the bias of diamond detectors or for the drift field of small TPCs.

Figure 3-4: From left to right: the modules N471A - N1471A - NDT1471 (CAEN)

The NDT1471 module has the advantage over the previous two to have 4 channels instead of two and the possibility of control through the Ethernet connection, providing the voltage up to 5.5 kV with greater precision (0.1 V) and lower ripple.

3.4 Single channel units, 0-6 kV or higher (passive divider)

The passive divider is certainly the simplest power supply system in absolute, but has low flexibility in setting of the field and gain of the detector, therefore less suitable for laboratory studies and development of detectors. It is typically used after the optimization studies as final power supply for the experiment. The partition current should be between 20 and 100 times higher than the maximum current drawn in operation by one of the stages: this ensures a few percent some stability of detector gain under changes in the particle flux.

Particular attention must be paid to the filters placed just before the detector in order to avoid that shorts on the detector can cause the partition current to reach the single stage. For the LHCb chambers an HV system was designed with three channel in input: one for the third GEM, one for the other 2 GEMs and one for the Drift, with the scheme shown in Figure 3-5.

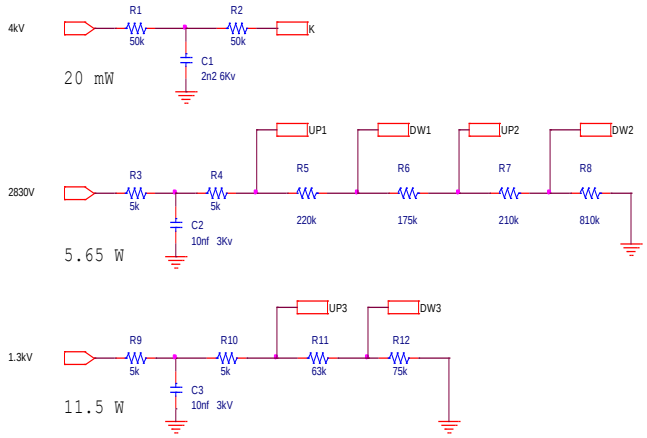

Figure 3-5: Schematics of a resistive divider for the LHCb Triple GEM with three HV channels input and seven outputs.

The divider must be made on an alumina substrate with dissipating bottom layer, paying special attention to the edge insulation. Resistors must be trimmed with 1% tracking and must be made with resistive paste at least 50 ppm. The total power dissipation of the passive divider was 17.5 Watts This divider was built as prototype but not used for the experiment, for which the floating system was preferred.

For systems in which the stability of the detector gain is not an issue, this type of solution can be used because it reduces the cost and the complexity of the system. For example, it has been adopted for the HV supply of the Multilayer Boron converter for thermal neutron detector (Muraro *et al.*, 2021), Figure 3-6.

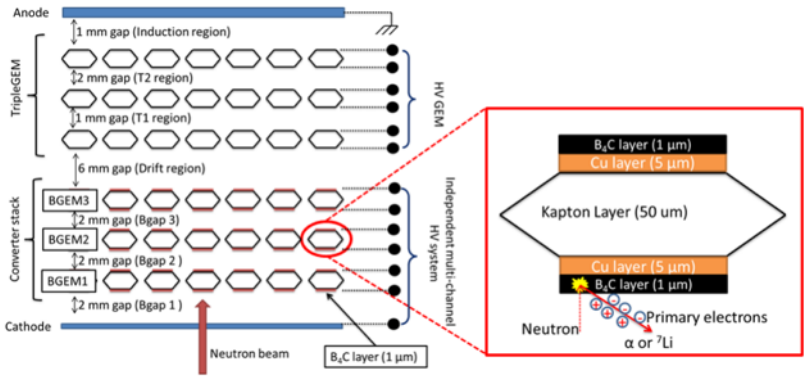

Figure 3-6: The multiboron GEM converter stack (lower part in the picture) for thermal neutron detection can be easily supply with a passive divider when the working point has been established.

3.5 Crate-based, interface controlled single and multiple units

To satisfy the need to power a triple GEM with 7 independent channels or a more complex detector (Muraro *et al.*, 2021) (Muraro *et al.*, 2021)the only solution is to use a HV crate system with one or more boards, depending on the characteristics of the detector or the number of channels to be powered. The crates of the SYx527 family are among the most reliable and allow remote control via Ethernet or USB even through LabVIEW programs (Figure 3-7).

(Figure 3-7: The HV crate system SYx527 with two typical boards 12 SHV output: on the left the A1561H with floating channels, on the right the A1535DN (CAEN).

The board used to power the triple GEM was the A1561H with 6 kV / 20 µA output range, available with either positive, negative or mixed polarity.

Particular attention must be paid to the management of switching on and off of the detector to avoid applying excessive voltage differences on individual GEM foil that could damage it permanently. In case of power supply through 7 independent channels all referred to ground it is necessary to adjust the ramps (UP and DOWN) in a proportional way to the final value of voltage; this ensures that a single GEM can never be powered at a value higher than the final.

This type of management is very often realized with the help of a LabVIEW programs that allow to set at the same time the UP/DOWN ramps for each modification of the fields and gain voltages, through the graphic interface (Figure 3-8).

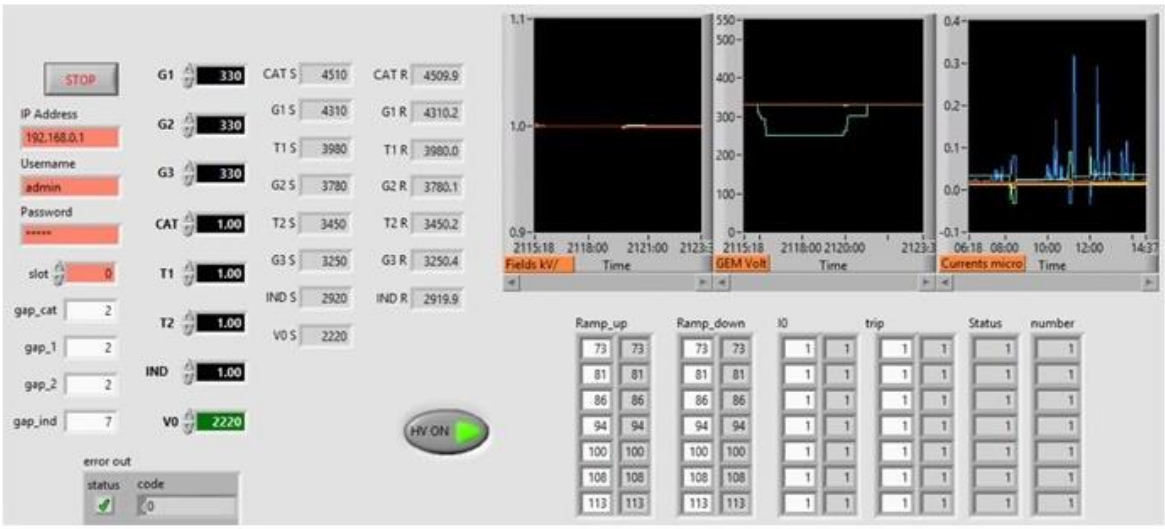

(Figure 3-8: The LabVIEW control of the HV crate with ramp values proportional to the voltage setting as a function of the shutdown time.

A particular expedient must be used for the trip management of the power systems. It is known that it is possible to turn off one or more channels of a power supply when the current exceeds a certain threshold value for more than an interval of time; this can happen when a continuous discharge is induced by ionization channels inside the detector that could permanently damage it. In this case it is important to set the system parameters so that in case of trip the shutdown sequence follows the ramps set on the system for all the channels involved.

Following the successful operation of the floating power supplies (Corradi, Murtas and Tagnani, 2007), the A1535DN board has been developed that reproduces substantially the same characteristics with 12 SHV output channels.

3.6 Floating High Voltage dividers

A first prototype of an Active Voltage Divider has been designed and realized in Frascati in 2006 (Corradi, Murtas and Tagnani, 2007) with seven floating power supply; the module and its equivalent scheme are shown in Figure 3-9.

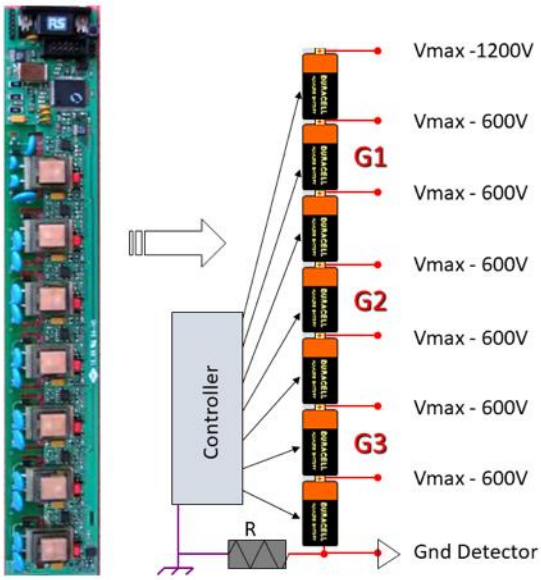

Figure 3-9: The HVGEM scheme with 7 floating channel controlled by Controlled Area Network (CAN bus).

The low operating voltage (12V) and power consumption (1.2W) are some of the most remarkable characteristics reported in the following performances:

- six channels max 600 V and 200 µA;
- one channel max 1200 V and 100 µA;
- 5 KV isolation between HV and ground;
- CANBus controller;
- read and write voltages, temperature and PS monitoring

Another commercial device built in standard 2-units NIM with the same output characteristics was designed a few years after for detector development purposes, with each channel having a high sensitivity current meter able to detect the GEM discharge and consequently protect the detector.

The HVGEM NIM module and the electric scheme are shown in Figure 3-10; they can be controlled through CANBus for voltage monitoring and settings. The performed measurements show a very good stability and a noise reduction on the triple GEM chamber readout, allowing a 2 fC threshold setting on the front-end electronics. This HVGEM has been used in the GEMPix developments (Murtas, 2020) for its flexibility in gain and field settings and never resulted in a permanent damage on the Timepix readout, also with some GEM discharge. It is currently used in some permanent installations for tokamak plasma diagnostics (Pacella *et al.*, 2013) and some hadron-therapy and gamma-therapy studies (Leidner, Murtas and Silari, 2021). Also in this case the control of the module can be through Labview programs (Figure 3-11).In some cases, it has been used together with a temperature and pressure sensor placed inside the detector to keep the gain constant within 10%.

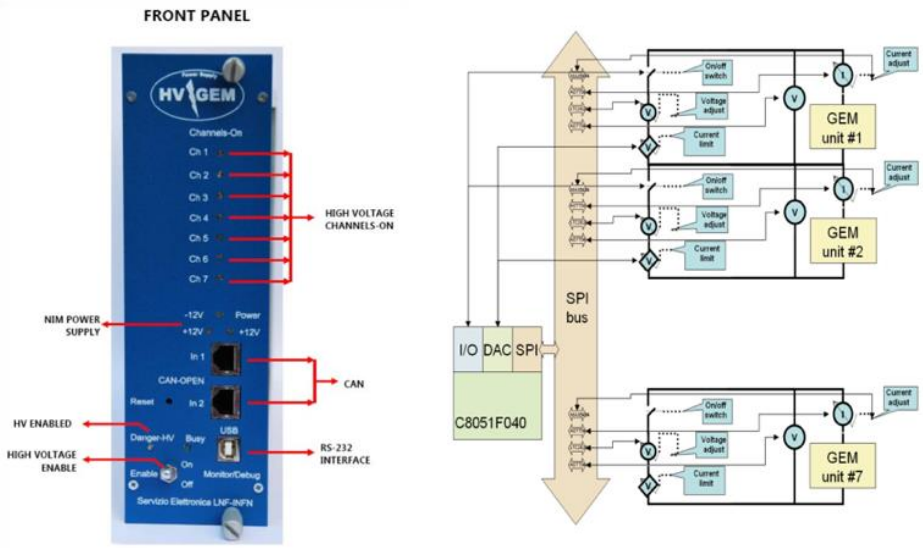

Figure 3-10: HVGEM NIM module front panel and the electrical scheme (ARTEL).

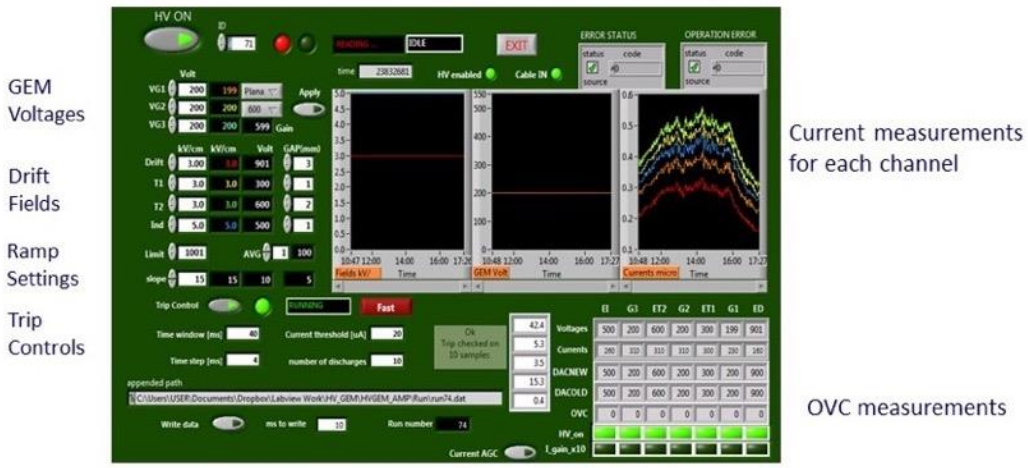

(Figure 3-11: Labview display for the HVGEM monitoring and control.

A custom HV Crate was built for the 24 LHCb triple GEM chambers using this technology (Bencivenni *et al.*, 2002). The crate, shown in Figure 3-12, was assembled with 24 HVGEM boards and 24 nano-ammeter for the control of the current driven by the GEM3 lower face of each chamber. The system has operated flawlessly with no card replacements for 5 years. The cables used from the crate to the detector were 50 m long with a final Redel connector attached to the filter shown in Figure 3-3.

Figure 3-12: LHCb High-Voltage System with 24 HVGEM modules and nano ammeter; on the left the current and voltage monitoring system developed by LHCb.

3.7 Voltage distribution, connectors and cables

One of the most crucial points is the distribution of the high voltage from the power supply to the detector. Typically, multi-core cables are used like those used for the Kloe Drift Chamber. The single poles are made of a single conductor made with an alloy resistant to rupture; in the past, wire breakages have been observed with other types of cables, leading to problems that are difficult to find. The connectors typically used are Redel 51 pins or 22 pins, Figure 3-13. Redel connectors exist in five types depending of the position between the source and detector:

- panel HV emitter . . . . . : contains the male pins
- extension cable connector . : contains male pins
- cable receiver: . . . . . : contains female pins
- cable emitter. . . . . : contains male pins
- panel receiver . . . . . : contains 4 female pins

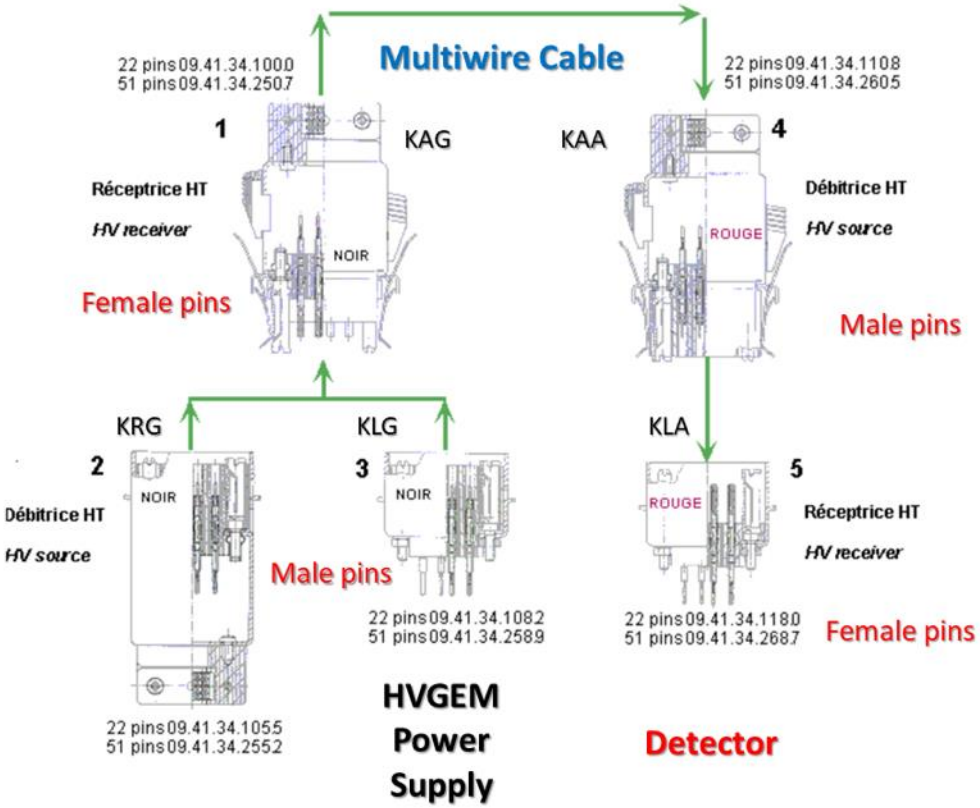

Figure 3-13: Five Redel connectors types (LEMO).

A trick used on HVGEM systems is to have two wires inside the cable used as remote sensing of detector presence. The two wires are short-circuited only by the detector: only when it is really connected to the power supply is the voltage reduced. In Figure 3-14 note the disposition of the 7 wires for the HVGEM systems, in order to avoid as much as possible discharges inside the connector itself. Another useful expedient is the use of small heat-shrinks around the soldering of the wire on the pin. This will decrease the voltage difference between the wires. This decreases the exposure of the conductor to the air and mechanically strengthens the junction between wire and pin.

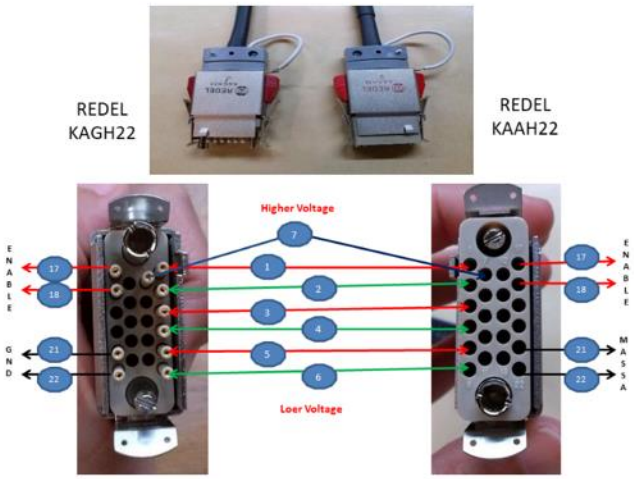

Figure 3-14: The seven-conductor poles of a GEMPix connector. Other two poles are used to enable the HV.

Where the high voltage system has detector-driven current monitoring, it is good practice to ensure that conductors throughout the path from the power supply to the detector are exposed as little as possible to the air. Take in mind in fact that a small change in the air humidity is enough to increase the leakage currents measured by the system. The current measured in Figure 3-11 were induced by an air conditioner placed near the detector with an exposed HV wire.

An important action is to seal the filters just before the detector in a resin bath typically made with Ciba 2011 glue; the connector-filter used for triple GEM detectors 10x10 cm^2 and the filter mounted on the cathode board of the GEMPix detector were shown in Figure 3-3.

4 IONIZING RADIATIONS

4.1 Overview

All along their development and construction, gaseous detectors undergo systematic verification and test procedures in the laboratory; some of the testing systems remain integral part of the completed devices when operated in experimental setups. Methods and protocols for monitoring the gas composition, flux and purity, as well as to control the value and stability of the low and high voltage supplies will be described in the next chapters.

A fundamental tool to assess the performances of detectors relies on the exposure to ionizing radiation emitted from various sources, observing and recording their response as a function of operating parameters (gas composition, applied voltage). The following sections summarize the most commonly used sources of radiation. The ionization yields in a range of gases commonly used in detectors are discussed in chapter 5.

4.2 Cosmic Rays

Cosmic rays of galactic or extragalactic origin invest earth with a flux of energetic particles. Mainly composed of protons and helium ions (93% and 6 %, respectively) they have an exponentially decreasing energy spectrum and almost isotropic distribution. Interacting with the upper atmosphere, primary ions generate a cascade of secondary charged and neutral particles; owing to the generation process, the secondary particles create extended showers. At ground level, the charged radiation field is composed mostly of positive and negative muons, with average energies of a few tens of GeV, with a small percentage of other particles (pions, electrons, photons). The vertical muon flux ($\theta=0$) is around 70 particles/$m^2 s^{-1} sr^{-1}$, traditionally quoted as 1 per cm^2 per minute, decreasing towards large incidence angles θ roughly as $\sim\cos^2\theta$. For a concise review of the primary and secondary radiation fluxes see for example Chapter 30 of the Review of Particle Physics (Zyla, 2020)

In the laboratory, to study efficiency and localization properties, detectors are usually placed between two or more scintillation counter slabs operated in coincidence, permitting to select direction and energy of the cosmic radiation. With two scintillators of 10x10 cm^2 placed at 10 cm, the solid angle subtended is about one steradian and the raw cosmic radiation flux ~ 0.7 Hz. The majority of the particles are minimum ionizing muons, emulating the conditions met in high-energy physics; the occurrence however of events with two or more tracks within the sensitive area can bias the measurement of single-particle efficiency this can be limited by the use of appropriate geometry and reconstruction algorithms. Events are accepted within a time window that depends on the type of detector under test, from tens of ns for fast devices to tens of microseconds for long drift chambers.

To avoid false triggers outside the sensitive area of the detector under test caused by the production of Cherenkov light in the glass windows of the phototubes, sensors are usually mounted on opposite sides of the scintillators. An example of laboratory setup is illustrated in Figure 4-1, built for systematic tests of the CMS resistive plate chambers production modules (Abbrescia *et al.*, 2005). Pairs of scintillation counters on each side of the detector's stack supply the coincidence signal for fast charged particles; two additional counters, covering half of the sensitive area each, provide, when in coincidence, a veto signal against multiple tracks; a further selection is done by software, recognizing multiple events within the resolution time. Up to ten detectors could be operated together; despite the low event rates, analyzing the events as a function of position the performances can be studied as a function of position over large areas, an achievement that would be difficult to obtain using other radiation sources.

Used to monitor the muon flux on the surface generated by pp collisions at LHC, the MATHULSA system is a good example of test stand using scintillation counters and Resistive Plate Chambers position-sensitive detectors (Alidra *et al.*, 2021).

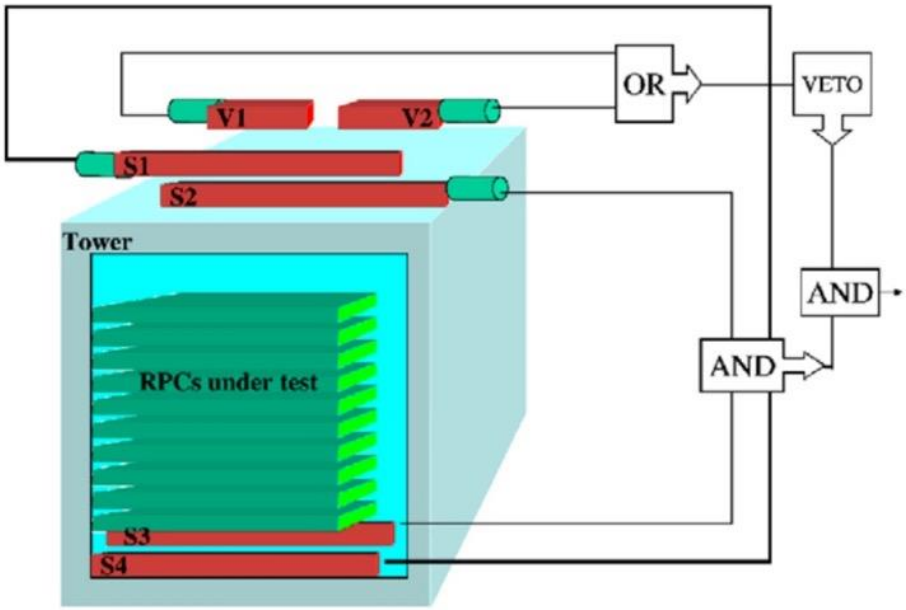

Figure 4-1: Experimental setup used for testing the CMS resistive plate chambers. Four scintillators (S1 to S4) mounted in pairs on each side of the detectors define the trigger; two additional scintillators (V1 and V2), covering half of the sensitive area each, are used as veto for extended showers (Abbrescia *et al.*, 2005).

Figure 4-2 is an example of measured efficiency as a function of operating voltage, both for individual RPC planes and for double-gap detectors; the events displayed in Figure 4-3 correspond to a single and a double recorded track in a nine RPC modules stack under test.

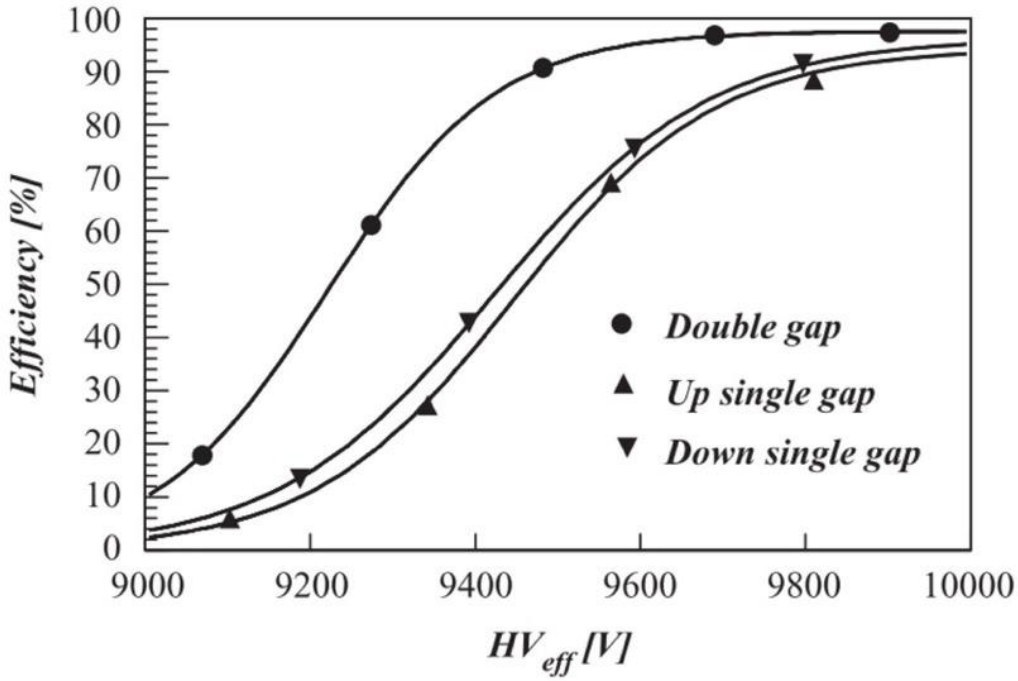

Figure 4-2: Single and double gap RPC detection efficiency on cosmic muons as a function of operating voltage (Abbrescia *et al.*, 2005).

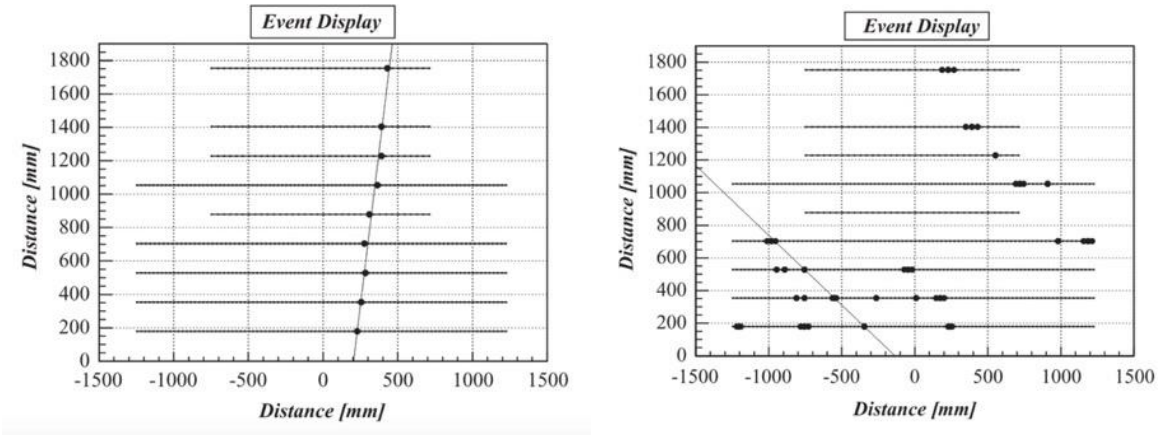

Figure 4-3: Single (left) and double (right) track recorded in the nine detectors stack (Abbrescia *et al.*, 2005).

Muon telescopes of are used for demonstration purposes and tutorials; well-known examples are the spark chamber stack operated in CERN's Microcosm exhibit and several other laboratories. With movable scintillation counter bars for detection and localization, and named Astroparticle Outreach (AstrO), an electronic cosmic telescope has been developed for use by high-school students for the study of geographical and angular flux dependence and attenuation due to high-density surroundings (Grazzi *et al.*, 2020).

Named muon imagers or muographs, electronic telescopes of various designs are used to assess the density and mass distribution of extended objects; the presence of hidden chambers in the Chefren pyramid has been studied with a micro-pattern gaseous detector setup (Procureur, 2018).

4.3 Particle beams and accelerators

Contributed by E. Oliveri, C. Rembster and H. Wilkens

Particle accelerators constitute the best tool for testing detectors in realistic operating conditions, well corresponding to the final experimental conditions of use. Most particle physics laboratories offer temporary or long-term access both to charged, neutron and photon beams; an updated survey of world-wide facilities can be found in a CERN compilation, classified by radiation field, source type and country (‘CERN Facilities Data Base’, 2020)(Gkotse and Gorine, 2020). From this source,

Table 4.1 provides information on type of particles and momentum range, as well as on contacts for access requests.

Facility Name	Institute Name	Beamline Name	Country	Particle Type	Particle Energy	Coordinator
CERN PS	CERN	T9	Switzerland	electrons, hadrons, muons	0.5 - 10 GeV/c	sps.coordinator@cern.ch
CERN PS	CERN	T10	Switzerland	hadrons, muons	up to 10 GeV/c	sps.coordinator@cern.ch
CERN PS	CERN	T11	Switzerland			sps.coordinator@cern.ch
CERN SPS	CERN	H2	Switzerland	electrons, protons, hadrons, muons, ions	10-400GeV/c	sps.coordinator@cern.ch
CERN SPS	CERN	H4	Switzerland	Electrons, hadrons, muons, ions	10 to 400GeV	sps.coordinator@cern.ch
CERN SPS	CERN	H6	Switzerland	hadrons, muon, electrons	10 - 120 (206) GeV/c	sps.coordinator@cern.ch
CERN SPS	CERN	H8	Switzerland	primary protons, hadrons, muons, electrons, ions	10-400GeV/c	sps.coordinator@cern.ch
CLEAR	CERN	CLEAR	Switzerland	electrons	50-250 MeV/c	CLEAR-Info@cern.ch
DESYII Test Beam Facility	DESY	TB 21	Germany	electrons, positrons	1-6 GeV/c	testbeam-coor@desy.de
DESYII Test Beam Facility	DESY	Beamline	Germany	electrons (prim.)	6.3 GeV/c	testbeam-coor@desy.de
FTBF	FERMILAB	Beamline	USA	protons (prim.)	120 GeV/c	FTBF_Co@fnal.gov
FTBF	FERMILAB	Beamline	USA	electrons, hadrons, muons (sec.)	1-66 GeV/c	FTBF_Co@fnal.gov
FTBF	FERMILAB	Beamline	USA	hadrons (tert.)	200-500 MeV/c	FTBF_Co@fnal.gov
IHEP Protvino	IHEP Protvino	Beamline	Russia	protons	70 GeV/c	alexandre.zaitsev@cern.ch
IHEP Protvino	IHEP Protvino	Beamline	Russia	protons, pions, muons, electrons (secondary)	1-45 GeV/c	alexandre.zaitsev@cern.ch
IHEP Protvino	IHEP Protvino	Beamline	Russia	C-12 (prim)	6-300 GeV/c	alexandre.zaitsev@cern.ch
LNF	INFN LNF	BTF-1	Italy	electrons, positrons, photons both primaries and secondaries	25-750 MeV/c	btf@lnf.infn.it

IHEP Beijing	Institute of High Energy Physics (IHEP)	Beamline	China	electrons (prim.)	1.1 - 2.5 GeV/c	hut@ihep.ac.cn
IHEP Beijing	Institute of High Energy Physics (IHEP)	Beamline	China	electrons (sec.)	100 - 300 MeV/c	hut@ihep.ac.cn
IHEP Beijing	Institute of High Energy Physics (IHEP)	Beamline	China	protons, pions (sec.)	0.4 - 1.2 GeV/c	hut@ihep.ac.cn
RCNP	Osaka University	Beamline	Japan	protons	~400MeV	director@rcnp.osaka-u.ac.jp
RCNP	Osaka University	Beamline	Japan	Heavy ions	~100AMeV	director@rcnp.osaka-u.ac.jp
RCNP	Osaka University	Beamline	Japan	neutrons	White n, max 400MeV, quasi mono-energetic: ~400MeV	director@rcnp.osaka-u.ac.jp
RCNP	Osaka University	Beamline	Japan	muon	24-110MeV/c	director@rcnp.osaka-u.ac.jp
piE1, piM1	Paul Scherrer Institute (PSI)	Beamline	Switzerland	pions, muons, positrons, protons	50-450 MeV/c	davide.reggiani@psi.ch
PIF	Paul Scherrer Institute (PSI)	Beamline	Switzerland	protons	5 - 230 MeV/c	wojtek.hajdas@psi.ch
ELPH	Research Center for ELectron PHoton Science (ELPH)	Beamline	Japan	photons (tagged)	0.7-1.2 GeV/c	suda@lns.tohoku.ac.jp
ELPH	Research Center for ELectron PHoton Science (ELPH)	Beamline	Japan	electrons, positrons (conv.)	0.1-1.0 GeV/c	suda@lns.tohoku.ac.jp
SLAC	SLAC	Beamline	USA	electrons (prim.)	2.5 - 15 GeV/c	hast@slac.stanford.edu
SLAC	SLAC	Beamline	USA	electrons (sec.)	1 - 14 GeV/c	hast@slac.stanford.edu
Compton Facility	SPRING-8	Beamline	Japan	photons (tagged)	1.3 - 2.9 GeV/c	yosoi@rcnp.osaka-u.ac.jp
Compton Facility	SPRING-8	Beamline	Japan	electrons, positrons	0.4 - 2.9 GeV/c	yosoi@rcnp.osaka-u.ac.jp
ELSA	University of Bonn	Beamline	Germany	electrons	1.2 - 3.2 GeV/c	elsner@physik.uni-bonn.de
MAMI	University of Mainz	Beamline	Germany	electrons	< 1.6 GeV/c	fischer@kph.uni-mainz.de
MAMI	University of Mainz	Beamline	Germany	gammas	< 1.6 GeV/c	fischer@kph.uni-mainz.de

Table 4.1: World-wide test beam facilities, from ('CERN Facilities Data Base', 2020). Courtesy H. Wilkens and C. Rembser.

4.4 Neutron beams

Contributed by G. Croci (Università Milano Bicocca)

Two main sources are used for neutron scattering research, as well as for testing dedicated detectors: extracted beams from fission reactors, and accelerator-based sources where neutron are produced by spallation on non-fissile materials (Klein, 2020)

Compiled with the CERN web-based tool, Table 4.2 gives a list of laboratories providing neutron beams; selected test facilities are listed in Table 4.3. For a review see for example (Muraro and Croci, 2019).

The Oak Ridge Spallation Neutron Source in the USA (Fomin *et al.*, 2015) provides a wide range of neutron beams and energies, both to physics experiments and detectors testing. Under construction in Lund, in northern Sweden, the European Spallation Source (EES) when completed in 2023 will be a major tool for research studies, materials and life sciences (*European Spallation Source*, 2020).

Institute Name	Country
CEA Valduc	France
CNESTEN	Maroco
CROCKER NUCLEAR LABORATORY (CNL) UCDAVIS, UNIVERSITY OF CALIFORNIA	USA
CROCKER NUCLEAR LABORATORY (CNL) UCDAVIS, UNIVERSITY OF CALIFORNIA	USA
CSL - University of Liège	Belgium
DTU NUTECH	Denmark
ENEA, Department of Fusion and Technology for Nuclear Safety and Security	Italy
ENEA, Department of Fusion and Technology for Nuclear Safety and Security	Italy
ENEA, Department of Fusion and Technology for Nuclear Safety and Security	Italy
ESS BILBAO	Spain
Fraunhofer INT	Germany
HELMHOLTZ ZENTRUM BERLIN (HZ)	Germany
INFNSPES	Italy
INSTITUT DE PHYSIQUE NUCLÉAIRE D`ORSAY - IPN	France
Institut Laue-Langevin (ILL)	France
Institute of Experimental and Applied Physics (UTEF)	Czech Republic
ISOTRON LTD	United Kingdom
JGU	Germany
Jožef Stefan Institute	Slovenia
Lawrence Berkeley National Laboratory (LBNL) 88-Inch Cyclotron	USA
LPSC	France
Maria Reactor	Poland
NATIONAL PHYSICAL LABORATORY (NLP)	United Kingdom
NATIONAL PHYSICAL LABORATORY (NLP)	United Kingdom
NATIONAL PHYSICAL LABORATORY (NLP)	United Kingdom
NATIONAL PHYSICAL LABORATORY (NLP)	United Kingdom
PHYSIKALISCH TECHNISCHE BUNDESANSTALT (PTB)	Germany
PHYSIKALISCH TECHNISCHE BUNDESANSTALT (PTB)	Germany
PHYSIKALISCH TECHNISCHE BUNDESANSTALT (PTB)	Germany
PNPI	Russia
Radiation Test Solutions, Inc.	USA
Science and Technology Facilities Counsil (ISIS)	United Kingdom
SCK-CEN	Belgium
SCK-CEN	Belgium
Svedberg Laboratory (TSL)	Sweden
Svedberg Laboratory (TSL)	Sweden
Technische Universität Wien Atominstitut	Austria
TRIUMF	Canada
TUM FRM2	Germany
UCL-Universite Catholique de Louvain	Belgium
University of California Davis	USA
Uppsala University	Sweden

Table 4.2: World-wide list of neutron facilities, compiled from ('CERN Facilities Data Base', 2020).

Laboratory	**Particles**	**Energy**	**Diagnostics**	**Availability**	**Information, Contacts**
National Physical Laboratory (UK)	Monoenergetic fast and thermal neutrons	20-144 MeV 25 meV	Diamonds, ^{3}He Tubes, Activation foil	Upon request	https://www.npl.co.uk/ david.thomas@npl.co.uk, neil.roberts@npl.co.uk,
UKRI-STFC Rutherford Appleton Laboratory - ISIS (UK)	Thermal and fast neutrons	0.01 meV-800 MeV	^{3}He Tubes, GS-20 and GS-10 Scintillators	Almost all year when not in shutdown	https://www.isis.stfc.ac.uk/ Two proposal rounds over the year
ENEA-Casaccia TAPIRO Reactor (IT)	Thermal neutrons	10 meV -2 MeV	Fission chambers	8 hours/day during working days	https://www.enea.it/it/centro-ricerche-casaccia/ alessia.cemmi@enea.it
ENEA-Casaccia TRIGA MARK II Reactor (IT)	Thermal neutrons	10 meV -2 MeV	Fission chambers	8 hours/day during working days	https://www.enea.it/it/centro-ricerche-casaccia/ mariagrazia.iorio@enea.it
ENEA-Frascati FNG Neutron generator (IT)	Fast neutrons	1 MeV-14 MeV	Fission chambers	8 hours/day during working days	https://www.enea.it/it/centro-ricerche-casaccia/ fng@enea.it

Laboratorio Energia Nucleare Applicata (LENA) - TRIGA MARK II Reactor (IT)	Thermal neutrons	Peaked at 25 meV	N.A.	8 hours/day during working days	https://lena.unipv.it saverio.altieri@unipv.it
TREFF - FRMII Reactor (DE)	Monochromatic thermal neutrons	3.64 meV	^{3}He counter	FRM2 normal operation: 60 days cycle, 4 cycles/year, 1-month reactor break	https://mlz-garching.de/neutron-optics Karl.Zeitelhack@frm2.tum.de
National Center for Scientific Research (NCSR) Democritos (GR)	Neutrons	0.1-25.7 MeV	N.A.	8 hours/day during working days	http://www.inp.demokritos.gr/ gkordas@ims.demokritos.gr
Budapest Neutron Centre (HU)	Thermal neutrons	Peaked at 25 meV	^{3}He counter HpGe	8 hours/day during working days	https://www.bnc.hu/?q=node/6 kasztovszky.zsolt@energia.mta.hu
Oak Ridge Spallation Neutron Source (USA)	Wide	Peaked at ~5 keV			https://www.ornl.gov
China Spallation Neutron Source (CN)	Thermal and fast neutrons	0.01 meV - 1.6 GeV (when in full power)	Ceramic THGEMS, ^{3}He tubes	Almost all year when not in shutdown	http://english.ihep.cas.cn/csns/index.html sunzj@ihep.ac.cn

Table 4.3: Selected laboratories providing neutron beams for detectors testing (Courtesy G. Croci)

4.5 Ionization energy loss of charged particles

Elementary particles interact with matter through strong, weak and electromagnetic processes; for charged particles, the process exploited for detection is the coulomb interaction between the electromagnetic fields of the projectile and of the molecules of the medium, leading to the release of trails of electron-ion pairs. The most probable ionization energy lost per unit length of matter, or differential energy loss, depends on the nature and charge of the particle and density of the medium, and has a characteristic dependence on velocity, described in chapter 5. In argon at STP, the primary ionization yield of fast particles is typically around 30 ion pairs per cm, and the total (primary plus secondary ionizations) around 100/cm. For a summary of these processes see Chapter 2 in (Sauli, 2014).

The ionization energy loss fluctuates around the average with a distribution, named Landau from the Russian physicist who described theoretically the process; it has been studied in detail experimentally in the course of development of the method for fast particle identification exploiting its slight dependence from the mass of particles with equal velocity; simulation programs permit to accurately compute the distributions, as shown by the example in Figure 4-4 (Smirnov, 2005). The relative energy loss resolution depends on the gas, and is better in heavy molecular gases, as seen in

Figure 4-5 (Lehraus, Matthewson and Tejessy, 1982); however, as the extent of relativistic rise is smaller, the particle identification power is not improved.

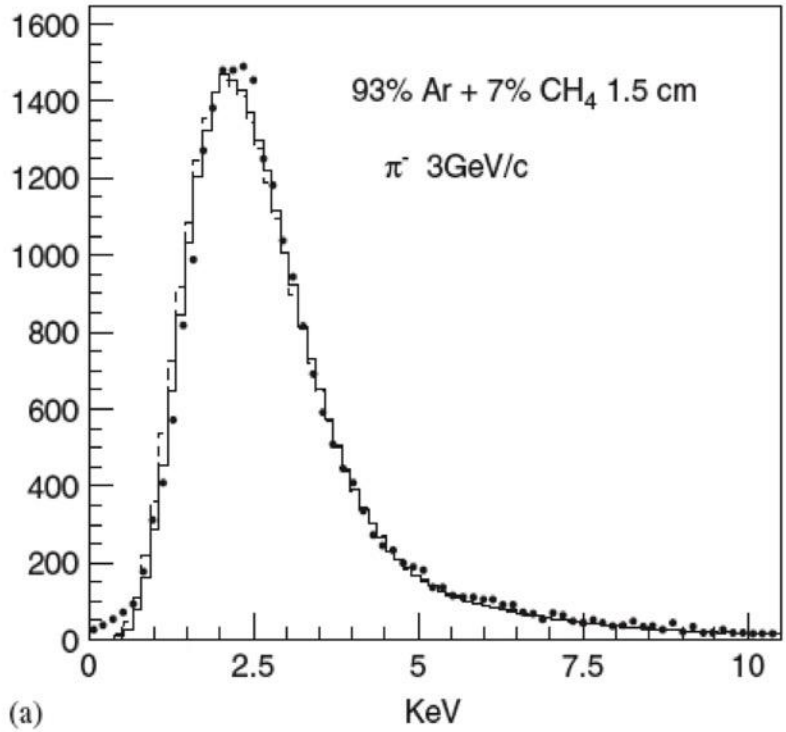

Figure 4-4: Computed and experimental ionization energy loss distributions of fast pions in 1.5 cm of gas at STP (Smirnov, 2005).

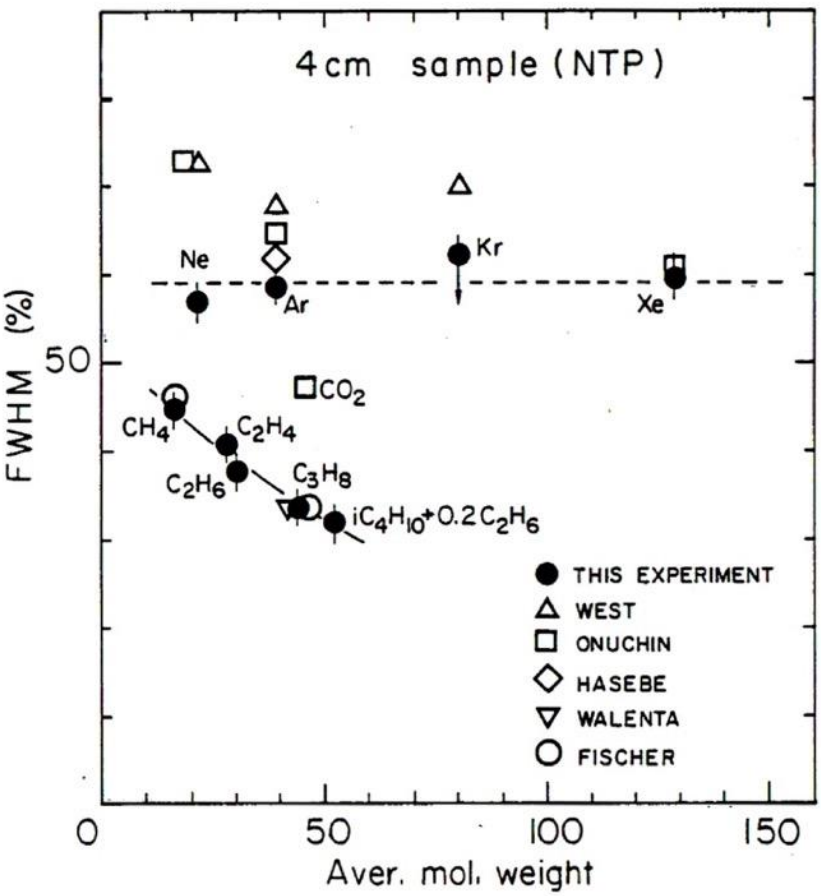

Figure 4-5: Relative ionization energy loss resolution for fast particles in several gases (Lehraus, Matthewson and Tejessy, 1982).

The basic setup to measure the detection efficiency consists in a set of scintillation counters placed on the beam line, covering part or all of the active surface of the detector. The charge signals sensed on the detector electrodes are amplified and recorded, either using analogue-to-digital electronics or simpler discriminators; a coincidence between the trigger and the timely pulses from the detector under study define the efficiency, normally measured as a function of operating voltages and discrimination threshold.

Figure 4-6 and Figure 4-7 are examples of efficiency measured for fast particles with a multi-wire proportional chamber as a function of voltage, discrimination threshold and time resolution.

The relative efficiency can also be measured with a set of identical devices aligned on the beam, varying the operating conditions of one, all others remaining constant and serving as reference. For extended tracks or multiple devices, a geometrical trajectory reconstruction can be used to determine the space localization accuracy. For three identical detectors at equal distances, the distance between fitted and measured coordinates is

$\Delta x = \frac{x_3 - x_1}{2} - x_2$

and the standard deviation of the distribution of residuals:

$\sigma_{\Delta x} = \sqrt{\frac{3}{2}\sigma}$ where σ is the position accuracy of each detector.

Figure 4-8 is an example of localization accuracy obtained from the residuals, difference between the coordinates measured in the detector under study and the value deduced from the coordinate reconstructed from a set of aligned devices. The space resolution is affected by the detector's operating performances (gain, electronic threshold) as well as by the statistical fluctuations of the energy loss process, namely the presence of long-range ionization electrons (delta rays), see chapter 5.

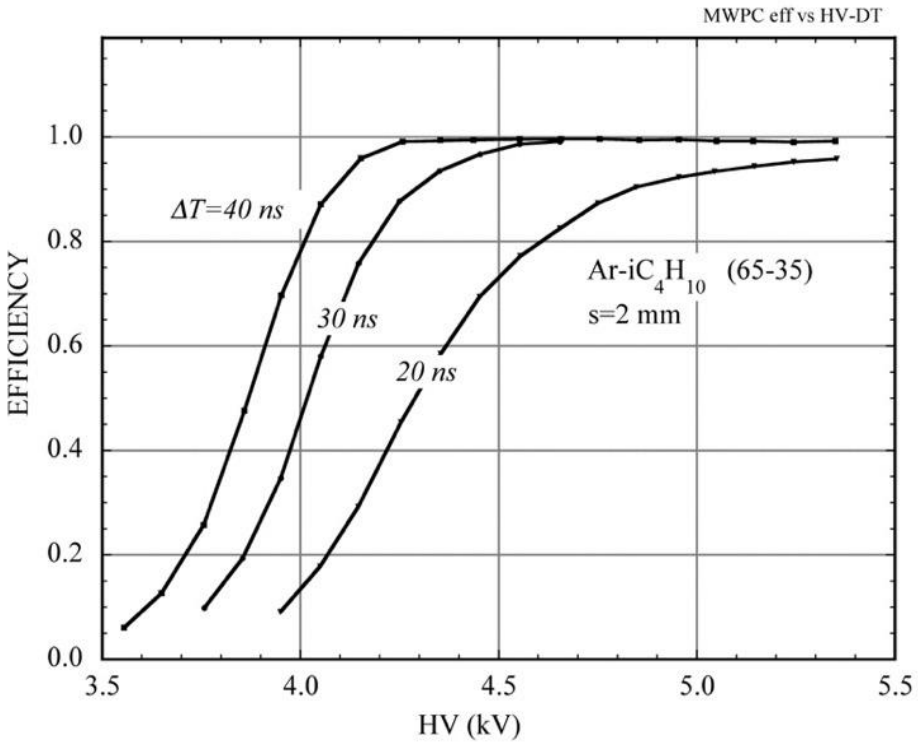

Figure 4-6: MWPC detection efficiency as a function of voltage for several coincidence gate widths (Schilly *et al.*, 1970).

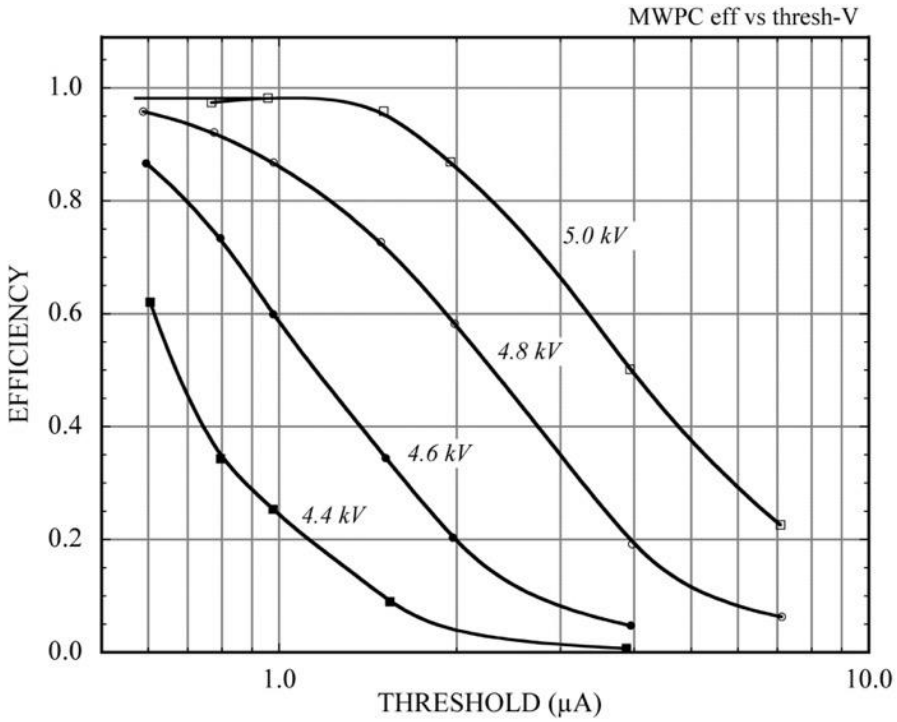

Figure 4-7: MWPC detection efficiency for fast particles as a function of discrimination threshold and for several values of operating voltage (Duerdoth *et al.*, 1975).

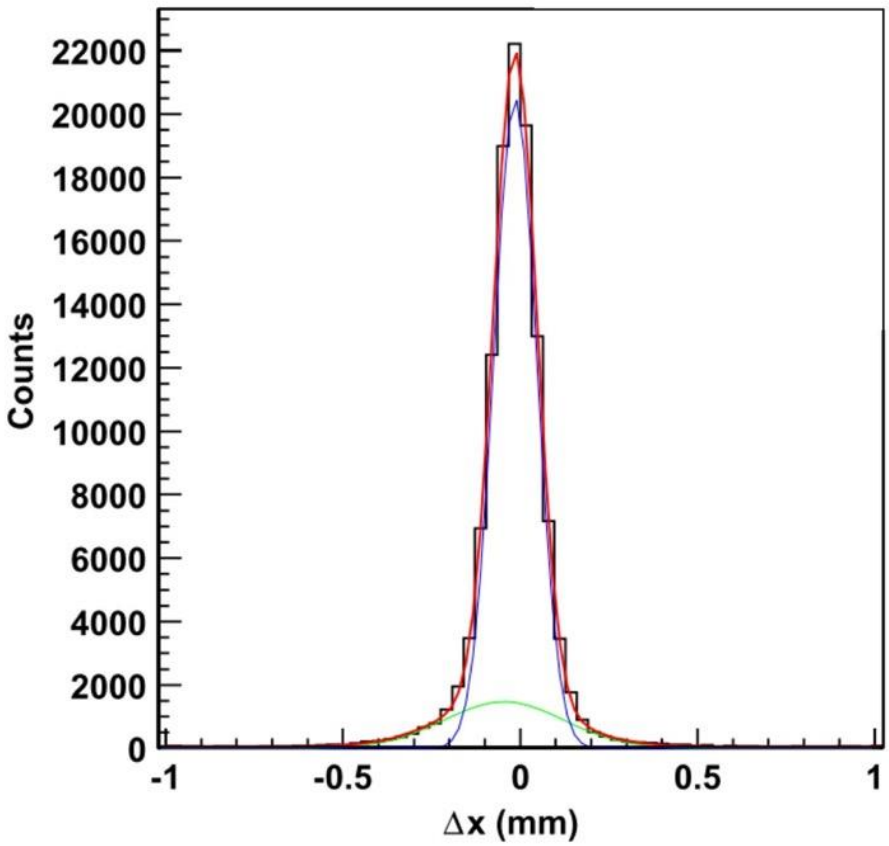

. For three identical detectors at equal distances, the distance between fitted and measured coordinates is

$\Delta x = \frac{x_3 - x_1}{2} - x_2$

and the standard deviation of the distribution of residuals:

$\sigma_{\Delta x} = \sqrt{\frac{3}{2}\sigma}$ where σ is the position accuracy of each detector.

Figure 4-8: Residuals distribution in one detector of the COMPASS Triple-GEM setup. The single detector position accuracy is about 70 µm (Ketzer *et al.*, 2001).

4.6 Radioactive sources

Contributed by Eraldo Oliveri (CERN)

4.6.1 Introduction

Providing a broad range of ionization yields and fluxes, radioactive sources are widely used for laboratory testing of detectors. Handling and use of the sources obeys strict safety rules, described by directives issued by the various laboratories; for CERN, the Radioactive Source Management Portal provides detailed information on their procurement, handling and use (CERN, 2020b)(CERN, 2020d).

Table 4.4, compiled from different sources, is a list of useful radionuclides. The emission is often not direct but occurs through a chain of decays with diverse lifetimes.

Artificial isotopes are produced through spallation, fission or fragmentation, bombarding a thick target with charged particles at accelerators, or by neutrons in reactors, and are separated by chemical or magnetic processing. An example of dedicated separator is the ISOLDE complex at CERN (CERN, 2020c).

Frequently used in the laboratory are ^{90}Sn and ^{106}Ru, emitting electrons with an energy spectrum up to the values indicated in the table, ^{55}Fe with an X-ray line at 5.9 keV and ^{241}Am radiating α particles of energy around 5.4 MeV. Of particular interest is ^{220}Rn, released in gaseous form from ^{228}Th through the indicated decay chain; introduced in detectors with the gas flow, it permits to generate heavy ionization trails without the thin windows needed for external alpha sources[1].

Radionuclide	Emissions	Energy (keV)	Intensity (%)	Lifetime
^{22}Na	β^+	545.7	90	2.6 y
	γ (annihilation)	511	180	
	γ	1275	100	
^{55}Fe		5.9	24.4	2.747 y
	^{55}Mn K X-rays	6.49	2.86	
^{60}Co	β^-	318.2	99.9	5.27 y
	γ	1163	99.8	
	γ	1332	100	
^{90}Sr	β^-	546	100	28.8 y
--> ^{90}Y	β^-	2280	100	2.67 d
^{106}Ru	β^-	39	100	371.5 d
-->^{106}Rh	β^-	3546	79	30.1 s
	γ	512	21	
	γ	622	10	
^{109}Cd	β^-	63	42	1.265 y
	β^-	84	44	
	γ	88	3.7	
	Ag K X-rays	22.9	29.8	
		22.16	56.1	
		24.91	4.8	
		14.94	88	

[1] The isotope is present in traces in natural thorium, and could be found in the metallic meshes used to enhance visible light emission in gas lamps. It has now been removed for safety reasons; many laboratories preciously keep a cartridge with an old thorium mesh as alpha emitter.

^{137}Cs	β^- β^- γ X X	514 1176 662 31.8 32.2	94 6 85 2 3.6	30 y
^{228}Th --> ^{224}Ra --> ^{220}Rn --> ^{216}Po	α β^- γ γ γ α α	5340 to 8780 334 to2246 239 583 2614 6400 5985 6778	 44 31 36	1.912 y 361 d 55.8 s 0.148 s
^{241}Am	α α γ	5442.8 5485.56 59.54	13.1 84.8 35.9	432.6 y
^{252}Cf	α 2-4 n (fission)	6076 6118 2000-14000	15 82	2.645 y

Table 4.4: Radioactive sources used for laboratory testing of detectors. Compiled from different sources: (Groom, 2019)(CERN, 2020d)(Wikipedia, 2020b)(Wikipedia, 2020c)(Prelas *et al.*, 2014).

4.6.2 Beta electron sources

Mean energy, number of electrons per transition and emission spectra for beta decay isotopes are given by (Cross, Ing and Freedman, 1983) and (Mantel, 1972). Redrawn from the first reference, Figure 4-9 and Figure 4-10 provide the beta emission yields for ^{90}Sn-^{90}Y and ^{106}Rh, daughter of ^{106}Ru. The spectra can be affected by the materials traversed before entering the detector, including the source itself, and in the detector.

The spectra provided correspond to the emission; the energy loss in the detector itself can be measured or computed. Based on a calculation performed by the authors of Ref. (Prelas *et al.*, 2014) for a thick target (silicon carbide), and assuming a linear dependence from density, Figure 4-11 gives the estimated range and differential energy loss of electrons from the ^{90}Sn-^{90}Y source, in absence of absorbers.

Two or more plastic scintillators are usually placed in front and/or behind the detector and used in coincidence as trigger, permitting to select the high energy part of the spectra thus emulating the ionization characteristics of minimum ionizing particles, as discussed in section 5.

Measured as part of a study on ionization cluster size (see 5.2), Figure 4-12 shows the energy loss spectra recorded with a plastic scintillation counter facing several beta-emitting sources, and the ^{90}Sn spectrum measured with a Geiger counter in coincidence, suppressing the photon-induced noise.

Owing to their light mass, electrons are multiple-scattered by the materials traversed and do not follow a straight line and can be scattered at the walls, setting limitations to the localization accuracy that can be investigated in the detectors.

Back-scattering of electrons from an external thick plate was exploited for the measurement of two-track separation in early drift chambers with the setup shown in Figure 4-13 (Breskin *et al.*, 1975). While supplanted by the use of high intensity particles or ionizing laser beams, the method remains an interesting approach.

Due both to the scattering processes and to the generation of bremsstrahlung photons with interactions on the walls, collimators on the source have to be used cautiously; the cleanest operating conditions are usually obtained avoiding collimation altogether.

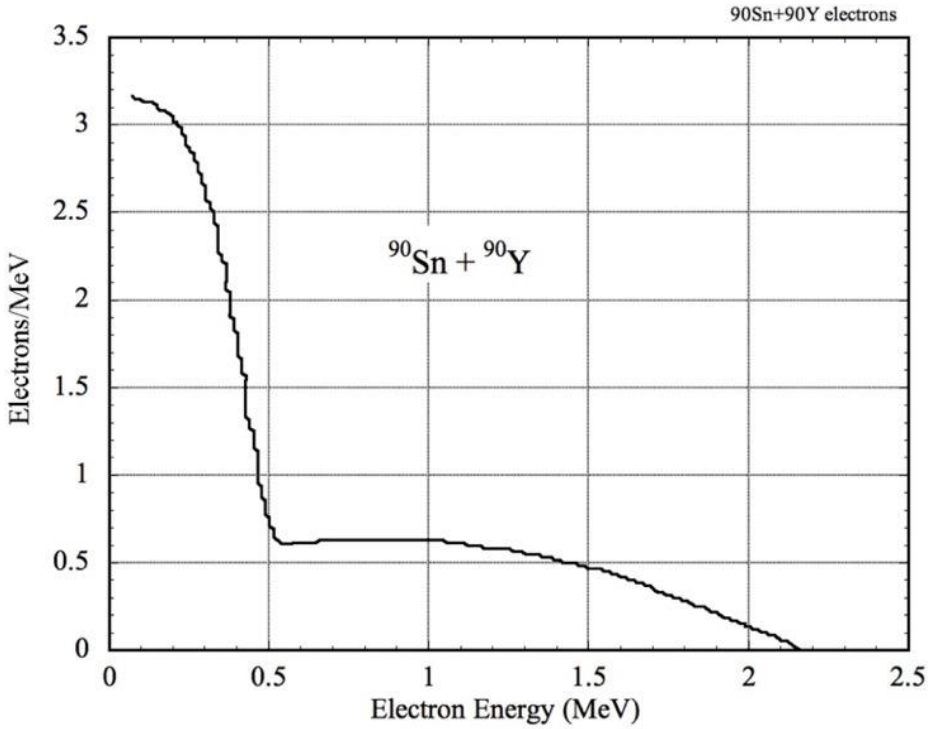

Figure 4-9: Combined beta emission spectra of ^{90}Sn and ^{90}Y. From (Cross, Ing and Freedman, 1983).

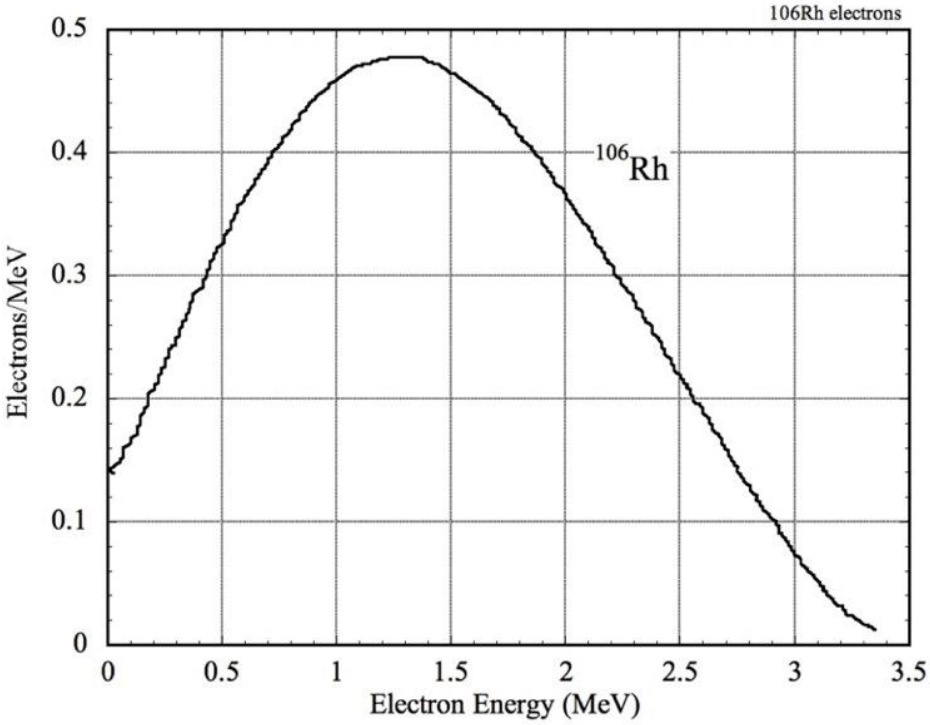

Figure 4-10: Emission spectrum of ^{106}Rh, daughter of ^{106}Ru. From (Cross, Ing and Freedman, 1983).

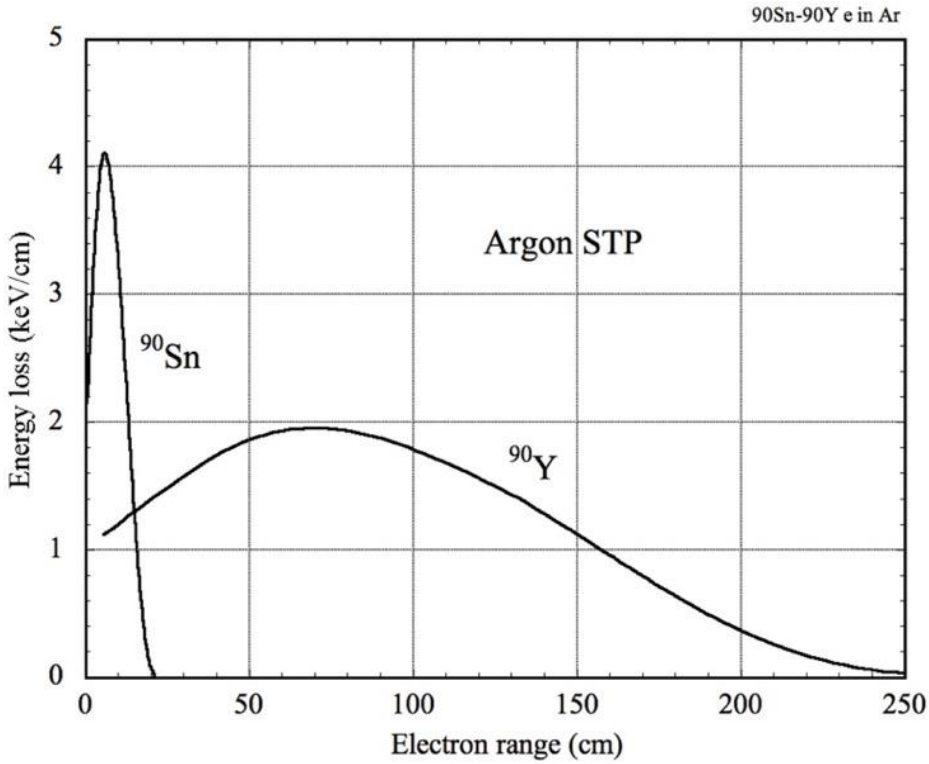

Figure 4-11: Computed range and differential energy loss of electrons from ^{90}Sn and ^{90}Y.

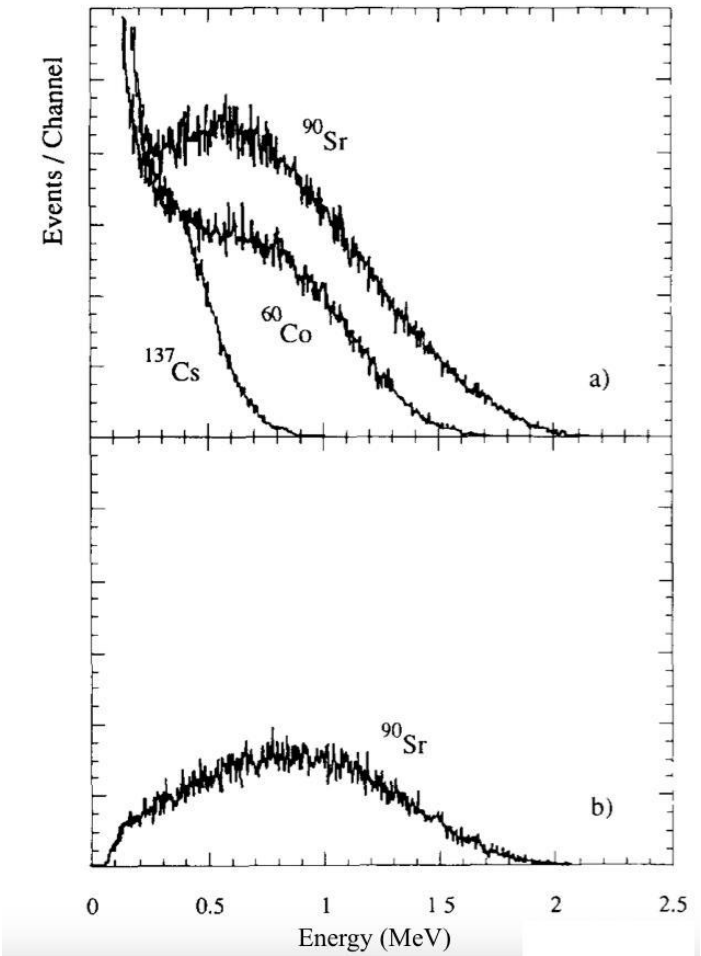

Figure 4-12: Energy loss spectra recorded with a single scintillation counter (a), and in coincidence with a Geiger counter in front (b) (Fischle, Heintze and Schmidt, 1991).

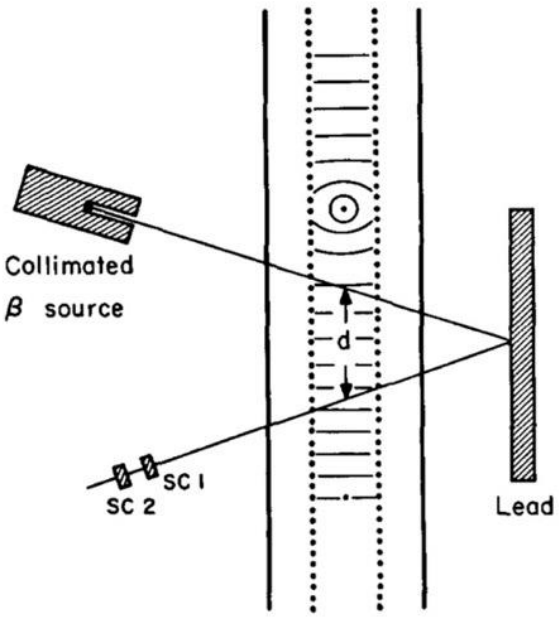

Figure 4-13: Back-scattering from an external lead plate permits to study the two-tracks resolution in drift chambers (Breskin *et al.*, 1975).

A miniature magnetic spectrometer has been developed at CERN permitting to select the high energy fraction of the electrons emitted by a beta source, Figure 4-14 (Arfaoui, Joram and Casella, 2015).

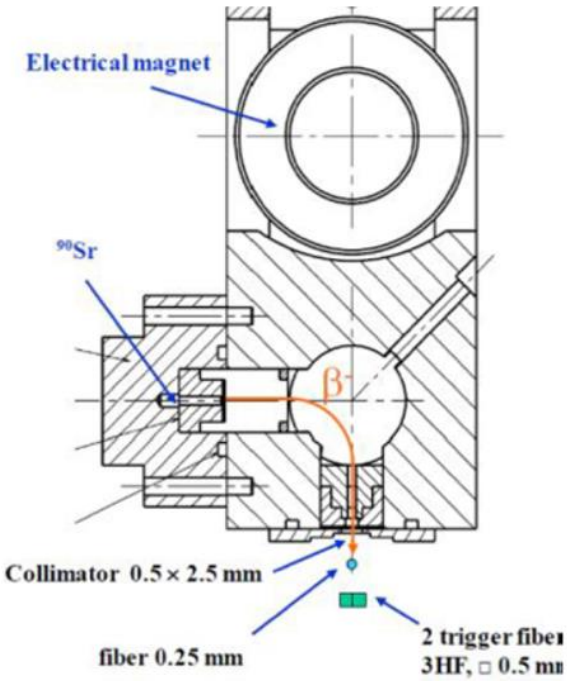

Figure 4-14: A miniature magnetic spectrometer providing a quasi-monoenergetic electron beam.

With a proper choice of geometry and a selection of the ~MeV fraction of the electrons energy the detectors can be tested in the laboratory in conditions close to their use in high-energy experiments. Figure 4-15 (left peak) is an example of pulse height recorded exposing a multi-wire chamber exposed to a beta source with the criteria outlined above; the energy loss spectrum has the characteristic Landau shape expected from fast particles. By comparison with the charge recorded for a ^{55}Fe source, with the characteristic 5.9 keV peak (left), and taking into account the detector

gai, the most probable ionization energy loss in the peak corresponds to around 2 keV. Figure 4-16 shows the detection efficiency for fast electrons as a function of voltage.

Intense ^{90}Sn and ^{106}Ru sources have been used to study the long-term survivability of gaseous detectors under irradiation; X-ray generators and dedicated gamma sources, as for example CERN's Gamma Irradiation Facility (CERN, 2020a)(Pfeiffer *et al.*, 2017) permit however a better control of the exposure.

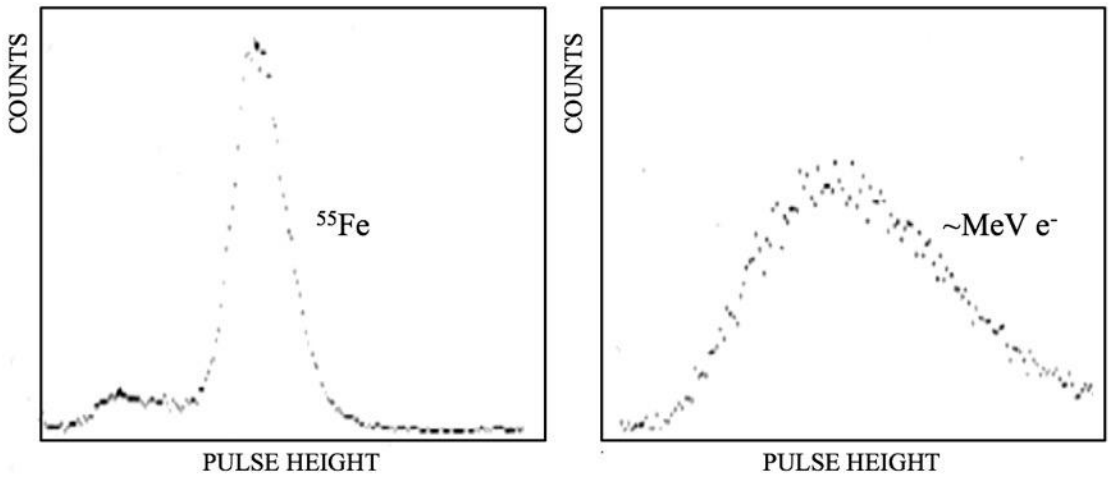

Figure 4-15: Pulse height spectra measured with a MWPC for and 5.9 keV X-rays and beta electrons (Sauli, 1977).

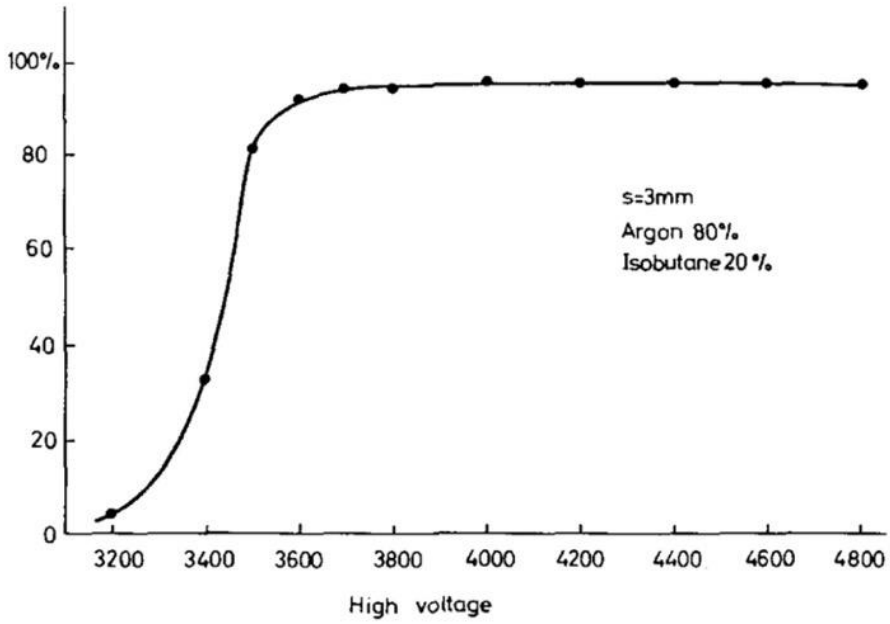

Figure 4-16: MWPC detection efficiency as a function of high voltage, measured with the electron source (Charpak, Rahm and Steinert, 1970).

Used as internal calibration source, ^{93}Kr has a complex decay sequence including low energy X-rays and Auger electrons; Figure 4-17 compares the energy loss spectrum computed from the known transition probabilities and as recorded in the NA49 TPC. The detailed shape of the distribution depends on the detector gas and geometry, due to the escape of gammas generated in the decay. The ^{93}Kr gas is generated by a ^{93}Rb cartridge mounted on a bypass of the gas system (Afanasiev *et al.*, 1999).

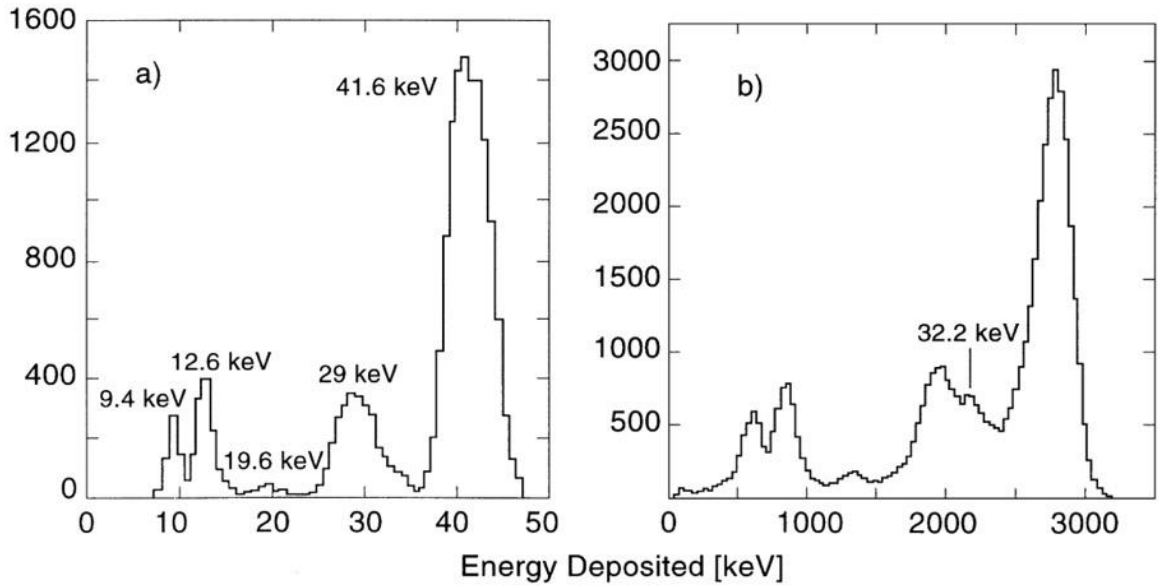

Figure 4-17: Computed (left) and measured energy loss spectrum of an internal ^{93}Kr source (Afanasiev *et al.*, 1999).

4.6.3 X-ray and gamma sources

One of the most widely used radiation sources for testing gaseous detectors is ^{55}Fe. With a main line at 5.9 keV and the daughter ^{55}Mn line at 6.49 keV, it emulates well the energy loss of fast charged particles in thin gaseous layers.

In gaseous counters, statistical dispersions both in the ionization process and in the subsequent charge amplification degrade the lines to broader distributions and limit the resolution that can be attained; for a discussion of these processes see for example Chapter 7.5 in (Sauli, 2014). Scintillation proportional counters, where the electric field is increased to enhance collisional photon emission but kept below the onset of charge multiplication, provide the best energy resolution for soft X-rays. Detection is performed with one or more photomultipliers, having a spectral response adjusted to the scintillation spectra; for a review see (Policarpo, 1977).

Figure 4-18 is an example of energy loss spectrum for ^{55}Fe X-rays recorded with a xenon-filled scintillation counter (Simons and De Korte, 1989); the ^{55}Mn is clearly visible, accounting for about 8% of the total events, as indicated in ; the FWHM energy resolution for the main peak is 7.3%.

In proportional counters operated with charge multiplication and detection the resolution is reduced due to the statistical fluctuations in the avalanche development.

Figure 4-19 is an example of pulse height recorded with a gas electron multiplier (GEM) at a charge gain of around 5.10^3 in an argon-filled counter; aside from the 5.9 keV peak, the spectrum shows the characteristic peak around 3 keV due to events where the fluorescence photon emitted by the return to ground of the K-shell of the argon atom has escaped detection. The resolution in the main 5.9 keV peak is around 17% FWHM, obscuring the presence of the ^{55}Mn line (Sauli, 2016). The expected ratio between the main and escape peak, around 0.5, is a good indicator of the proportionality of the counter response to energy loss.

Measured with a MICROMEGAS detector, Figure 4-20 shows the pulse height distribution for exposure to X-rays in a range of energies; at 22 keV, the ^{109}Cd Ag K X-rays, the resolution is 5.4 % FWHM, comparable to the one obtained with the best proportional counters (Charpak *et al.*, 2002).

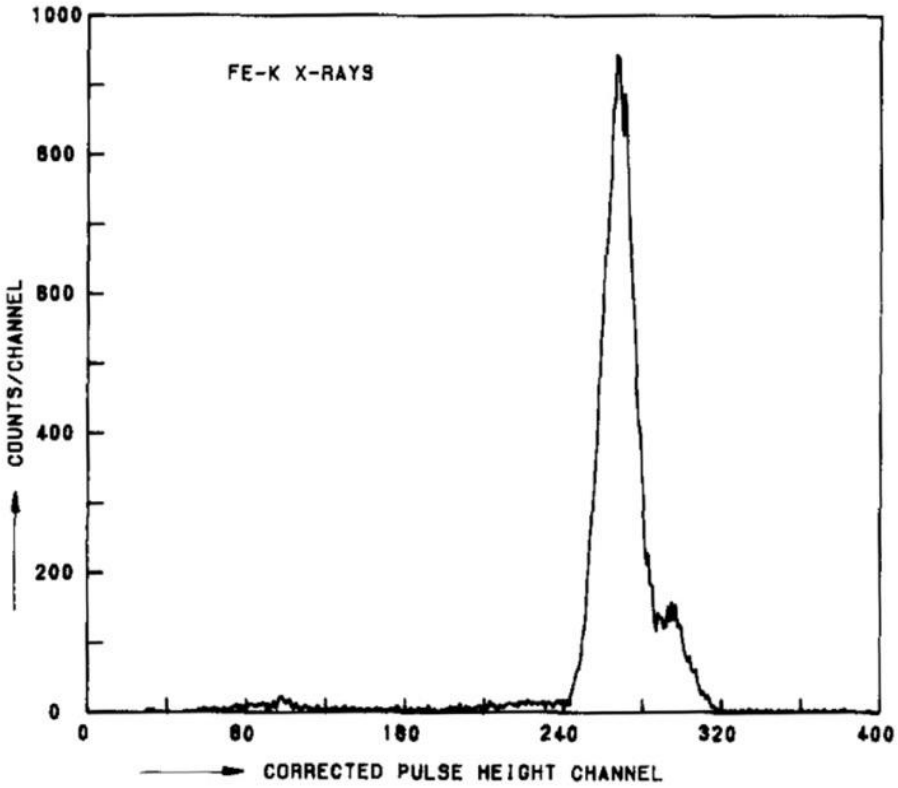

Figure 4-18: Pulse height distribution for ^{55}Fe x-rays recorded with a gas scintillation counter in xenon (Simons and De Korte, 1989).

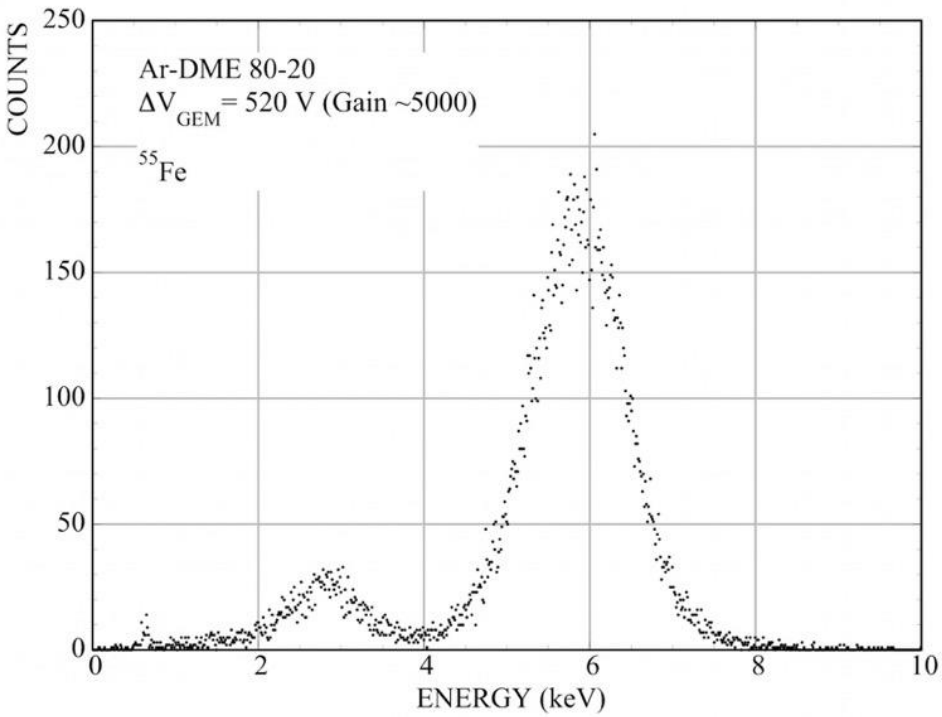

Figure 4-19: ^{55}Fe pulse height spectrum recorded with a GEM detector (Sauli, 2016).

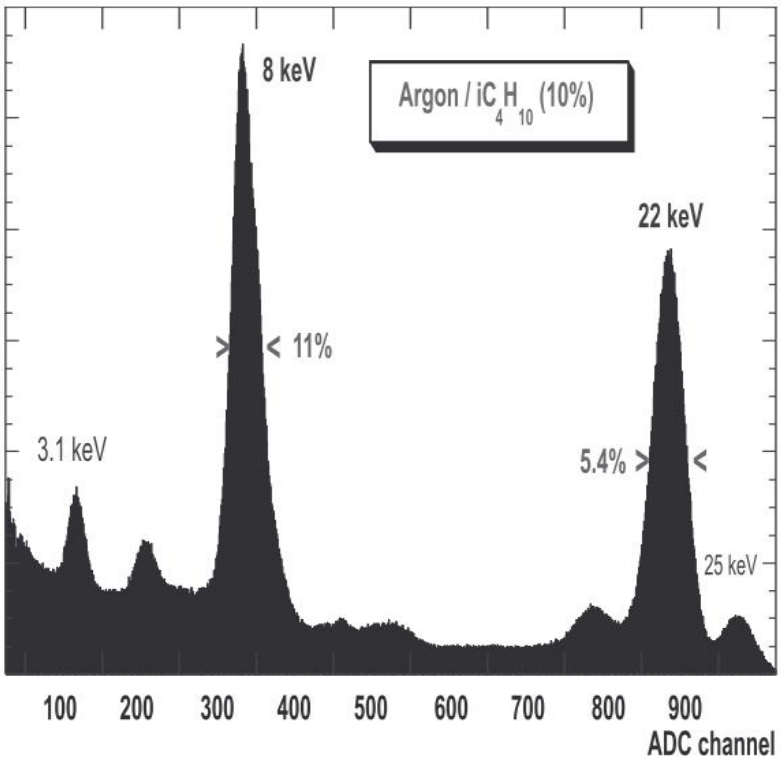

Figure 4-20 : Pulse height spectra recorded in range of X-ray energies with a MICROMEGAS detector (Charpak *et al.*, 2002).

To study the performance of counters for the detection of very soft X-rays, at energies where radioactive sources are not available, a method making use of fluorescence photons emitted by a target bombarded by alpha particles has been devised by the authors of Ref. (Sellers, Papadopoulos and Wilson, 1967). Figure 4-21 shows the setup used to investigate the energy resolution of scintillation counters at keV energies (P L Policarpo *et al.*, 1974); Figure 4-22 is an example of pulse height spectra recorded with carbon (227 eV), aluminum (1.49 keV) and manganese targets (5.898 keV).

For photon energies above few tens of keV, the conversion efficiency of gaseous counters strongly decreases, requiring the use of converters to achieve detection; an overview of the relevant cross sections is given in section 5.

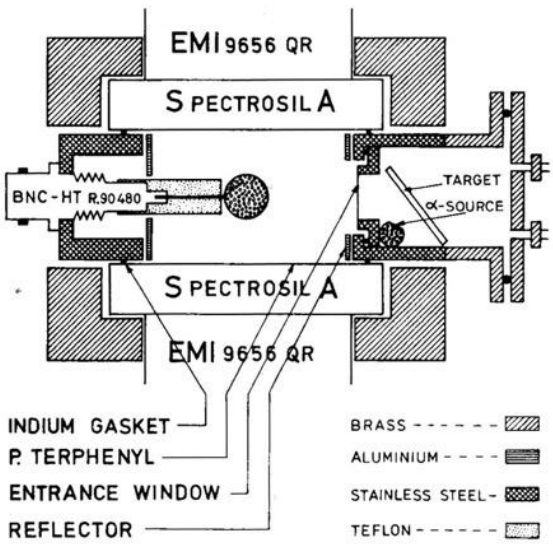

Figure 4-21: Setup used to generate X-rays in the keV region from the fluorescence of different target exposed to alpha particles (P L Policarpo *et al.*, 1974).

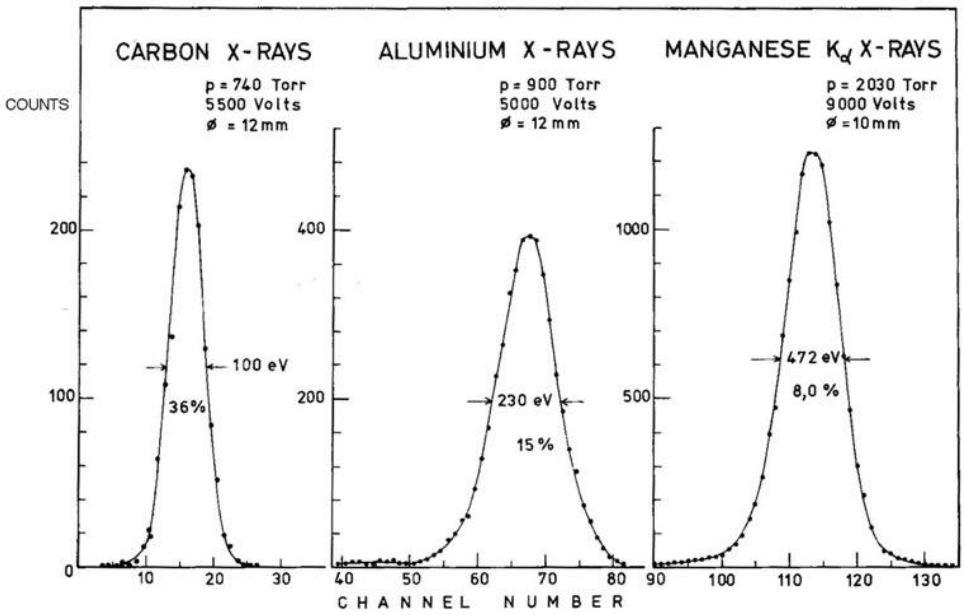

Figure 4-22: Pulse height spectra and resolution for C (277 eV), Al (1.49 keV) and Mn K_a (5.898 keV) fluorescence X-rays (P L Policarpo *et al.*, 1974).

Used with detectors developed for positron emission tomography, the ^{22}Na source has a positron emission, shortly followed by the decay in two quasi-linear 522 keV gammas; one of the photons provides then a coincidence signal permitting to study the efficiency of the detector under test. Due to the very low cross section of gases at this energy, the method has been used for devices exploiting internal converters of various kinds.

4.6.4 Alpha particle sources

As shown in Table 4.4, several radionuclides emit α particles with energy in the MeV region, directly or through their transmutation: ^{238}Th, ^{241}Am, ^{252}Cf and others. In gases at STP, the particles travel several cm releasing an essentially straight ionization trail, before stopping at the end of their range (see Figure 4-23) (Saito *et al.*, 2002).

Alpha particles can be easily colliated, and suffer a negligible multiple scattering deflection until the end of their range. The source can be mounted inside the sensitive volume; if installed outside the detector its energy will be reduced by losses in the window; in polyethylene, 5 MeV alphas lose about 1 MeV in a 10 µm layer (see section 5).

Recorded with a solid-state camera with a scintillating GEM detector, Figure 4-24 shows the measured energy loss profile along a 5.48 MeV α track, deduced from the differential scintillation yield (Margato *et al.*, 2004). For the measurement, the source has been mounted inside the detector, to avoid the absorption losses of even thin windows.

Using the internal ^{220}Rn source described in section 4.6.1, both the main 6.4 MeV and the daughter ^{216}Po emission have been imaged with the optical GEM detector; Figure 4-25 shows examples of single and double track events, as well as the differential energy loss profile along the top track in the double event (Brunbauer *et al.*, 2018).

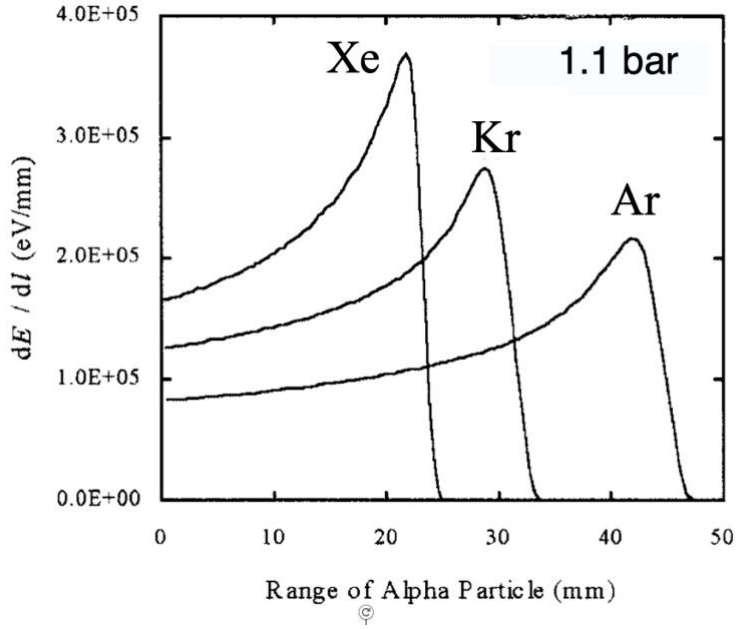

Figure 4-23: Range-differential eergy loss for 5.49 MeV α particles in noble gases at pressure near atmospheric. Figure 4-23

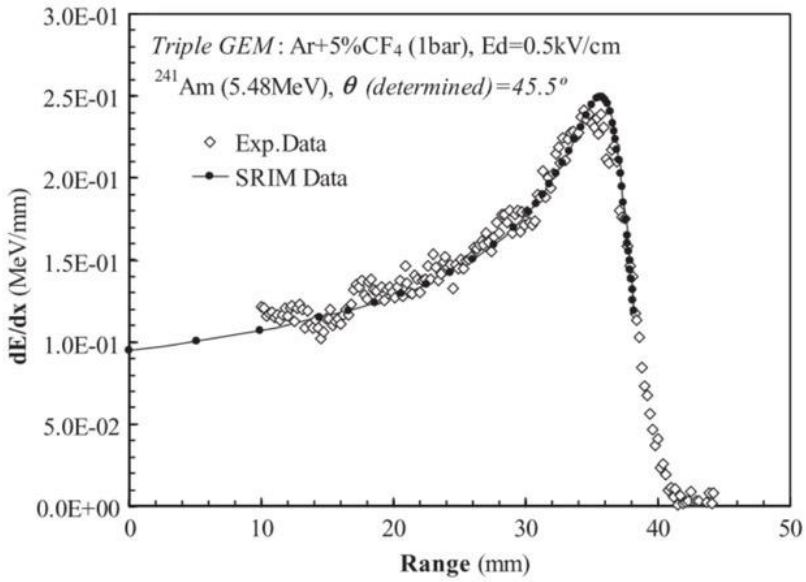

Figure 4-24: Differential energy loss of a 4.48 MeV a particle recorded in A-CF_4 at STP with the optical GEM detector (Margato *et al.*, 2004).

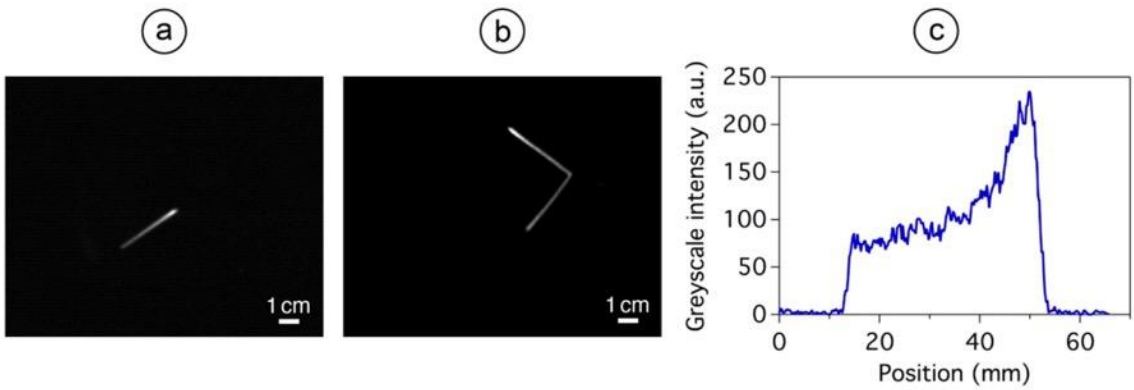

Figure 4-25: Single (a) and double alpha tracks (b) emitted by the internal ^{220}Rn source, and differential energy loss profile for the top track in (b) (Brunbauer *et al.*, 2018).

4.7 X-Ray Generators

Commercially available in a wide range of performances, X-Ray tubes are a practical laboratory tool to generate ionizing radiation. Mostly based on the original Coolidge design, developed in the early years of last century, the tubes have a cathode source of electrons, emitted by thermionic effect by a heated filament and accelerated in vacuum by the applied high-voltage to hit a metallic anode. X-rays are emitted by bremsstrahlung, with a continuum energy spectrum up to the maximum available, accompanied by peaks or edges corresponding to the energies of the electronic shells of the metal used as anode. Additional electrode structures can be used to focus the electron beam on the anode and produce smaller spot sizes; high power tubes need suitable cooling systems.

Photons are extracted through a thin widow, usually in beryllium, placed in front or on the sides of the tube; the intensity of the source is controlled by the current of the filament. Collimators are used to reduce the beam size if needed.

X-ray tubes of moderate power are generally used in the laboratory for testing detectors. For a recent review of high-power generators used for medical diagnostics see (Behling and Grüner, 2018). A short handbook gives useful information on the use and handling of X-ray tubes (Panalytical, 2007).

Figure 4-26 shows a small size X-ray generator, produced by AMPTEK. Various models of the tube have Ag, Au, Rh or W anodes, maximum voltage of 50 or 70 kV and power up to 10 W; Figure 4-27 gives the X-ray energy spectra for different anode materials of the tube, and Figure 4-28 is an example of X-ray spectra for a silver anode at increasing operating voltages (AMPTEK, 2020).

Figure 4-26: The Mini-X2 X-Ray generator by AMPTEK.

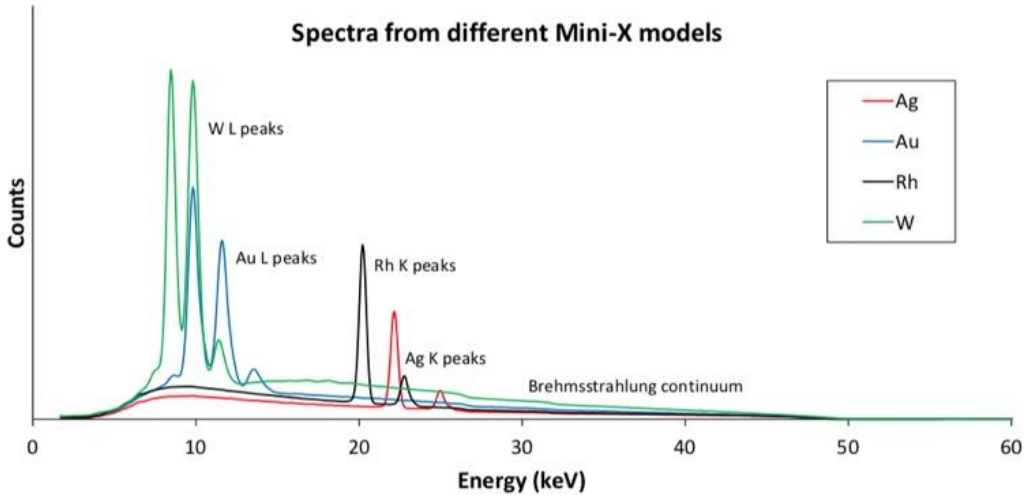

Figure 4-27: X-ray emission spectra for different anode materials (AMPTEK, 2020).

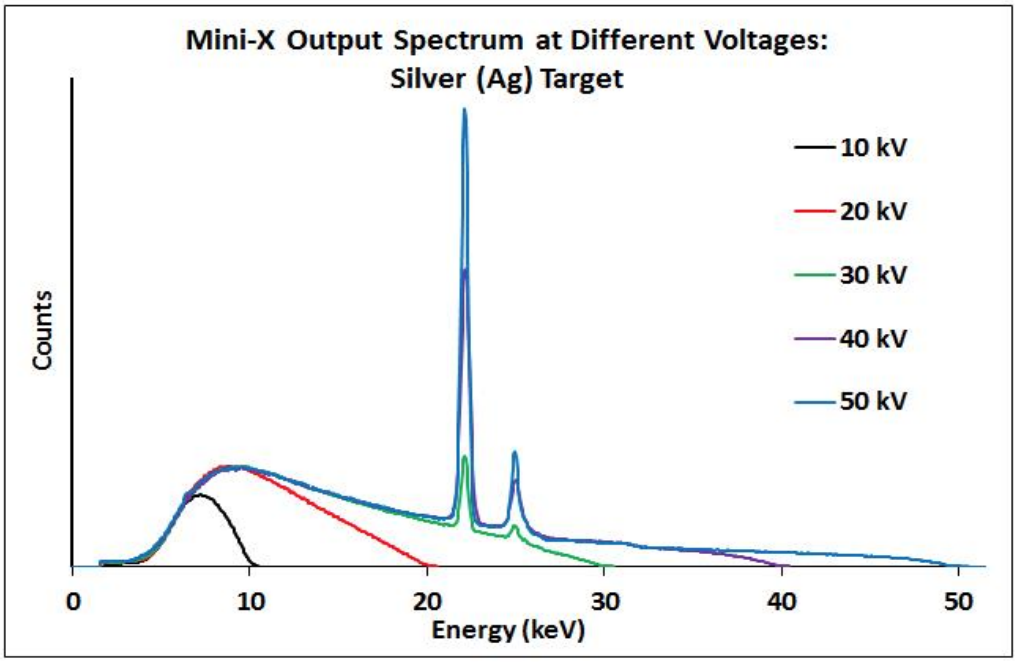

Figure 4-28: Output spectra of the Mini X2 with silver anode at increasing voltages (AMPTEK, 2020).

The emission spectra can be modified by materials inserted between the source and the detectors to act as filters, or part of the detector itself, Figure 4-29; by comparison with the previous figure it can be seen that the high-energy bremsstrahlung component is strongly enriched. Secondary fluorescence induced on materials internal to the counter can add background radiation.

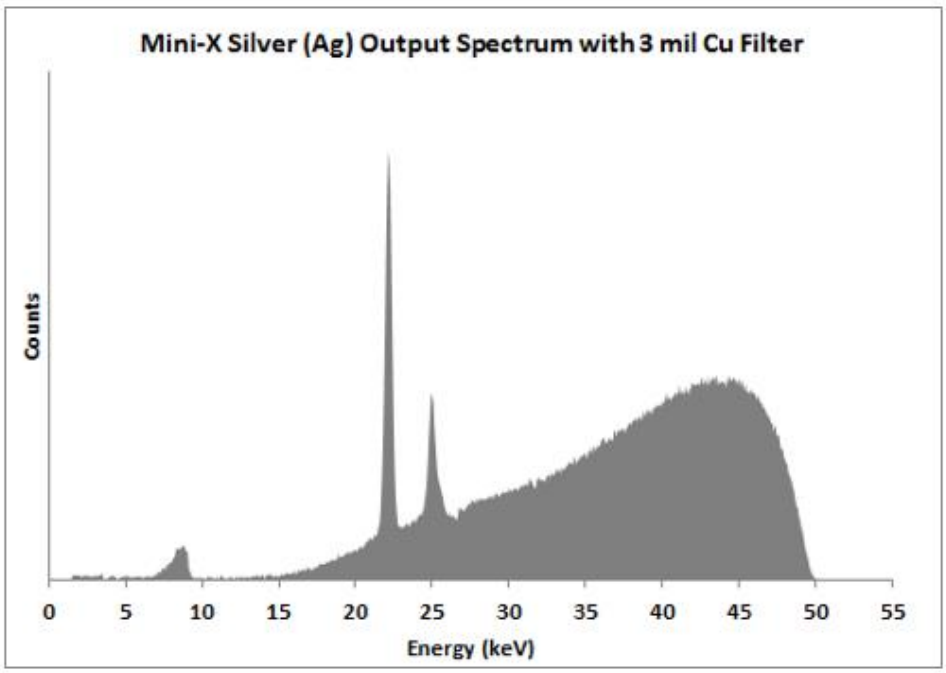

Figure 4-29: Output spectrum of the X-ray tube with Ag anode and a 3 mil (76 µm) Cu filter (AMPTEK, 2020).

The ionization charge released in a detector is a convolution of the emission spectrum of the tube and of the X-ray absorption cross section of the gas fillings, see chapter 5.

Based on a patented concept (Gendreau *et al.*, 2015) a triggerable and time-stamped soft X-ray generator has been developed by the CERN-GDD group. A seen in Figure 4-30, the generator is triggered by a pulsed UV flash hitting a photocathode contained in a vacuum vessel. Electrons emitted by the electrode are amplified by a Micro-Channel Plate, and accelerated by a strong electric field before hitting a target; depending on the field and the material, keV-X-rays are emitted and made available through a thin window. Timing resolutions of few hundred ps have been achieved (Resnati, 2016).

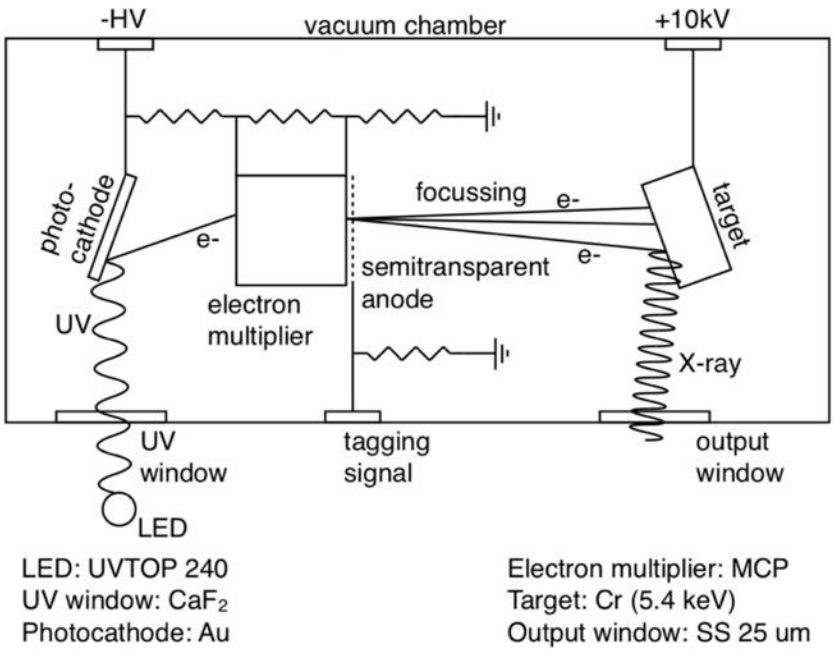

Figure 4-30: Triggerable and time-stamped soft X-ray generator (Resnati, 2016).

4.8 UV Light sources

Discharge lamps operating in low-pressure hydrogen or deuterium are used as light sources with a broad spectrum at far and vacuum UV wavelengths. In its simplest conception, Figure 4-31, a flash lamp consists in a sealed glass tube with two electrodes; the UV-transparent window is pasted on one side of the tube. With the powering scheme shown in Figure 4-32, application of a voltage above threshold initiates a self-sustained recurrent discharge with a frequency defined by the RC time constant (100 Hz in the example); an electrical signal is provided for triggering.

The wavelength of the emission is in the range between 160 and 400 nm (8 to 3 eV) (Berlman, Steingraber and Benson, 1968); this reference provides a detailed discussion of the dependence of the light yield from various manufacturing parameters. Figure 4-33 is an. example of measured emission spectrum (Stapelmann *et al.*, 2014).

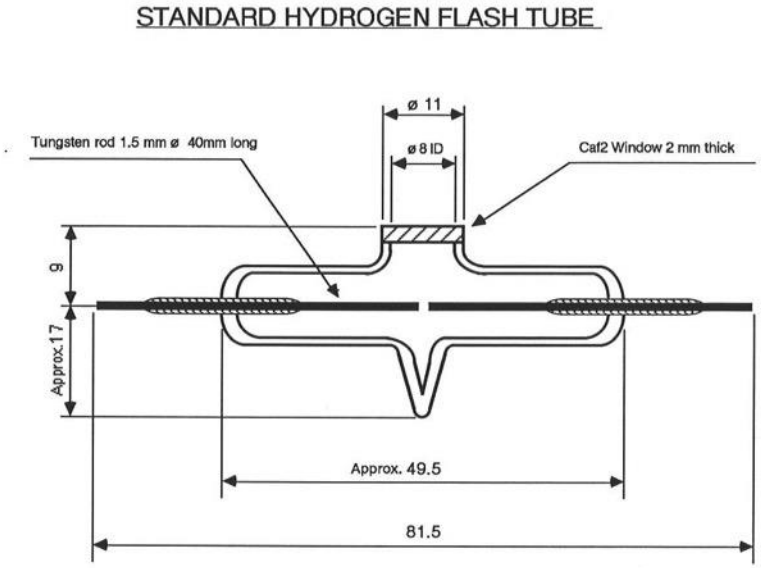

Figure 4-31: Sealed hydrogen flash lamp (Courtesy A. Braem, CERN).

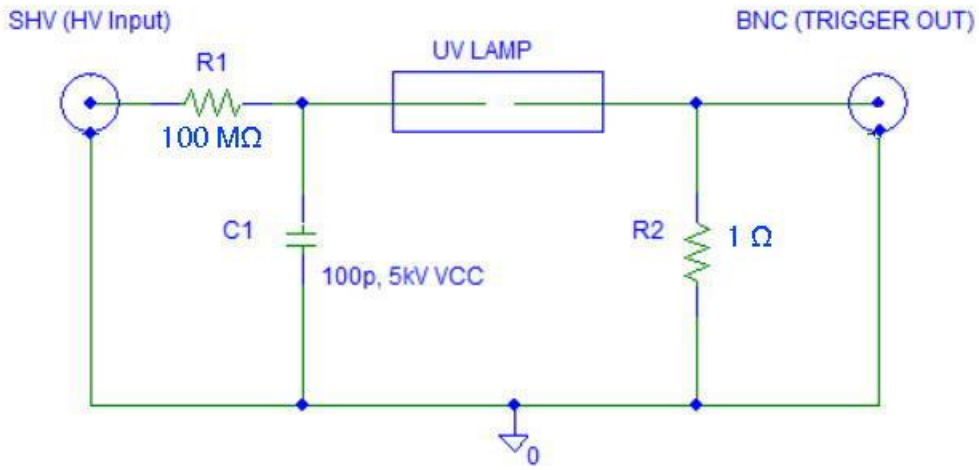

Figure 4-32: Powering scheme of the UV lamp.

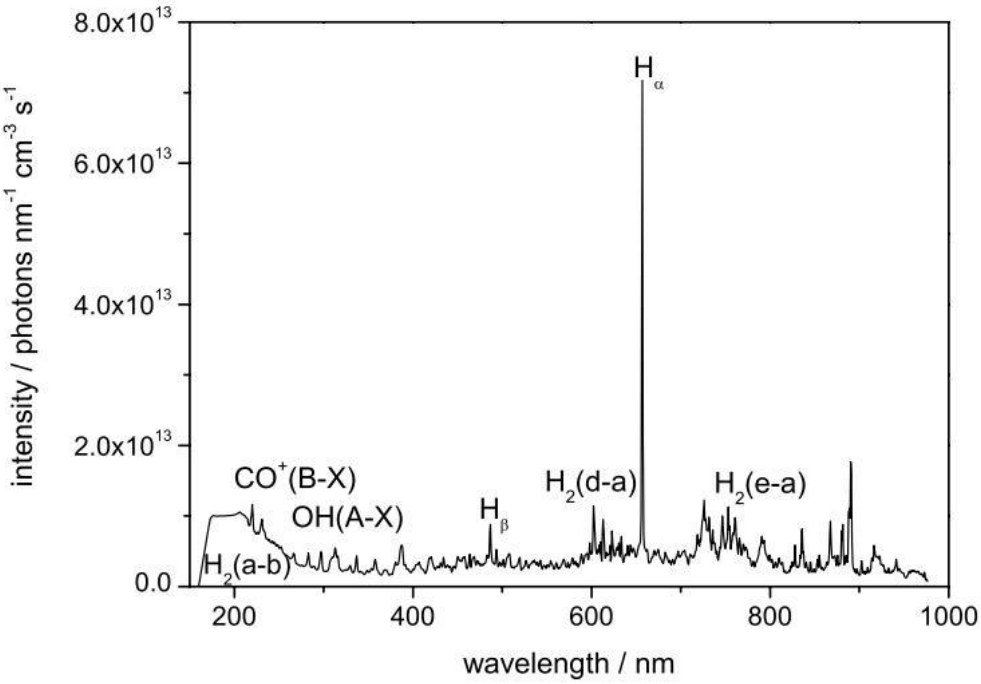

Figure 4-33: H_2 discharge emission spectrum (Stapelmann *et al.*, 2014).

In higher power devices, the emission of electrons from a hot filament initiates a discharge, whose intensity can be controlled by an applied voltage; the potential drops after the discharge to reduce heating. To be transparent in the UV region, the housing is realized with fused silica, UV glass or magnesium fluoride. Figure 4-34 is an example of a commercial deuterium arc lamp and its emission spectrum (Wikipedia, 2020a). A wide selection of arc lamps for laboratory used is proposed for example by Lambda Scientific (Light_Sources, 2020).

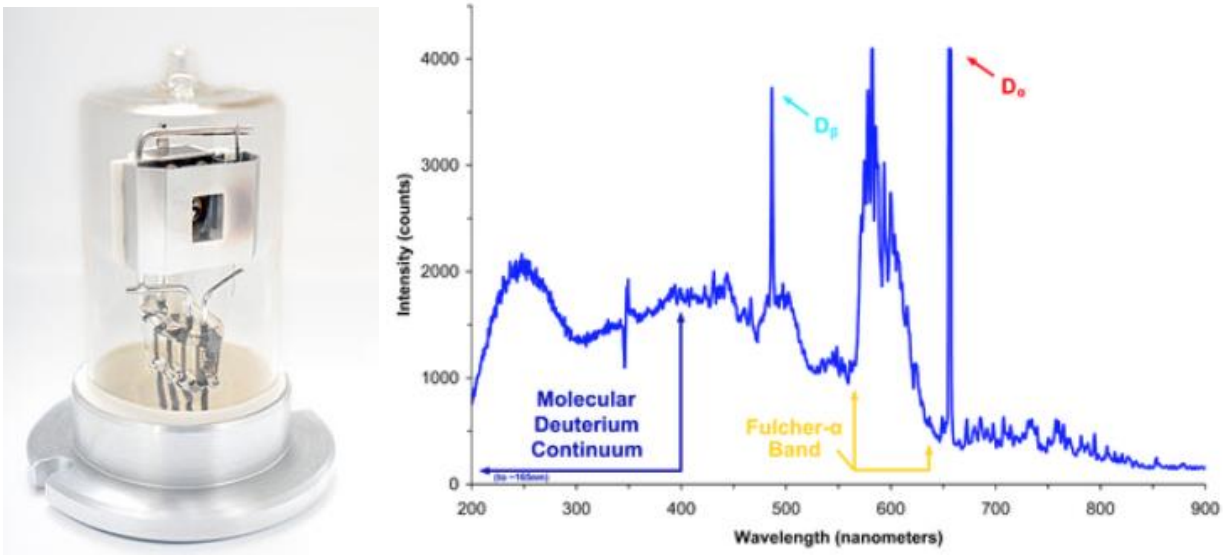

Figure 4-34: Deuterium discharge lamp and its emission spectrum.

A discharge in argon, triggered with a spark plug, was used in the early developments of the photosensitive MWPCs; with filters and collimators, the intensity of the UV emission could be reduced to emulate the single photoelectron patterns generated by Cherenkov effect in radiators (Charpak *et al.*, 1979). Simple to manufacture and operate, the scheme generates high noise levels and is inadequate when using high-sensitivity electronics.

Figure 4-35, Figure 4-36 and Figure 4-37 show the emission spectra under discharge of helium, krypton and xenon at pressures above few hundred torr (Stewart *et al.*, 1970) While the primary atomic excitation of rare gases occurs at vacuum UV wavelengths, at increasing pressures the process of dimers formation displaces the fluorescence spectra at longer wavelengths, as described for example in Chapter 5.2 of (Sauli, 2014).

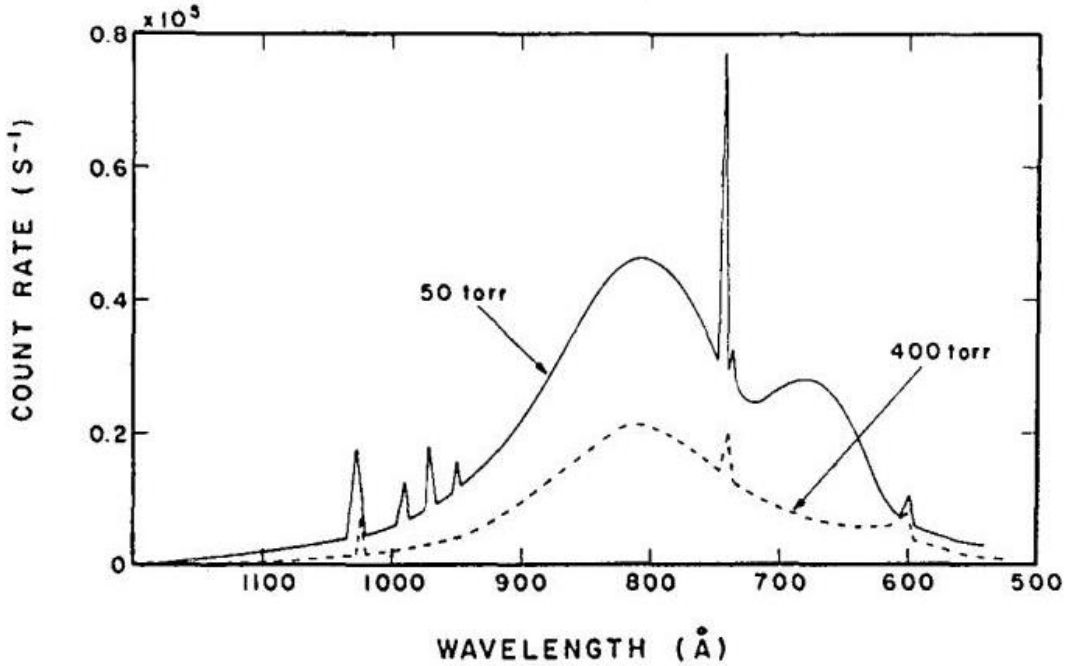

Figure 4-35: Discharge emission of Helium (Stewart *et al.*, 1970).

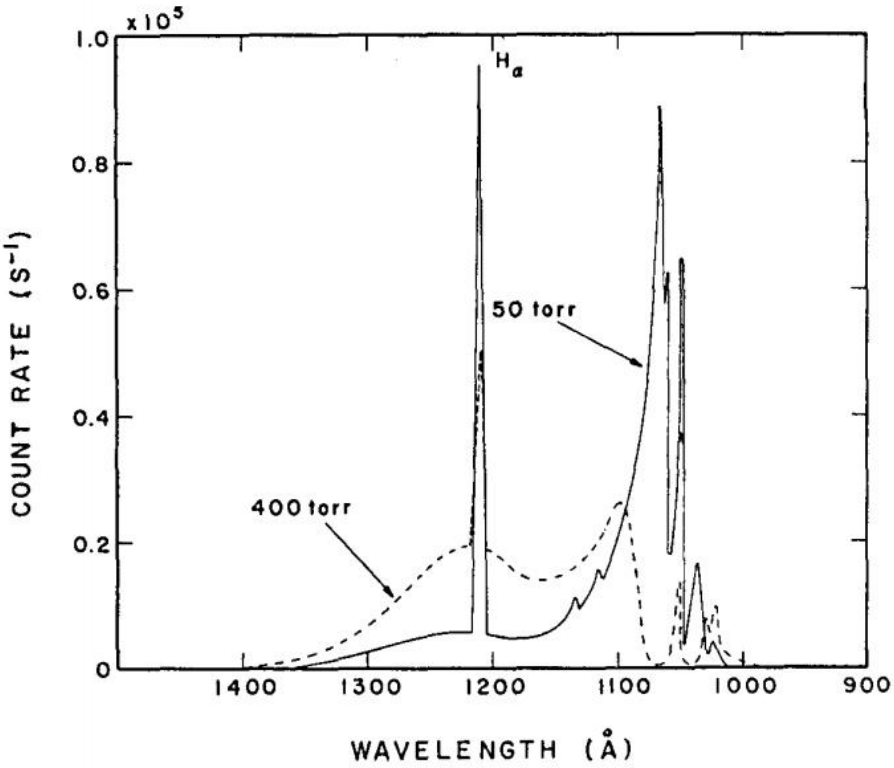

, Figure 4-36 Discharge emission of Argon (Stewart *et al.*, 1970).

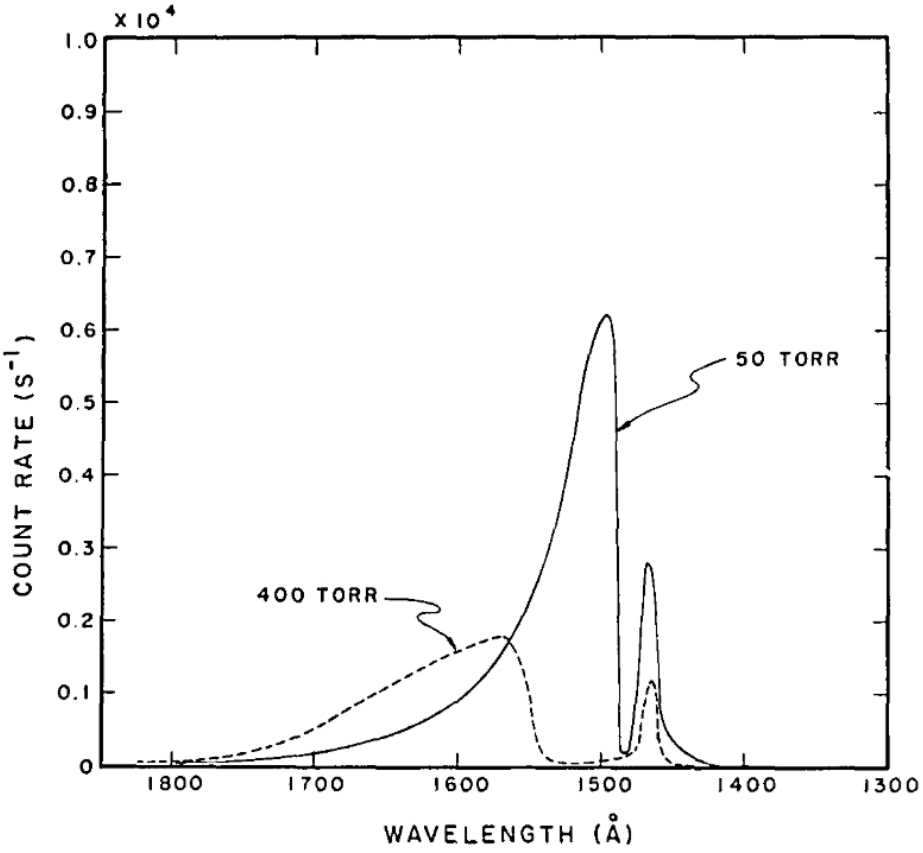

Figure 4-37: Discharge emission of Xenon (Stewart *et al.*, 1970).

A timing UV photon source, exploiting the primary and field-induced scintillation of a gas produced by an internal alpha particles, is shown in Figure 4-38 (Bouclier *et al.*, 1983). Filled with krypton at one bar, it has a broad emission spectrum centered around 8.6 eV (145 nm), with an intensity that can be enhanced increasing the voltage applied between the source holder and the grid. The time of the flash is obtained detecting the collected charge on the grid. To avoid absorption losses, the source could be attached to the detector's window with a vacuum flange.

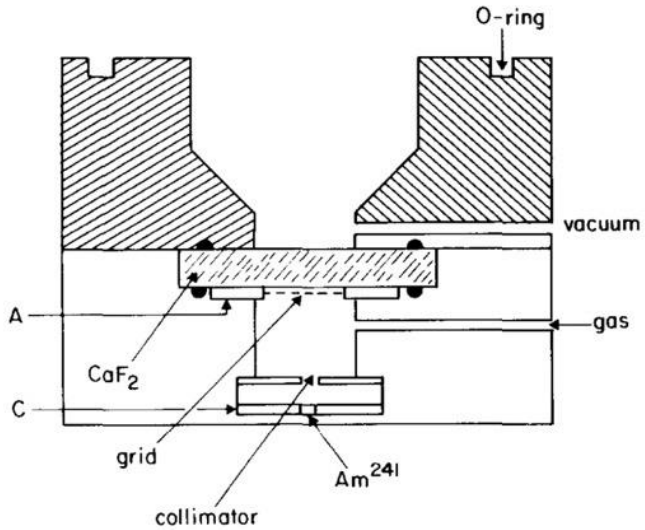

Figure 4-38: A timing UV lamp exploiting the radiation-induced scintillation of a gas.

Low energy pulsed lasers can extract photoelectron clusters from internal metallic electrodes, with intensities that can be reduced down to single electrons; the photon beam position and size can be controlled to few hundred microns, permitting to study the localization properties of the detector. This method has been extensively used in the development of Cherenkov Ring Imagers. Depending

on the detector capacitance and amplifier's noise, gas gains above 10^5 are generally needed to detect single electrons.

To ensure that the detected signal corresponds to single electrons, the intensity of the source is reduced until around 10% of events in coincidence generate a signal, as shown by the example in Figure 4-39, thus reducing the probability of multiple photon events below a percent.

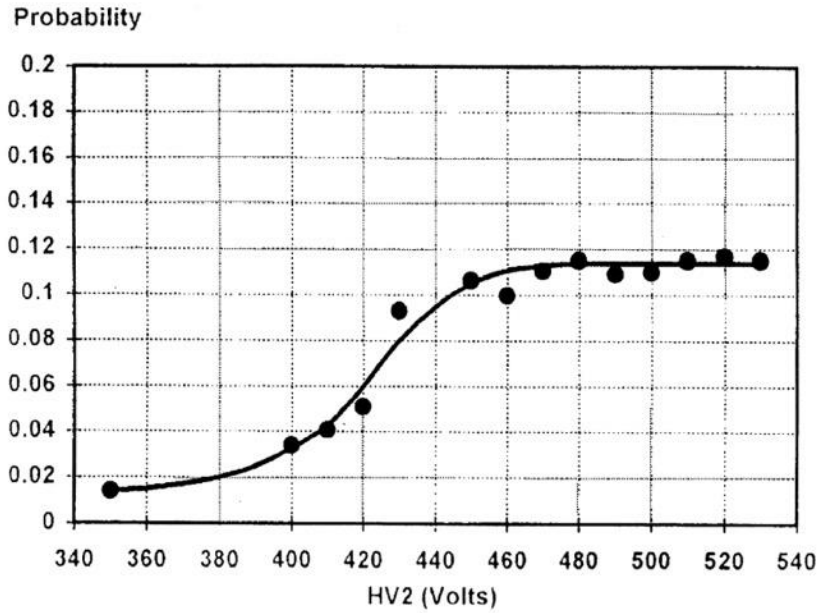

Figure 4-39: Single photon counting efficiency as a function of voltage of a MICROMEGAS detector (Derré *et al.*, 2000).

The single electron pulse height spectrum, exponential at moderate fields, evolves to peaked distribution at very high gains, see Section 5.4 in (Sauli, 2014). The shape is described by the Polya law, function of a parameter θ:

$$P(x,q) = \left[x\left(q+1\right)\right]^q e^{-x(q+1)} \qquad (4\text{-}1)$$

where $x = n/\bar{n}$ is the number of electrons in the avalanche, with average value $\bar{n}$. For $\theta=0$, the expression reduces to a simple exponential, Figure 4-40.

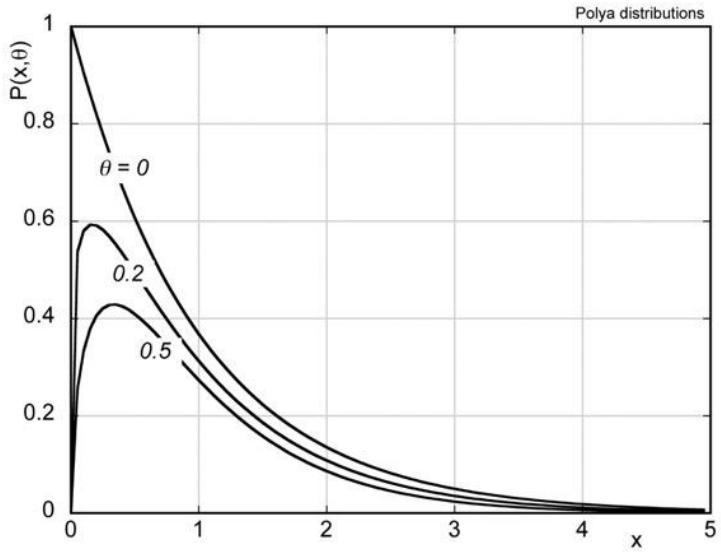

Figure 4-40: Polya single electron avalanche distribution for increasing values of the parameter θ.

Figure 4-41 is an example of evolution to peaked distributions at increasing voltage, recorded with the multistep proportional chamber that permits to reach gains above 10^7 (Sauli, 1986).

Due to the appearance of discharges, such large values of gains can rarely be attained in MPGD structures. In GEM-based structures, where the discharge problem is solved cascading several lower gain multipliers, the single electron statistics is dominated by the moderate field in the first electrode, and remains exponential at high gains, Figure 4-42 (Meinschad, Ropelewski and Sauli, 2004).

In MICROMEGAS detector, where large gains are obtained within a high field gap, the single electron distributions approach a peaked shape, Figure 4-43 (Zerguerras *et al.*, 2009); the peak at small pulse heights is due to noise.

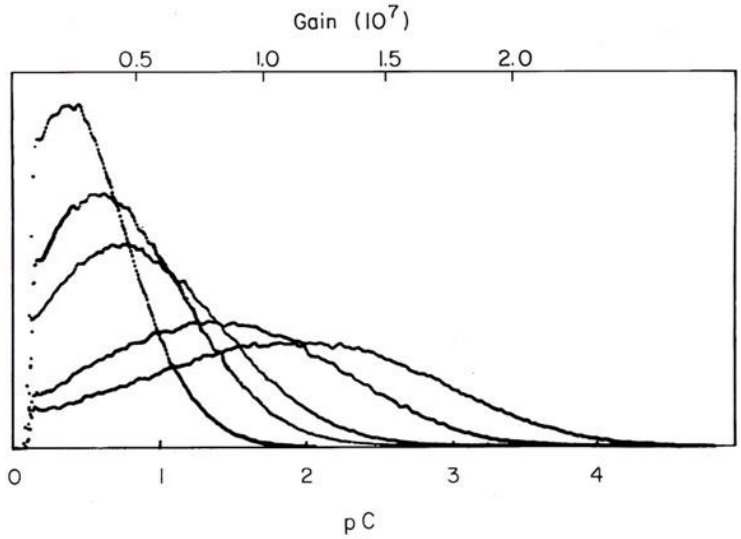

Figure 4-41: Single electron pulse height distributions at increasing gains recorded with the multistep chamber.

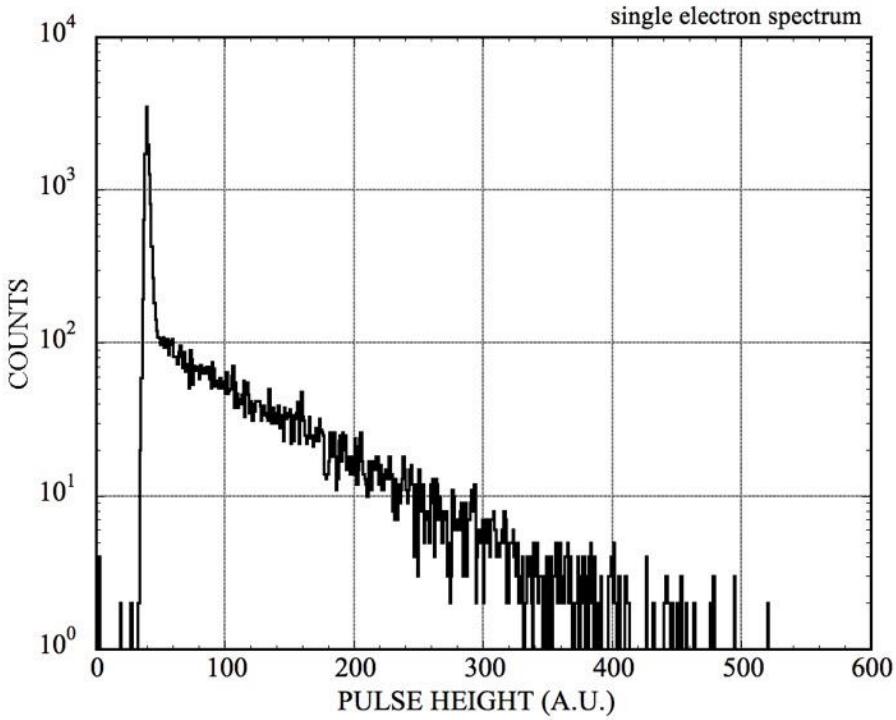

Figure 4-42: Single electron pulse heigh spectrum recorded with a multi-GEM detector (Meinschad, Ropelewski and Sauli, 2004).

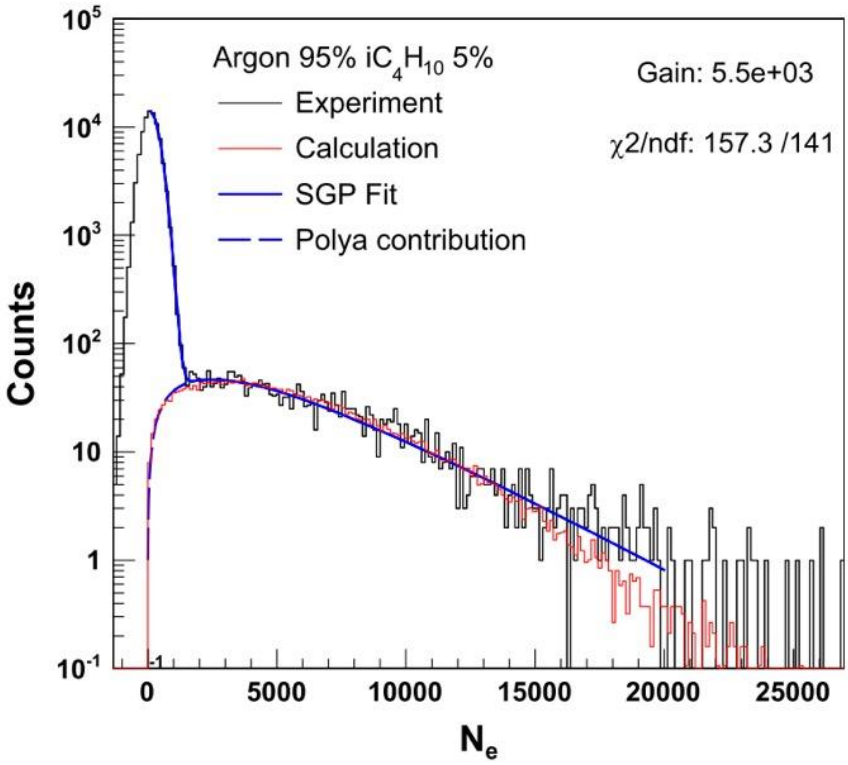

Figure 4-43: Single electron pulse height distribution recorded with a MICROMEGAS detector.

High power pulsed UV lasers have been used since the early development of large volume drift chambers to emulate straight ionization tracks traversing the sensitive volume. Unaffected by the magnetic field, they permit correction of the distortions encountered in large detectors; for a review see (Hilke, 1986). The wavelength of standard UV lasers however is not short enough to directly ionize the gases commonly used in the detectors: 337 nm (3.7 eV) and 266 nm (4.7 eV) for frequency-quadrupled Ne-YAG and N_2 lasers, respectively. A mechanism of two- and three-photons resonant absorption by impurities has been invoked to explain the observations. Use of additives strongly enhances the ionization yield (Hubricht *et al.*, 1985) (Beingessner *et al.*, 1988) but raises concerns on long-term performance of the detectors and has been essentially abandoned.

Figure 4-44 shows schematically the laser calibration system of the ALICE TPC (Alme *et al.*, 2010); an optical system of semi-transparent beam splitters, mirrors and prisms distributes the beams to cover all the sensitive volume. Two Nd-YAG lasers provide ~130 mJ/pulse of 5 ns duration with a 10 Hz frequency; the ~mm wide beams have enough power density to generate ionization trails by multiple photon absorption on residual impurities in the gas.

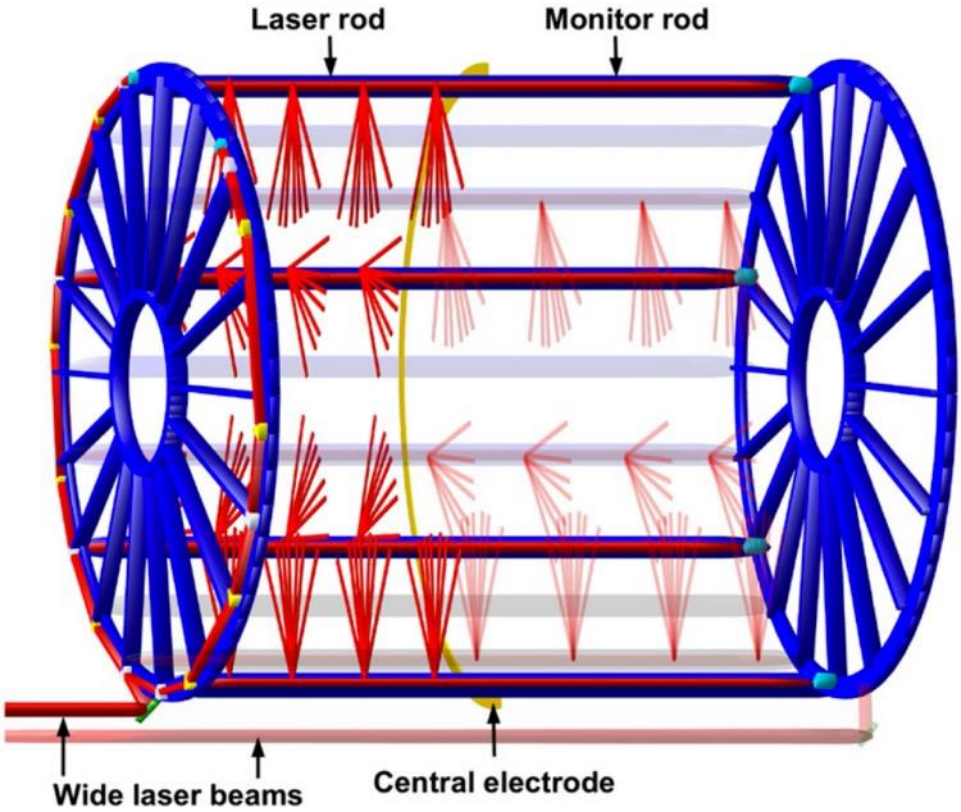

Figure 4-44: The ALICE TPC laser calibration system (Alme *et al.*, 2010).

5 PHYSICAL PROPERTIES OF GASES AND VAPORS

5.1 Energy loss of charged particles

Charged particles lose energy in matter through multiple electromagnetic Coulomb interactions, releasing ionization electrons and ions along their trail.

Table 5.1 is a compilation of physical constants of gases used in detectors; the ionization losses values refer to unit charge heavy particles at the minimum of ionization.

Gas	Density ($mg\ cm^{-3}$)	E_x (eV)	E_I (eV)	W_I (eV)	$dE/dx\|_{min}$ ($keV cm^{-1}$)	N_P (cm^{-1})	N_T (cm^{-1})
H_2	0.084	10.8	13.6	37	0.34	5.2	9.2
He	0.179	19.8	24.6	41.3	0.32	3.5	8
Ne	0.839	16.7	21.6	30	1.45	13	50
Ar	1.66	11.6	15.7	25	2.53	25	106
Xe	5.495	8.4	12.1	22	6.87	41	312
CH_4	0.667	8.8	12.6	30	1.61	37	54
C_2H_6	1.26	8.2	11.5	26	2.92	48	112
iC_4H_{10}	2.49	6.5	10.6	26	5.67	90	220
CO_2	1.84	7.0	13.8	34	3.35	35	100
CF_4	3.78	10.0	16.0	54	6.38	63	120

Table 5.1: Physical constants for various gases, and approximate values of energy loss and number of ion-pairs for unit charge minimum ionizing particles at normal temperature and pressure (NTP, 20 ^{0}C 1 bar). Data from (Sauli, 2014).

The differential energy loss as a function of particle velocity, also named stopping power, has a characteristic profile with a fast decrease reaching a minimum, followed by a moderate increase (the relativistic rise). Normalized to the medium density, Figure 5-1 gives the differential energy loss, for unitary charge heavy particles as a function of velocity in a range of materials (Workman et al., 2022). The actual energy loss for given temperature and pressure conditions is obtained multiplying the reduced values by the gas density, see

Table 5.1.

Computed with the web-based calculator of the National Institute of Standards (*PSTAR*, 2020), Figure 5-2 and Figure 5-3 provide the differential energy loss for protons in noble gases and some molecular gases at standard temperature and pressure, 0 ^{0}C 1 bar (STP).

For the lighter electrons, the energy scale is shifted, with the minimum around 1 MeV; losses due to bremsstrahlung add up for larger energies. The computed energy loss in argon at STP is shown in Figure 5-4 (*ESTAR*, 2020); MeV electrons as those emitted by the radioactive sources described in 4.6.2 lose a few keV per cm of path in the gas. Figure 5-5 and Figure 5-6 provide the normalized CSDA[2] range of protons and electrons as a function of energy in some materials.

Radioactive sources emitting alpha particles in the MeV range are used in the laboratory for development and testing of gaseous detectors, see 4.6.4. Computed with (*ASTAR*, 2020), Figure 5-7 shows the range of helium in several gases in the relevant energy range. The range in given pressure and temperature can be computed dividing by the gas density, and in mixtures adding up the different fractions.

[2] CSDA: Continuous Slowing-Down Approximation

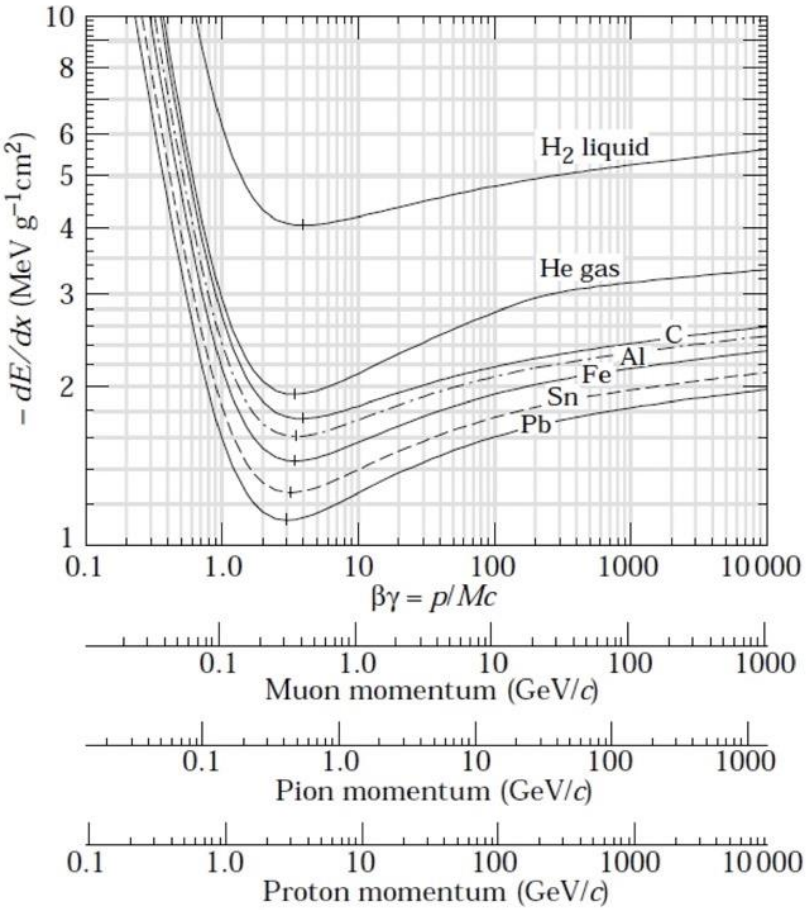

Figure 5-1: Differential energy loss as a function of particle velocity (Workman and et al., 2022)

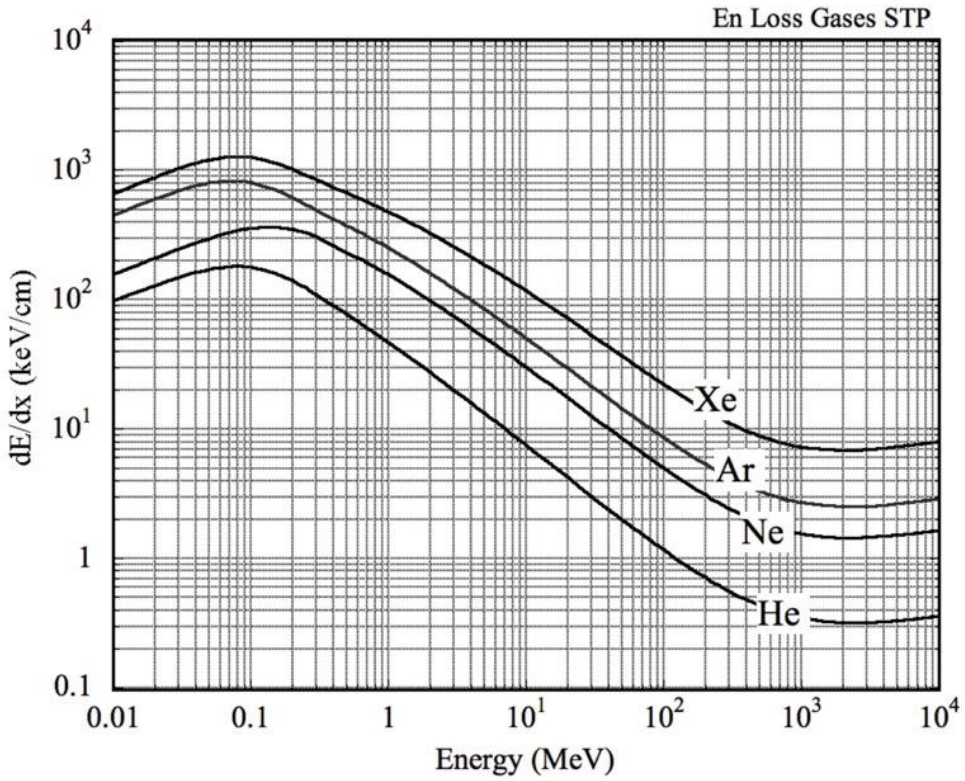

Figure 5-2: Differential energy loss for protons in noble gases at STP. From (*PSTAR*, 2020).

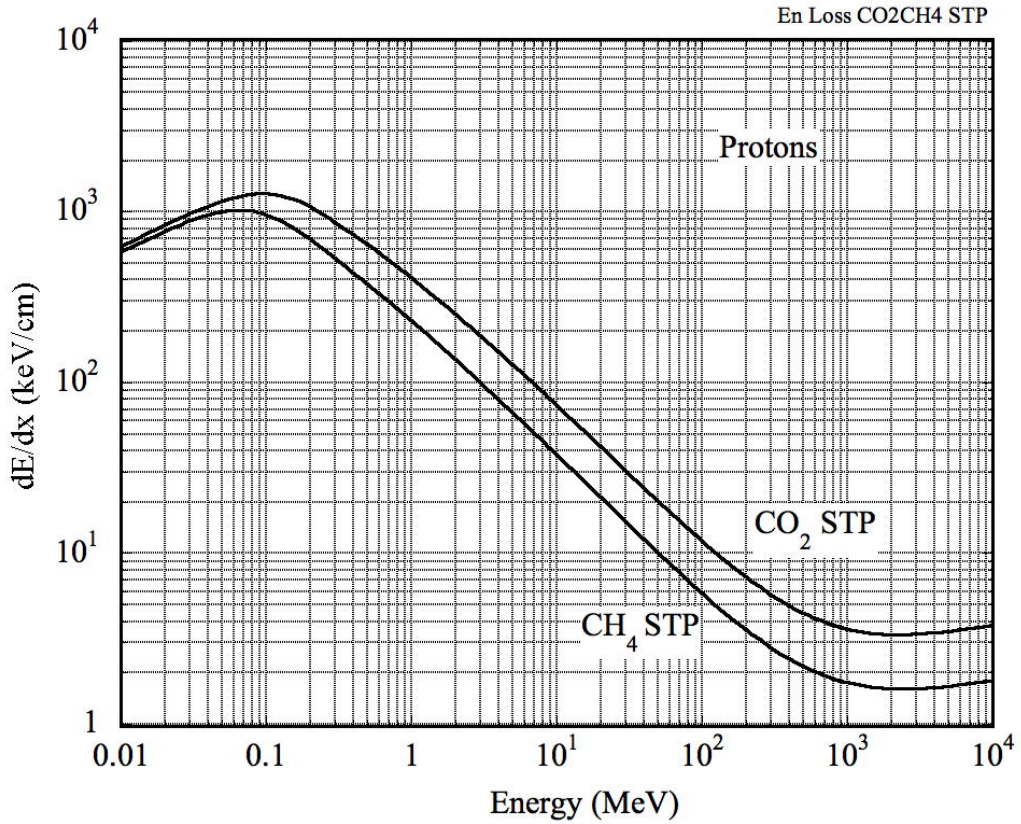

Figure 5-3: Differential energy loss for protons in carbon dioxide and methane at STP. (*PSTAR*, 2020).

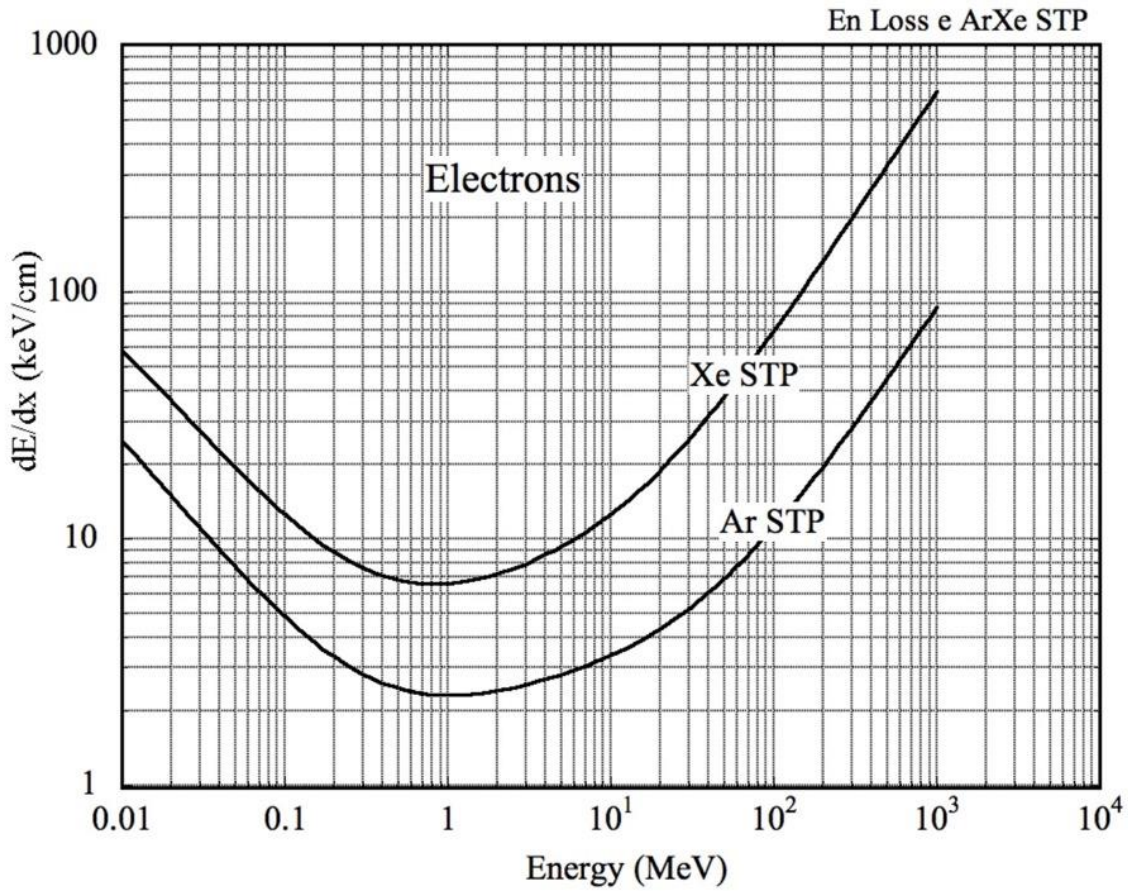

Figure 5-4: Differential energy loss for electrons in argon and xenon at STP (*ESTAR*, 2020).

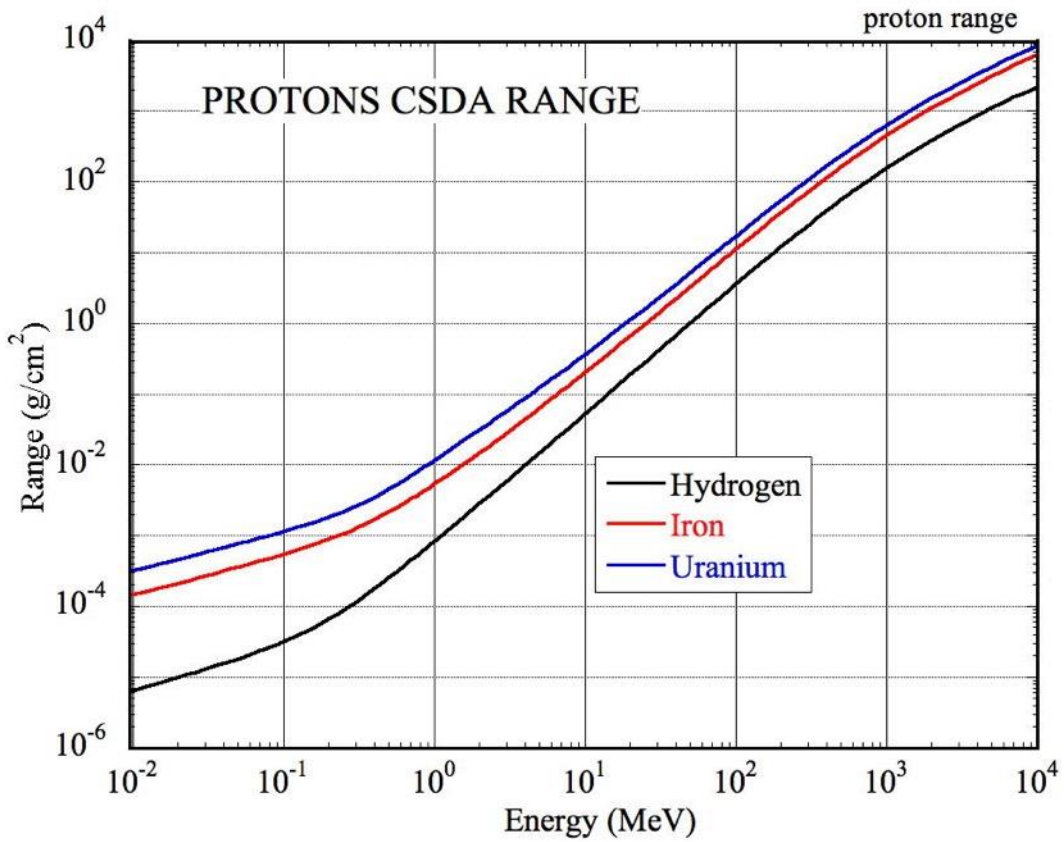

Figure 5-5: Protons range in some materials (*PSTAR*, 2020).

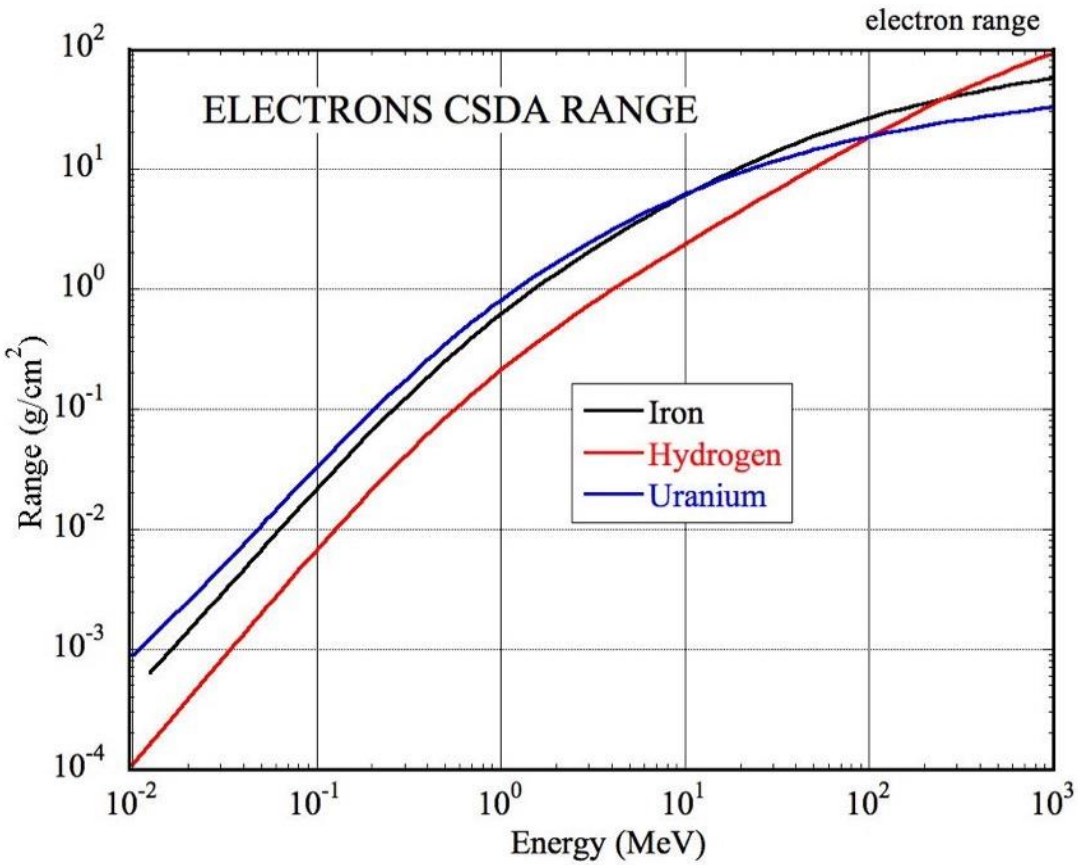

Figure 5-6: Electrons range in some materials (*ESTAR*, 2020).

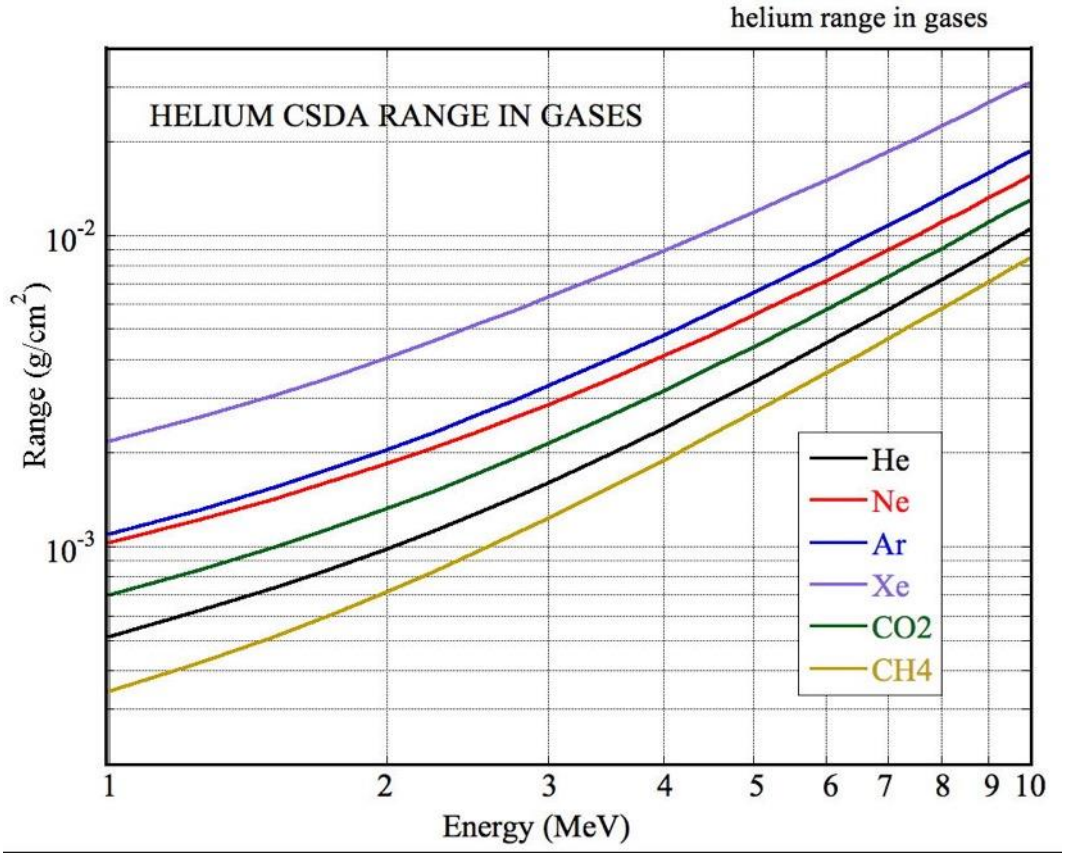

Figure 5-7: Range of helium in different gases (*ASTAR*, 2020).

5.2 Ionization clusters

The outcome of the multiple electromagnetic interactions between charged particles and the medium interactions is the creation of a trail of primary electron-ion clusters; their number depends on the energy of the projectile and on the type and density of the medium. Experimental values and prediction of a simple model of the number of clusters for various gases at NTP are shown in Figure 5-8 (Smirnov, 2005). Note that the clusters density does not follow a simple atomic or molecular weight law. For mixtures, one can use a simple average weighted with the percentages of components.

The electron within a cluster can receive enough energy from the interaction to be able to further ionize the gas; The average total number of clusters is between two and four times the primaries, see also Table 5.1. Figure 5-9 shows measured probability distributions of the cluster size for argon and methane (Fischle, Heintze and Schmidt, 1991); data for other rare and molecular gases are provided in the reference, but differ little from those shown in the figure.

Primary electrons with energy exceeding ~1 keV, referred to as delta rays, play a crucial role in determining the statistics of the energy loss process and the limits in position accuracy that can be obtained with gaseous counters. Beam tracks images recorded with the optical GEM show clearly the presence of long-range delta electrons, Figure 5-10 (Brunbauer *et al.*, 2018). When recording the particles coordinates with electronic systems, the presence of these rare but energetic encounters is revealed by non-gaussian tails in the position accuracy distributions.

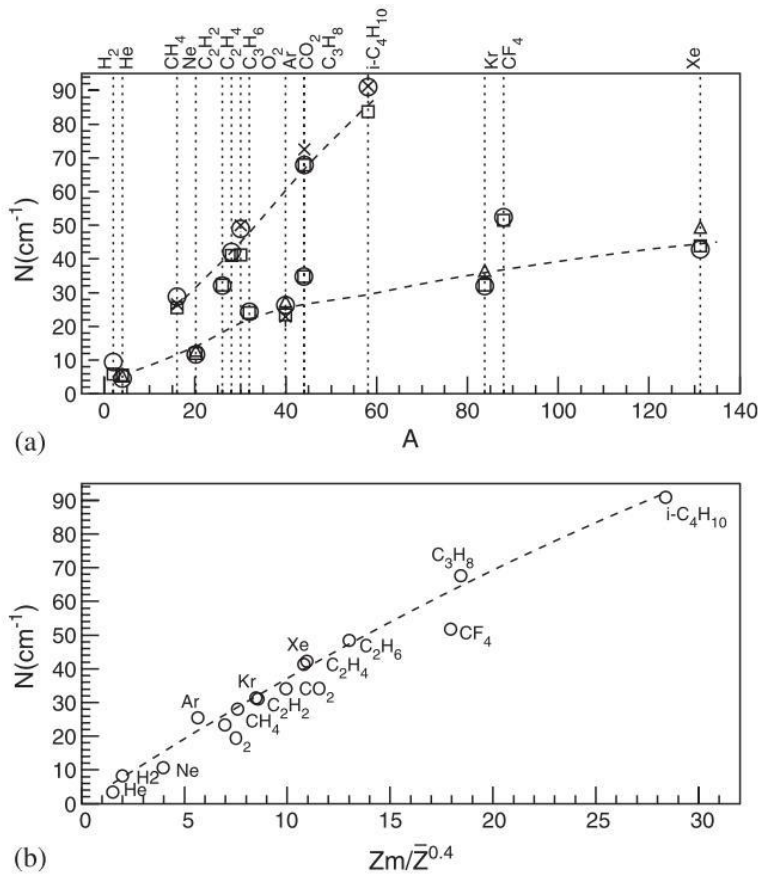

Figure 5-8: (a): Experimental values and model calculation (dashed lines) of the number of clusters per cm released by fast particles in gases at NTP. (b): Computed number of primary clusters per cm. The horizontal axis is the ratio of total and average molecular charge (Smirnov, 2005).

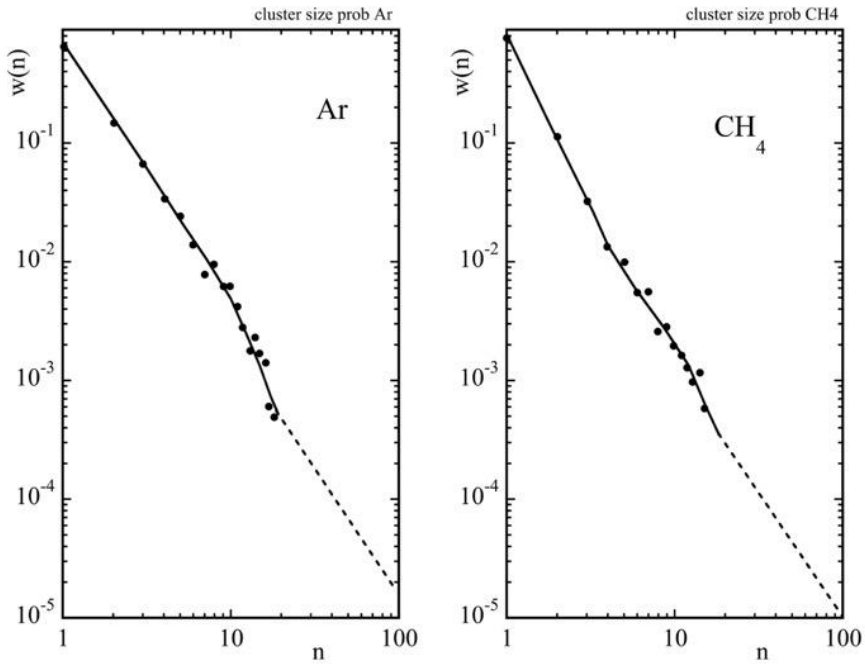

The average total number of clusters is between two and four times the primaries, see also Table 5.1. Figure 5-9: Cluster size probability for fast particles in argon and methane. The full line is an eye-fit to the data, the dashed line is the prediction of a simple model (Fischle, Heintze and Schmidt, 1991).

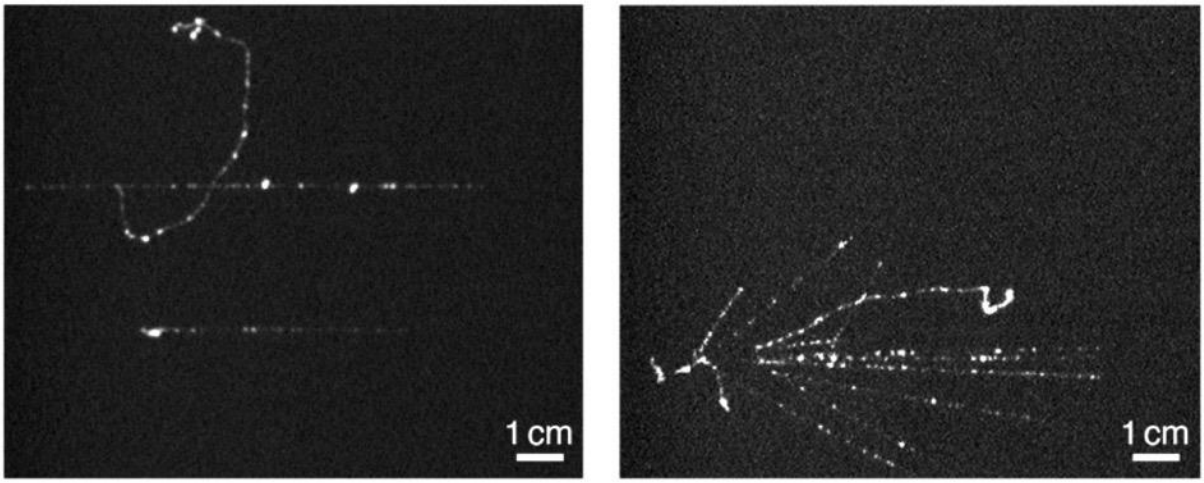

Figure 5-10: Optical GEM images of beam tracks with long-range delta electrons (Brunbauer *et al.*, 2018).

5.3 Detection of photons

Unlike charged particles, releasing ionization all along their trajectory, photons interact with atoms and molecules with single encounters through several electromagnetic processes, depending on energy: radiation-less absorption, photoelectric, Compton scatter, pair production. The absorption process is described by an exponential law:

$$I=I_0 e^{-\mu\rho x}=I_0 e^{-\alpha x} \qquad (5\text{-}1)$$

where μ is the mass absorption coefficient (in cm^2/g), ρ the material density (in g/cm^3) and $\alpha=\mu\rho$ the linear absorption coefficient (in cm^{-1}). The fraction of photons removed from the beam, or absorption efficiency, is then

$$\varepsilon=1-e^{-\alpha x} \qquad (5\text{-}2).$$

The linear absorption coefficient relates to the absorption cross section σ (in cm^2) through the expression $\alpha=N\sigma$, where N is the number of atoms or molecules per unit volume of the medium:

$$N=N_A\rho/A \qquad (5\text{-}3)$$

where N_A=6.0247x10^{23} is the Avogadro number and A the atomic weight of the material (in g/mole). For an ideal gas at STP $N=2.687x10^{19}$ molecules/cm^3. Expressing the cross section in megabarn (1 Mb=$10^{-18}cm^2$):

$$\alpha_{STP}(cm^{-1})=26.87\ \sigma(Mb). \qquad (5\text{-}4)$$

The linear absorption coefficient in different conditions can be computed using a density-dependent scaling.

Data in the following sections are presented as a function of photon energy E; the corresponding wavelength λ can be obtained from the expression:

$$\lambda(nm) = 1240/E(eV) \qquad (5\text{-}5).$$

5.3.1 Visible to ultraviolet range

Gases are largely transparent for visible and near ultraviolet photons, with absorption cross sections opening at vacuum UV and shorter wavelengths. For rare gases, absorption occurs above an energy threshold corresponding to their ionization potential, resulting in the emission of a photoelectron; for molecular gases the absorption begins at lower energies, resulting in radiation-less mechanical dissipation. Absorption cross sections as a function of photon energy are given for molecular gases of interest in detectors in Figure 5-11, Figure 5-12, Figure 5-13, Figure 5-14, Figure 5-15, Figure 5-16.

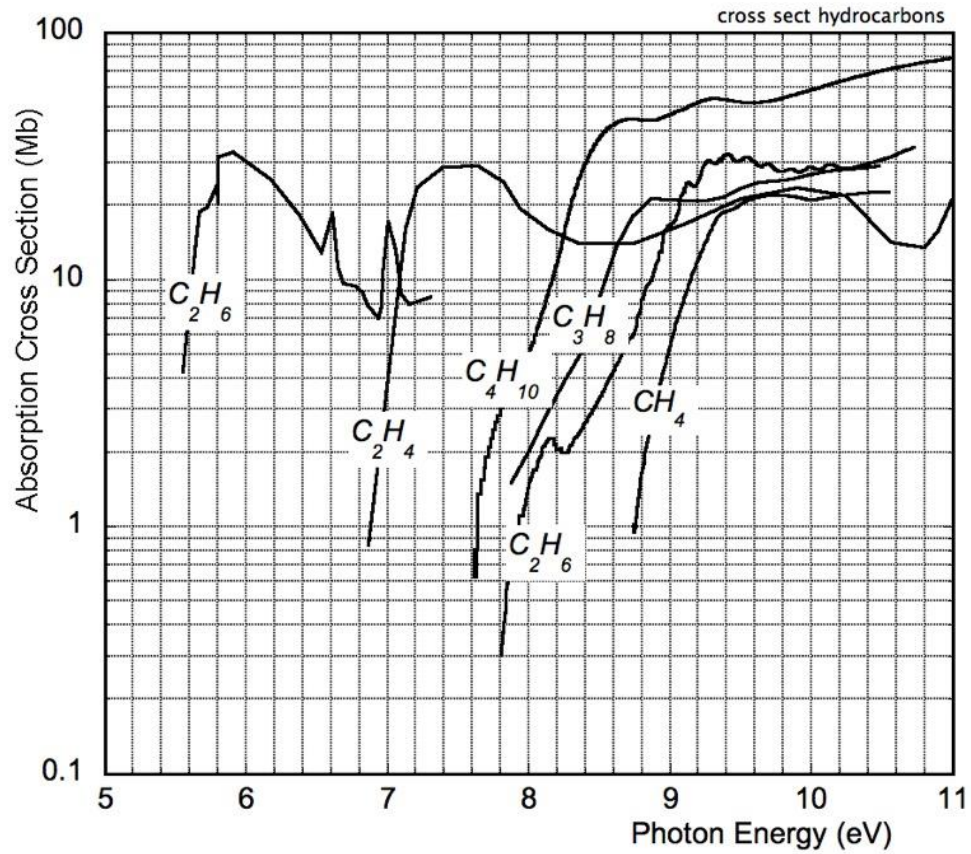

resulting in radiation-less mechanical dissipation. Absorption cross sections as a function of photon energy are given for molecular gases of interest in detectors in Figure 5-11: Photon absorption cross section for saturated hydrocarbons. Data from (Bélanger, Sauvageau and Sandorfy, 1969).

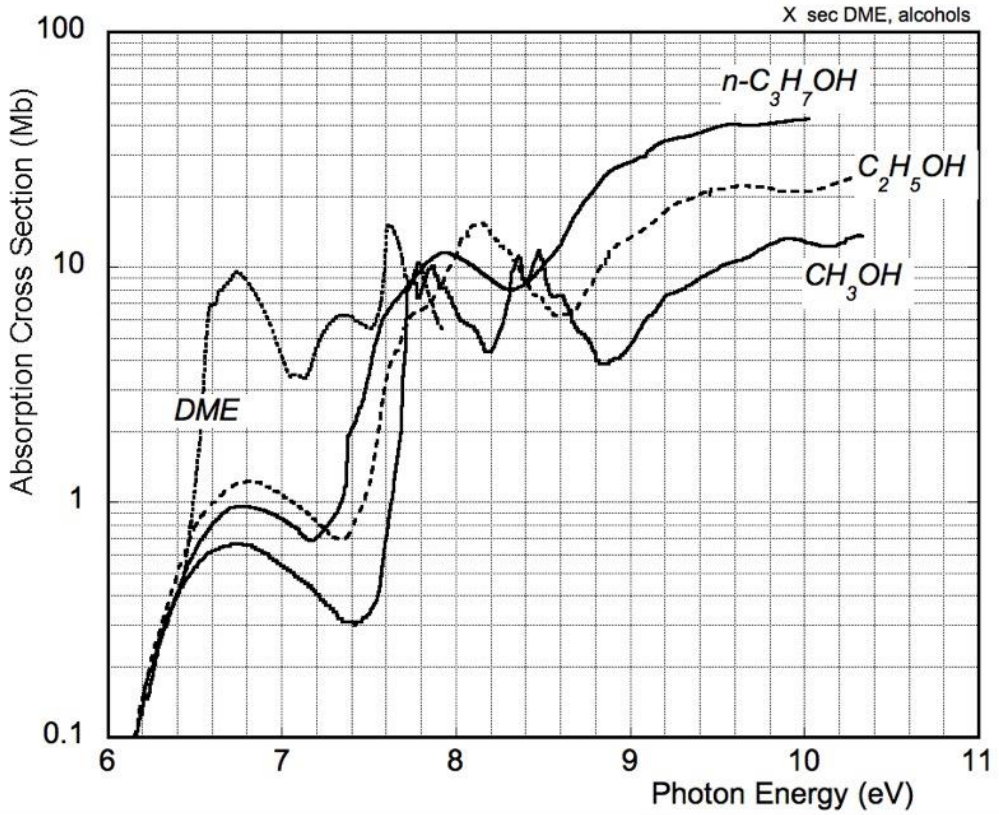

Figure 5-12: Photon absorption cross section for several alcohols and vapors. Data from (Calvert and Pitts, 1966) and (Au *et al.*, 1993).

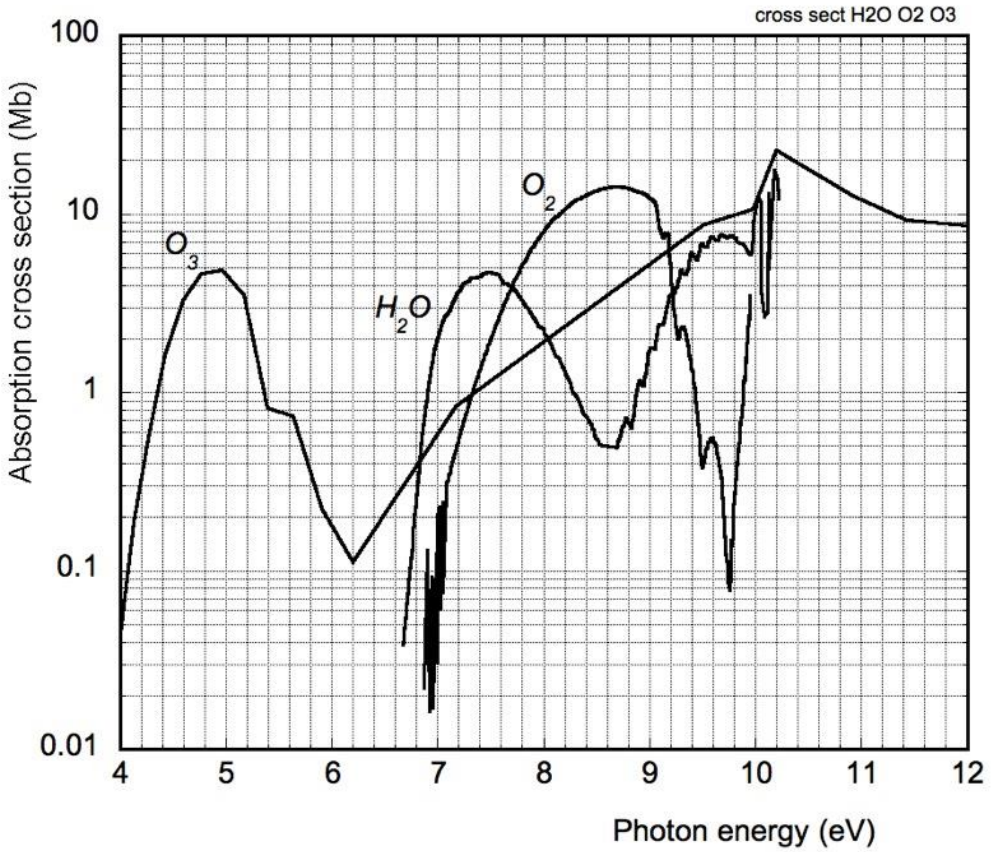

Figure 5-13: Absorption cross section for several molecular gases. Data from (Watanabe and Zelikoff, 1953)(Friedman, 1960)(Tanaka, Inn and Watanabe, 1953).

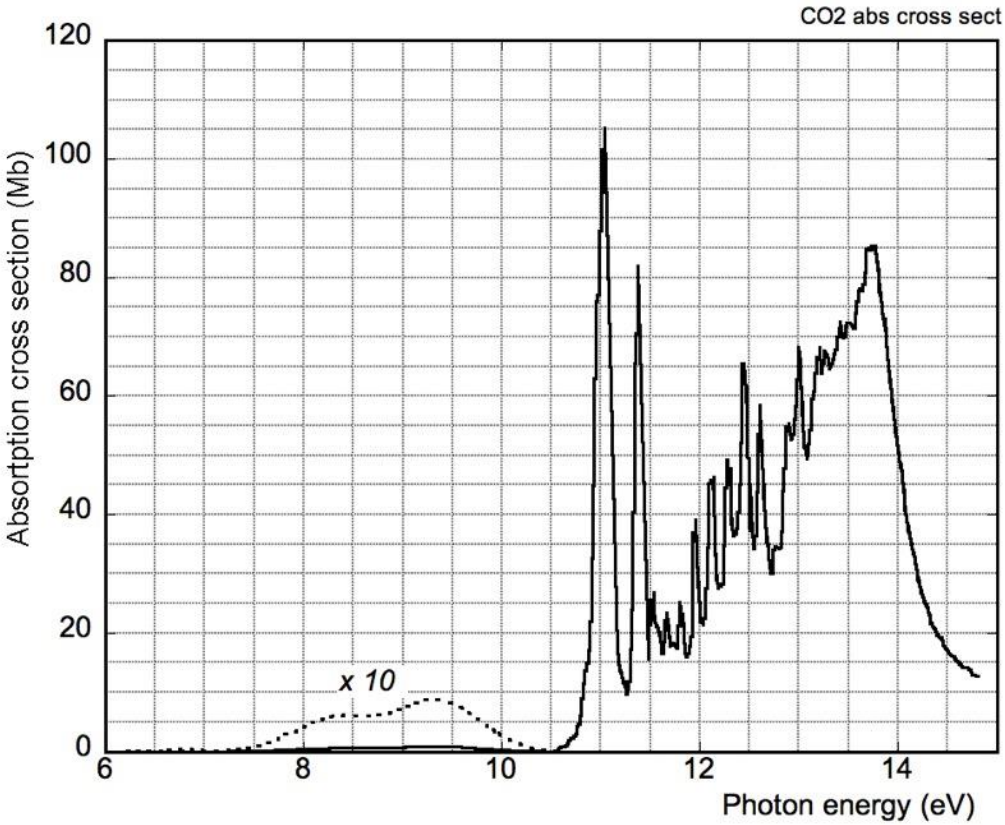

Figure 5-14: Absorption cross section of carbon dioxide. Data from (Chan, Cooper and Brion, 1993).

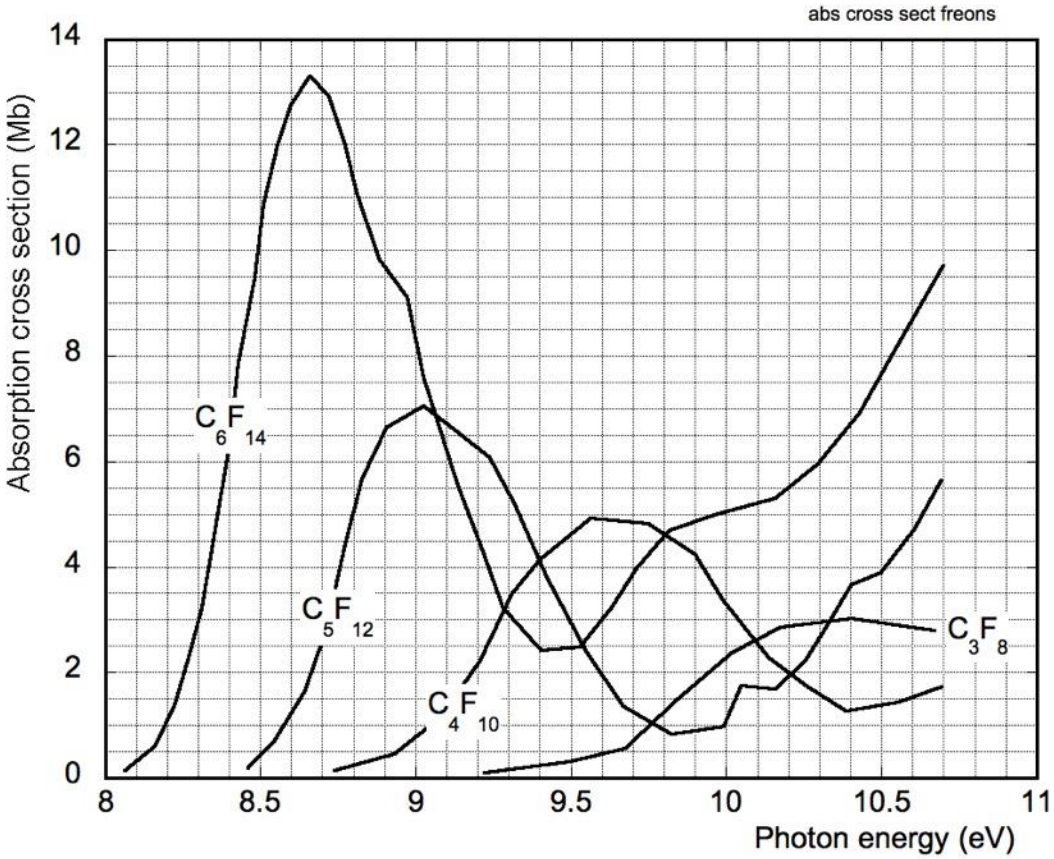

Figure 5-15: Absorption cross section of fluorinated carbon molecules. Data from (Bélanger, Sauvageau and Sandorfy, 1969).

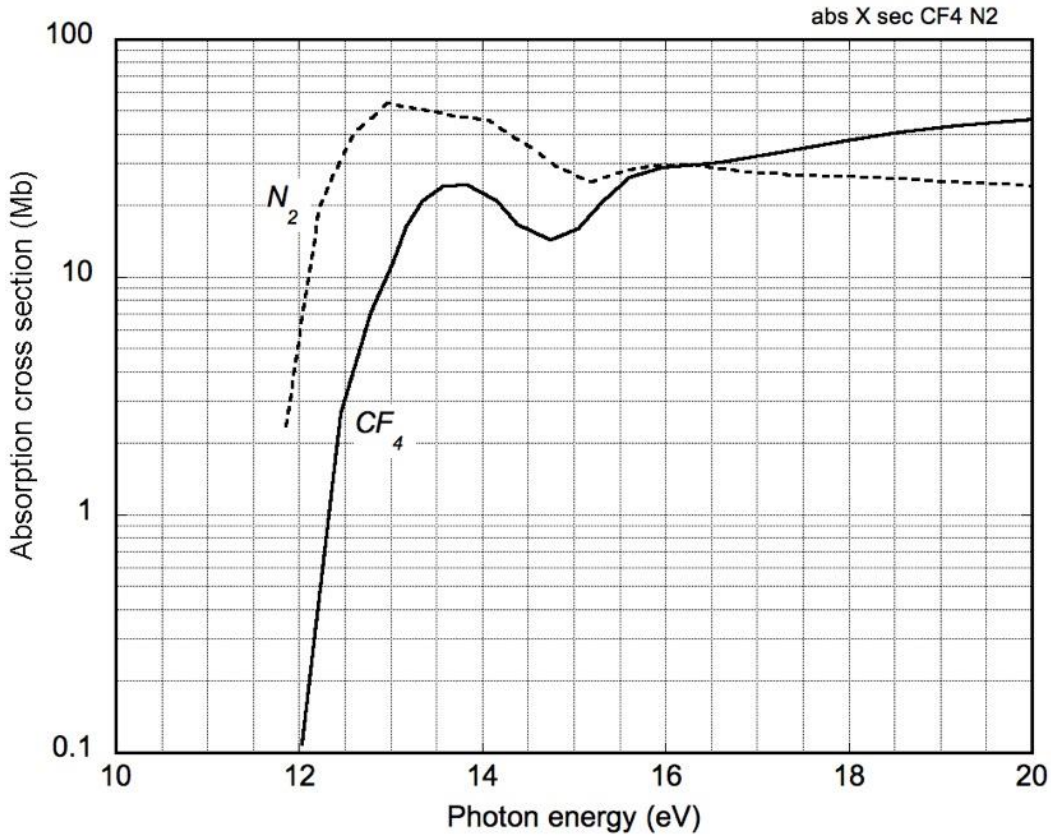

Figure 5-16: Absorption cross section of nitrogen and carbon tetrafluoride. Data from (Chan, Cooper and Brion, 1993) (Zhang *et al.*, 1989).

When the photon energy exceeds the photoionization threshold of the molecule, a photoelectron can be emitted with a probability defined by the energy-dependent quantum efficiency of the material. Some vapors have a particularly low photoionization threshold, and have been used for Cherenkov Ring Imaging (RICH) and other applications, Table 5.2.

COMPOUND	W_i (eV)	Peak QE (%)	P (NTP) (Torr)
Ethanol C_2H_6O	10.4	20	44.6
Acetone $(CH_3)_2CO$	9.65	31	251
Benzene C_6H_6	9.2	62	95.2
Triethyl amine (TEA)	7.5	33-42	73.2
Tetrakis dimethyl amino ethylene (TMAE) $C_2[(CH_3)_2N]_4$	5.3	29-40	0.5
Cesium iodide CsI	5.9	20-35	Solid
Diamond Like Carbon (DLC)	6.1-6.6	3-10	Solid

Table 5.2: Photo-ionization thresholds, peak quantum efficiency and vapor pressure of photosensitive gases and compounds. The quoted QE values depend on sources.

Special gases materials are used in the detection of photons in the near and vacuum ultraviolet range, for applications in Cherenkov Ring Imaging; Table 5.3 summarizes the main properties of selected radiator materials.

GASES (NTP)	$\mathbf{E_{TC}}$ **(eV)**	**(n-1)** $\mathbf{10^6}$ **(at 7eV)**	$\boldsymbol{\gamma_T}$	$\boldsymbol{\theta_M}$ **(°)**	$\mathbf{N_{PH}}$ **/cm**
He		33	123	0.48	0.005
Ne		67.3	86	0.66	0.01
Ar	16	300	41	1.4	0.05
CH_4	8.6	510	31	1.83	0.08
CF_4	12.5	488	32	1.80	0.08
C_2F_6		793	25	2.28	0.13
i-C_4H_{10}	8.3	1500	18		0.24
LIQUIDS (NTP)		**n (at 6.5 eV)**			
C_5F_{12}	7.5	1.262	1.638	37.6	30
C_6F_{14}	8.3	1.278	1.606	38.5	31
SOLIDS		**n (5.5 eV)**			
LiF	11.6	1.42	1.41	45.2	43
MgF_2	10.8	1.41	1.41	44.8	40
CaF_2	10	1.47	1.36	47.1	43
Fused silica	7.5	1.52	1.33	48.8	45

Table 5.3: Transparency cut-off energy $\mathbf{E_{TC}}$, refraction index **n** or **(n-1)**, Cherenkov threshold velocity $\boldsymbol{\gamma_T}$, maximum emission angle $\boldsymbol{\theta_M}$ and photons per cm of radiator at saturation $\mathbf{N_{PH}}$ detected with a figure of merit N_0=80 cm^{-1} (Sauli, 2014).

Figure 5-17 and Figure 5-18 show the total cross sections and quantum efficiency for TEA and TMAE, and Figure 5-19 the quantum efficiency of cesium iodide.

A promising thin-layer photocathode is Diamond-Like Carbon (DLC), due to its better stability when exposed to air (not the case for CsI). Several deposition methods have been investigated, mostly based on Chemical Vapor Deposition, providing often conflicting results. Figure 5-20 is an example of quantum efficiency measured for thin-film diamond photocathodes manufactured with various methods (Nitti *et al.*, 2008).

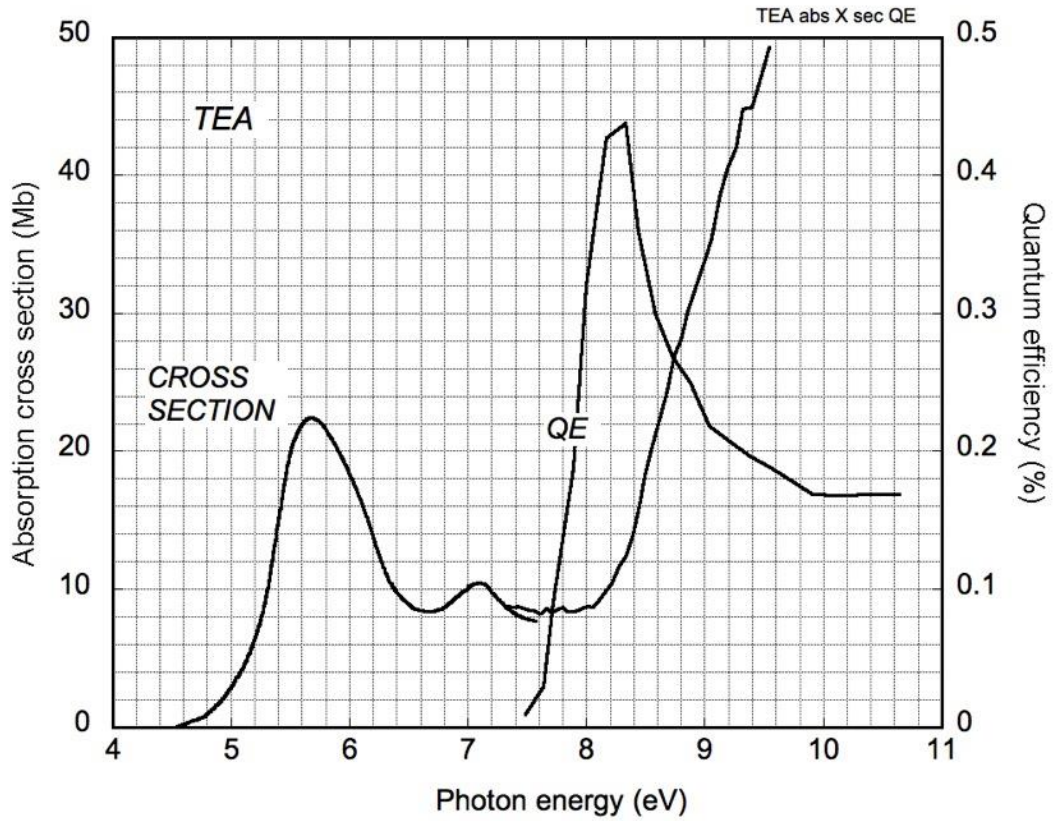

Figure 5-17: Absorption cross section and quantum efficiency of TEA. Data from (Holroyd *et al.*, 1987).

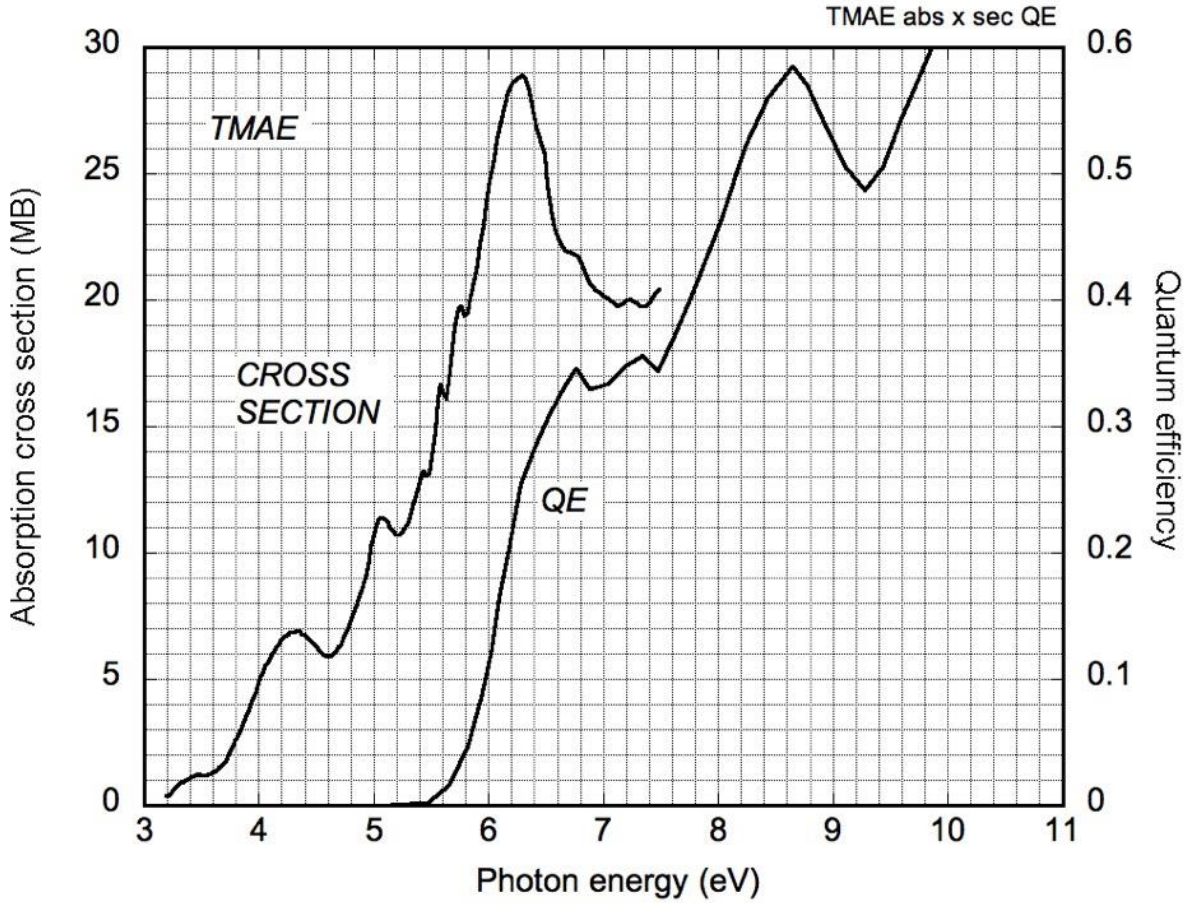

Figure 5-18: Absorption cross section and quantum efficiency of TMAE. Data from (Holroyd *et al.*, 1987).

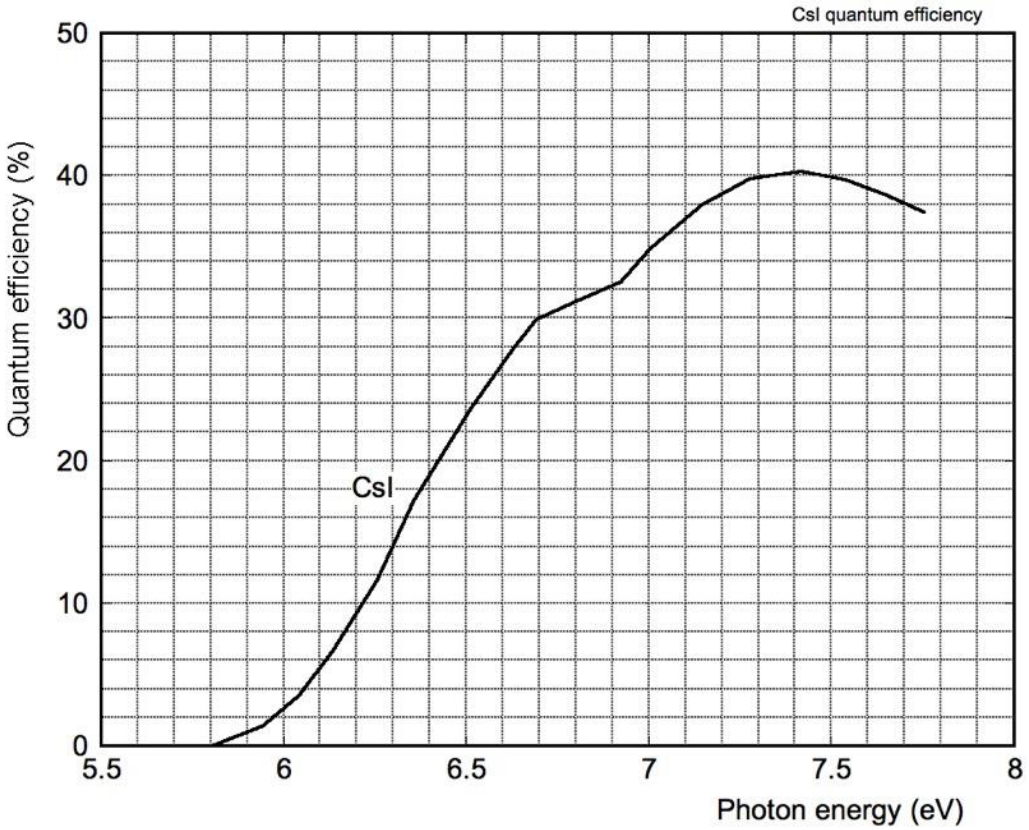

Figure 5-19: Quantum efficiency of CsI. Data from (Séguinot *et al.*, 1990).

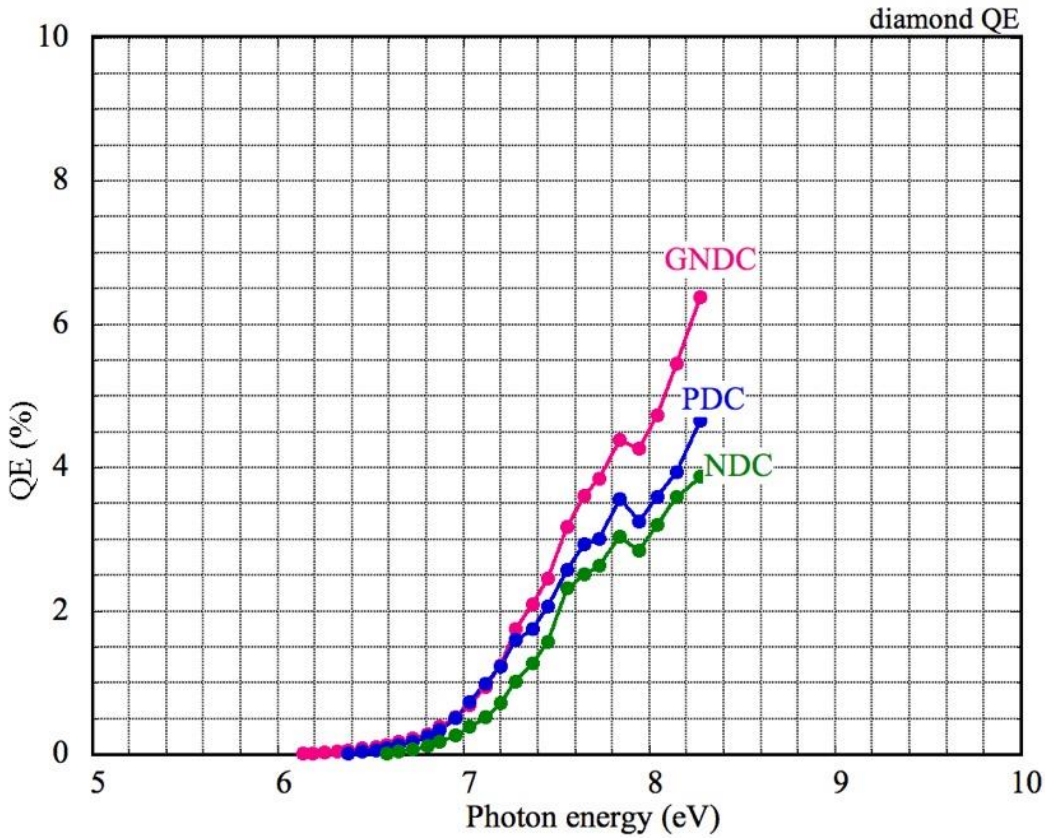

Figure 5-20: Quantum efficiency of diamond-like carbon layers deposited with different methods. Data from (Nitti *et al.*, 2008).

5.3.2 Soft to hard X-rays

Maximum just above the ionization potential, the absorption cross section has a characteristic decreasing dependence from energy, with sudden jumps when the photon energy exceeds the binding energy of the various electronic shells. The photoelectric effect is dominant up to photon energies of about one MeV, followed by coherent and incoherent Compton scattering and, above an energy corresponding to twice the electron mass, production of e^--e^+ pairs, see Figure 5-21 and Figure 5-22 for argon and xenon, respectively.

The photoelectric interaction results in the excitation of an electronic level followed by the transition to a lower level. The energy of the emitted photoelectron matches the difference between the two levels; below the K-orbital, it almost equals the photon energy, due to the very low energy of the lower levels. For photons of energy E_γ above the K edge, the de-excitation from K to L results in the appearance of an electron of energy E_γ-E_K, accompanied by the emission of a lower energy fluorescence photon or one or more Auger electrons. This gives the characteristic energy loss spectrum observed in the detection of ^{55}Fe X-rays (5.9 keV) in argon-based gas mixtures (see for example Figure 4-19).

Web-based calculators provide the mass attenuation coefficient of elements and many composite materials (see Chapter 13); a concise and useful compilation is the LBL X-ray Data Booklet, that can obtained in a printed form or downloaded at (Thompson and et al, 2009).

The binding energies of the elements increases with the atomic number, as shown in Figure 5-23; Table 5.4 provides the values for the K and L shells of noble gases and some elements commonly used in gaseous detectors.

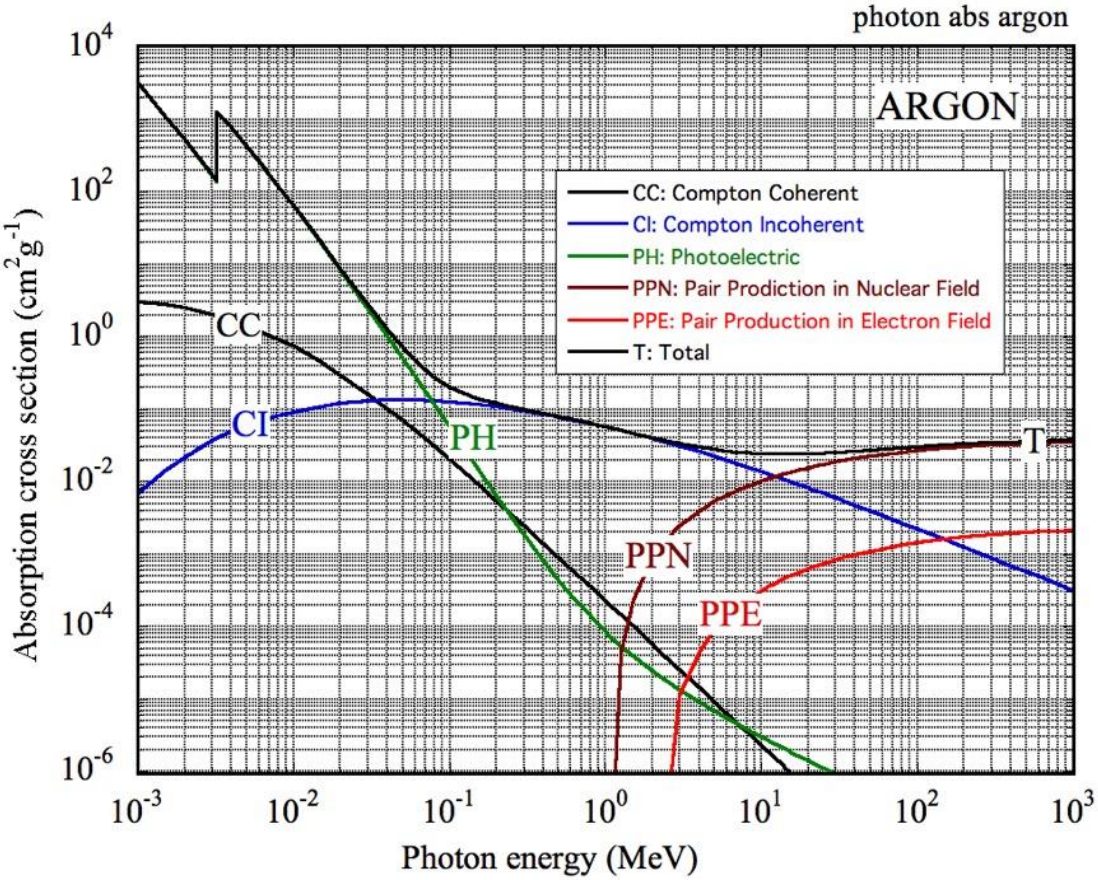

Figure 5-21: Absorption cross sections as a function of photon energy for Argon.

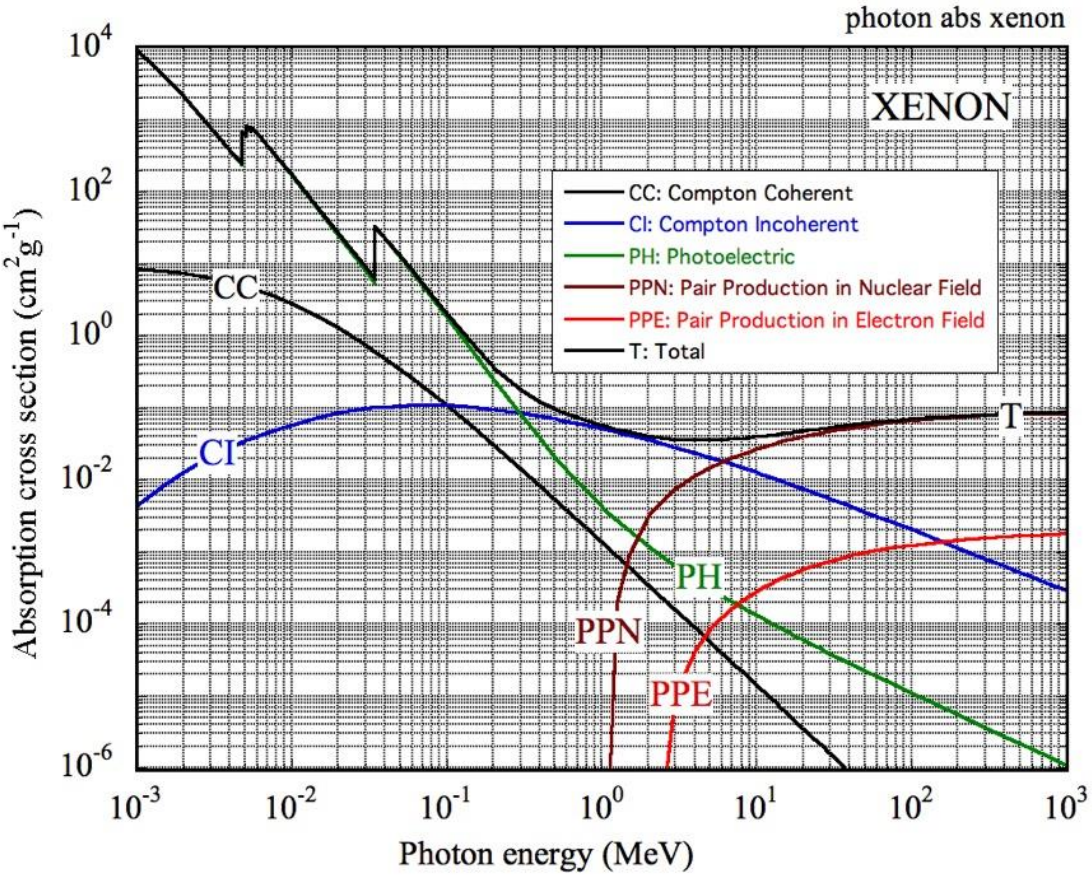

Figure 5-22: Absorption cross sections as a function of photon energy for xenon.

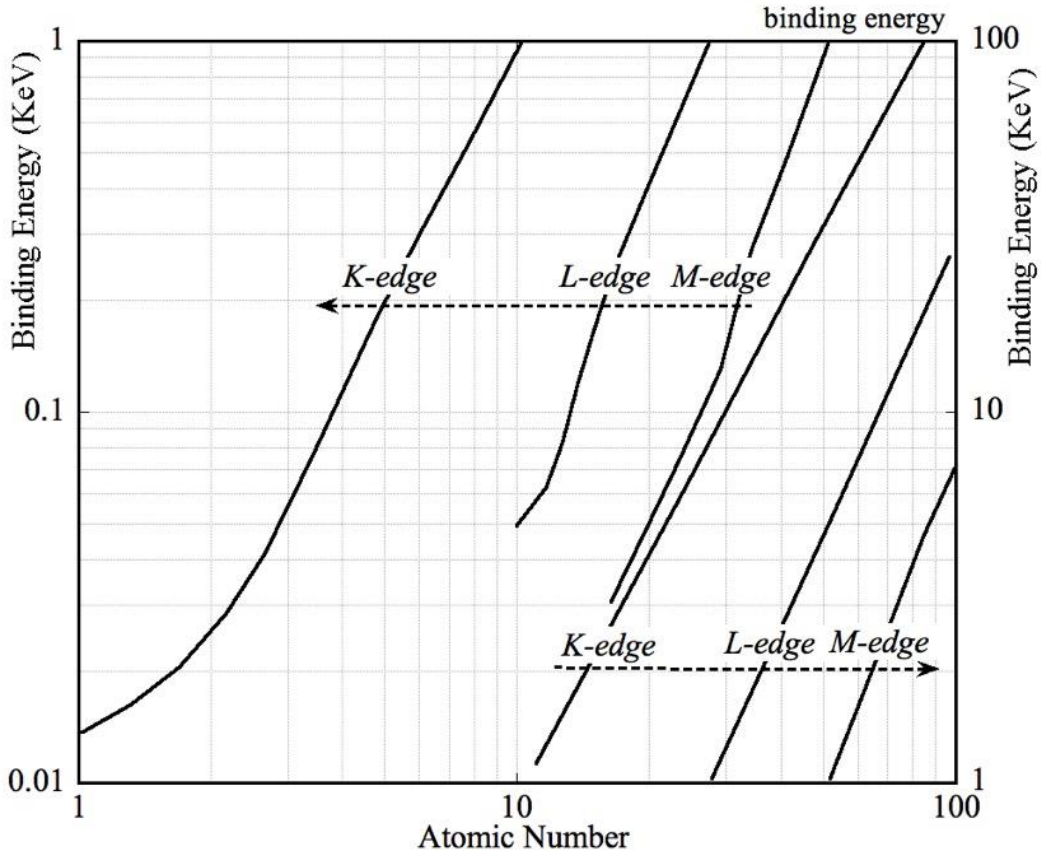

Figure 5-23: Binding energy as a function of atomic number for K, L and M shells.

Atom	Z	A	W_i (eV)	K (eV)	L1, L2, L3 (eV)	M1, M2, M3, M4, M5 (eV)
He	2	4.003	24.59	25		
Ne	10	20.18	21.56	867		
Ar	18	39.95	15.74	3202	287, 250.6, 248.4	27, 15.9, 15.7
Kr	36	83.8	13.99	14322	1920, 1726, 1765	288, 222.2, 214.4, 95, 93.8
Xe	54	131.29	12.13	34582	5452, 5100, 4781	1143, 1002.1, 940.6, 689, 676.4
H	1	1.008	13.598	14		
C	6	12.01	11.26	284		
N	7	14	14.53	402		
O	8	16	13.62	537		
F	9	18	17.42	686		

Table 5.4: Electronic shells binding energy for rare gases and other atoms.

Absorption cross sections as a function of photon energy for the rare gases and some saturated hydrocarbons are given in Figure 5-24 and Figure 5-25.

The plot in Figure 5-26, obtained multiplying the cross sections by the gas density at normal temperature and pressure conditions, permits to evaluate the efficiency of detection for a given detector thickness, through the expression (5-2).

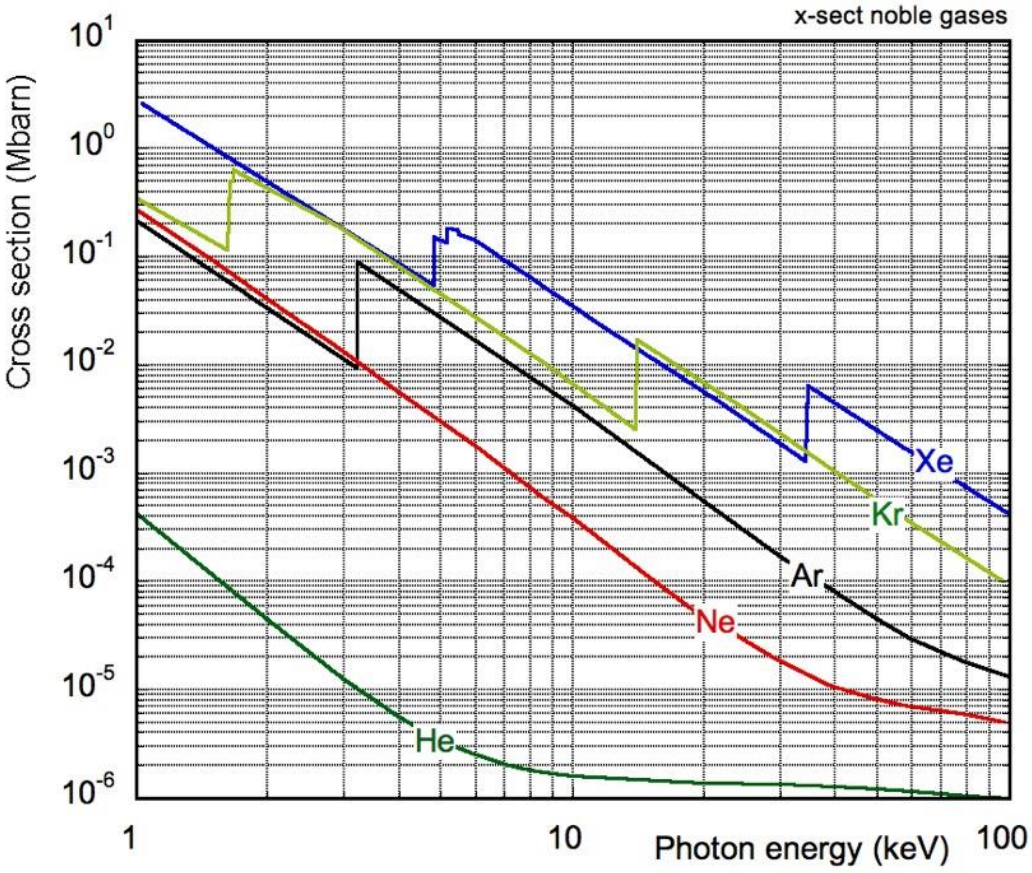

Figure 5-24: Photon absorption cross section for noble gases.

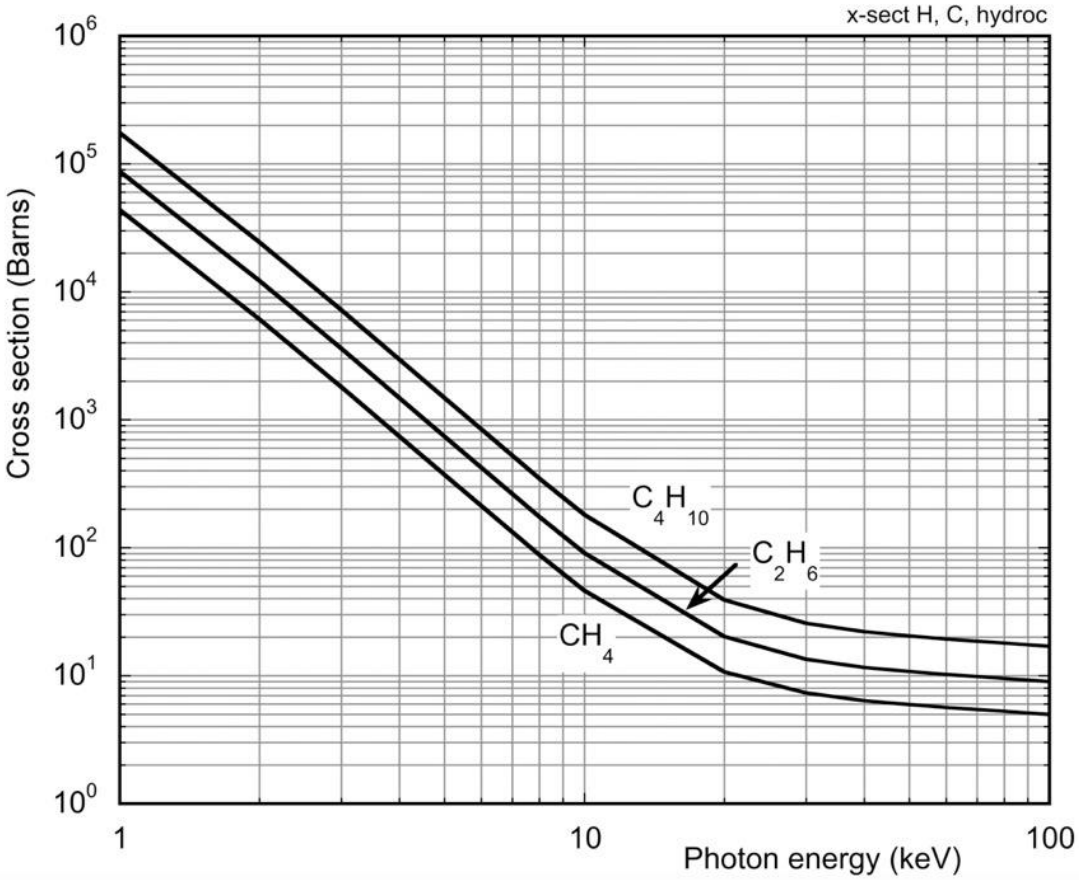

Figure 5-25: Photon absorption cross section for saturated hydrocarbons.

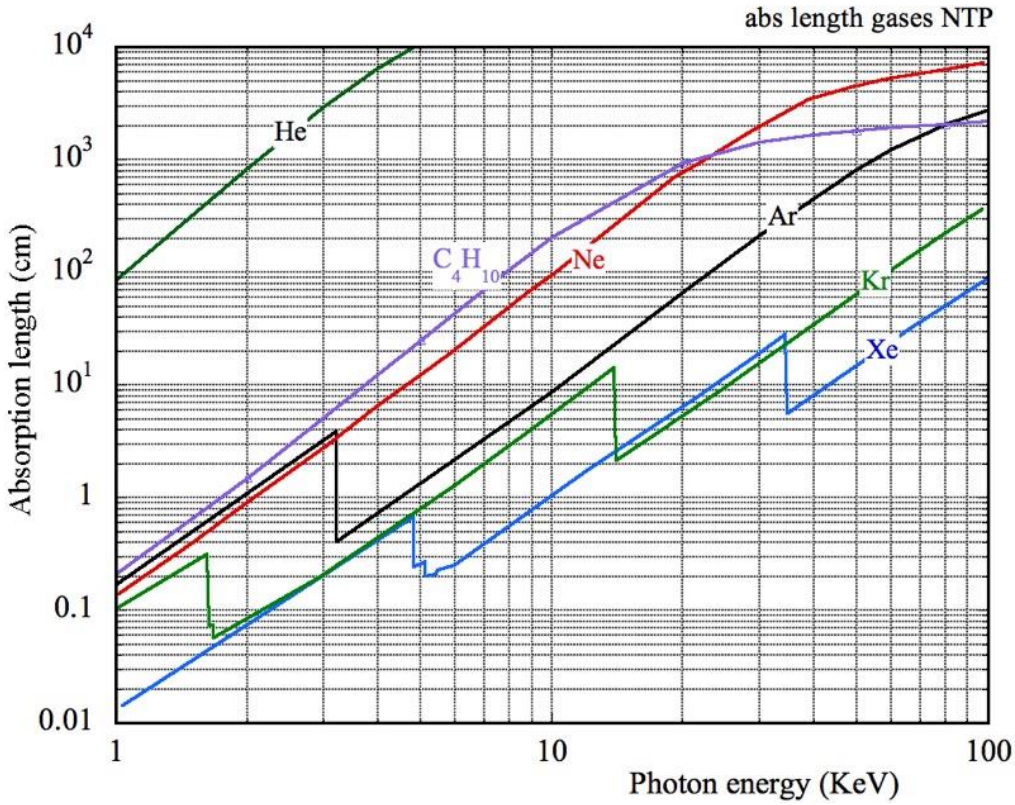

Figure 5-26: Absorption length of gases at NTP.

5.4 Wavelength Shifters

In most materials, atomic and molecular excitations stimulated by ionizing radiation or field-induced collisions result in the emission of far and vacuum ultraviolet photons, generally self-

absorbed by the medium. To permit extraction and detection of the photons, suitable dopants, named wavelength shifters (WLS), can be added to the scintillating material to convert the photons to longer wavelengths.

A wide choice of WLS compounds is available as dopant for plastic scintillators; combinations of several WLS are used to convert, in successive steps of absorption and emission, UV to visible photons; see for example the Eljen Technology catalogue. Deposited in thin layers on the detector windows, they serve as converters for the primary and secondary VUV light emitted in gases. Figure 5-27, Figure 5-28, Figure 5-29, Figure 5-30 and Figure 5-31 are selected examples of the relative absorption and emission spectra for polystyrene and three aromatic molecules commonly used in plastic scintillators: anthracene (C_4H_{10}), P-terphenyl ($C_{18}H_{14}$), POPOP ($C_{24}H_{16}N_2O_2$) and tetraphenyl butadiene TPB (Berlman, 1971).

Mostly employed in gaseous detectors as photosensitive material, cesium iodide (CsI) can also be used as wavelength shifter; Figure 5-32 provides its absorption spectrum (Said and Green, 1977) and the emission spectrum measured under excitation with electrons (Abdrakhmanov *et al.*, 1992).

In the framework of the development of liquid argon TPCs, WLS materials suitable for detection of the LA fluorescence, centered around 128 nm, have been investigated. Figure 5-33 is a compilation of emission spectra of various materials, measured at room temperature and in cryogenic condition at 87 K (Kuźniak and Szelc, 2020).

Figure 5-34

shows the WLS conversion efficiency of TPB at extreme UV wavelengths, suitable for the detection of noble gases scintillation

Originally studied as detection media for VUV photons, owing to their very low ionization potential, some vapor as TEA and TMAE have also a conspicuous emission in the near ultraviolet and visible range, and act therefore as gaseous WLS in admixtures with noble gases. Figure 5-35, shows the absorption and emission spectra of TEA (Holroyd *et al.*, 1987). Used as photosensitive agent in early Cherenkov Ring Imagers, it led also to the development of imaging detectors (Sauli, 2018).

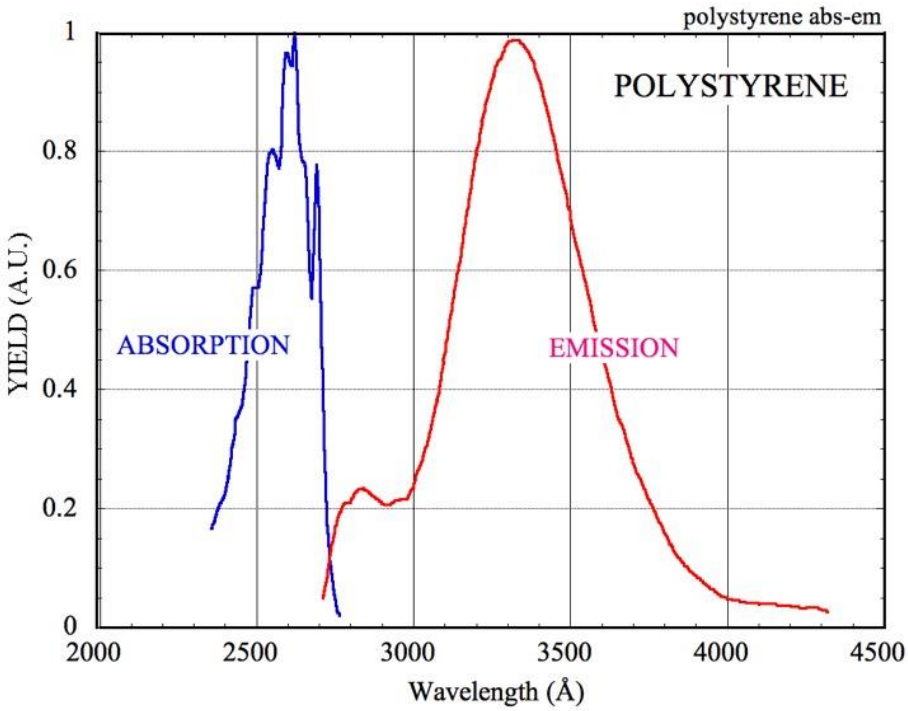

Figure 5-27: Photon absorption and emission spectra for polystyrene. Redrawn from (Berlman, 1971).

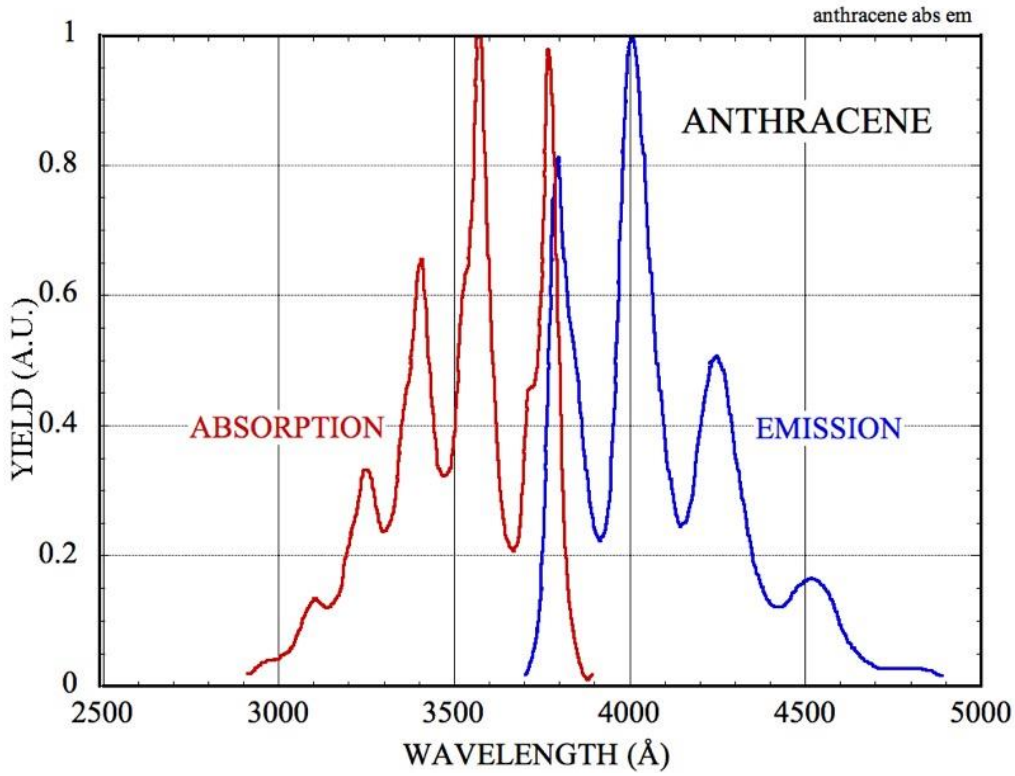

Figure 5-28: Photon absorption and emission spectra for anthracene. Redrawn from (Berlman, 1971).

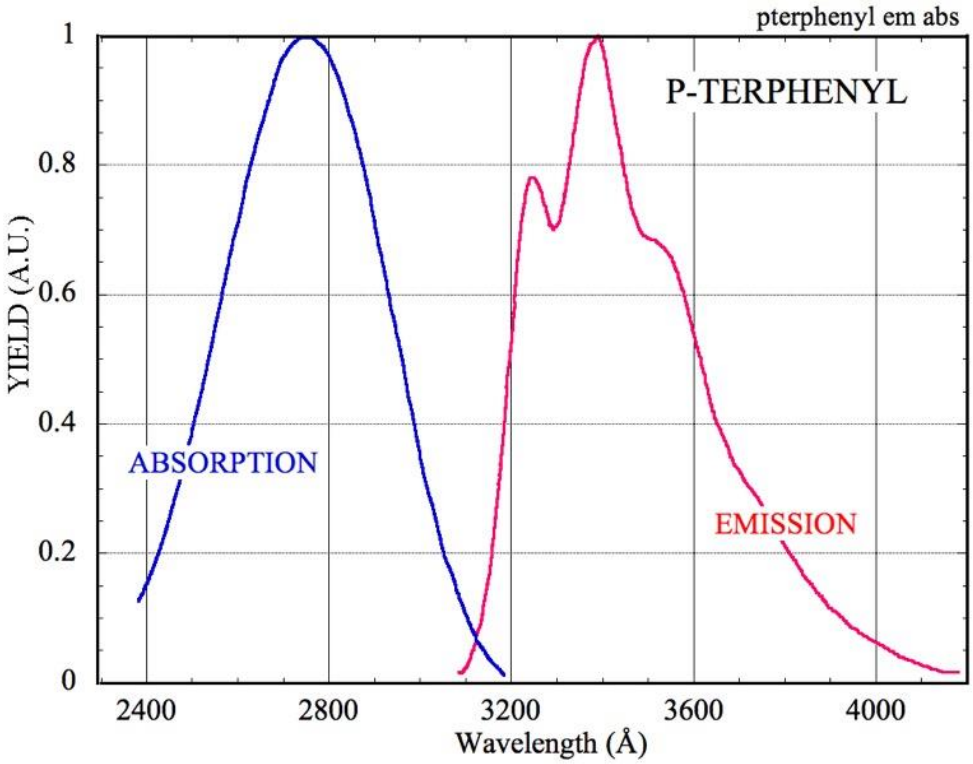

Figure 5-29: Photon absorption and emission spectra for P-terphenyl. Redrawn from (Berlman, 1971)

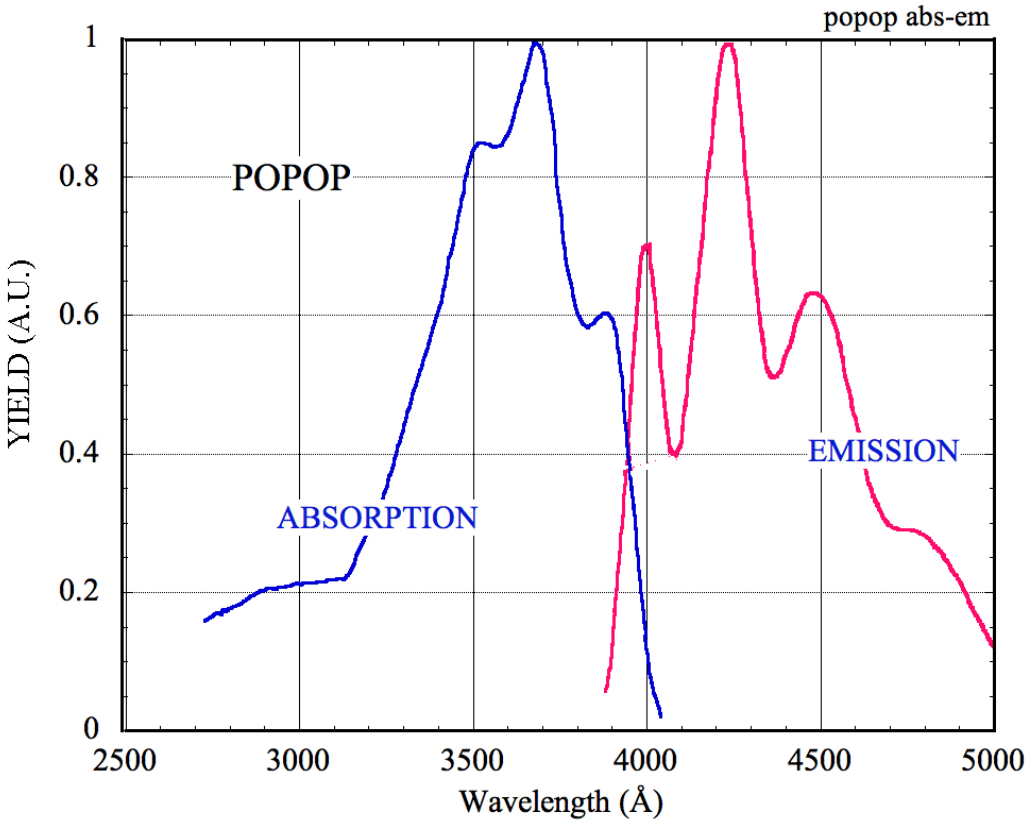

Figure 5-30: Photon absorption and emission spectra for POPOP. Redrawn from (Berlman, 1971).

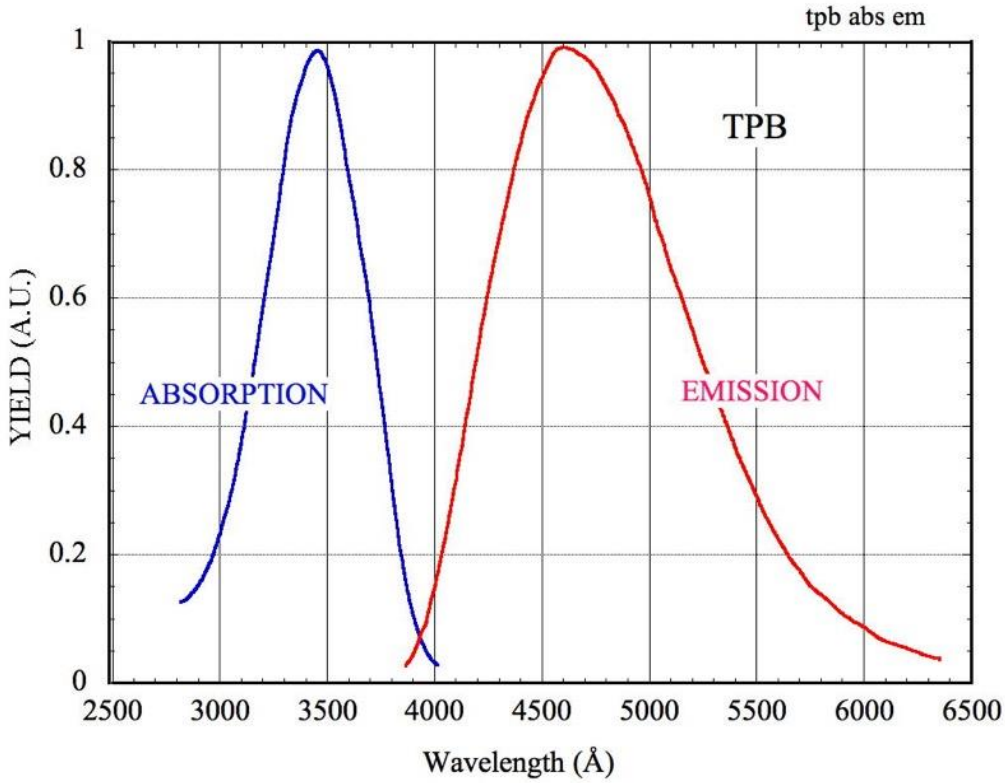

Figure 5-31: Absorption and emission spectra of tetraphenyl butadiene (TPB). Redrawn from (Berlman, 1971) .

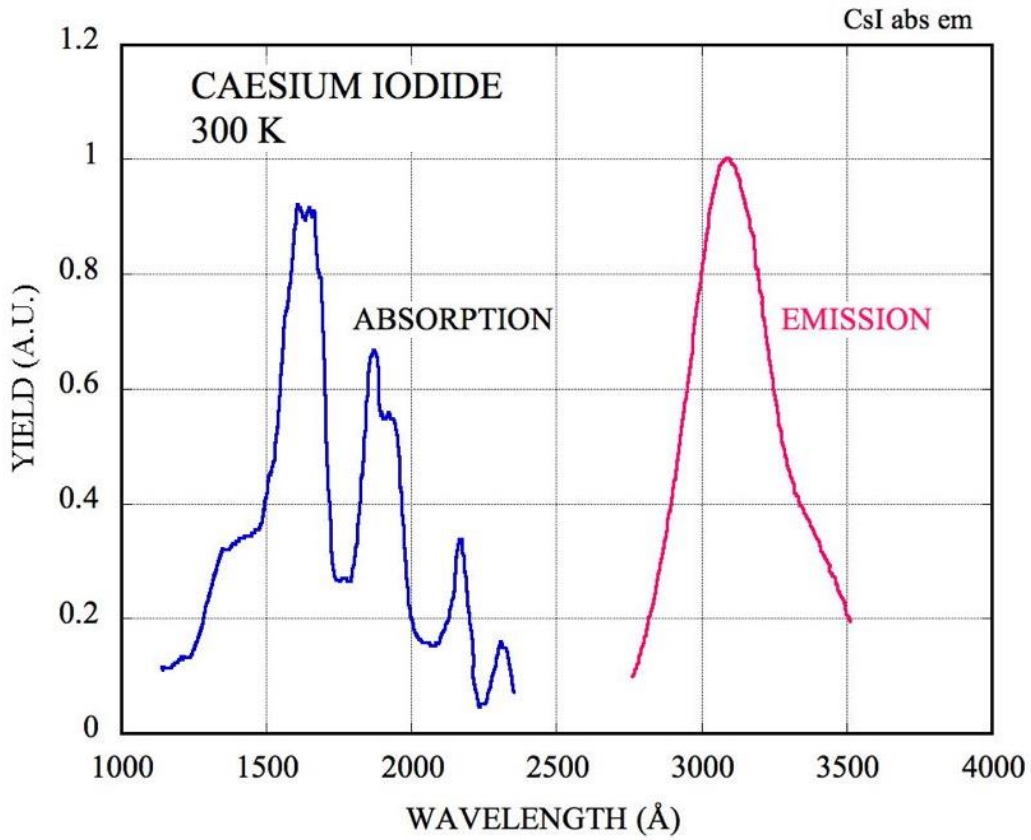

Figure 5-32: CsI absorption (from (Said and Green, 1977)) and fluorescence emission (from (Abdrakhmanov *et al.*, 1992)).

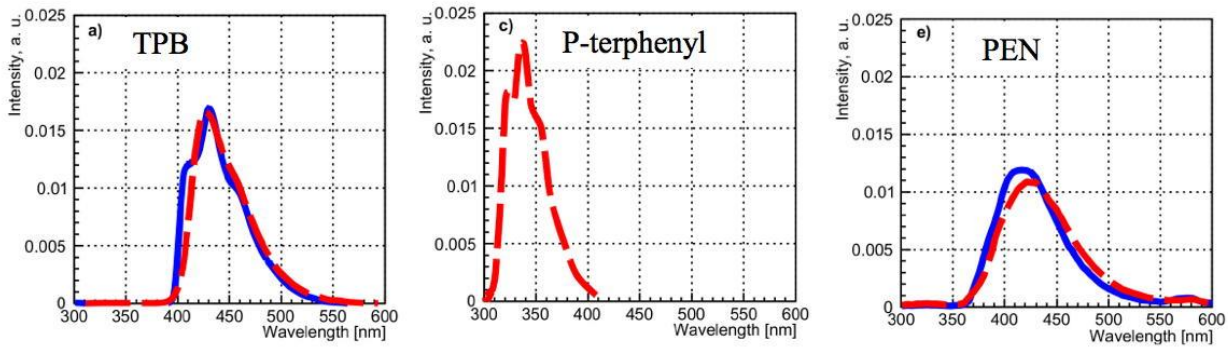

Figure 5-33: Emission spectra of WLS suitable for liquid argon detectors: 1,1,4,4-tetraphenyl- 1,3-butadiene (TPB), P-terphenyl and polyethylene naphthalate (PEN). Spectra measured at room temperature are shown in red and at 87 K in blue (Kuźniak and Szelc, 2020).

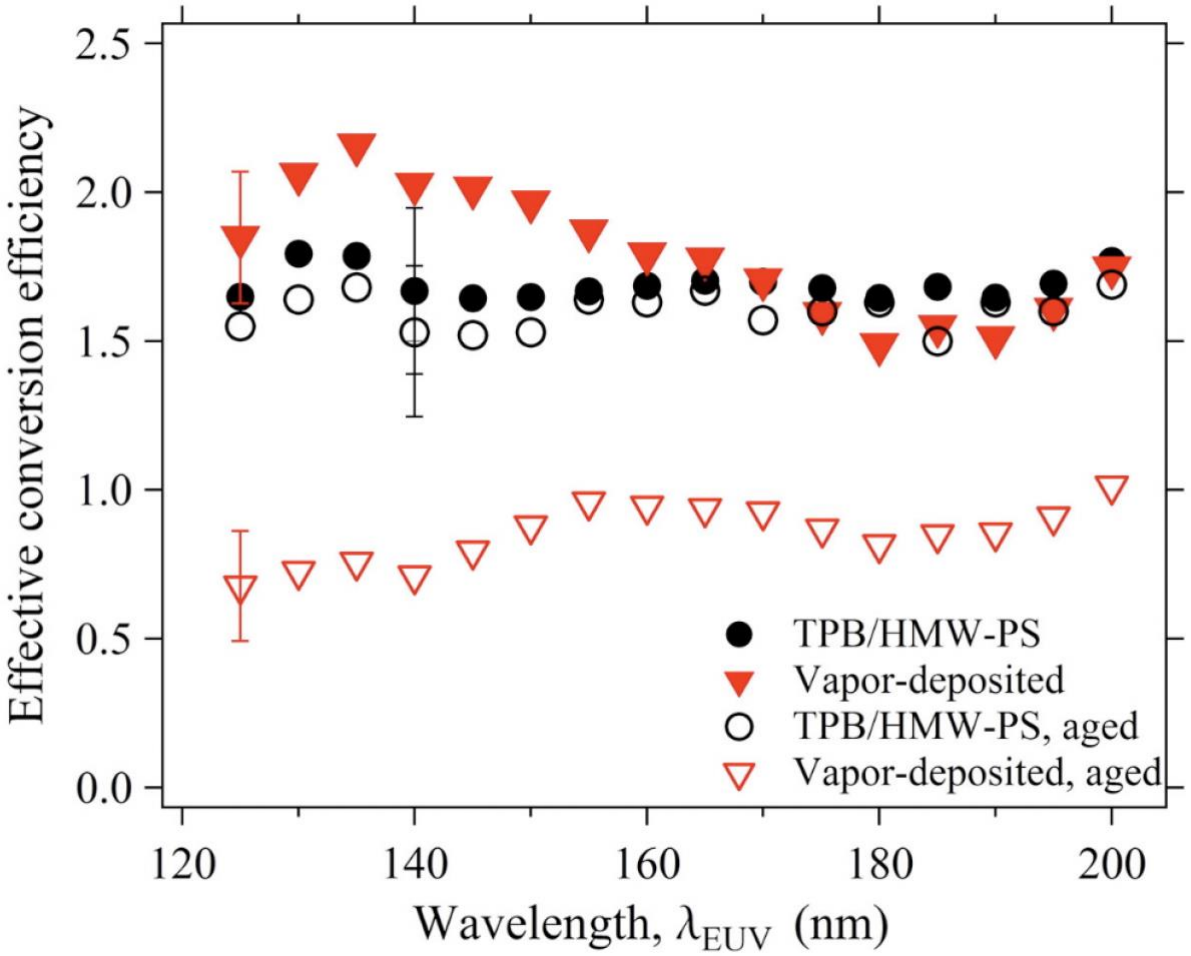

Figure 5-34: Conversion efficiency of TPB at VUV wavelengths (Graybill *et al.*, 2020).

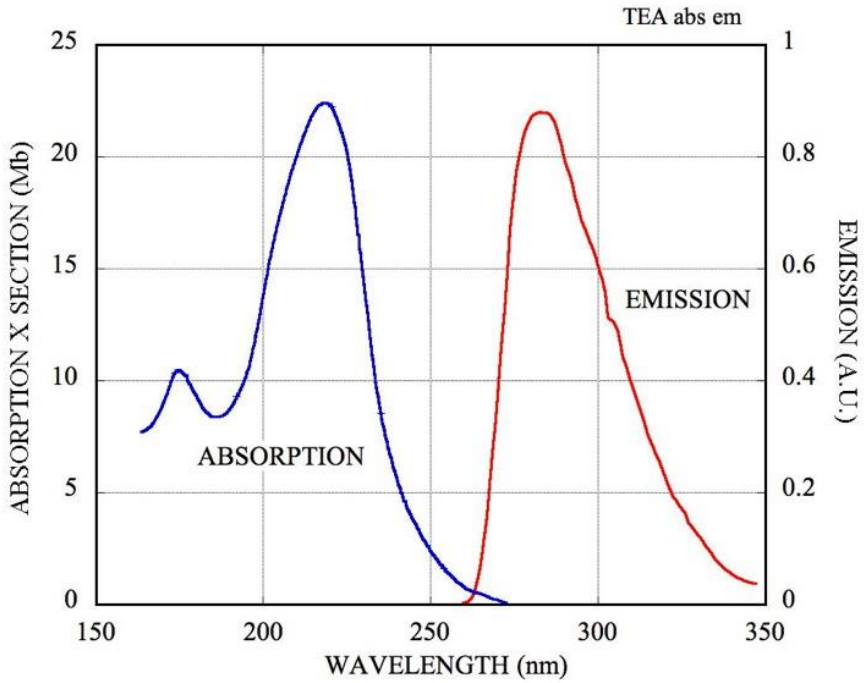

. Figure 5-35: Absorption and emission spectra of triethyl amine (TEA) (Holroyd *et al.*, 1987).

5.5 Radiation and field-induced fluorescence

The interaction of radiation with the gas molecules results in an almost equal sharing of energy loss between excitations and ionization. The ionization yield was discussed in Chapter 4; excited atoms/molecules return to the ground state emitting photons.

Radiation-induced fluorescence spectra of noble gases stimulated by 4 MeV protons, also called primary scintillation, are shown in Figure 5-36, Figure 5-37 and Figure 5-38 (Stewart *et al.*, 1970). The spectra are similar, but not identical, to those measured by the same authors under discharge conditions (section 4.8). For low pressures, most of the emission is due to atomic transitions, while at increasing pressures a longer wavelength contribution due to molecular processes (dimers formation) becomes predominant.

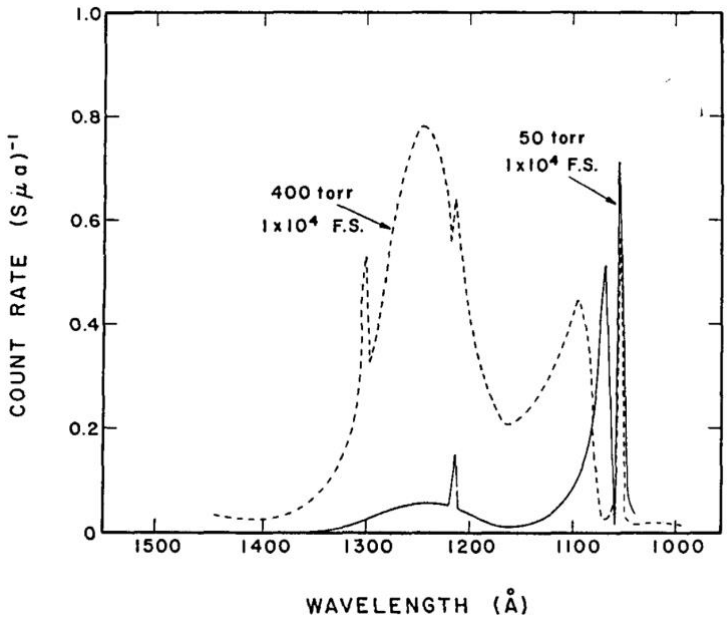

Figure 5-36: Proton-induced fluorescence emission in argon (Stewart *et al.*, 1970).

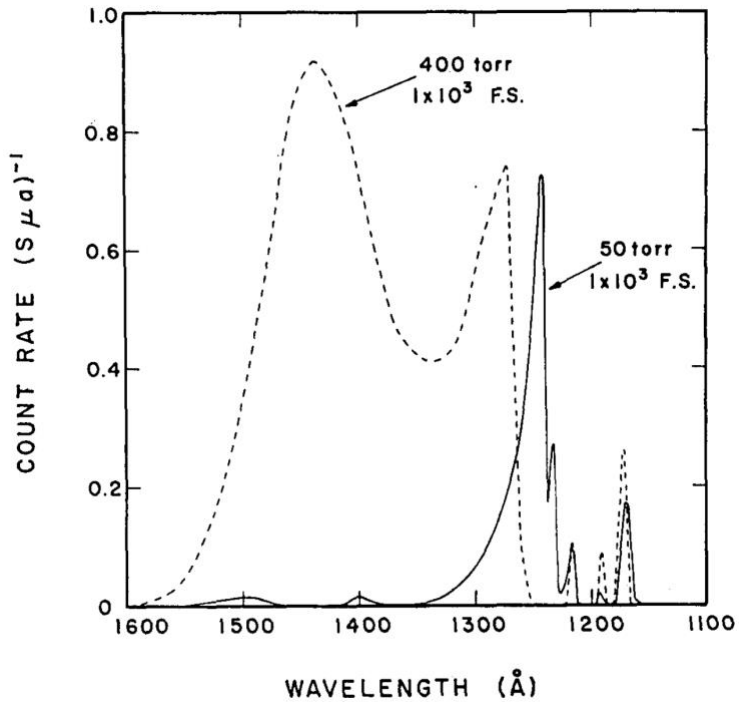

Figure 5-37: Proton-induced fluorescence emission in Krypton (Stewart *et al.*, 1970).

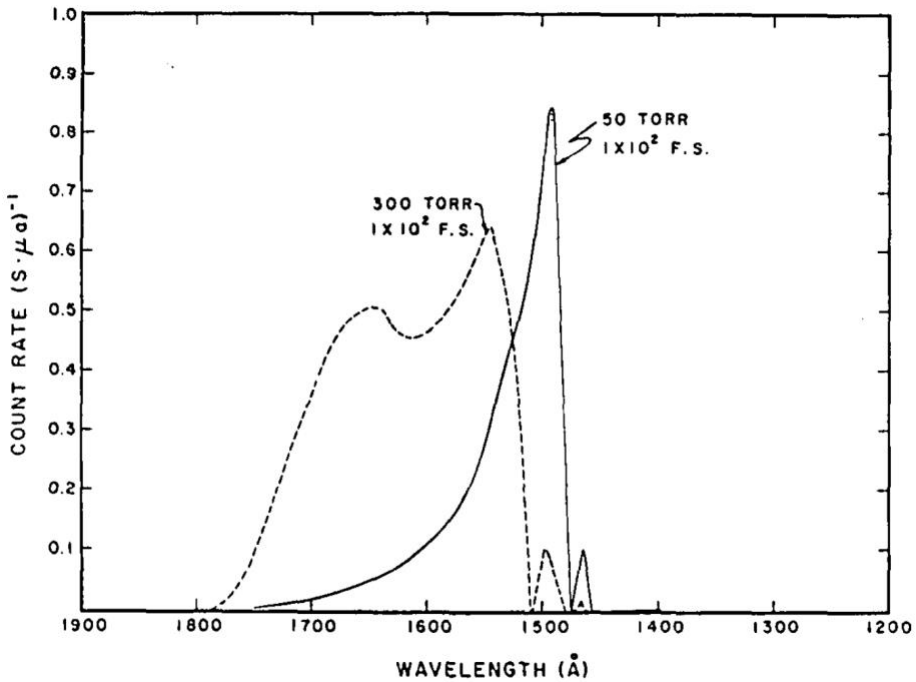

Figure 5-38: Proton-induced fluorescence of Xenon (Stewart *et al.*, 1970).

Fluorescence emission under discharge and exposure to radiation has been extensively studied for nitrogen, in view of numerous applications for example in the detection of atmospheric cosmic showers. Figure 5-39 is an example of N_2 emission spectrum in dry air excited with keV electrons from a ^{90}Sr source (Lefeuvre *et al.*, 2007). The photon absorption spectrum was given in Figure 5-16. Nitrogen has been used as internal wavelength shifter in counters, albeit at relatively lowe efficiency.

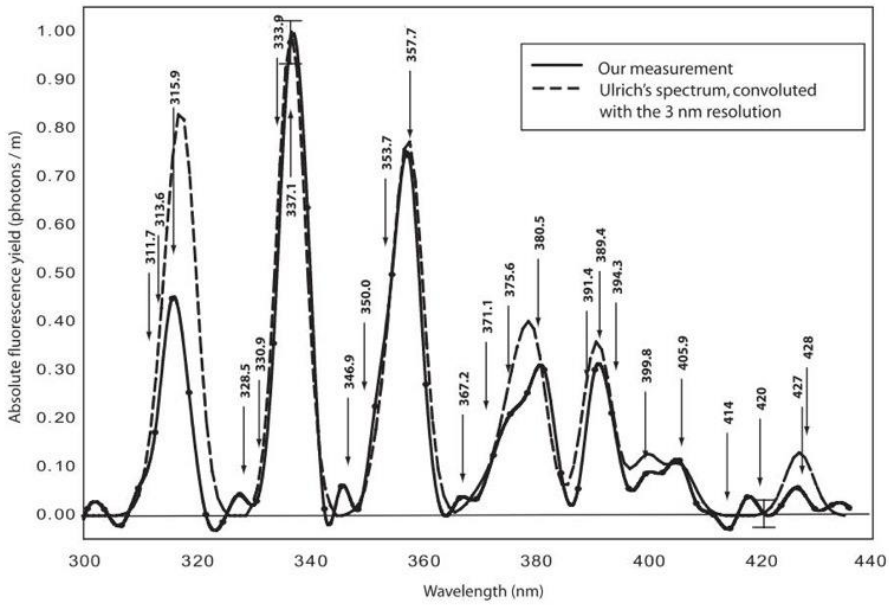

Figure 5-39: Nitrogen fluorescence spectra under keV electron excitation at atmospheric pressure (Lefeuvre *et al.*, 2007).

Carbon tetrafluoride (CF_4) is a very efficient scintillator, with emission around 650 nm (2 eV), conveniently in the visible range. MeV α particles induced spectra in a range of pressures are given in Figure 5-40 (Morozov *et al.*, 2010); the emission matches well the spectral response of modern solid-state sensors (see chapter 9).

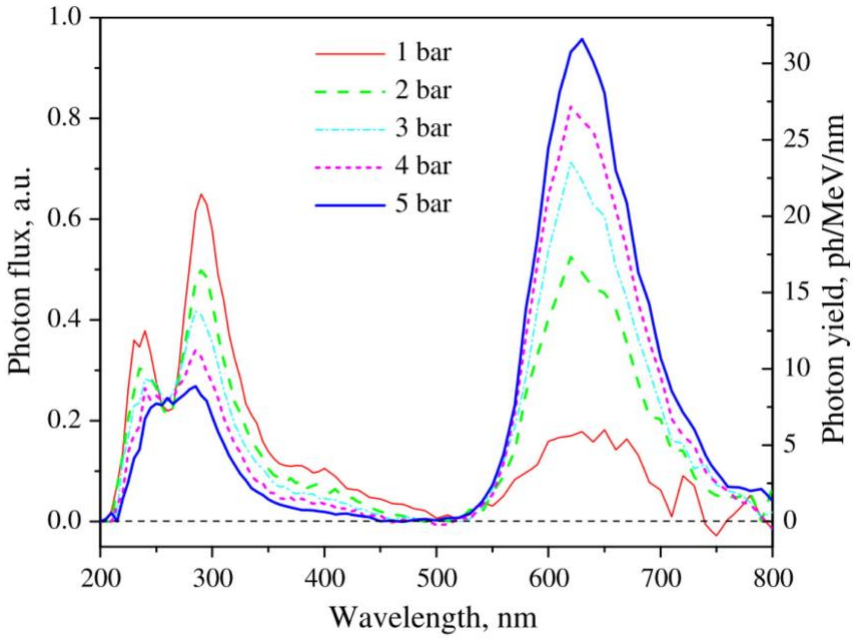

Figure 5-40: MeV α-induced primary fluorescence spectra of CF_4 at increasing pressures (Morozov *et al.*, 2010).

At moderate to high values of electric fields, as those present in gaseous counters, the inelastic collisions between ionization electrons and molecules result in copious emission of fluorescence photons, the so-called secondary photon emission, with wavelengths spanning from the VUV to the infrared. The fluorescence yield depends on the gas and electric field, and is particularly high for noble gases and their mixtures, as shown in Figure 5-41.

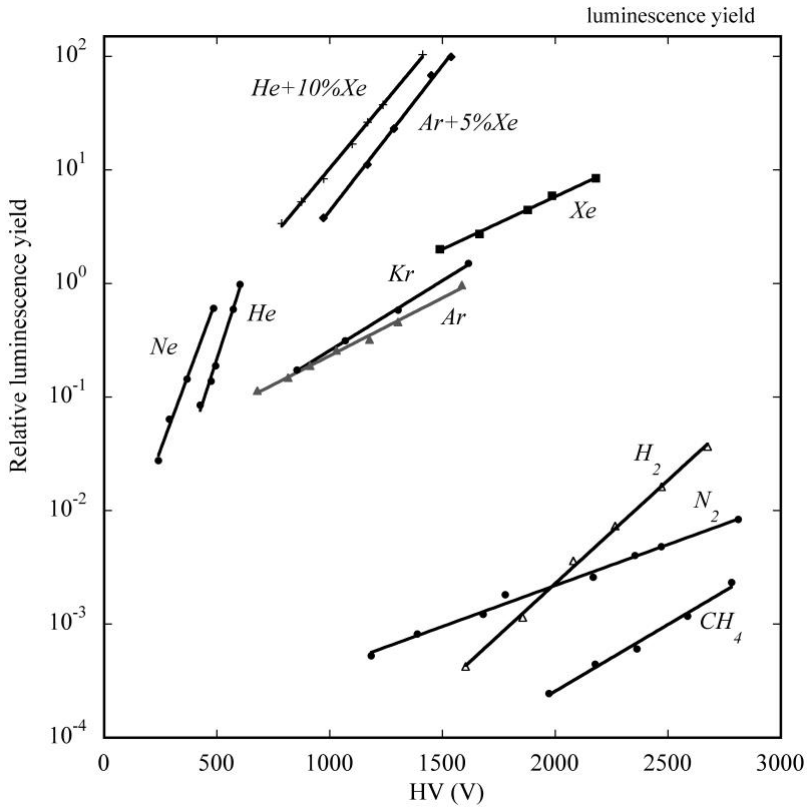

Figure 5-41: Relative secondary fluorescence yield at atmospheric pressure as a function of field (Keirim-Markus, 1972).

Figure 5-42 provides the secondary emission spectra of noble gases, at pressures close to atmospheric. The emission is due to the formation and decay of temporary excited molecules, named dimers, and is exploited in gaseous scintillation counters, providing better energy resolution than proportional counters (Policarpo, 1981).

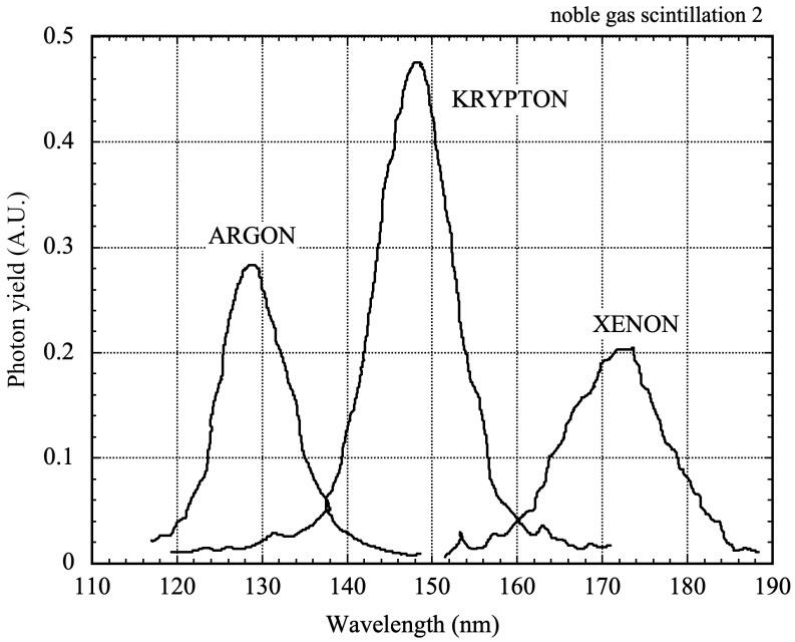

Figure 5-42: Secondary emission spectra of rare gases at pressures close to atmospheric. Data from (Stewart *et al.*, 1970).

Excited noble gases emit photons in the far ultraviolet region, requiring for detection the use of VUV sensors or suitable thin wavelength shifter layers deposited on the windows. A convenient alternative is to add to the main gas mixtures a gas acting as internal wavelength shifter. Several vapors used to detect UV photons, thanks to their low ionization potential, have been found to fluoresce at wavelengths close to or in the visible range: examples are triethyl amine (TEA) and tetrakis dimethyl amino ethylene (TMAE), Table 5.2. Figure 5-43 shows the secondary (field-induced) emission spectra in TEA and TMAE; Figure 5-44 andFigure 5-45 the secondary emission for pure CF4 (Morozov *et al.*, 2012) and He-CF4 and Ar-CF_4 mixures (Fraga *et al.*, 2003).

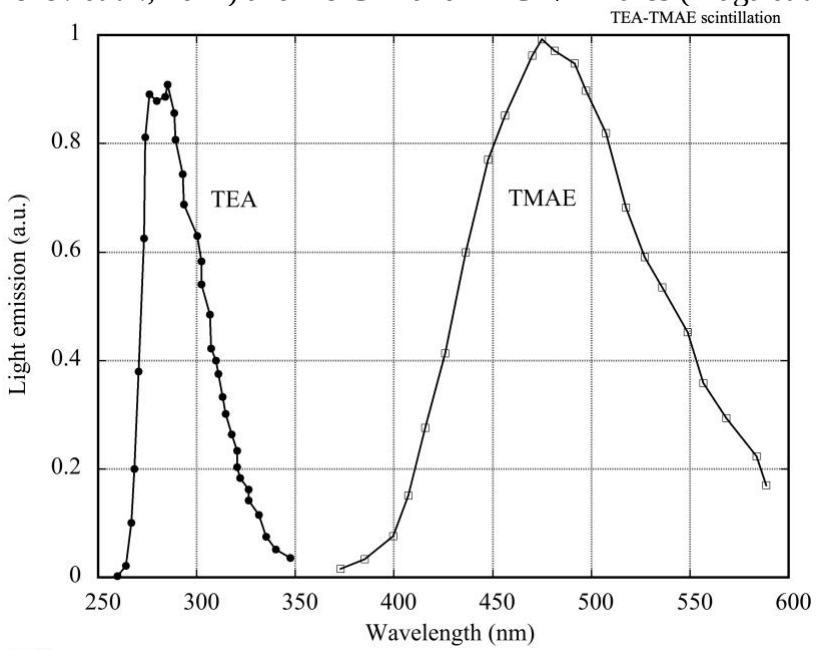

Figure 5-43: Secondary photons emission spectra in TEA and TMAE. Data from (Suzuki *et al.*, 1987) (Charpak *et al.*, 1988).

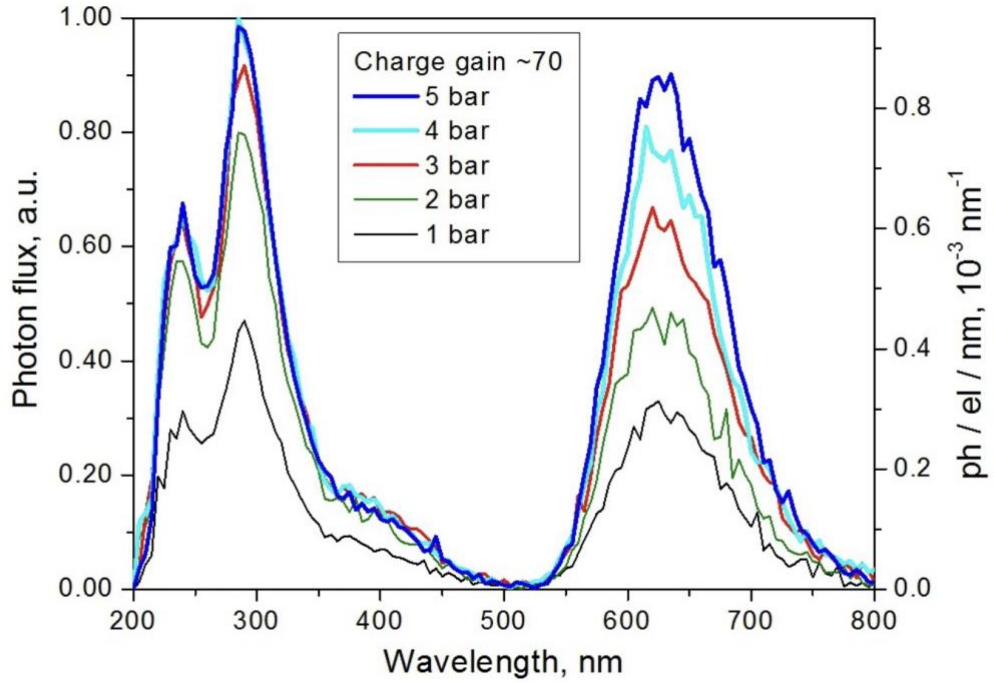

Figure 5-44: Secondary fluorescence of CF_4 (Morozov *et al.*, 2012).

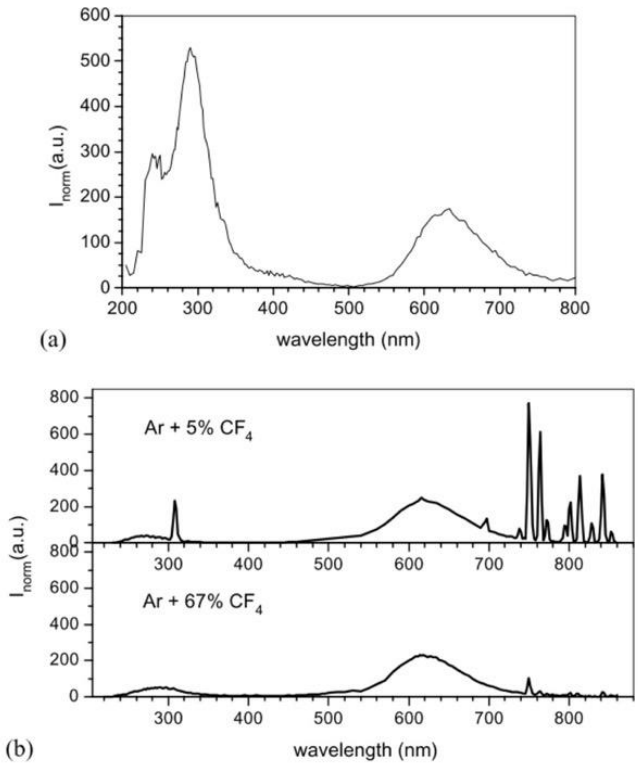

Figure 5-45: Secondary scintillation spectra in He-CF_4 (60-40) and in two Ar-CF_4 mixtures (Fraga *et al.*, 2003).

5.6 Windows

With the exception of uncommon air-operated counters, detectors require a window to separate the filling gas from the atmosphere. Depending on the window material and thickness, a fraction of the external radiation may be absorbed, reducing the detection efficiency. For fast charged particles, only a small fraction of the energy is lost in the window, not affecting the detector response; for heavy, low energy ions as alpha particles the radiation can instead be completely absorbed. Table

5.5 provides relevant data for selected polymer foils commonly used for gaseous detectors construction. For detailed tables of mechanical, electrical and physical properties of plastic materials see for example (Omnexus, 2020).

Material	Producer	Notes	ε	Thickness μm	δ (g/cm^3)	ρ (Ω cm)
Mylar Hostaphan Polyethylene terephthalate PET	Mitsubishi	1)	3.2	5-80	1.39	10^{19}
Nylon Polyamide			3.14		1.15	
PS Polystyrene			2.6		1.05	
Polypropylene			2.3			
Teflon PTFE Polytetrafluoroethylene	Chemours		2.1		2.2	10^{18}
PVA Polyvinyl acetate			3.5		1.19	
PVC Polyvinyl chloride			2.9		1.38	10^{16}
Kapton HN Polyimide	DuPont	2)	3.4		1.42	10^{9}
Aclar Polychlorotrifluoroethylene or Kel-F $(CClF–CF_2)_n$	Honeywell	3)		15-200	2.12	
Novaclad Copper-clad polyimide	Sheldahl	4)	3.4	12, 25, 50	1.42	
Expanded polyurethane Polymethacrylimide (PMI)	Rohacell	5)	1.3-1.6		0.75-1.50	

Table 5.5: Dielectric constant, density and bulk resistivity of thin-foil polymers

NOTES:

1) Mechanically and chemically very stable, hygroscopic, water permeability 8 g/m^2 per day
2) Hygroscopic
3) Water transmission 0.047 g/ m^2 per day
4) 50 μm polyimide, clad with 5 μm Cu, used for MPGD manufacturing
5) Laminated to polymer foils on each side it is used as light structural material for detectors.

Figure 5-46 provides the range of α particles in polyimide and aluminum; at 5 MeV, typical energy of the ions from a source (see Table 4.4) the range in Kapton is about 30 μm. For 5 μm, a practical minimum thickness for a window, the ions would lose about twenty per cent of their energy, hence the common practice of installing the sources internally.

As seen in Figure 5-47 fluoride crystals have the widest transparency range, up to 12 eV for lithium fluoride; at the lower energy edge, UV quality fused silica has an energy cutoff at 7.5 eV.

Thin polymer foils used for gas tightness have some transparency in the near UV region (Figure 5-48); this can create problems if the detectors are exposed to fluorescent lamps, emitting short wavelengths, since materials and gases used in the construction have some residual photosensitivity. Mechanically sturdy and easy to handle, mylar (polyethylene terephthalate) is a common choice as window for detectors and cuts off short wavelengths; rather permeable to water it might affect the hygrometry of the filling gas. A common choice in the early developments of MWPC was to use double-layer foils, obtained laminating mylar and aclar , a polymer with very low water permeability for large window areas.

With excellent mechanical and chemical stability, polyethylene terephthalate (PET) is commercialized with thickness from 5μm as Hostaphan (Mitsubishi, 2020) and can be used to manufacture very thin windows for gaseous detectors, in particular to serve as entrance window for MeV alpha particles.

No practical windows for photons exist above ~12 eV up to a few hundred eV, where some light materials provide some transparency, as seen in Figure 5-49; Figure 5-50 provides the transparency of thin foils of aluminum and beryllium at soft X-ray energies.

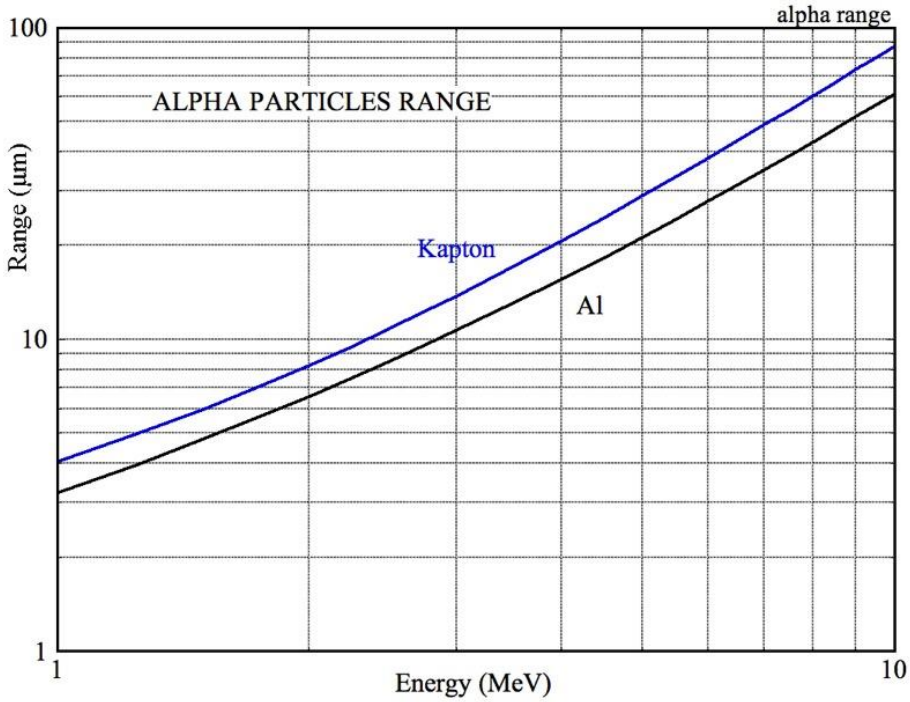

Figure 5-46: Range of alpha particles as a function of energy in Kapton and aluminum.

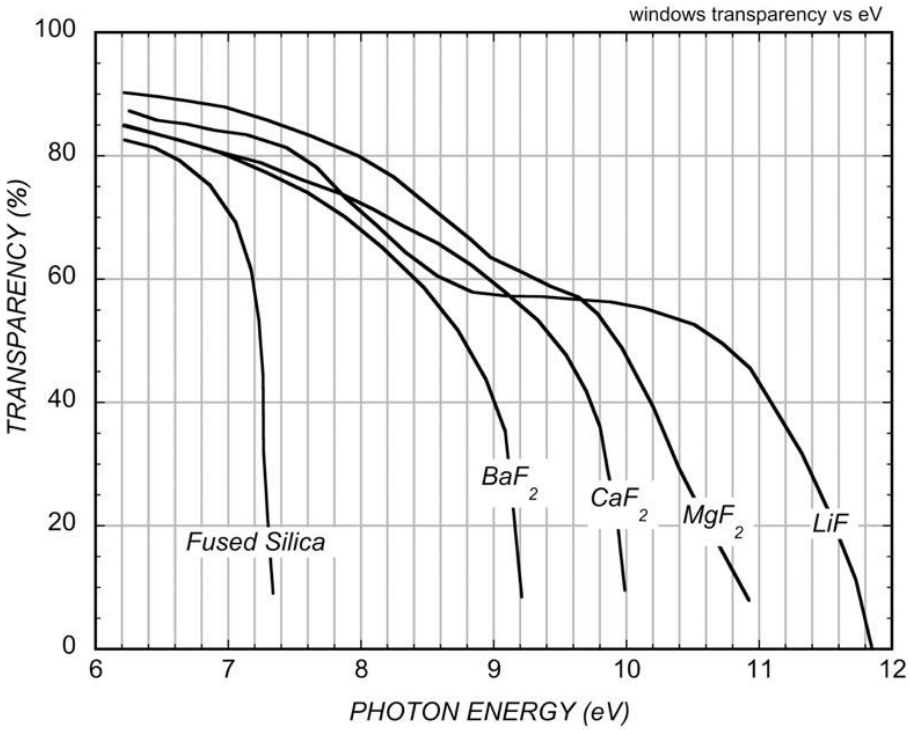

Figure 5-47: Photon transparency of fluoride crystals and fused silica as a function of energy.

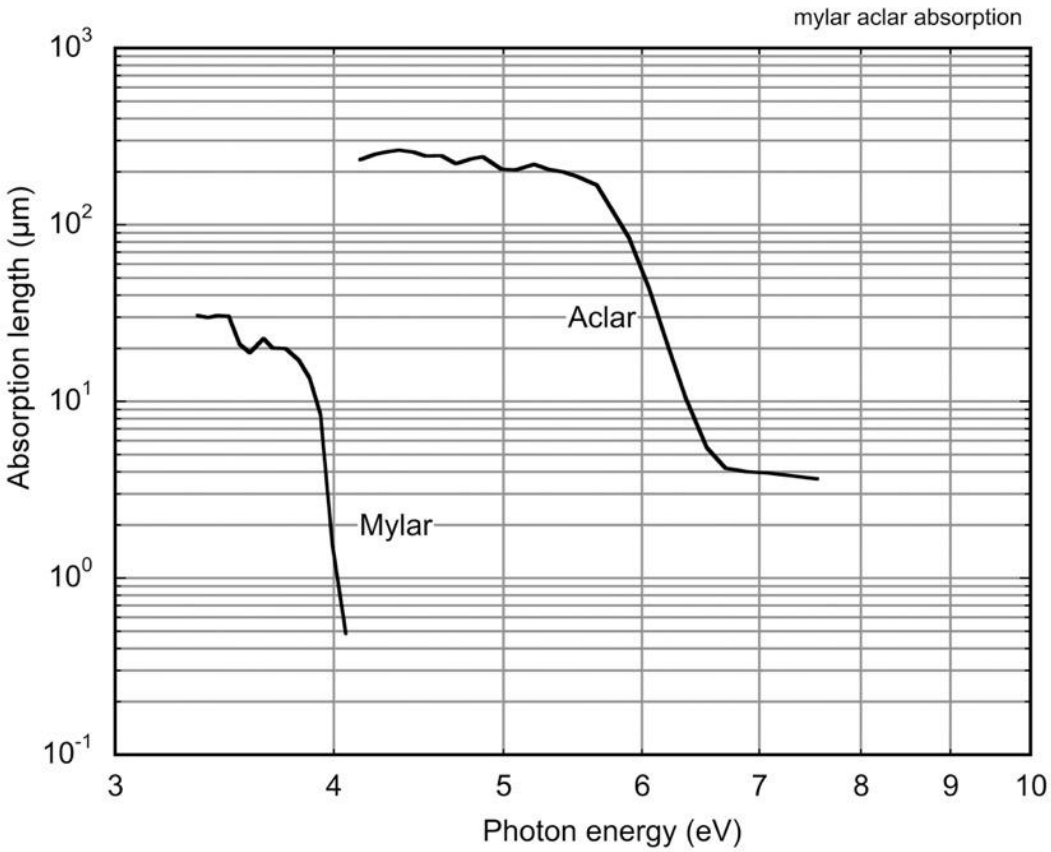

Figure 5-48: Photon absorption length of mylar and aclar.

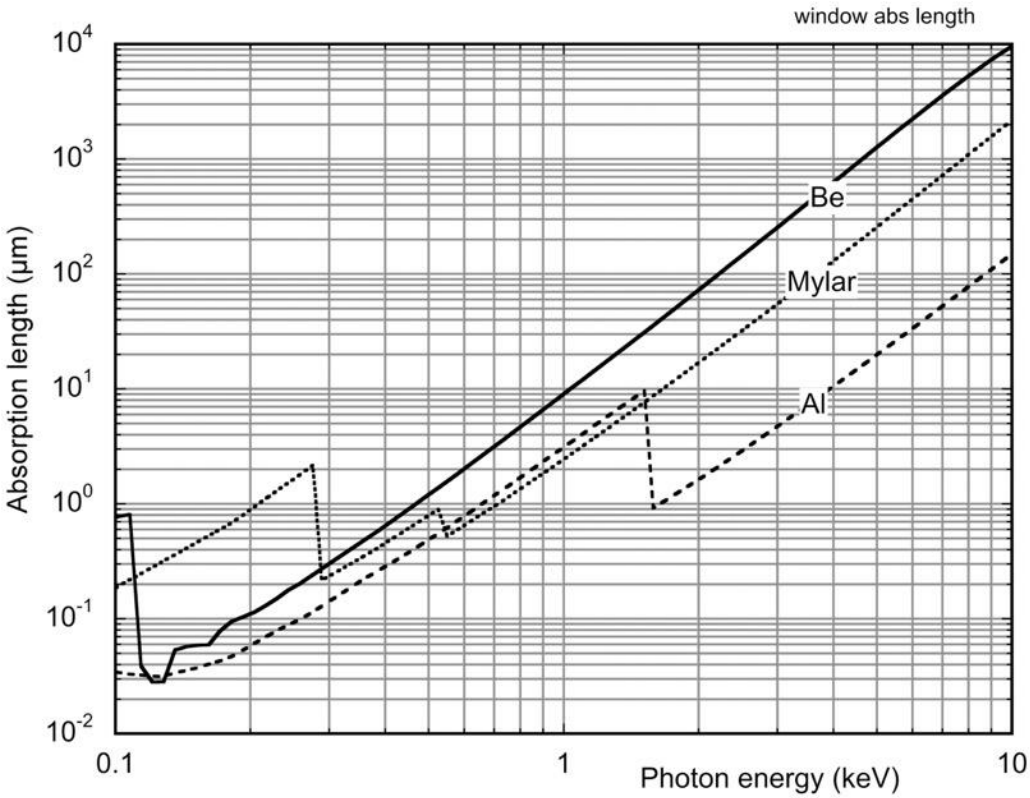

Figure 5-49: Absorption length for soft X-rays of light materials.

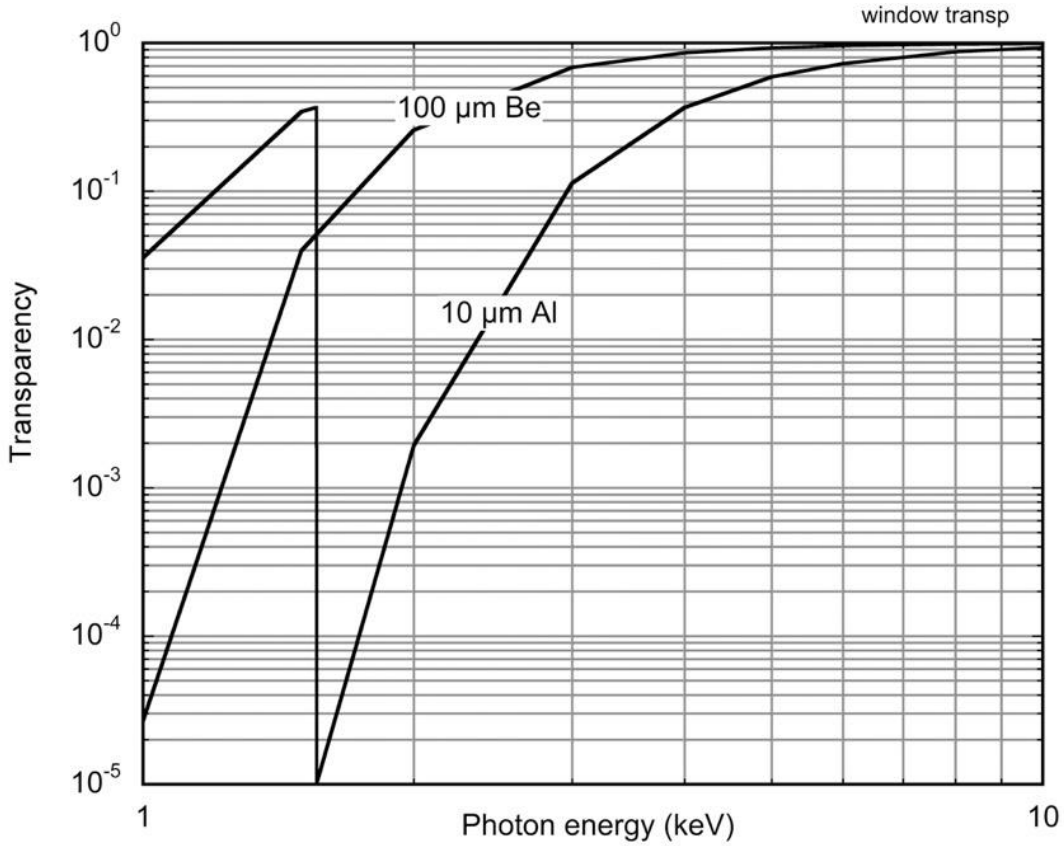

Figure 5-50: Thin windows transparency for soft X-rays.

5.7 Multiple Scattering and Radiation Length

Charged particles passing through a medium undergo electromagnetic interaction with the molecules, mostly encompassing small transfers of energy. Collectively named multiple Coulomb scattering, these collisions sum up resulting in a deflection of the particle from the original trajectory. Following an approximate theory due to Molière (Molière, 1947)(Gottschalk *et al.*, 1993), the particle's angular spread is described by a two-dimensional gaussian distribution centered around the original direction and with a projected standard deviation given in radians by:

$$\theta_{MS} = \frac{13.6}{p\beta}\sqrt{\frac{X}{X_0}}$$

where p is the particle momentum (in MeV), b the relativistic velocity, X the thickness of the material and X_0 its radiation length expressed in the same units.

The extended compilation of Atomic and Nuclear Properties in PDG Particle Data Group provides values of radiation length of more than 350 materials; references (M. Gupta, 2010) and (Knasel, 1970) embrace calculation methods for composite materials. Selected values of radiation lengths from the quoted sources are given in Table 1 for elements and composite materials commonly used for MPGD construction and operation; the corresponding values in cm can be obtained multiplying by the material density. For gases, the density is given at Normal Temperature and Pressure (NTP, 20^0 and 1 atm).

Material	Density (g cm^{-3})	Radiation length (g cm^{-2})
He	0.179 10^{-3}	94.32
Ne	0.839 10^{-3}	28.93
Ar	1.662 10^{-3}	19.55
CO_2	1.842 10^{-3}	36.2
CH_4	0.667 10^{-3}	46.47
Be	1.148	65.19
C	2.210	42.7
Al	2.699	24.01
Cu	8.960	12.86
Au	19.32	6.46
Fe	7.874	13.84
Pb	11.35	6.54
H_2O	1.00	36.08
Polyethylene	0.89	44.78
Borosilicate glass	2.23	28.17
Mylar	1.40	39.95
Kapton	1.42	40.58
Polystyrene	1.06	43.79
Epoxy	1.190	41.22
G10 Fibreglass	1.800	32.17

Table 1: Radiation length of materials (from Particle Data Group, Atomic and Nuclear Properties pdg).

5.8 Refractive index

The refractive index (or index of refraction) *n* is a dimensionless number expressing the light bending power of transparent materials, generally wavelength-dependent. The value of the index determines the fraction of light bent or refracted when entering a material, and is described by Snell's law:

$$n_1 sin\theta_1 = n_2 sin\theta_2$$

where q_1, q_2 are the angles of incidence and refraction of a beam crossing the interface between two media with index of refraction n_1 and n_2, respectively.
The beam of light is totally reflected if the incidence exceeds a critical angle q_c given by:

$$\theta_C = arcsin\frac{n_2}{n_1}$$

Table 2 provides values of the refraction index at visible wavelengths for a range of materials used as optical windows or radiators in MPGD-based Cherenkov threshold and ring imaging counters (from PDG, WIKIPEDIA and other sources). Refractive Index provides values as a function of wavelenghts for a wide range of materials.

Material	**Refraction Index**
Gases at 0 ^{0}C 1 atm	
Air	1.000293
Helium	1.000036
CO_2	1.00045
CF_4	1.000088
C_2F_6	1.000793
C_4F_{10}	1.001530
C_5F_{12}	1.001720
Liquids at 20 ^{0}C	
Water	1.333
Ethanol	1.36
C_6F_{14}	1.283
Solids	
Ice	1.31
Fused silica (quartz)	1.48
BaF_2	1,474
MgF_2	1.413
CaF_2	1,3999
PMMA (acrylic, plexiglass)	1.49
Borosilicate glass	1.52
Polycarbonate (Lexan)	1.58
Diamond	2.417

Table 2: Refraction index of gaseous, liquid and solid media, from various sources (WIKIPEDIA, Refractive Index, (Hallewell, 2011)(Arnold *et al.*, 1988)(Ullaland, 2005))

6 IONIZATION CHARGES MOBILITY AND DIFFUSION

6.1 Ions

Charges released by ionization in the gas diffuse with random thermal velocities until neutralizing between them or on the walls. Under the effect of an applied electric field, ions and electrons drift in opposite directions, diffusing by collisions with the molecules. At low to moderate fields, the ions' mobility (ratio of drift velocity and field) is constant but tends to decrease at high field values, while for electrons the velocity varies with the field and the nature and conditions of the gas. For a classic coverage of ion mobility theory and experiments see (McDaniel and Mason, 1973).

The mobility for several ions in their own and other gases are given in Table 6.1 (from (Sauli, 2014); values differ depending on sources. In a mixture of gases G_1 G_2 ...G_N the mobility of ion G_i can be computed with Blanc's law:

$$\frac{1}{\mu_i} = \sum_{j=1}^{n} \frac{p_j}{\mu_j}$$

where p_j is the concentration of gas j in the mixture, and μ_{ij} the mobility of ion G_i^+ in the gas G_j.

Ion	***Gas***	***μ ($cm^2V^{-1}s^{-1}$)***
H^+	H_2	13.0
He^+	He	10.2
Ar^+	Ar	1.7
Ar^+	CH_4	1.87-2.07
Ar^+	C_2H_6	2.06
Ar^+	C_3H_8	2.08
Ar^+	i-C_4H_{10}	1.56-2.15
Ar^+	CO_2	1.72
CH_4^+	CH_4	2.22
$C_2H_6^+$	C_2H_6	1.23
$C_3H_8^+$	C_3H_8	0.79
i-$C_4H_{10}^+$	i-C_4H_{10}	0.61
O_2^+	O_2	2.2
CO_2^+	CO_2	1.09
H_2O^+	H_2O	0.7
CF_4^+	CF_4	0.96
CF_4^+	CH_4	1.06

Table 6.1: Mobility of ions in their own and other gases.

The ions mobility can be measured with a dedicated drift chamber having a region of uniform electric field between an anode wire and a cathode made thin wires or a double mesh (Frisch grid) create a high field region enhancing the signal induced by ions. Exposing the counter to a source, the ions mobility is obtained from the time difference between the signal due to electron multiplied at the anode and the arrival of ions at the cathode. Figure 6-1 shows schematically the detector used by (Schultz, Charpak and Sauli, 1977) in the early developments of drift chambers; a similar device is described for example by (Yamashita *et al.*, 1989). Figure 6-2, from the last reference, is an example of measured mobility of positive ions in argon-methane and carbon-tetrafluoride mixtures, as a function of the methane content. Although the type of ion is not identified, a fit with Blanc's law and values of mobility as given in the table suggest that the drifting ion is CH_4^+, the ion with the lowest ionization potential.

Part of a systematic study, Figure 6-3 shows the ions mobility measured with the drift time recording method in mixtures of xenon and carbon dioxide; in this case Blanc's law suggests that the drifting ion is Xe_2^+. This is generally an assumption for most of the experiments relying on a drift time measurement, and not coupled to a mass spectrometer to perform ions identification.

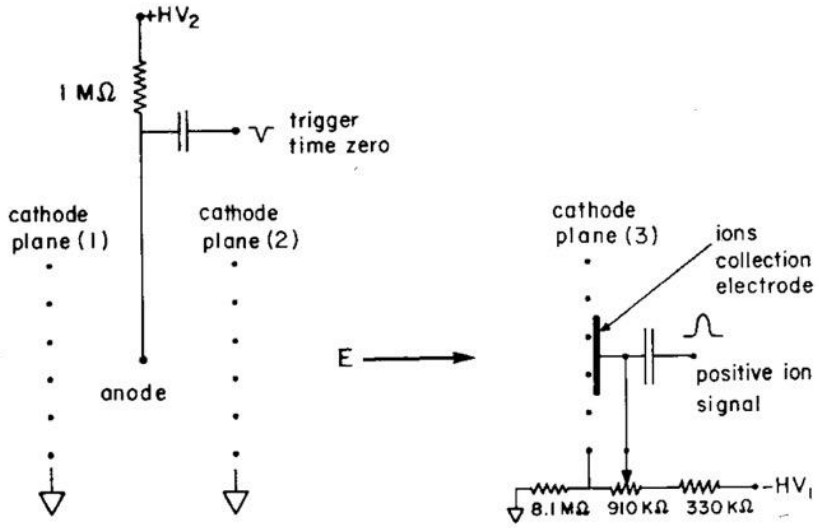

Figure 6-1: The detector used to measure ions mobility (Schultz, Charpak and Sauli, 1977).

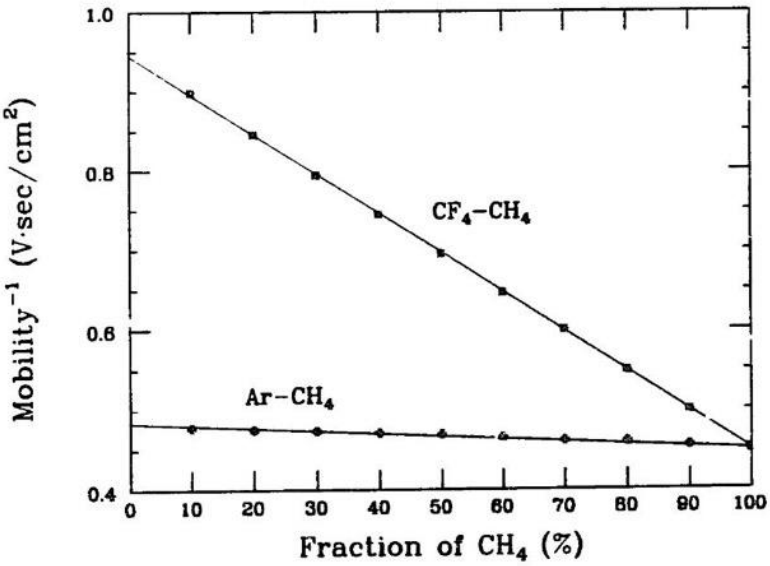

Figure 6-2: Ions' mobility in Ar-CH_4 and CF_4-CH_4 mixture as a function of methane fraction (Yamashita *et al.*, 1989).

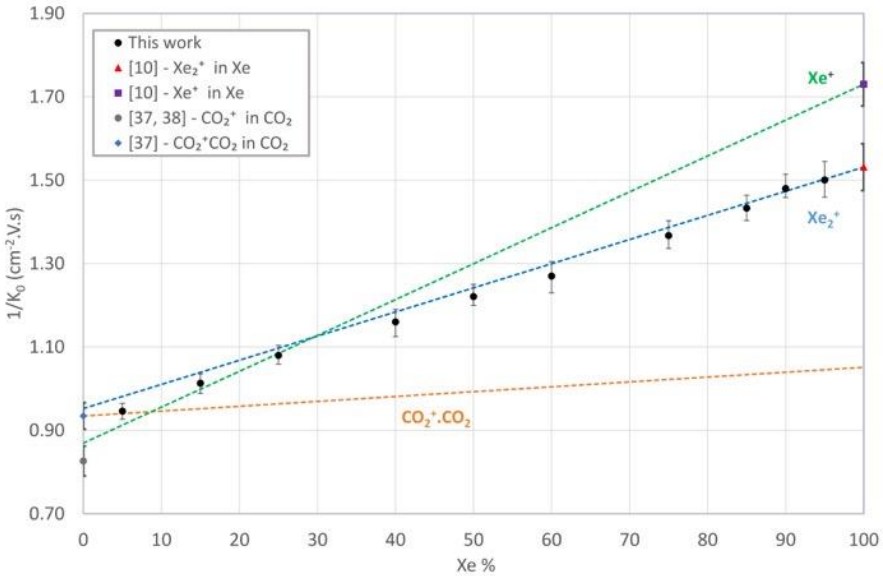

Figure 6-3: Ions mobility in Xe-CO_2 mixtures; the experimental data match the Blanc's law prediction for Xe_2^+ ions (Cortez, 2017).

An initial point-like distribution of ions diffuses symmetrically while drifting; the RMS of the gaussian-shaped cloud depends from the field but not on the type of ion, gas and conditions, Figure 6-4.

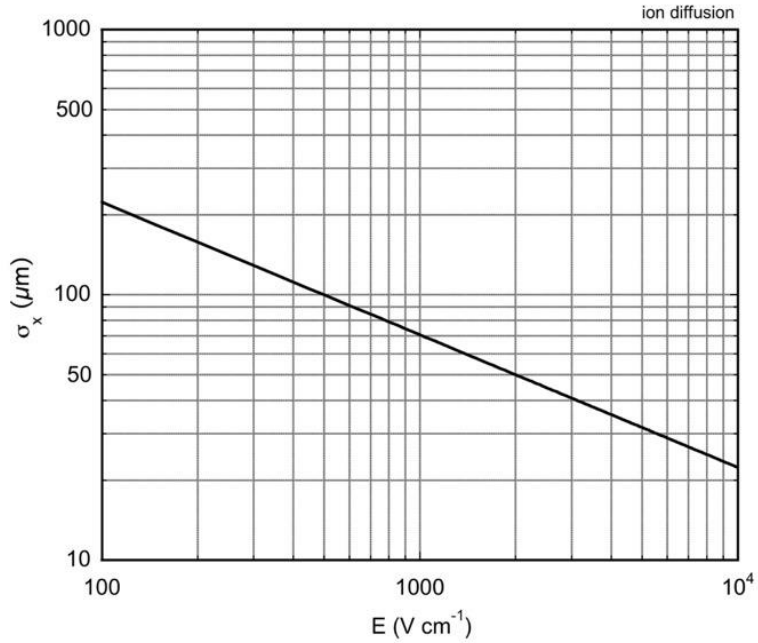

Figure 6-4: Standard deviation of the ion diffusion as a function of electric field.

6.2 Negative ions

In mixtures containing electronegative gases shortly after the ionization process negative ions replace the electrons as charge carriers; carbon disulfide (CS_2) and nitromethane (CH_3NO_2) are particularly efficient for this process. In high electric fields, the electrons can be detached from the ion and multiplied in avalanche to allow detection. (Dion, Martoff and Hosack, 2010). The low mobility and diffusion of negative ions offer advantages for the operation of time projection chambers (Ligtenberg *et al.*, 2021). The mobility of negative ions is very close to the one of positive ions of identical mass, and has been measured directly for several electronegative molecules. Figure 6-5 shows the drift velocity as a function of field for CS_2 at 21 and 40 torr, and mixtures of nitromethane and CO_2 at several pressure ratios (Dion, Martoff and Hosack, 2010).

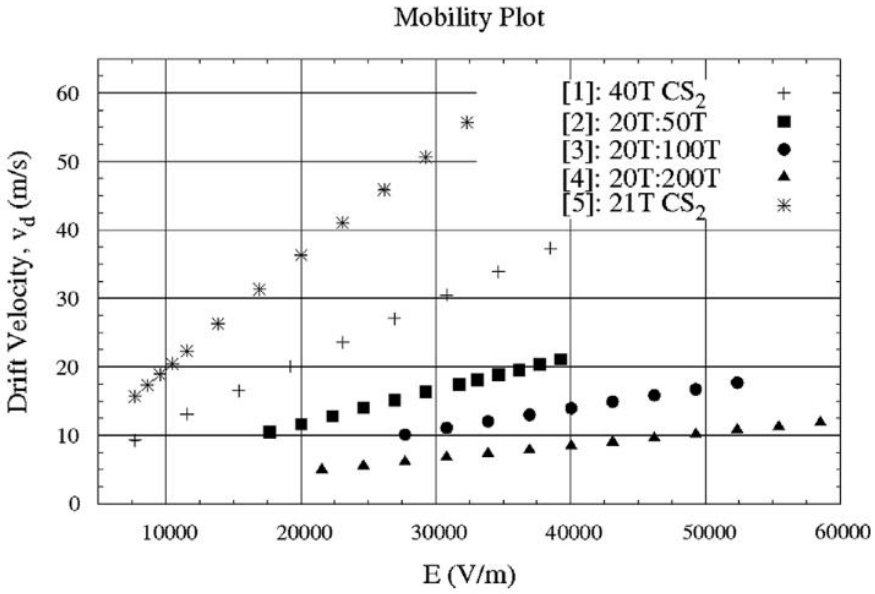

Figure 6-5: Negative ions drift velocities for CS_2 at 21 and 40 torr, and CH_3NO_2-CO_2 mixtures at different pressure ratios.

6.3 Electrons

The field dependence of the drift velocity of electrons differs largely between gases. The velocity has been measured for many gases, see for example the classic data in (Christophorou, 1971) and the compilation by (Peisert and Sauli, 1984). It can be computed for a wide choice of pure gases and their mixtures with dedicated software programs (Veenhof, 2019)(*BOLSIG+*, 2019) or from a web-based compilation of electron and ion scattering cross sections and swarm parameters calculator (*LXCat*, 2020)[3].

Except for extreme temperature and pressure conditions, not met in gaseous counters, the electron drift velocity is a unique function of E/N_0, ratio of the electric field and the Loschmidt constant, or number density:

$$N_0 = \frac{P_0}{k\,T_0}$$

where P_0, T_0 are pressure and absolute temperature of the gas and k the Boltzmann constant. In this work, the drift properties are given at normal temperature and pressures (NTP: 20^0C, 760 mmHg); for other conditions, the horizontal scale has to be normalized to the ratio of densities:

$$E(T,P) = E(T_0,P_0)\frac{\rho(T,P)}{\rho(T_0,P_0)}$$

for an ideal gas at temperature and pressure T, P:

$$\rho(T,P) = \frac{T}{273.14}\frac{760}{P}\,\rho(T_0,P_0)$$

Figure 6-6 collects drift velocities as a function of field for pure gases; Figure 6-7 for mixtures of argon and carbon dioxide, Figure 6-8 for mixtures of argon and methane, Figure 6-9 for argon-isobutane, Figure 6-10 and Figure 6-11 for argon and helium-carbon tetrafluoride.

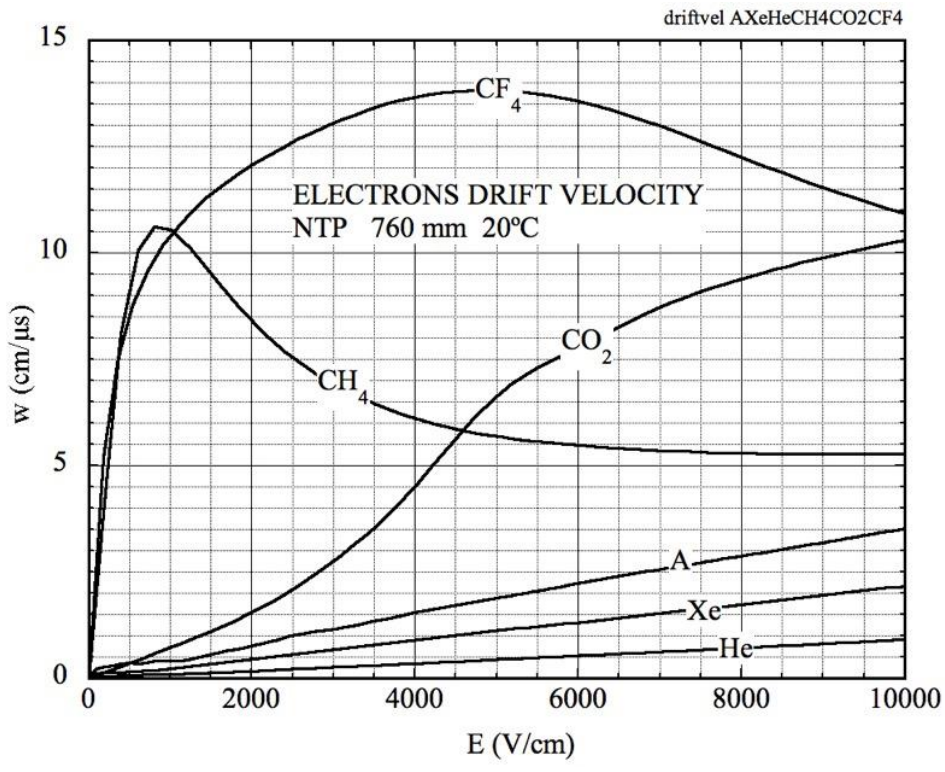

$N_0 = \frac{P_0}{k\,T_0}$

[3] While MAGBOLTZ provides swarm parameters in common units, BOLSIG and LXCat give results normalized to the gas number density, that have to be multiplied or divided by the appropriate value of N for the temperature and pressure of the gas.

where P_0, T_0 are pressure and absolute temperature of the gas and k the Boltzmann constant. In this work, the drift properties are given at normal temperature and pressures (NTP: 20^0C, 760 mmHg); for other conditions, the horizontal scale has to be normalized to the ratio of densities:

$$E(T,P) = E(T_0,P_0)\frac{\rho(T,P)}{\rho(T_0,P_0)}$$

for an ideal gas at temperature and pressure T, P:

$$\rho(T,P) = \frac{T}{273.14}\frac{760}{P}\,\rho(T_0,P_0)$$

Figure 6-6: Electron drift velocity for pure gases.

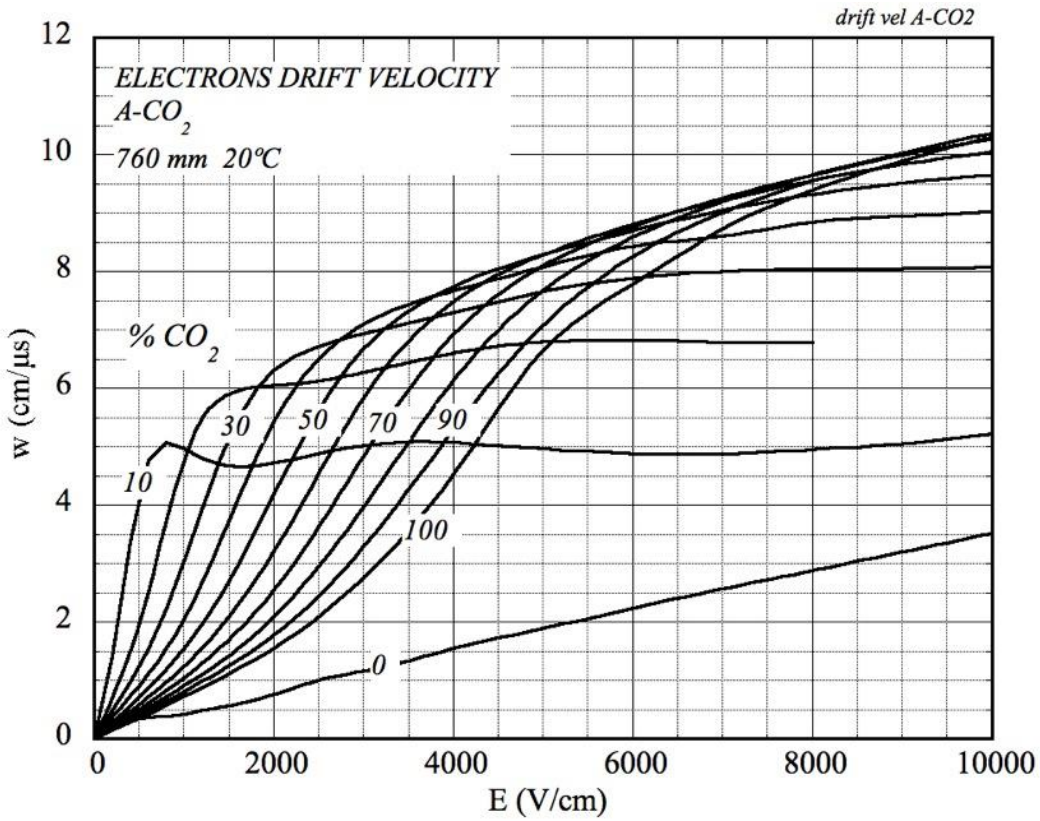

Figure 6-7: Electron drift velocity for argon-carbon dioxide mixtures.

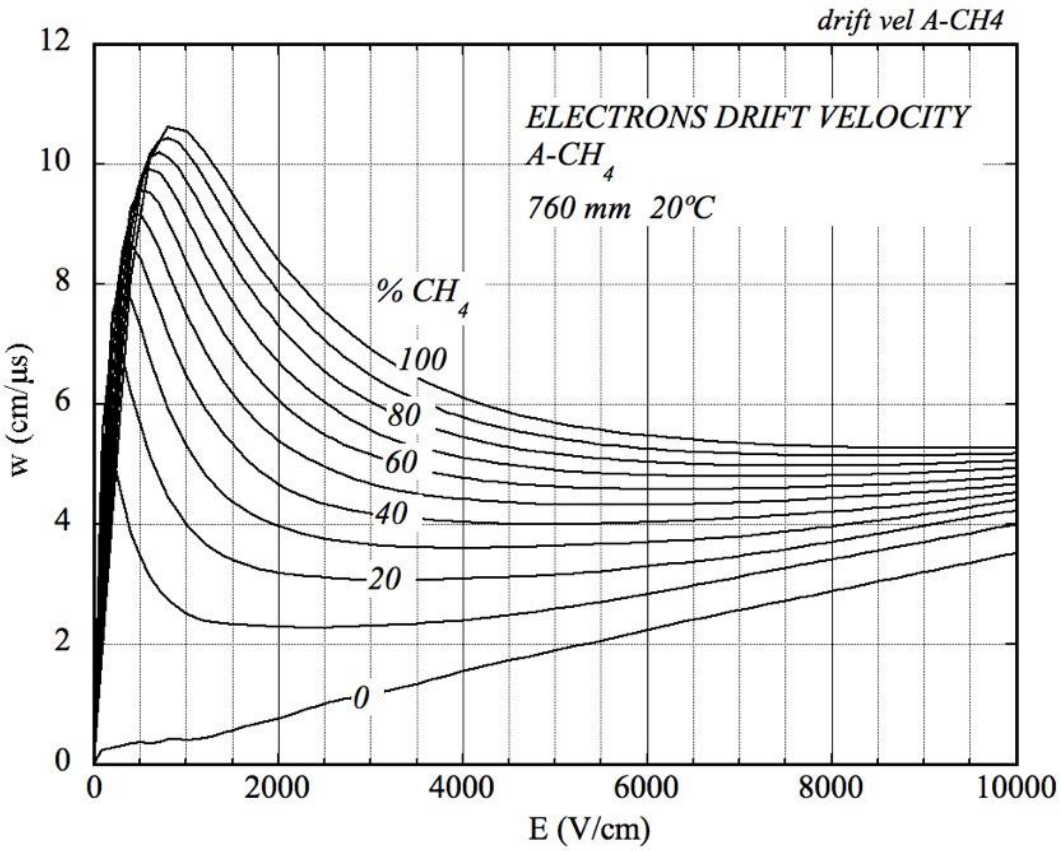

, Figure 6-8: Electron drift velocity for argon-methane mixtures.

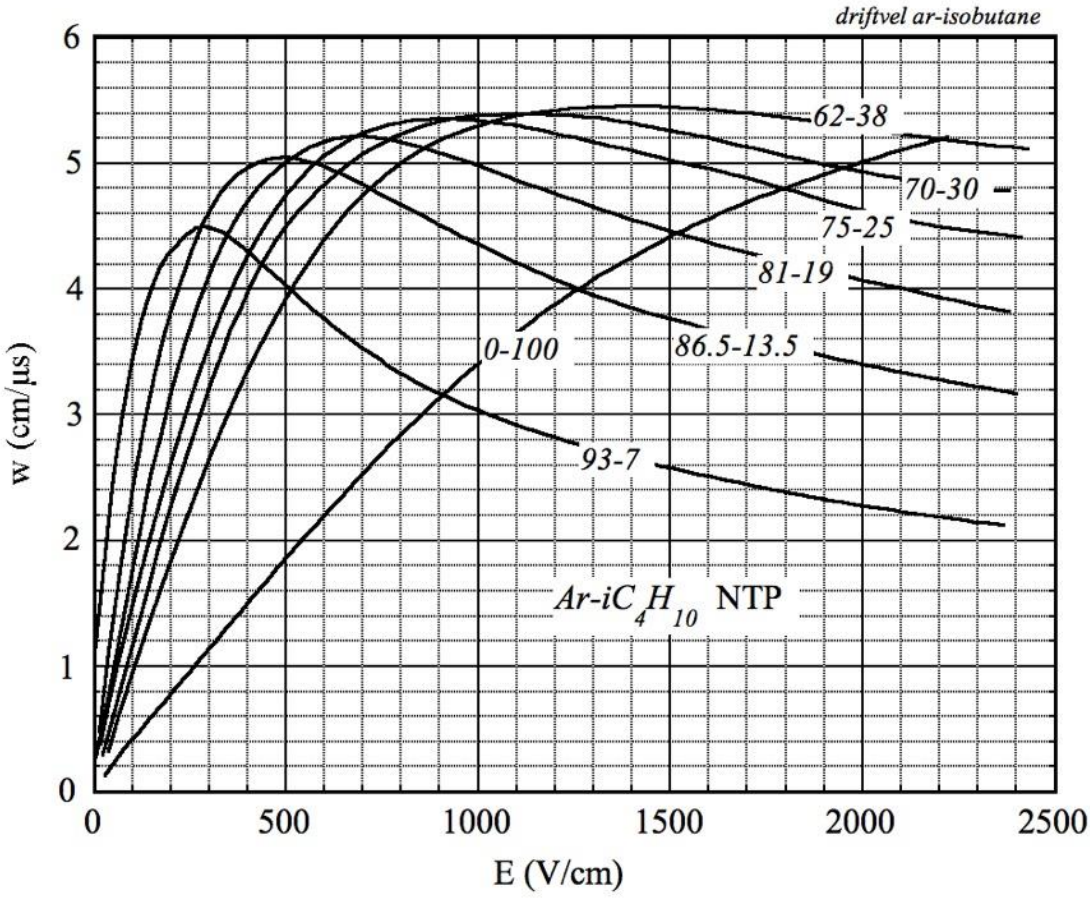

, Figure 6-9: Electron drift velocity for argon-isobutane mixtures.

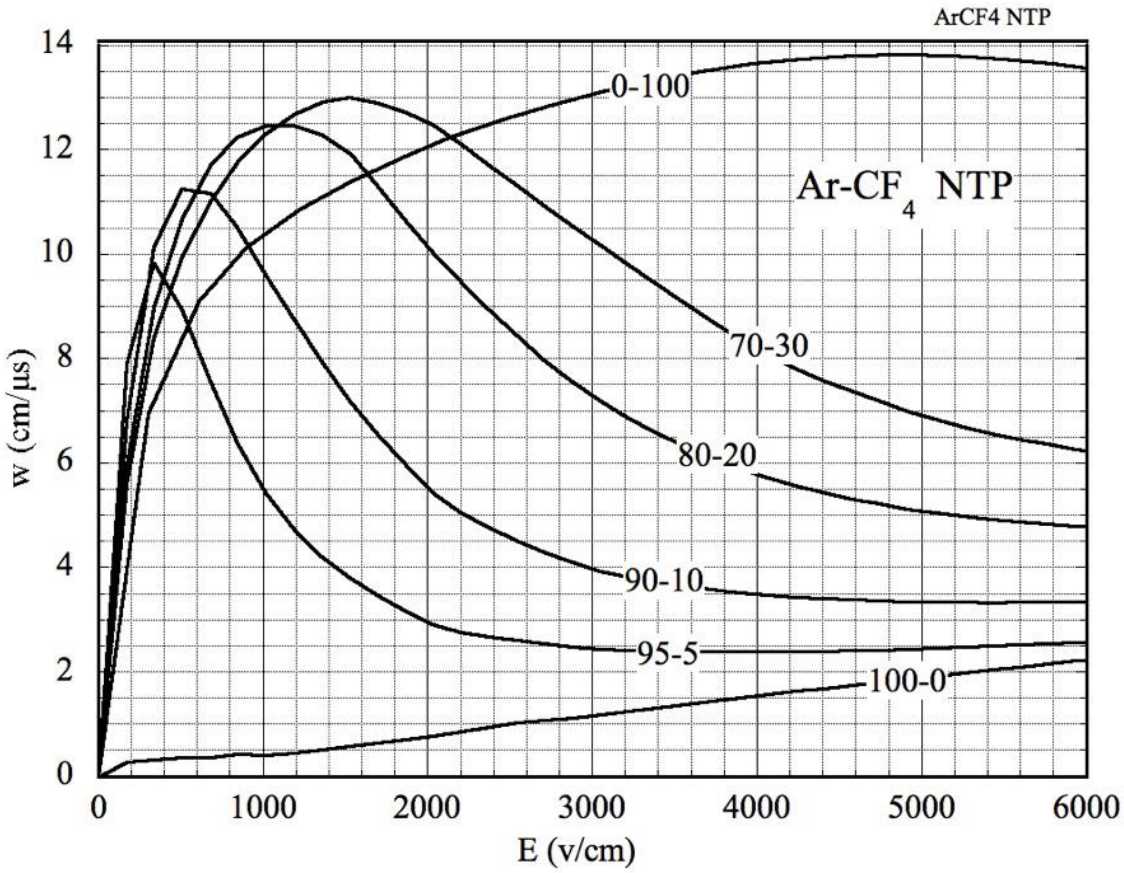

Figure 6-10: Electron drift velocity for argon-carbon tetrafluoride mixtures at NTP.

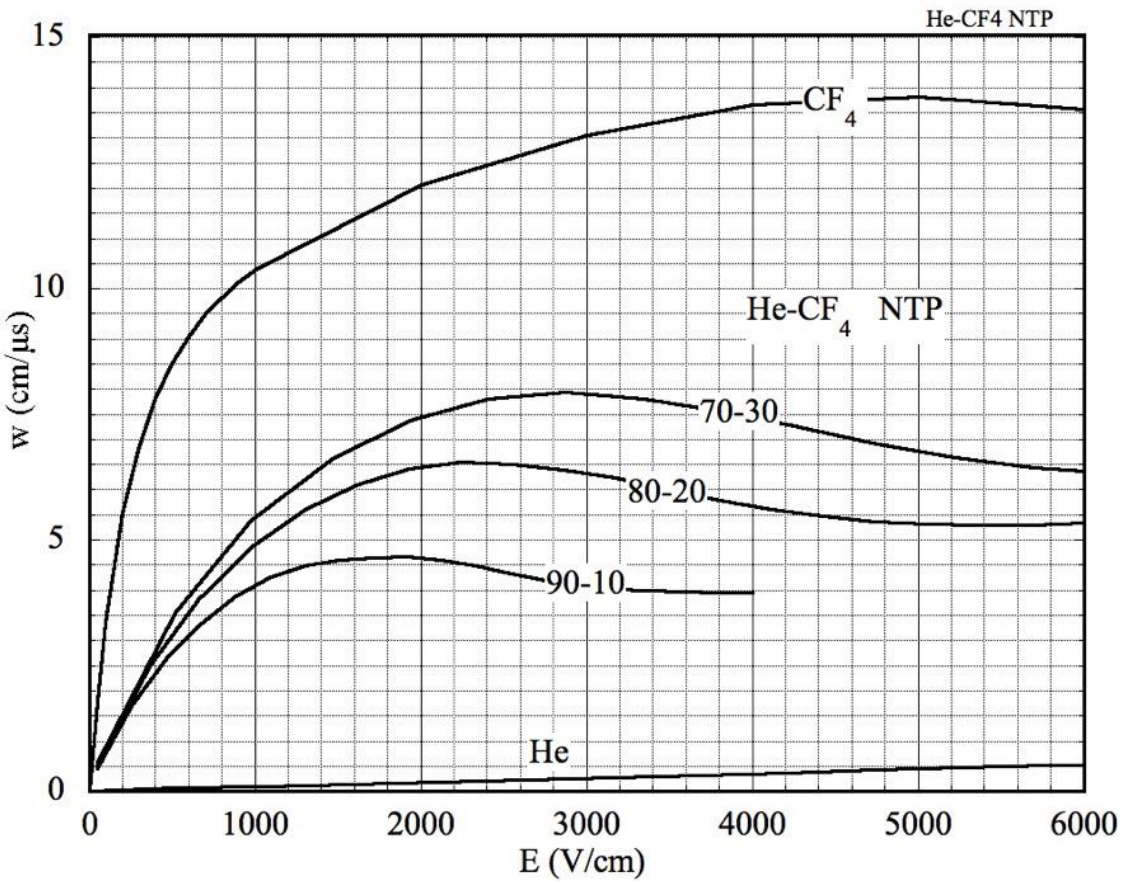

Figure 6-11: Electron drift velocity as a function of field for helium-carbon tetrafluoride mixtures at NTP.

During the drift in electric fields, and as a result of multiple collisions with molecules, electrons diffuse spreading the initially localized charge cloud. The extent of diffusion depends on the gas, but also strongly on *E*, due to the increase of the electron energy; the distribution has a gaussian shape with rms along a direction x given by $\sigma_x = \sqrt{2Dt}$, where D is a diffusion coefficient. At high values of field, the longitudinal diffusion along the direction of drift, described by a coefficient D_L, differs from the transverse diffusion D_T. As seen in the expression, the diffusion increases with the square root of the distance, and is generally given in units of $\mu m\sqrt{cm}$. As a general trend, the diffusion is smaller for gases in which electrons remain thermal up to higher fields, the so-called cold gases. Figure 6-12 and Figure 6-13 are examples of longitudinal and transverse diffusions for argon-CO_2, argon-CF_4 and helium-CF4 mixtures.

In presence of an external magnetic field, as in time projection chambers, the longitudinal diffusion is unaffected, while the transverse diffusion is reduced, improving the space localization properties of the detector (see for example Chapter 4.6 in (Sauli, 2014)).

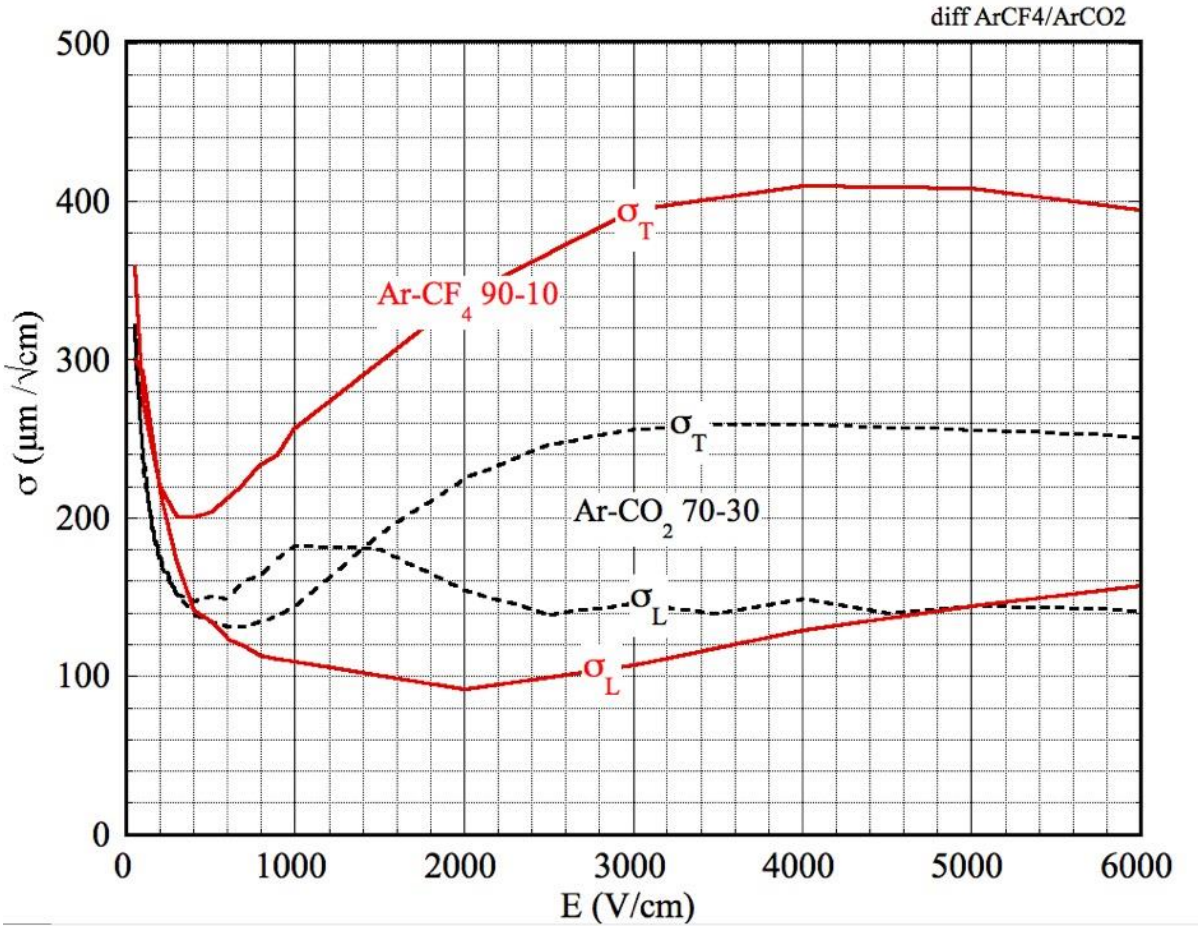

Figure 6-12: Longitudinal and transverse diffusion in Ar-CO_2 and Ar-CF_4 mixtures.

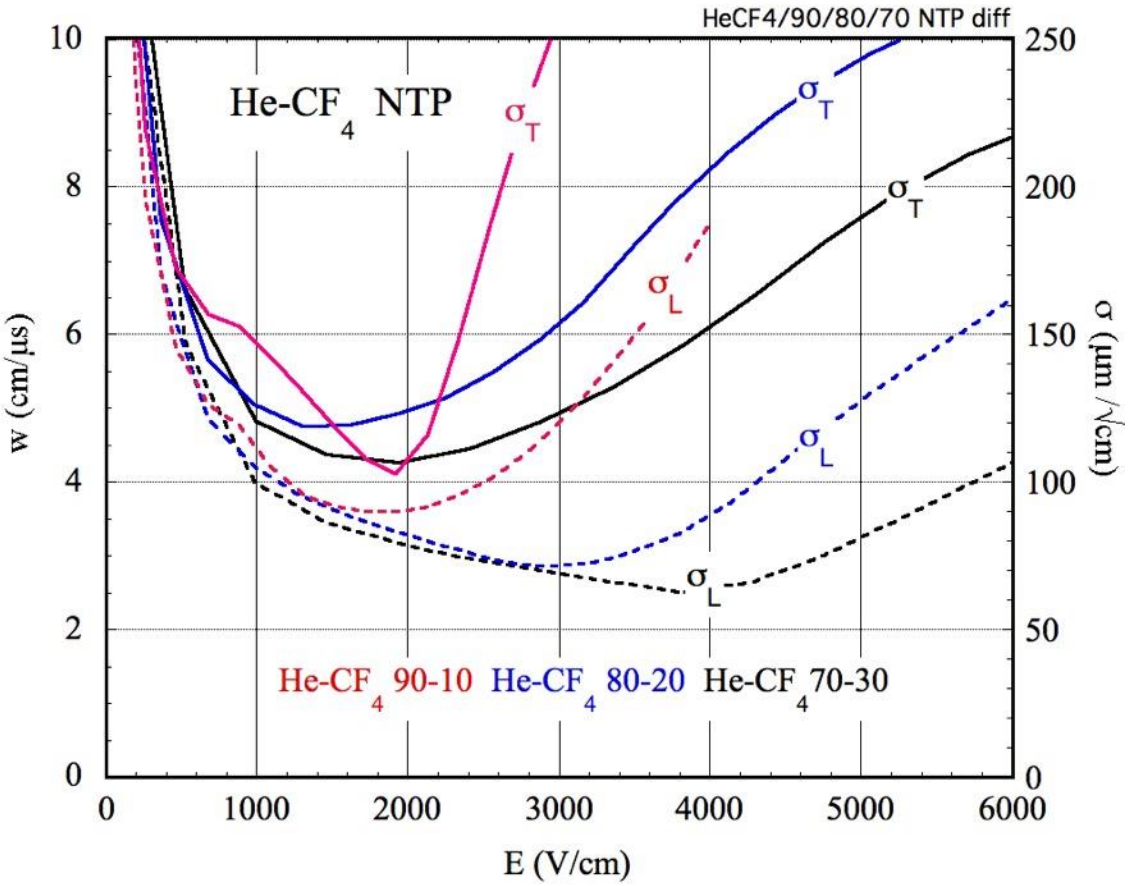

Figure 6-13: Transverse and longitudinal diffusion in He-CF_4 mixtures.

6.4 Electron attachment

Diffusing in the gas, electrons can be captured by molecules with electronic affinity creating negative ions; the attachment probability depends on the electron energy and therefore on the electric field. Negligible for the noble gases, it has finite values for most other gases, including carbon dioxide, oxygen and water, and is particularly large for some molecules as freons, named electronegative, that can effectively absorb part or all of the ionization charge if present even in very small quantity. In mixtures, the capture process can be enhanced by multi-body interactions. Due to the strong dependence of the attachment probability from the electron energy, that depends itself on the gas, the same amount of electronegative pollutant may result in very different losses equal being all other conditions. For a more detailed discussion on gas purity and contamination see chapter 7.

The capture losses are described by the expression:

$$n = n_0 e^{-x\,h}$$

where n_0 and n are the initial and surviving numbers of electrons, x the drift length and h a field-dependent attachment coefficient or rate (captures per unit length). Computed with MAGBOLTZ, Figure 6-14 provides the attachment coefficient for several common gas mixtures, pure or with the addition of 1% of oxygen.

Electron capture is particularly high at high fields in gases containing carbon dioxide. Part of a study on alternative gases for the CMS upgrade, Figure 6-15 shows the computed high-field capture probability for several gas mixtures (Al-Rashdi *et al.*, 2021). These field values are only encountered in the charge multiplication process, and electron capture affects the estimated value of gain.

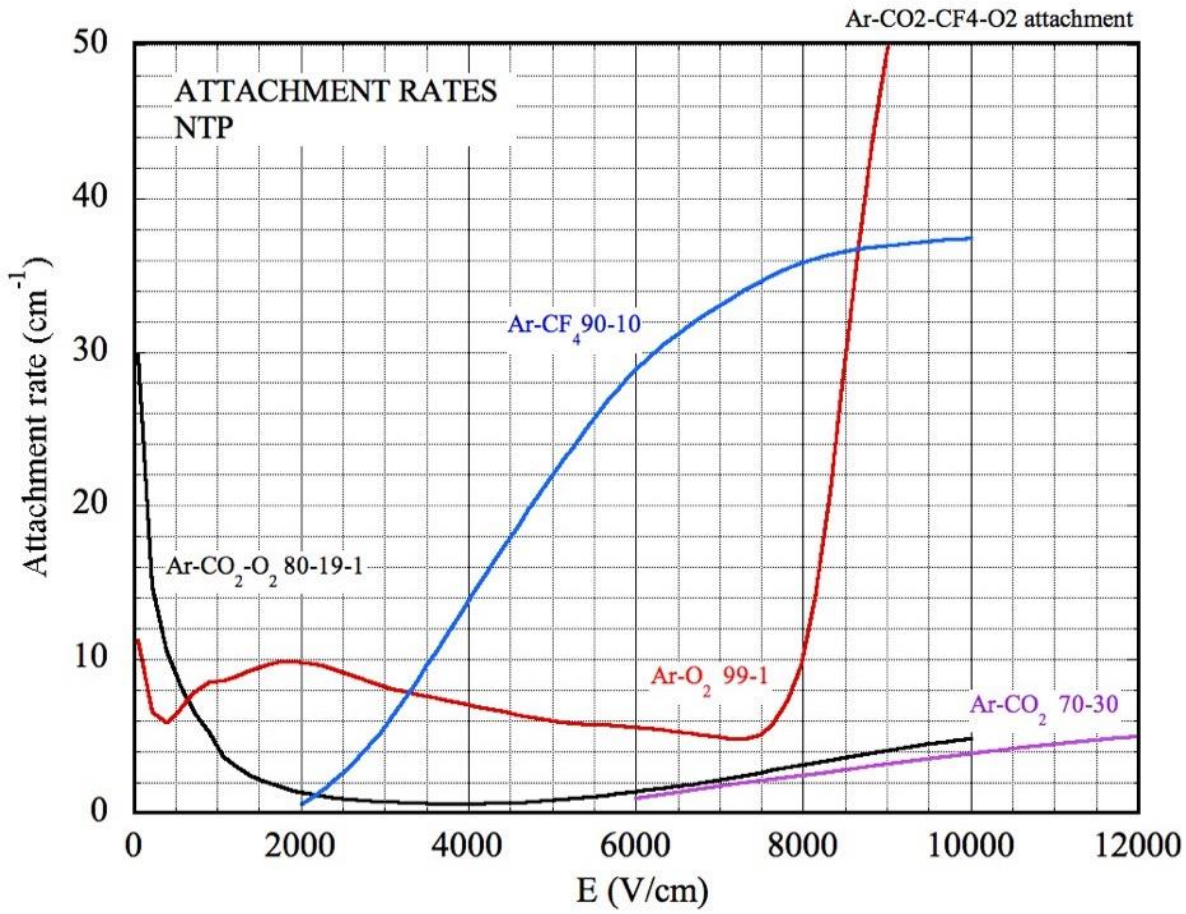

Figure 6-14: Computed attachment coefficient at NTP for several gas mixtures, pure and with addition of 1% of oxygen.

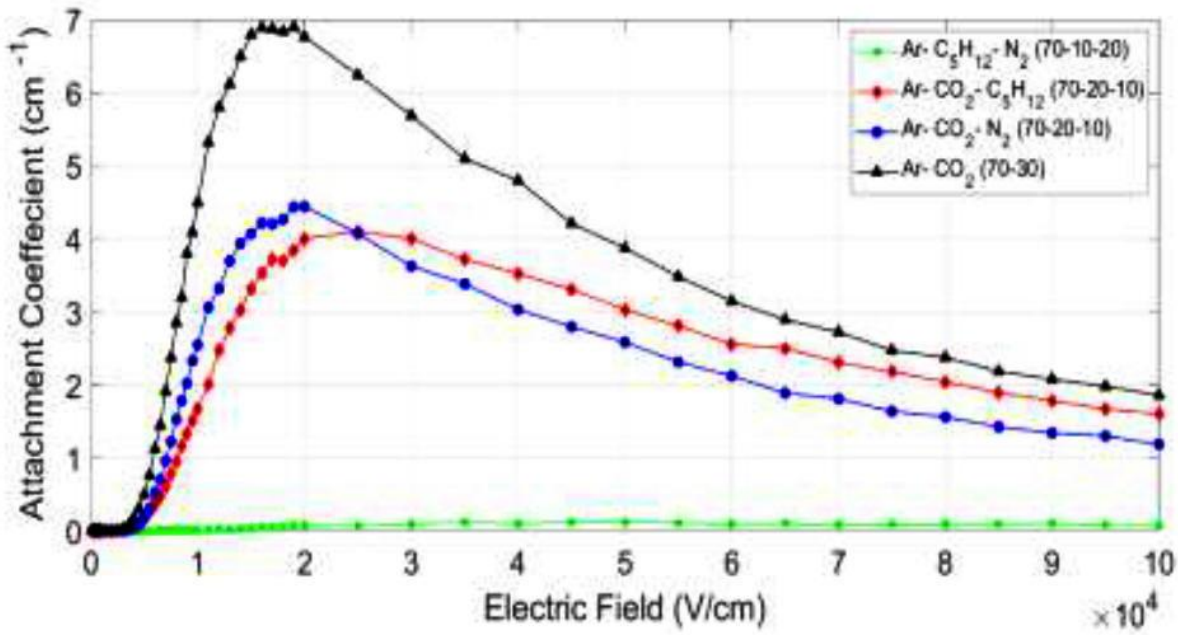

Figure 6-15: High field electron capture probability in several gas mixtures (Al-Rashdi *et al.*, 2021).

6.5 Charge multiplication

When the electric field exceeds a gas-dependent threshold value, inelastic electron-molecule collisions may result in the creation of an electron-ion pair. Progressing along the field, electrons experience further ionizing collisions, leading to the development of an ion-electron avalanche. The multiplication factor M, or gain, defined as ratio of the total charge Q to the initial Q_0 grows exponentially with the applied field, until reaching saturation or discharges. In the simplest case of uniform field, the gain can be written as:

$$M = \frac{Q}{Q_0} = e^{\alpha x}$$

where α is the ionization or first Townsend coefficient, and x the length of propagation of the avalanche. In a wide range of pressures P and in absence of secondary processes, α/P is a sole function of the reduced field E/P.

Classic values of the Townsend coefficient as a function of field for pure rare gases are provided for example by (Druyvesteyn and Penning, 1940), Figure 6-16, see also Chapter 5 in (Sauli, 2014).

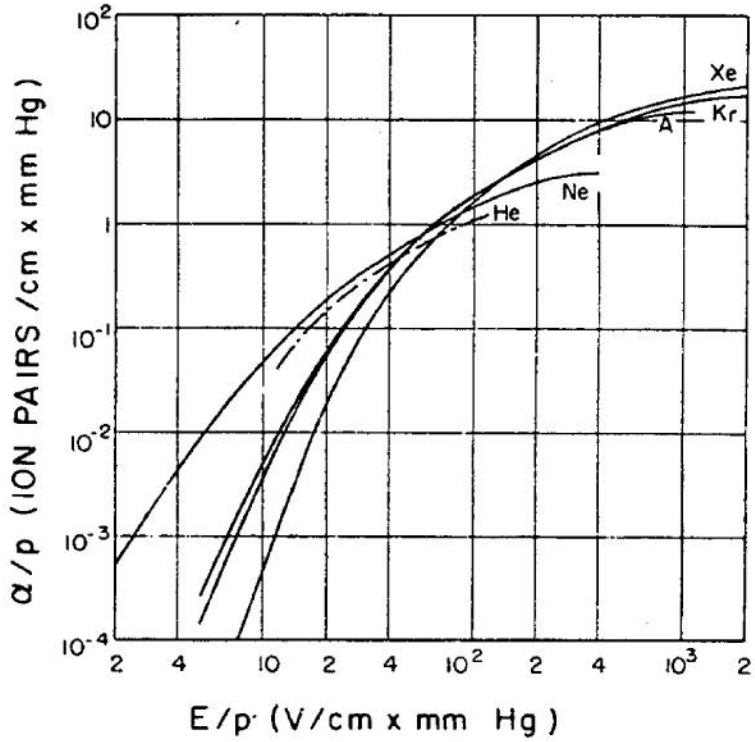

Figure 6-16: First Townsend coefficient of rare gases as a function of reduced field (Druyvesteyn and Penning, 1940).

The coefficients can be computed with the tools described in the previous sections, or measured with ionization chambers consisting of a drift volume followed by a parallel plate multiplier, exposed to an ionizing source. While the accuracy of computed values has been validated, in comparing to experimental values one should take into account that the exponential increase of gain with the field implies a strong dependence of the results from the gas fractions in mixtures and from the presence of even very small contaminants.

Figure 6-17 is a recent compilation of measurements of the coefficient for carbon dioxide and methane, compared to the Magboltz predictions (Petri *et al.*, 2017); the sources are mentioned in the reference. Examples of experimental measurements for mixtures are shown in Figure 6-18 and Figure 6-19 (Sharma and Sauli, 1993). The reference describes also the device and method used for the measurement.

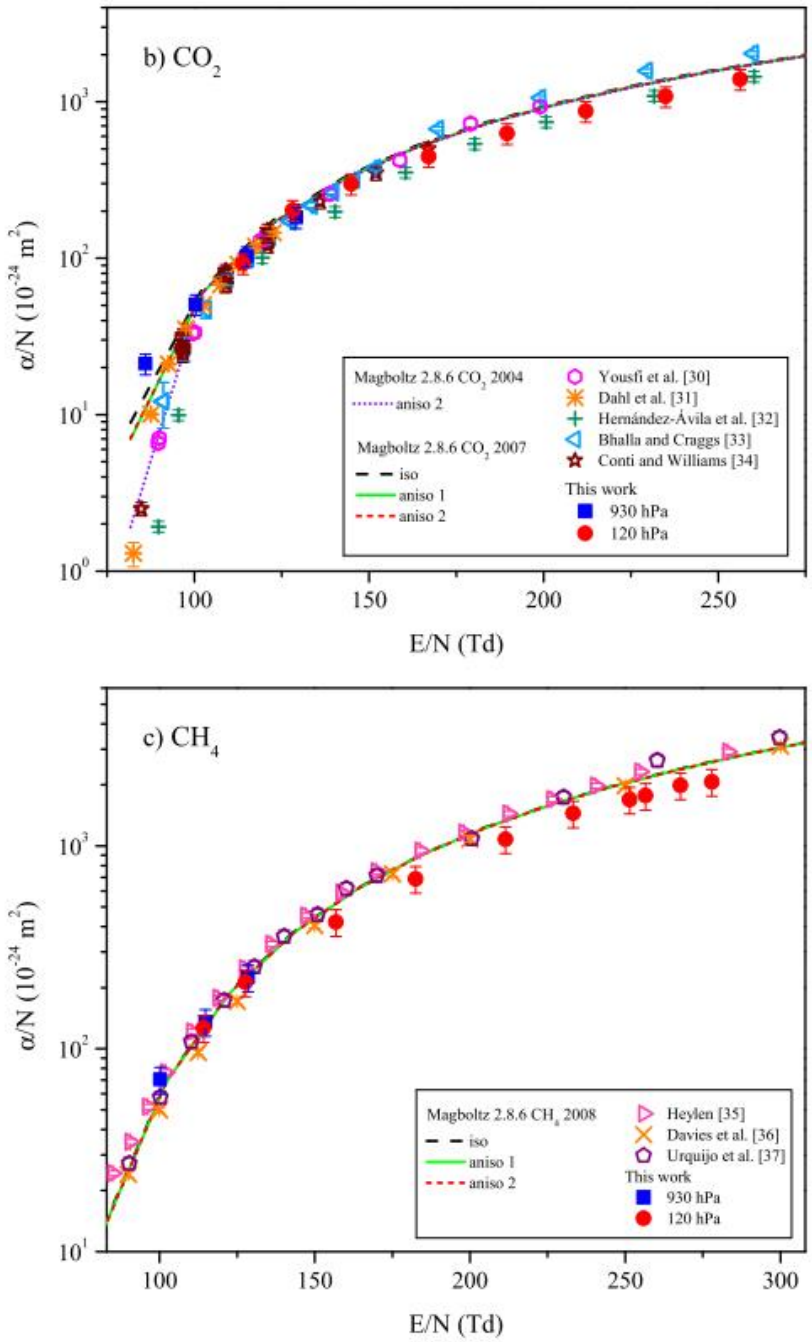

Figure 6-17: Measured and computed values of the first Townsend coefficient (Petri *et al.*, 2017). For the units used see footnote in chapter 6.3.

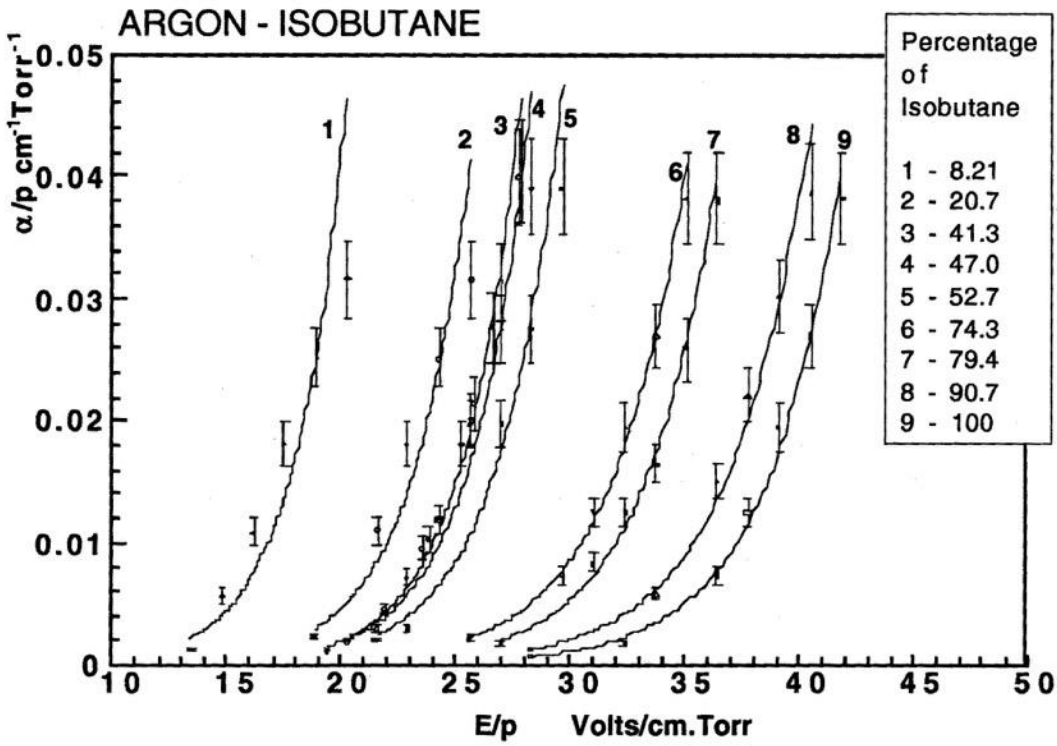

in Figure 6-18: First Townsend coefficient for argon-isobutane mixtures (Sharma and Sauli, 1993).

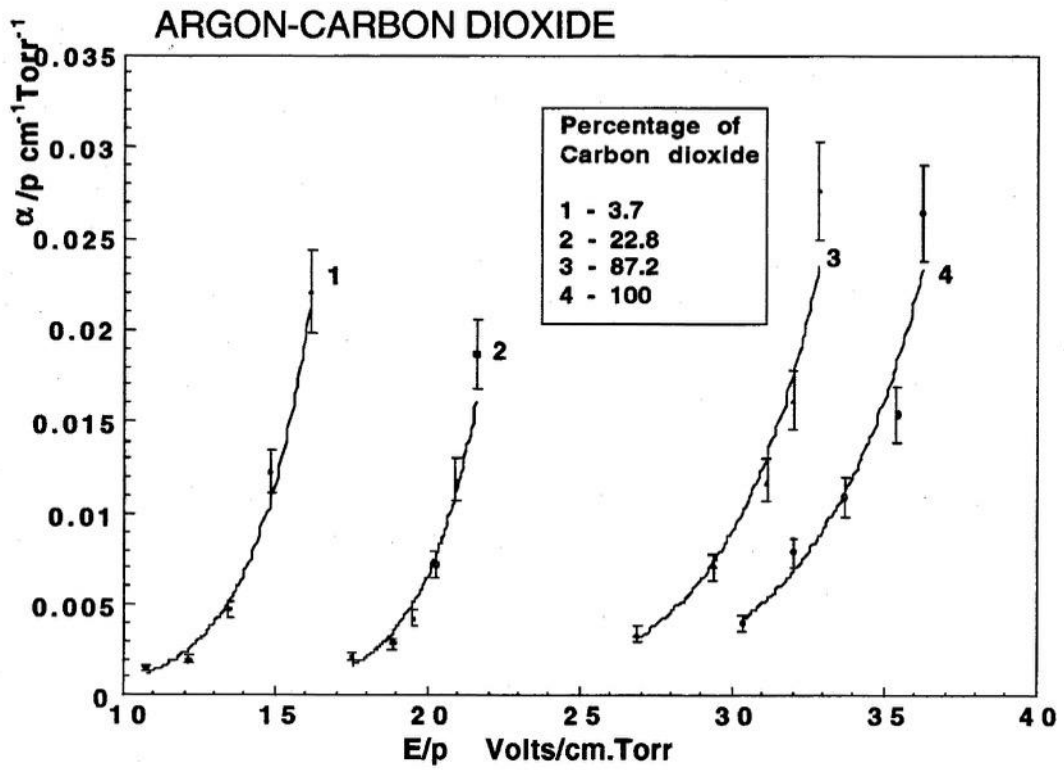

Figure 6-19: First Townsend coefficient for argon-carbon dioxide mixtures (Sharma and Sauli, 1993).

7 GAS MIXING, DISTRIBUTION AND QUALITY CONTROL

Contributed by Mara Corbetta (CERN)

This section illustrates the key way of supplying and monitoring the gas mixtures used in gaseous detectors. An introduction to primary and pre-mixed gas bottles is followed by information on preparing and distributing the desired gas mixture to table-top laboratory gaseous detectors setups. Finally, an overview is given of instruments used to monitor the gas mixtures composition and quality.

7.1 Primary gas supply

The correct preparation and delivery of the mixtures for gaseous detectors starts from the primary gas supply, as purity of components and correct handling of gas connections are paramount to obtain a mixture of good quality.

7.1.1 Pure components

One way to supply the desired mixture to gaseous detectors is to prepare it from pure gases. Gases can be produced with different grades of purities, depending on the final usage of the gas, so different options are present on the market, with consequently a range of prices. The grade of purity of a gas is generally labelled with a code that indicates the "number of nines" in the precision of the gas concentration. For example, a gas classified as N4.0 will have a purity of 99.99%, i.e. with four nines. An additional indication of purity level can be the second digit of the code, where for example N4.6 means a minimum purity of 99.996%.

Table 7.1 summarizes the range of common purity grades of gases available on the market. The same classification can also be found with different labels (ex: Ar N4.6 = Ar 4.6 = Ar 46).

Grade	***Minimum Purity***	***Total Impurities***
N2.0	99%	1%
N3.0	99.9%	0.1% = 1000 ppm
N4.0	99.99%	0.01% = 100 ppm
N5.0	99.999%	0.001% = 10 ppm
N6.0	99.9999%	0.0001% = 1 ppm
N7.0	99.99999%	0.00001% = 10 ppb

Table 7.1: Impurity levels of pure gases.

For gaseous detector applications, clearly the highest purity available would be optimal, but super high-purity gas bottles could reach very high costs. Normally, one would want to settle around a purity of N5.0 - N6.0 for primary components.

The impurities present in pure gases normally come from the production process, and they are always indicated in the specification sheet of the product; common impurities are O_2, N_2, H_2O and hydrocarbons. An example of an Argon technical sheet from the company Linde is given in Table 7.2, with the different purities available and relative impurities.

	Argon 4.8	Argon for spectrometry	Argon 5.0
Purity, %:	≥ 99.998	≥ 99.998	≥ 99.999
Impurities, ppm:	O_2 ≤ 3 N_2 ≤ 10 H_2O ≤ 5 C_nH_m ≤ 0.5	O_2 ≤ 3 N_2 ≤ 10 H_2O ≤ 5 C_nH_m ≤ 0.5	O_2 ≤ 2 N_2 ≤ 5 H_2O ≤ 3 C_nH_m ≤ 0.2

Table 7.2 Argon product specification sheet from Linde, https://www.linde-gase.de/download/Spec.Gases.e.02.02.pdf

All pure gases commonly used for gaseous detectors are nowadays commercially available. Table 7.3 provides a non-exhaustive list of the available gases with an indication of the companies where they can be purchased.

Name	***Formula***	***Gaseous detectors***	***Company***
Argon	Ar	drift chambers, MPGD	Linde, Air Liquide
Carbon Dioxide	CO_2	drift chambers, MPGD	Linde, Air Liquide
Tetrafluoromethane	CF_4 (R14)	drift chambers, MPGD	Linde, Multigas
1 1 1 2-tetrafluoroethane	$C_2H_2F_4$ (R134a)	resistive chambers	PanGas, Multigas
Isobutane	iC_4H_{10}	resistive chambers	Linde, Air Liquide
Sulfur-hexafluoride	SF_6	resistive chambers	Linde, Air Liquide
Oxygen	O_2		Linde, Air Liquide
Noble Gases	He, Ne, Kr, Xe	RICHes,	Linde, Air Liquide
n-Pentane	nC_5H_{12}		Linde, Air Liquide
1,3,3,3,-tetrafluoropropene	HFO (R1234ze)	(low GWP) drift chambers, resistive chambers	Multigas

Table 7.3: Pure gases suppliers. For the address of companies see the references for this section.

7.1.2 Pre-mixed solutions

Another possible way to deliver the desired gas mixture to gaseous detectors is to use pre-mixed gas bottles. These bottles are available on order for commonly used gas mixture, in variable fractions. While on one side the use of pre-mixed bottles allows to skip the mixture preparation phase, on the other hand it limits the possibilities of varying the concentration of the components. As for pure gases, for pre-mixed bottles there exists a classification to determine the purity of the mixture and the precision with which the mixture is prepared, measured and certified. Two parameters are used to classify pre-mixed gas bottles: realization error and uncertainty. The realization error represents the maximum difference in percentage between the nominal concentration and the concentration achieved during production, which normally depends on the

production technology. The uncertainty represents instead the accuracy of the measurement of the concentrations, i.e. the difference in percentage between the measured and the true concentration. This uncertainty depends on the measurement technology, and it is the value used to certify the purity of a bottle: the smaller the uncertainty, the more precise will be the mixture composition. For most suppliers, the classification is done according to these two parameters, though with different nomenclature and range of error and uncertainty. An example of a classification table is reported in Table 7.4.

Regardless of the predefined ranges and classes, it is fundamental to take into account the realization error and uncertainty of the pre-mixed bottle before using it, to be sure that it is suitable for the desired application.

Class	Share of admixtures	Preparation tolerance	Measuring uncertainty
PEH	1 - 99 ppm 100 - 999 ppm 0.1 - 4.9 % 5 - 50 %	± 2 % rel. ± 1 % rel. ± 0.5 % rel. ± 0.1 % rel.	± 1 % rel. **
1	1 - 99 ppm 100 - 999 ppm 0.1 - 4.9 % 5 - 50 %	± 10 % rel. ± 5 % rel. ± 2 % rel. ± 1 % rel.	± 2 - 5 % rel. ± 2 % rel. ± 2 % rel. ± 1 % rel.
2	100 - 999 ppm 0.1 - 4.9 % 5 - 50 %	± 10 % rel. ± 5 % rel. ± 2 % rel.	± 5 % rel. ± 2 % rel. ± 2 % rel.
3	0.1 - 4.9 % 5 - 50 %	± 10 % rel. ± 5 % rel.	* *

Table 7.4 Linde products specification sheet, https://www.linde-gase.de/download/Spec.Gases.e.02.02.pdf

7.1.3 Primary gas distribution

Regardless of the primary gas supply of choice, i.e. pure gases or pre-mixed bottles, it is fundamental to correctly handle gas cylinders to assure minimum changes on gas quality as well as to comply with safety regulations. One should keep in mind that bottled gases, to fit significant volumes into cylinders of manageable size, are compressed to significantly high pressures (up to 150-200 bar). To use gases for composing gaseous detectors gas mixture pressures of few bars are required, so to transfer bottled gases to mixing devices it is fundamental to make use of pressure reducers and regulators. Commonly used pressure regulators consist of a valve that simply controls the pressure of the gas, possibly with a reading of the upstream pressure, the one contained in the gas cylinder, and a reading of the downstream pressure, the one at the output of the valve that can be regulated according to necessity.

Figure 7-1 shows an example of pressure regulator for gas cylinders, with manometer reading of upstream and downstream pressure.

Figure 7-1 Example of pressure regulator from Emerson
https://www.emerson.com/documents/automation/catalog-wega-1-pressure-regulator-gas-tescom-en-5387110.pdf

Purchasing or using these pressure regulators, attention should be paid to the type of connectors that are going to be used to attach the device to the gas cylinders. Different types of gases typically are linked to specific types of connectors, and pressure reducers are usually already classified according to their final usage (neutral gases, flammable gases,).

7.2 Gas mixing from pure components

Once primary gases are connected and ready, they can be used to prepare the desired gas mixture for the detector in use. This section illustrates how, starting from pure primary components, a given gas mixture can be obtained with a simple laboratory table-top setup.

Before starting with practical considerations, a short theoretical reminder is given on how to deal with gas mixtures and their composition. In the gaseous detector field, gas mixture compositions are always given in terms of volume (or molar) fractions. Hence a gas mixture referred to as, for example, Ar/CO_2 70/30 will indicate a mixture with 70% Argon and 30% CO_2, with fractions given in terms of volumes. However, when dealing with specific instrumentation measuring gas flows, most of the time the key parameter for the instrument working principle is a gas intrinsic property, such as density or thermal conductivity. It should therefore be remembered that in many cases such instruments will need some calibration, as the outcome of their measurement will depend on the type of gas or gas mixture in use.

The most common way to prepare a gas mixture starting from primary gas components is to make use of Mass Flow Controller (MFC) devices. In this way, the flow of each component can be controlled and set to be the desired fraction over the total flow obtained by adding up the flows of all the mixture components.

The main elements to realize a mixing setup are the input pure gases, MFCs (one per pure component) and possibly a mixing volume. Pure gases lines coming from gas cylinders are connected to MFCs, where the output gas flow is regulated according to the desired value, and such outputs from all components are hence connected to a mixing volume where the different components can blend and form an homogeneous mixture that will be distributed to detectors. Figure 7-2 shows schematically a typical setup.

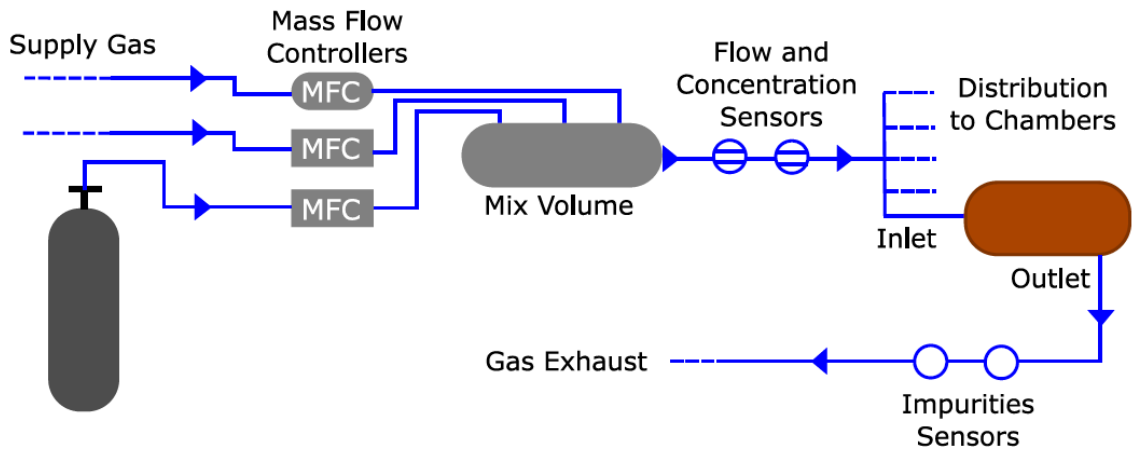

Figure 7-2 Schematics of a gas distribution system, including the most common elements https://www.emerson.com/documents/automation/catalog-wega-1-pressure-regulator-gas-tescom-en-5387110.pdf

As the key components for a correct preparation of the mixture are MFC devices, a short description is given here on their working principle, as well as an example on how they can be used and regulated. MFCs are usually made with a turbulence filter, a laminar flow element, a thermal mass flow sensor and a control valve, see Figure 7-3. The incoming gas is converted into a laminar flow by a series of thin layers with small openings, and their impedance allows the gas to pass through the mass flow sensor. The latter consists of a capillary tube with a heater placed between two temperature sensors, that measures the temperature difference which is proportional to the mass flow of the gas. Given the mass flow, the exit valve can then be opened or closed based on the desired gas output. MFCs are remotely controlled with a dedicated software, through a PC BUS connection; the software allows to set the desired flow for each component, to obtain a total flow with the correct proportion of the components for the desired gas mixture.

When using a MFC, it must be taken into account that, as the flow measurement depends on intrinsic properties of the gas, the measured flow will vary depending on the type of gas flowing through the MFC. Therefore, each MFC will be characterized by a specific calibration curve, normally provided by the supplier and saved inside the device memory. It is hence very important to use suitably calibrated MFC for each type of gas, as well as for the required operation range. MFC are indeed characterized by a certain uncertainty on the supplied flow, which depends on the measured value but also on the full calibration scale. Working in the lowest or highest part of the calibration range can yield significant errors in the supplied flow, therefore in the final gas mixture proportions. Uncertainty of common MFC devices can vary around the 0.5-1% of the measured value and 0.1-1% of the full calibration scale.

Finally, it is also fundamental to use MFCs within the specified range, in particular for the input and output pressures. If the input pressure is too low with respect to design values, the device will not open enough to give the preset gas flow; if the input pressure is too high, there is a risk to break the internal components. The design output pressure will have to be compatible with what is requested from the downstream elements of the setup (i.e. valves, composition measuring devices).

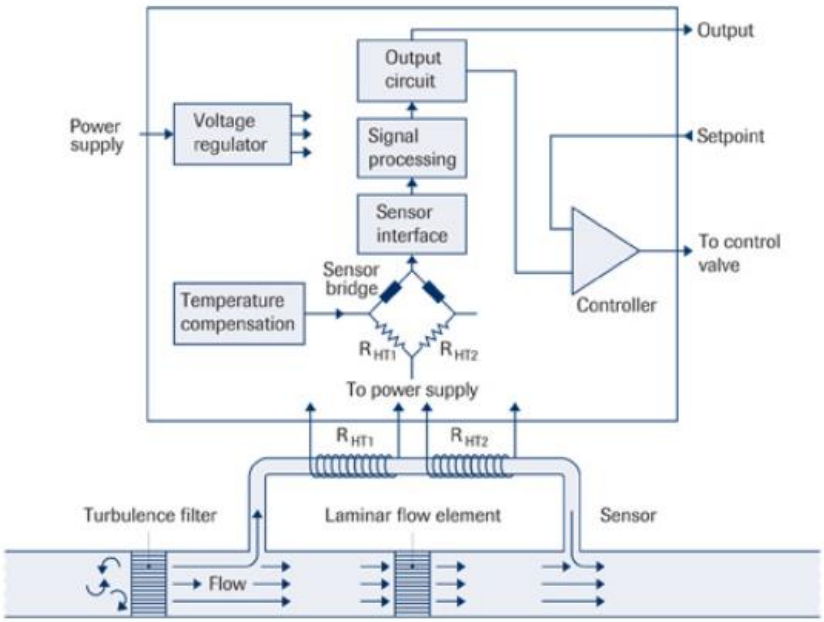

Figure 7-3 Schematics of a Mass Flow Control system from Bronkhorst https://www.bronkhorst.com/int/service-support-1/technologies/thermal-mass-flow-sensor-for-gases-bypass-principle/

Once the flow rate of each component of the gas mixture is properly set, the output of Mass Flow Controllers is normally sent to a mixing volume, of a size chosen depending on the total gas flow. The various components injected in the volume will then mix inside, before being sent to a single output pipe as a uniform gas mixture. Before distributing the mixture to detectors, it can be convenient to pass it through a filter to remove mechanical impurities, mainly dust from the environment around the setup. Different types of filters exist, with various filtering fineness down to ~ 10 μm.

A last consideration that concerns both mixture preparation as well as the following gas distribution is the choice of gas piping. Ideally, the piping connecting the various elements of a gas system should be as transparent as possible for the gas handling. It should not introduce pressure differences, gas leaks or air intakes, and it should not contribute to the creation of gas pollution by environmental impurities adsorption (for example humidity). On the other hand, piping in most cases needs to be versatile to comply with space-necessities of the setup, and help to nicely fit all the equipment in small spaces. Various options for piping exist, as well as various connection options, and their choice will depend on what is more relevant for the part of the setup in question. Stainless steel pipes connected by welding are the most secure in terms of introduction of gas leaks, but requires qualified manpower to be bent and adapted, and welding needs even more specific expertise. In small setup, connections are commonly simply realized through gas connectors, that generally ensure a good tightness if managed properly. Stainless steel piping also comes in a flexible option, which however is much more expensive. A cheaper piping option that allows to avoid impurities adsorption but provides a good adaptability to different shapes is to use copper tubes. Being a malleable material, it can be easily shaped as needed while keeping solid connections. Finally, when impurities are a minor concern, the easiest piping to handle is the plastic one, coming in different rigidities and with different material properties, the most common being polyamide, but always allowing quick and flexible connections.

Finally, when impurities are a minor concern, the easiest piping type to handle is the plastic one. Plastic pipes come with different rigidities and different material properties, the most common being polyamide (in the form of Nylon, Rilsan and Kevlar) and polyvinyl (PVC). While all of these allow quick and flexible connections, plastic is notably known for its permeability to air and humidity. In

particular, the use of PVC piping can imply a high humidity intake that could affect the gas mixture purity and therefore detector operation.

7.3 Gas mixture distribution

To correctly deliver gas mixture to the detectors two main variables should be considered: the gas pressure and the flow rate. The gas mixture pressure at the chamber level often plays an important role in the correct operation of the detector. Moreover, pressure variations can affect the integrity of the detector itself. It is therefore fundamental to regulate and monitor the pressure of the gas mixture inside the detector, as well as at its input and output. On the other hand, gas mixture flow is also important as it determines the velocity at which the gas is replaced within the detector volume, allowing to always have fresh gas reaching the chamber. This section illustrates how gas mixture can be distributed to gaseous detectors keeping these two parameters under control with a variety of tools suitable for a simple laboratory setup.

7.3.1 Flow measurement and regulation

The simplest and most common way of measuring the gas flow rate is the use of a rotameter, a device that measures the volumetric flow rate of the gas stream through a closed tube. Its working principle is the one of the so-called variable area meters, in which measurable effects are caused by the cross-sectional area variation in response to the variation of the flow rate. In particular, a rotameter is made with a tapered tube containing a weighted float that rises as the rate increases. When the weight of the float is balanced by the drag of the gas stream, the float position stabilizes in a position that, thanks to calibration procedures, gives the reading of the volumetric gas flow rate. Adding a simple flow regulation valve at the input of the device allows to combine the flow regulation with its analogue reading. Examples of a regulating rotameter are shown in Figure 7-4.

Given the working principle of the device, mainly based on gravity, one of its limitations is the fact that it has to be placed in a vertical position, with the gas stream flowing from the lower to the upper part of the tube. Moreover, the analogue nature of the measurement does not allow to obtain an very precise values, also considering the uncertainties introduced by the possible float oscillations and reading parallax errors.

Figure 7-4 Examples of Gas Flowmeters from Voegtlin
https://www.voegtlin.com/data/139-2017_en_infoQ-flow.pdf

While the rotameter working principle is based on the measurement of the volumetric gas flow rate, most other techniques to quantify gas stream velocity are based on the measurement of the mass gas flow rate. As already described in the previous section, Mass Flow Controllers are based on such working principle, and they can be used in their Mass Flow Meter version for gas distribution purposes. However, their relatively high cost makes them a less preferred choice for distribution, especially when, from a central supply source, the gas has to be delivered to multiple chambers separately. Alternative devices that can be used are Micro Electro-Mechanical System (MEMS) heat wire flowmeters, but they are only suitable for monitoring purposes and not for gas

flow rate regulation. This type of sensor measures the heat loss on the wire caused by the thermal convection generated by the gas stream in the device, with the heat loss being proportional to the mass flow rate. The sensor output can then be readout and converted into flow rate values through calibration curves. It should be kept into account that each different gas or gas mixture will have different calibration curves, and that most of the commercially available MEMS flow sensors provide standard calibration in air or N_2. To be used with other gases, as in most of the cases, the proper conversion should be applied to the sensor readout value.

7.3.2 Pressure measurement and regulation

The second parameter that needs to be properly regulated when distributing gas mixture is its pressure at the different stages of the gas system. As mentioned in the previous section, at the stage of mixture preparation the devices in use will determine a given pressure for the outgoing flow, normally around 500 mbar. If the chambers to which the gas mixture is distributed do not need particular pressure constraints, the standard way to go is to simply let the gas flow through the chambers and leave their gas output open to air. In this case, the gas pressure from the supply point will drop when encountering the different elements of the system (sensors, filters, …) until reaching the atmospheric pressure at the detector stage. When the detector needs to work in overpressure (with gas mixture pressure higher than atmospheric pressure), such condition could ideally be achieved by closing the output connection of the detector and regulating the pressure at its entrance. However, this does not allow to have any safety measure to avoid overcoming the desired relative pressure value and puts the chamber at risk of breaking if too high pressure is reached.

Different devices exist to prevent this to happen, the most common being safety valves and gas bubblers. Safety valves are simple devices equipped with a membrane that would open only if a pressure higher than a given value is applied, and they are normally installed in parallel to the main gas stream. Safety valves can be calibrated for the desired pressure value (starting from few tens of mbar), and once open they would let out gas until the pressure goes back below the threshold value. Gas bubblers are instead pieces of glassware, with single or double bulbs filled with a certain amount of fluid (distilled water or silicone oil). The input of the bulb is connected in parallel to the main gas line, in a position that could either be at the input or output of the detector depending on the specific requirements. The outlet of the bulb is instead vented to air. These devices act as one-way valves, preventing air from flowing backwards inside the gas system. Moreover, the gas would bubbler through the fluid before being vented to atmosphere, allowing a visual feedback on the gas actually flowing out of the gas system. The bubbler also allows to have a raw regulation of the system output pressure, that will be in overpressure with respect to the atmospheric level depending on the fluid level. Depending on the fluid density, the height level will be equivalent to a different overpressure, that correspond what it takes to push the gas bubble into the fluid (about 1 mbar per 1 cm in water or silicon oil).

Gas pressures can be measured both with analogue and digital devices; examples are shown in Figure 7-5. Analogue measurements can be realized with a simple manometer; manometer usually made with a thin flexible pipe curved into a circumference (or multiple windings). Depending on the pressure of the gas surrounding the pipe, it will assume a different curvature radius, with a directly proportional dependence on the relative pressure of the gas. The open end of the pipe is therefore fixed to the device, while the close end is left free to move and connected to a lever mechanism that amplifies its movement and translates it into the circular movement of a needle along a graduated scale. If a digital readout is needed, a pressure transmitter can be used. This type of detector can be based on different technologies, for example piezo-resistive ceramic sensors or other capacitive micro electro-mechanical systems. The sensor itself is housed in a case that allows to connect it in parallel to the gas line, therefore without interfering with possible pressure drops on the main gas stream.

Figure 7-5 Example of a Pressure Gauge (https://fdpp.com/articles/Anatomy-pressure-gauges.htm and of a ES Systems Pressure Sensors and Transmitters, https://esenssys.com/product/espp-mit1/

In cases where the chamber pressure needs to be stable at a specific value, pressure regulators are necessary. As described in the first section of the chapter for primary gas supply, analogue pressure regulators are widely available on the market and once the proper regulation range is chosen, they can be used also for gas mixture distribution purposes. Digital pressure regulators are available in the form of electronic pressure controllers. With a working principle similar to one of simple pressure transmitter, the digital pressure controllers can measure the relative or absolute pressure of the gas stream and regulate it with a dedicated control valve, adjusted by means of a Proportional-Integral-Derivative (PID) controller. The PID controller uses a loop control mechanism that calculates the error of the measured pressure with respect to the desired setpoint, and adjusts its output consequently. Both for analogue and digital pressure regulation devices, it should be noted that they are either set to regulate downstream pressure (standard pressure regulators) or to regulate upstream pressure (backpressure regulators).

Finally, the latest technology upgrades have made possible the realization of commercially available digital pressure controllers with integrated flow measurement. These devices allow to measure both pressure and mass flow rate of the gas stream and regulating it according to the variable more relevant in the specific application. The device working principle combines the ones of pressure and volumetric flow sensors, Figure 7-6. Thanks to the measurement of the two parameters, the device adjusts the internal valve position through a PID regulation, that can have as setpoint either a pressure or a volumetric flow value.

Figure 7-6 : Example of a Flow-Pressure Regulation device from Voegtlin https://www.voegtlin.com/en/mass-flow-meters-and-controllers-for-gases/red-y-smart-pressure-controller/

7.4 Gas mixture quality monitoring

Once a gas system is set up and running, it can be extremely useful to monitor the effective quality of the gas mixture delivered to detectors. This section illustrates some common techniques to quantitatively measure the gas mixture composition and monitor the possible presence of impurities.

7.4.1 In-line gas mixture composition sensors

A possible way to continuously monitor the concentration of a given component of the gas mixture is to use an in-line infrared (IR) or ultraviolet (UV) sensor. Such detectors consist of a source of light, with dedicated optical filters to select the desired wavelength in relation to the component one wants to detect. With the gas flowing through the sensor volume, part of the light energy is absorbed by gas molecules, and the amount of light remaining at the specific wavelength is measured. As the amount of absorbed light is directly proportional to the amount of the specific component present in the gas stream, its concentration can be accurately measured. These types of detectors often use two wavelengths: one used for specific gas absorption, and the other as a reference to compensate the dependence of the detector signal from environmental factors (temperature, humidity).

Gas components that can be measured with such technique, relevant for gaseous detectors operation, are typically CO_2, CF_4 and iC_4H_{10}.

Various factors should be taken into account when considering this type of detector, mainly influencing the calibration curve of the instrument. The first is the range of concentration of the component to measure, that should correspond to the range of values one expects to be measured by the device. Moreover, as the other gases present in the mixture can influence the absorption spectrum, it is fundamental to have a calibration curve realized with a gas mixture as close as possible to the one the device will be used for. IR and UV gas analyzers are characterized by quite low maintenance needs, though periodical punctual calibrations can help to keep their precision at good levels through time.

7.4.2 Gas mixture pollutants

The gas mixture quality can be undermined by the presence of impurities, some of which can be adsorbed for example from the release of detector materials or from air intakes due to non-tight gas connections. The presence of these impurities is in most cases relevant for detector operation, as they can affect detectors' signal formation or operating point.

The most common sources of pollutants are of course from air, specifically O_2, N_2, and H_2O from environmental humidity. Given its inert nature, N_2 cannot be measured with simple devices, while it can be detected and quantified with more complex techniques such as Gas Chromatography (see 7.4.3). On the other hand, O_2 and H_2O levels can easily be quantified with commercially available in-line sensors.

Common O_2 transmitters are based on the measurement of the electrical output generated by a chemical reaction, occurring in an electro-galvanic fuel cell. When the gas streams through the cell, O_2 molecules are dissociated, the created ions diffuse through the electrolyte and a lead anode is oxidized. The produced current is proportional to the partial pressure of O_2, allowing to measure its concentration in the flow streaming through the chemical cell. The transmitter can be controlled through a microprocessor, thus making it possible to set the desired measurement range and to perform calibrations. Figure 7-7 shows examples of oxygen transmitters.

Figure 7-7 Baker Hughes Panametrics Oxygen Transmitters
https://www.bakerhughesds.com/sites/g/files/cozyhq596/files/2020-01/ge_panametrics_oxy.iq_oxygen_transmitter_specifications_920-603d_ltr.pdf

The H_2O concentration can instead be monitored through the measurement of the gas stream dew point, defined as the temperature to which air needs to be cooled for water vapor to condense into dew (see Figure 7-8). Among other technologies, dew point transmitters make use of capacitive polymer sensors bonded with a resistive temperature sensor. The first is a capacitive sensor, with two water-permeable electrodes and a hygroscopic polymer middle layer. The capacitance across the electrodes changes with the amount of water adsorbed by the middle layer, allowing the sensor to measure humidity in terms of the amount of water molecules in the gas flowing through the sensor (RH, relative humidity). The temperature sensor measures the temperature of the polymer sensor itself. From the combination of these two values, the dew point temperature can be calculated with a microprocessor integrated in the device.

Figure 7-8 Vaisala Dew Point Transmitter
https://www.vaisala.com/sites/default/files/documents/DMT143-Datasheet-B211207EN.pdf

Beside those due to environmental pollution, other types of impurities can be created during gaseous detector operation caused by gas degradation phenomena. This is the case for detectors operated with fluorinated gases ($C_2H_2F_4$, CF_4) whose molecules are subject to break processes when exposed to high-rate radiation and in presence of high electric field. The release of highly reactive products could be critical as they could either create polymerized deposits or cause material etching that could compromise detector performance and accelerate aging processes. For example, if H_2O is present in the gas mixture, it can react with Fluoride components forming Hydrofluoric Acid,

which could corrode detector material or readout boards, compromising proper detector performance.

Fluoride-based impurities can be measured with an Ion Selective Electrode station (ISE) specific for the measurement of Fluoride (F^-) in solution, see Figure 7-9. The technology is based on the exchange of F^- ions between the sample under measurement and the solid-state inorganic membrane contained in the electrode body, which creates a measurable voltage difference. However, F^- ions first need to be collected from the gas sample under study. For doing so, the sample gas stream can be bubbled into a dedicated liquid sampling solution, where F^- ions are released. The properties of such alkaline solution-allow both to collect the ions from the gas stream and to keep constant the ionic strength of the sample making the electrode response proportional to the F^- ions concentration in the sample. It is important to remember that when performing such measurement, the measured quantity is the concentration of F^- ions in the sampling solution volume, and it does not represent the concentration of the impurity in the detector volume or the gas system. It however remains a useful quantitative measurement when comparing the presence of such impurities in various operation conditions.

Figure 7-9 Hanna Instruments ISE Station,
https://www.hannainst.com/hi4110-fluoride-combination-ion-selective-electrode.html

7.4.3 Gas Chromatography

If a full quantitative analysis of the gas mixture composition is necessary, the appropriate technology is Gas Chromatography (GC); a laboratory analysis allowing the separation and quantification in terms of concentration of the different components of a gas mixture (Figure 7-10). For gas components typically contained in gaseous detector mixtures, the technique of micro-GC is normally used, with a compact Gas Chromatograph built by integration of micro-fabricated components. The basic elements of the instrument are a micro injector, one or more analytical columns and dedicated Thermal Conductivity Detectors (TCDs). The gas mixture to be analyzed is inserted into the micro-GC through a micro injector, along with a pure known gas, the so-called carrier gas. As the gas sample enters the column, all the components are mixed and spatially close to each other. The separation is realized thanks to the material coating the inside surface of the column that reacts with different intensities (Wan der Waals forces) with different gas components. Some of the components will hence be more delayed in their flow through the column with respect to others, separating in this way the original gas mixture in terms of arrival times at the output of the column, where the TCD is located.

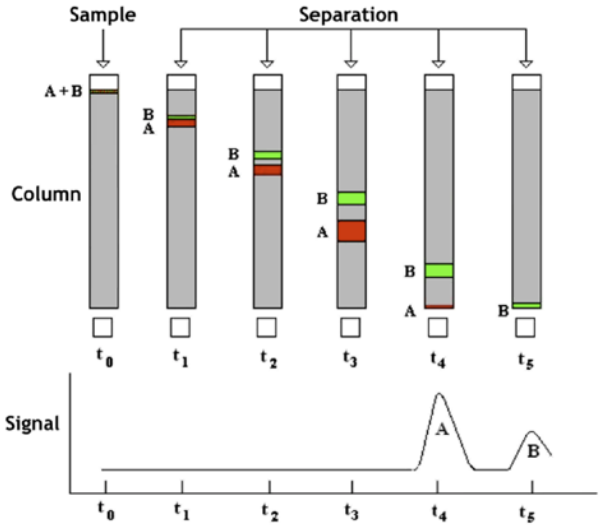

Figure 7-10: Schematics of a Gas Chromatography system.

The TCD is capable of sensing changes in thermal conductivity of the column stream, comparing it to the reference flow of the carrier gas. When the analytical flow contains components other than the reference, the heat capacities of the sample molecules cause fluctuations in the detector temperature producing a voltage signal. The TCD signal is amplified by the electronics and the final chromatogram is obtained, as a trend in time of the measured voltage variations. As the mixture components are separated in time by streaming through the column, a voltage variation (peak) in the chromatogram at a typical retention time will correspond to each component. An example of chromatogram is shown in Figure 7-11.

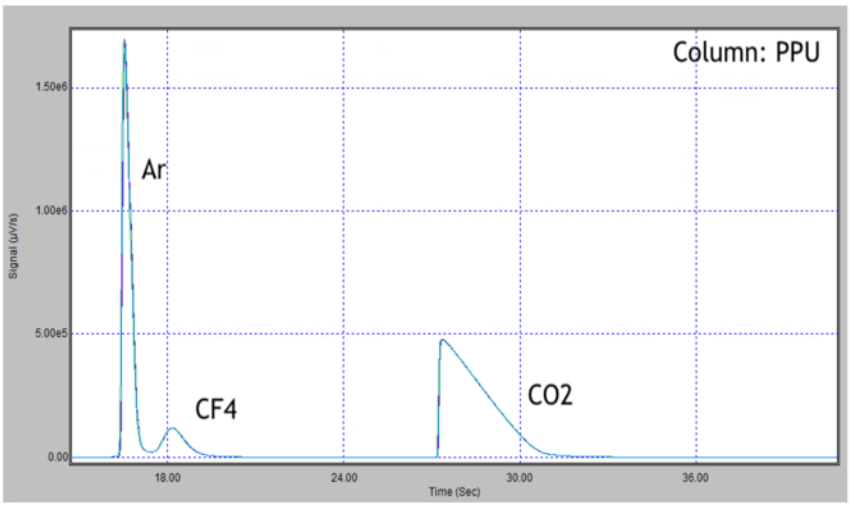

Figure 7-11 Example of Gas Chromatogram,
https://cds.cern.ch/record/2765846/files/CERN-THESIS-2021-036.pdf

The concentration of each component can be obtained calculating the area of the corresponding peak, that is proportional to their concentration following a calibration curve. It should be taken into account that the GC calibration curves are unique for every component and depend on the combination of column type and set of operational parameters. Moreover, the area dependence on the component concentration is linear only for low concentrations (< 20%), while it flattens for higher values. It is therefore fundamental to perform calibrations with dedicated samples containing the desired component in a known concentration to obtain a reliable conversion factor between peak area and concentration, and to ensure that the reference sample concentration is as close as possible

to the final value the instrument will be measuring. The micro-GC is capable to detect components with concentrations down to few ppm, with an accuracy of about 1% on the area value. However, given the characteristics of the calibration curve, it is more difficult to correctly quantify components in the higher concentration range (> 30-40%).

Many separation columns exist, differentiated mainly by the material coating their inside surface, and their choice depends mainly on the nature of the mixture components to be analyzed. Two specific columns are particularly suitable for characterizing gaseous detectors mixture composition:

- **PPlot U**:
  Made of Divinylbenzene/Ethylen-glycoldimethacrylate, designed to separate C1 to C4 hydrocarbons, CO_2, CF_4, H_2O, H_2S, SO_2. For common gaseous detectors mixtures, this column is capable of separating $Ar/CO_2/CF_4$ mixtures, as well as the typical RPC detectors gas mixture (SF_6, $C_2H_2F_4$ and iC_4H_{10}) and their relative impurities.
- **MolSieve**:
  5A zeolite molecular sieve, designed to separate H_2, He, CO, N_2, O_2. This kind of column is particularly useful for the analysis of gas mixture as it can well separate and quantify O_2 and N_2, typical pollutants coming from leaks and gas system components.

Together with the column coating type, several parameters should be considered to optimize the component separation:

- Column length: variable from 8 meters up to 30 meters, it determines the capability of separating in time different gas components, as the longer the column the more time the components have to be separated from each other. Such property is chosen when purchasing the instrument, as it should be determined by the components that one plans to analyze.
- Carrier gas: typical carrier gases are Argon and Helium, while Nitrogen and Hydrogen are less used. Helium is the most versatile carrier gas, as it can be used in most of the column-types allowing to have only one carrier for multiple columns.
- Column parameters: the operational pressure and temperature of the column are key parameters to obtain well-separated peaks, as they influence the intensity of the interacting forces between the sample molecules and the column material. They can normally be selected via software and optimized depending on the gas mixture to analyze.

If impurities at extremely low concentration need to be detected and measured, the Gas Chromatograph can be coupled with a Mass Spectrometer (MS). The gas sample flowing out of the GC, with components already space-separated, can be injected in the MS, where the sample is further separated according to the mass-to-charge ratio of each component. The detection power of the GC-MS technique reaches the level of tens of ppb, that for some gaseous detector application can already be significant enough to affect detector performance.

References

This section provides a collection of references, related to the information reported in the various sections of the Chapter, as well as a list of companies and resellers from which all the material quoted in the various sections can be found.

Section 7.1

Details on pure gases and pre-mixed cylinders classification and handling can be found at:

- Guidelines for Gas Cylinders Safety
  https://www.boc-gas.com.au/en/images/BOC%20Guidelines%20for%20Gas%20Cylinder%20Safety-AUSTRALIA-NO-RRP-FA-web_tcm351-82369.pdf

- Guide to Gas Cylinders
  https://www.worksafe.govt.nz/assets/dmsassets/WKS-4-Hazardous-substances-guide-to-gas-cylinders.pdf

Main gas suppliers and resellers in Europe:

- Linde, https://www.linde-gas.com/en/index.html
- Air Liquide, https://www.airliquide.com/
- Pangas, https://www.pangas.ch/it/index.html
- Multigas, https://www.multigas.ch/produits/gaz-specifiques/

Section 7.2

Mass Flow Controllers:

- Voegtlin,
  https://www.voegtlin.com/en/mass-flow-meters-and-controllers-for-gases/
- Bronkhorst,
  https://www.bronkhorst.com/int/products/gas-flow/controllers/
- Sensirion,
  https://www.sensirion.com/en/flow-sensors/flow-controllers-for-gases/

Piping and connections:

- Swagelok tubing and connections,
  https://products.swagelok.com/en/tubing-tube-accessories/c/800?clp=true
- Festo polyamide pipes and pneumatic fitting systems,
  https://www.festo.com/cat/en_IR/products_071000
- Rilsan piping by Alkema, https://www.zecspa.com/en/products/pneumatics/industrial-automation/rilsanr-pa11-sf

Section 7.3

Gas distribution components:

- Voegtlin Variable Area Flowmeters,
  https://www.voegtlin.com/en/variable-area-flowmeters-and-control-valves/va-flowmeters-v-100/#types
- Omron MEMS Flow Sensor,
  https://omronfs.omron.com/en_US/ecb/products/pdf/en-D6F_series_users_manual.pdf
- Voegtlin Battery Powered Digital Mass Flow Meters and Regulators,
  https://www.voegtlin.com/data/329-2017_en_infocompact.pdf
- First Sensor OEM Pressure Transmitter,
  https://www.first-sensor.com/cms/upload/datasheets/DS_Standard-CTE-CTU8000_E_11508.pdf
- ES Systems Pressure Transmitter,
  https://esenssys.com/product/espp-mit1/
- Bronkhorst Pressure Controller,
  https://www.bronkhorst.com/int/products/pressure/
- Voegtlin Digital Pressure Controllers with Integrated Flow Measurement
  https://www.voegtlin.com/en/mass-flow-meters-and-controllers-for-gases/red-y-smart-pressure-controller/

Section 7.4

References on Gas Analysis:

- Dew point sensing technologies, https://www.vaisala.com/sites/default/files/documents/VIM-GLO-IND-HUM-Dewpoint-sensing-technologies-App-note-B211092EN.pdf
- Fundamentals of Gas Chromatography, *https://www.agilent.com/cs/library/usermanuals/public/G1176-90000_034327.pdf* *https://www.youtube.com/watch?v=M8d1u7kFZe0*
- An introduction to Gas Chromatography - Mass Spectrometry, https://www.ucl.ac.uk/chemistry/sites/chemistry/files/gc_ms_mscaac_2018_1110_v9.pdf

Gas analysis devices:

- Emerson Binos Series Gas Analyzers, *https://www.emerson.com/documents/automation/manual-binos-100-series-analyzers-including-oxynos-100-hydros-100-cat-100-5th-ed-rosemount-en-69718.pdf*
- Vaisala Miniature Dew Point Transmitter, *https://www.vaisala.com/sites/default/files/documents/DMT143-Datasheet-B211207EN.pdf*
- Baker Hughes Panametrics Oxygen Transmitter, *https://www.bakerhughesds.com/sites/g/files/cozyhq596/files/2020-01/ge_panametrics_oxy.iq_oxygen_transmitter_specifications_920-603d_ltr.pdf*
- Hanna Instruments Fluoride Combination Ion Selective Electrode, *https://www.hannainst.com/hi4110-fluoride-combination-ion-selective-electrode.html*
- Thermo Fisher Scientific Orion Fluoride Electrodes Agilent GC Systems, *https://www.thermofisher.com/order/catalog/product/9609BNWP*
- Inficon Gas Analyzer, *https://www.inficon.com/en/products/micro-gc-fusion-gas-analyzer*
- Thermo Fisher Scientific GS-MS, *https://www.thermofisher.com/order/catalog/product/ISQ7K-VPI*

8 SIGNALS AMPLIFICATION AND RECORDING

Contributed by Hans Muller (CERN)

8.1 Charge detection

The number of electrons released by ionizing interactions in gaseous counters may vary between 10 fC to a few tens of pC where the charge unit 1fC corresponds to 6250 electrons. The gain of a detector should be chosen to match the dynamic range of the amplifier. Further, the detector capacitance, or the number of electrons produced per Volt of electronic potential, varies largely between detector types and electrode sizes between 10pF to 1nF. Amplifiers can measure this electronic charge in different ways, either copying it on an active capacitor and measuring the resulting voltage, or by measuring the current directly. The first method is used by charge amplifier, the latter by current amplifiers. In both cases the goal for best signal-over-noise ratio is to transfer a maximum of the charge from the detector capacitance to the amplifier input in real time without added time constants. For charge amplifiers this is achieved with the amplifier input appearing as a capacitor of much higher value than the detector capacitance with the corresponding charge transfer ratio. In the case of current amplifiers the input capacitance is very low, hence the input impedance should be as low as possible in order to discharge the detector capacitance. In both cases the ideal case can only be approximated in that charge losses and non-ideal time constants may limit the quality of the measurement. The principle current and charge amplifiers is depicted in Figure 8-1.

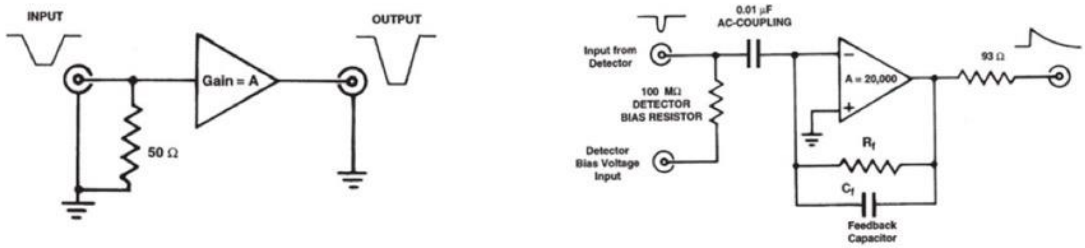

Figure 8-1 Left: Schematics of the current-amplifier. Right: principle of the charge-sensitive preamplifier (ORTEC, 1991).

With advances in amplifier technology and careful design rules, it is however possible to measure weak charges down to 1/10 fC, provided the noise contribution from the detector and the interconnections is not superior. The detector noise consists of series noise, increasing quadratically with detector capacitance and the parallel thermal current noise of the resistors in the bias and termination networks. In general, low noise detectors have a low detector capacitance. The addition of bandpass filters after the signal preamplifiers suppresses a most of detector noise by selecting a bandpass frequency that passes the essential signal frequency in a narrow frequency band suppressing non-essential noise parasites around the signal. The bandpass frequency f_s corresponds to a shaping time constant $\tau_s = 1/(2p\ f_s)$ which relates to the peaking time of the semi-gaussian output signal as $\tau_p = n\ \tau_p$ where n is the order of the filter.

Multichannel ASICs like the VMM implement a 3rd order shaper, other ASICs provide 2nd or 4th order shaping. The optimal peaking time at the noise minimum increases with detector capacitance; the best way to find the optimum is found connecting a spectroscopy amplifier with variable peaking times and measuring the relative noise as function of peaking time. A simpler way to measure relative noise levels is via DAQ software integrated S-shape algorithms. The measurement of pulse-height spectra of a ^{55}Fe source is used as standard to compare values of the relative noise comparing to the FWHM of the 5.9 keV main peak. Absolute noise measurements are considerably more difficult to implement and require elimination of all parasitic noise sources including ground loops, pickup, and supply filtering.

8.2 Detector signals

For best amplitude and time resolution, the electronics should match the properties of the detector. Table 8.1 shows typical parameters of radiation and particle detectors. Multichannel ASICs designed for the readout of specific detector types are available with matched properties but normally also provide adaptable parameters allowing to use them for readout of a wider range of detectors.

	Detector gain	Dynamic range [fC]-[pC]	Signal source	Signal	Polarity	Rate capability	Intrinsic risetime and duration (ns)	Detector capacity [pF]	Detector type
GEM, N-stages	N x 10^3	1-1	Hi-Z anodes	Avalanche N stages	(-)	> MHz/cm^2	10 -50	~ size 50-500	MPGD
uMEGAS strips	10^3-10^4	1-2	Hi-Z anodes	avalanche drift and gap	(-)		1 (e-)- 40 (I)	~ size 20-1000	MPGD
uMEGAS mesh	10^2 (tbd)	10-10	Med- Z mesh	Induced	(+)	-	10-50	~ surface 500-10000	MPGD
RPC	10^6-10^7	10-100	V-Hi-Z	Resistive Geiger	(-)	100 Hz/cm^2	0.3 -5	tbd	gas
Psec	10^6	1-100 1pe - 100pe	Hi-Z anode	cathodic electrons	(-)	-	0.05-10	20-50	MPGD

Table 8.1: Signal types and properties of gaseous detectors.

Figure 8-2 shows a charge sensitive preamplifier produced by ORTEC (ORTEC, 2020) that can be used with low capacitance detectors, some models offer equivalent noise down to a few keV. For detector performance studies, the preamplifier outputs can be shaped with crate-based amplifiers and directly recorded or discriminated for counting.

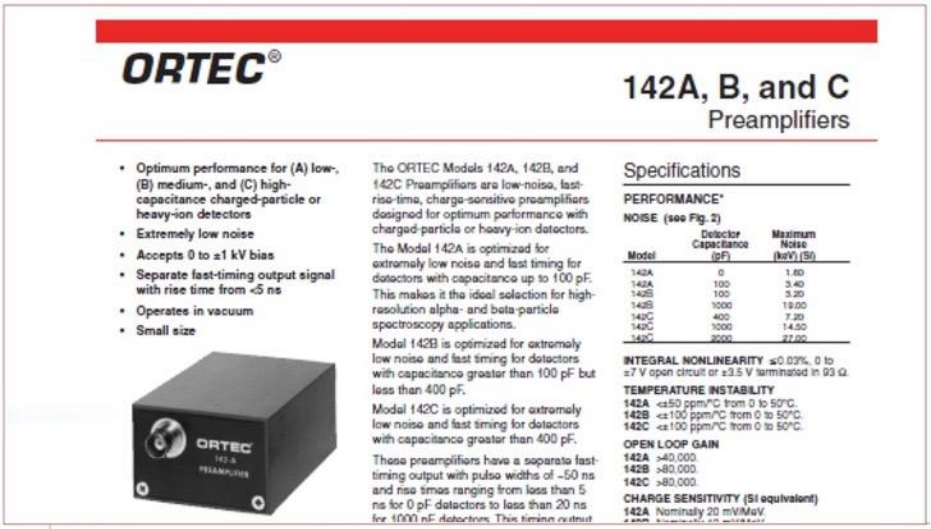

Figure 8-2: ORTEC Charge Preamplifier model 142.

Whilst single-channel amplifiers are indispensable for research and test of detectors, the readout of MPGD's requires a large number of channels, hence a large number of amplifiers with the corresponding readout and digitization scheme required for the readout and processing of the data in computers.

For this purpose the RD51 collaboration developed the scalable readout system (SRS) whose basic components are shown depicted in Figure 8-3. From left to right, the figure shows a small GEM detector equipped with 128 channel hybrids, linked to electronic frontend concentrator cards (FECs) transmitting formatted events to a computer for data analysis.

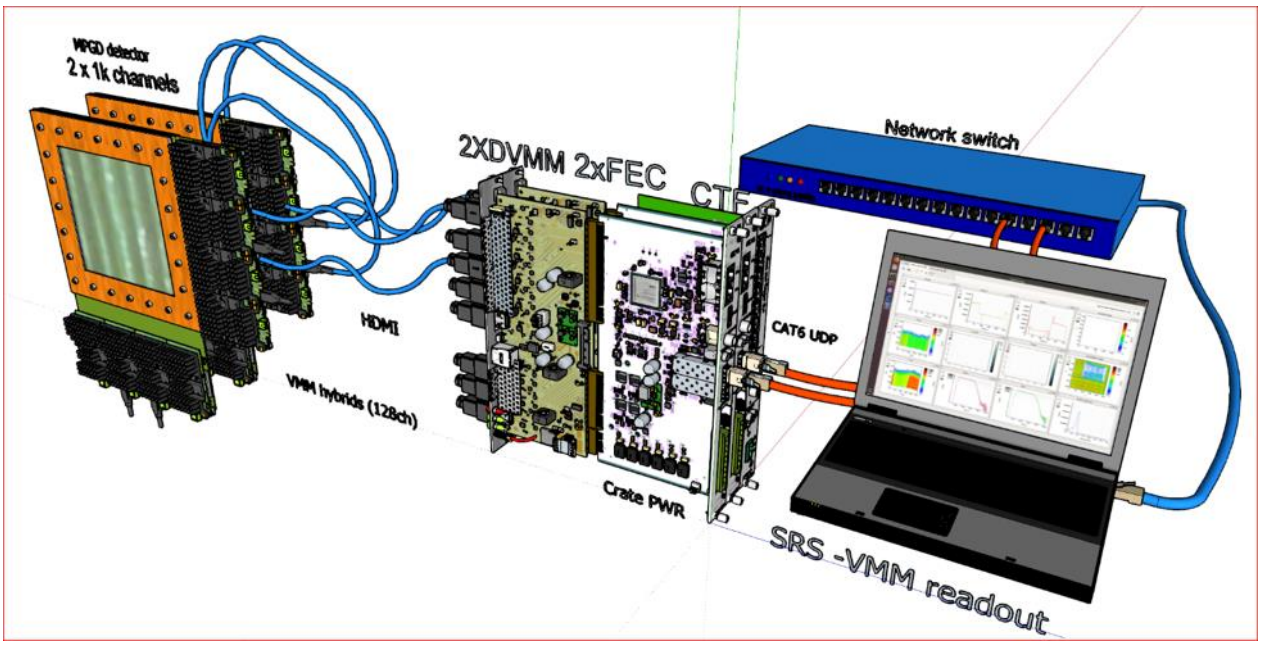

Figure 8-3: SRS readout system.

A series of detector-pluggable hybrids with128 channels of charge preamplifiers integrated into custom ASICs have been designed and commissioned for SRS since 2010 as a baseline support for the MPGD community. These hybrids are known as APV or VMM3a according the names of the ASICs integrated on 128 channel carrier cards. The picture in Figure 8-4 shows a 128-channel VMM hybrid carrying two VMM3a ASICs **(**VMM) for a total of 128 channels.

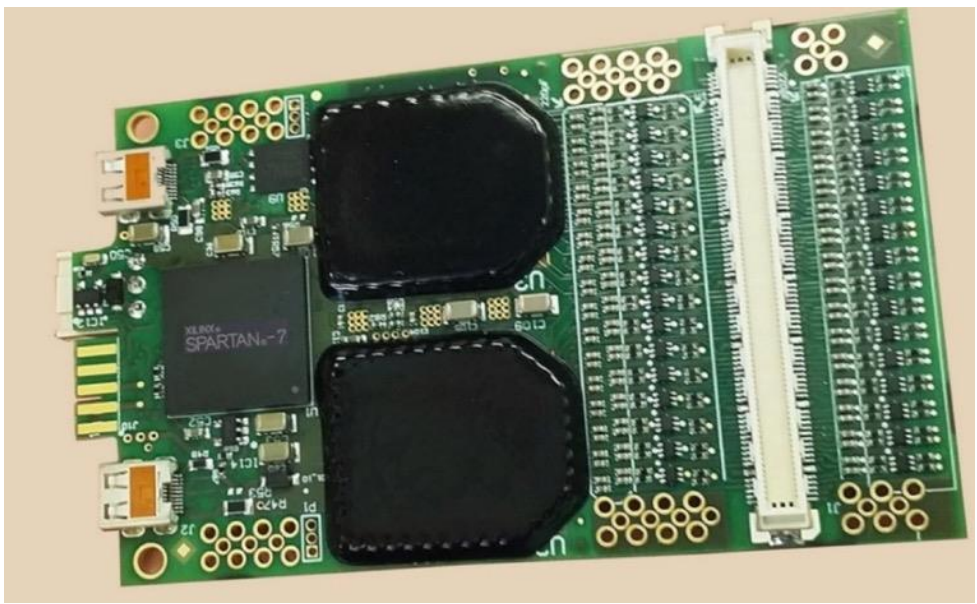

Figure 8-4: The 128 -channel hybrid carrier with two VMM3a ASICs and the 140 pin HRS connector for MPGD's [srstechnology.ch].

Hybrid circuits integrate all electronics required for a 'detector frontend': readout ASICs, spark protection, connectors, voltage regulators, readout link interface (FPGA), test connectors, sensors for voltages and temperatures and the connectors for readout links (u-HDMI in this example). Further information about SRS readout with the VMM frontend can be found in the Indico pages of the RD51 collaboration. For high-rate applications up to the MHz range the VMM3a hybrid is the preferred choice (VMM3a).

8.3 ASICs for detectors

Table 8.2 summarizes the multichannel ASICs presented in the 2021 RD51 Topical Workshop on FE electronics for gas detector (ASIC workshop). More readout ASICs are in preparation following the requirements of future large-scale detectors with ever advancing state-of-art technologies.

Name	Exp	Detectors	£Ch	Shaping	Noise	Range [ke]	Input signal	Pol.	ADC [#bits]	fs [MHz]	P/ch [mW]	Feature	Technology	Radhard
AFTER	T2K; T2K upgrade	TPC, micromegas end-plate	72	50-1000	(350-1800)e +(22-1.8)e/pF	4 ranges: 750/1500/2250/3800	current	both	external 12-bit ADC	1 to 50 SCA sampling	8	SCA	0.35 µm CMOS	N.D.
AGET	ACTAR, AT-TPC, SπRIT	MGPD+DSSD	64	25-500	(435-34000)e +(19-7.4)e/pF	4 ranges: 750/1500/6240/62400	current	both	external 12-bit ADC	1 to 100 SCA sampling	10	SCA; Triggerless; selective readout	0.35 µm CMOS	N.D.
DREAM	CLAS12	MGPD	64	25-450	(394-2140)e + (10-0.34)e/pF	4 ranges: 312/624/1248/3744	current	both	external 12-bit ADC	1 to 50 SCA sampling	10	SCA; Trigger	0.35 µm CMOS	N.D.
GEMROC	(Client under NDA)	GEMs	64	30-200	N.D.	1fC -> 500fC	charge	negative	N.D.	40MHz	1mW	//	0.35 SiGe	N.D.
HARDROC3	ILC CALICE sDHCAL	RPC	64	50-150 (Q) 20 (T)	N.D.	10fC -> 50pC	current	negative	N.D.	50MHz	1mW	Zero Suppression	0.35 SiGe	N.D.
PADI-X	CBM	RPC, Diamond, Straw Tubes, Silicon, Micro-Channel Plates, Channel Electron Multiplier, Scintilation, PMT	8	0	N.D.	1 fC - 2 pC	current	pos/neg	external	//	16.8	Setable Input impedance: 50 - 400 Ω	CMOS UMC-180 nm	2.4
PADI-XI	CBM	//	8	2.5-17	N.D.	1 fC - 2 pC	current	pos/neg	external	//	22	Setable Input impedance: 18 - 250 Ω	CMOS UMC-180 nm	2.4
PADI-XII	for future experiments	//	8 or 4 channels	2.5-17	N.D.	1 fC - 2 pC	current	pos/neg	external	//	24 for LED / 32 for PSA	Setable Input impedance: 18 - 250 Ω	CMOS UMC-180 nm	2.4
PETIROC2	CMS Muon	RPC (was designed for SiPM)	32	25-100 (Q)	N.D.	1mV (~1pe)	voltage	both	10 bits	N.D.	6mW	//	0.35 SiGe	N.D.
SAMPA_v4	ALICE	TPC-GEM / MCH-MWPC	32	160/320	550e+25e/pF	400/600 (@160ns) 3100 (@300ns)	charge	pos/neg	10 bits	10 MHz	20	Z.S. Baseline correction. Huffman.	130 nm	N.D.
SAMPA_V5	sPHENIX	TPC-GEM	32	80/160	550e+25e/pF	400/600	charge	pos/neg	10 bits	10/20 MHz	20	Z.S. Baseline correction. Huffman.	130 nm	N.D.
STAGE	HARPO	MGPD+DSSD	64	25-4000	(435-34000)e +(19-7.4)e/pF	4 ranges: 750/1500/6240/62400	current	both	external 12-bit ADC	1 to 100 SCA sampling	10	SCA; Triggerless; selective readout	0.35 µm CMOS	N.D.
STS/MUCH-XYTER2.2	CBM Experiment at FAIR	Microstrip silicon detectors at Silicon Tracking System, GEM detectors at Muon Chamber	128	90-260	550e+25e/pF	624ke with for GEM, 75ke for Silicon	charge	pos/neg	5	continuous-time	10	BaselineCorrection / PeakFinding	UMC 180 nm CMOS	N.D.
VMM3a	ATLAS	New small wheel, sTGC, Micromegas	64	25-200	depends configuration	2pC at 0.5mV/FC, in linear range	charge		3 ADCs per channel, 10b, 8b, 6b	200ns conv. time	~11mW	data driven, Baseline stabilization, neighbouring logic, fast digitisation, Peak Finding, timing information, and many more	130nm GF	>300kRad
WASA	CEPC	TPC, GEM	16	160	533e +9.1e/pF	748.8	charge	negative	10	100M max.	2.33	direct waveform output	65nm CMOS	N.D.

Table 8.2: Readout ASICs in 2021. For more details see (ASIC workshop)

8.4 R&D with detector signals

The development of new detector technologies requires the understanding of detector signals "at the root" in order to apply the best adapted technologies and choose the correct parameters for best resolutions in space, time and amplitude. R&D activities on detectors concentrate on a few detector channels using fast oscilloscopes with integrated signal processing. Linear, very high BW preamplifiers connected to detector anodes or cathodes preserve the signal shape and represent the most direct probe for studying the signal dynamics of a given detector. Active oscilloscope probes should however not be directly connected to a gas detector as they are not spark immune and rarely have the required gain of O(40dB). Alternatively, charge-integrating amplifiers like the above mentioned ORTEC 142 provide a direct measure of the electronic charge in less demanding time-domains like 25 ns. The results obtained from small-scale research on raw signals may lead to specific implementations which can get integrated in multi-channel ASIC projects. The increasing requirements of experiments drive a permanent evolution of specialized readout ASICs, which moves towards higher resolutions in time and energy, higher readout rates and higher channel densities.

8.5 Linear amplifiers

For discrete amplifier implementations, industrial wideband amplifiers (WBA) with 50 Ω signal termination are available off-the-shelf with a gain-bandwidth-product (GBP) up to 8 GHz. Commercially available development cards may be used as linear pre-amplifiers to investigate MPGD signals and their properties. With detector charge signals in the range O(1-100fC) and durations of O(1-80ns), concatenated WBA amplifiers achieve a sufficient gain of O(40dB) for output voltage levels which can be viewed and processed on oscilloscopes.

Figure 8-5 shows an 8 GHz WBA amplifier LMH5401 card of Texas Instruments with fixed 20dB gain (=V/V gain 10) and with two concatenated amplifiers; a gain of 40dB (V/V =100) is obtained. The screenshot from an irradiated 10cm x 10cm GEM shows a symmetrical differential signal amplitude of O(10 mV) with a time envelope of 15ns. Equipped with input termination

resistors, WBA's are like current amplifiers (H.Uhrmann, W.Gaberl and Zimmermann, 2008) in the sense that the detector current is measured over 50 Ω termination resistors. More dedicated, low-noise current amplifiers with tailored input impedances and matched gains are implemented in some recent multichannel readout ASICs.

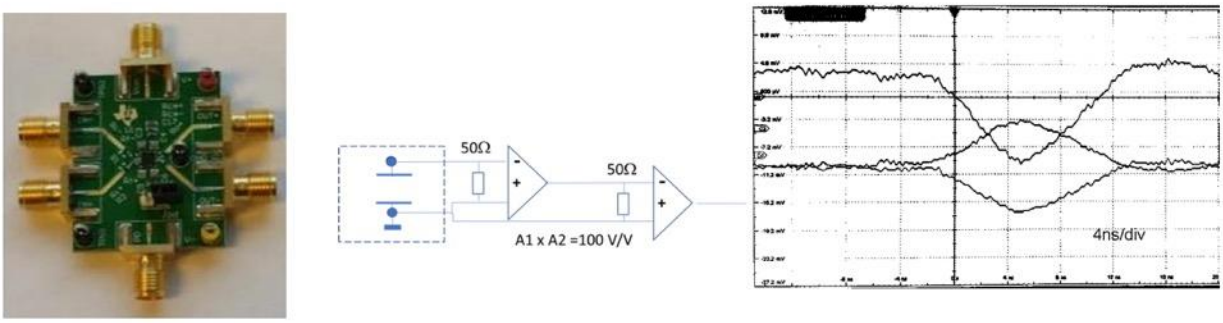

Figure 8-5 Left: WBA card LMH4501EVM. Center: dual stage current amplifier gain =100. Right: amplified GEM signal.

8.6 Signal types

Figure 8-6 is the photo of dual stage THS4501 WBA amplifiers of 2 GHz bandwidth, built in 2012 in the CERN gaseous detector laboratory for monitoring charge signals on 4 neighboring Micromegas detector channels. The persistence screenshot shows fast electron peaks with risetimes around few ns followed by slower, ion-induced signal with an envelope of around 60 ns.

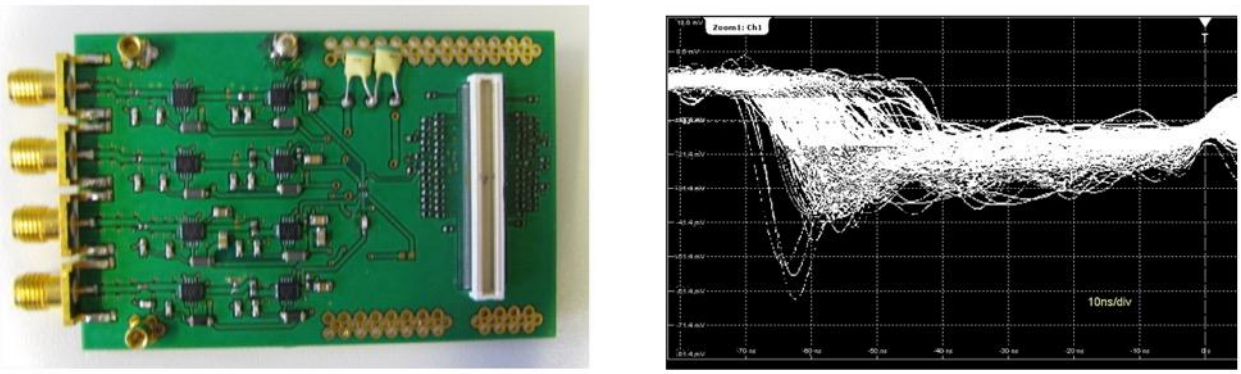

Figure 8-6: Left: quad WBA amplifiers pickup for MPGDs 2GHz V/V-100. Right: Persistence recording of Micromega electron-ion signals.

To interpret such signals a crude approximation is applied: the average 25mV amplitude over 50Ω with a gain 100V/V for an approximated rectangular pulse equivalent indicates $I_{in} \sim \Delta Q/\Delta t$ = 5uA. Multiplication with Δ_t= 60 ns yields ~300 fC pulse charge. With an estimated detector gain of 10^4 this would correspond to 0.03 fC for O(187) primary electrons released in the Micromegas drift gap operated with Ar-CO_2 and a SR^{90} electron source.

The measurements shown demonstrate fundamental differences in the footprint of the charge signals between the two mainstream MPGD detector types. For a given MPGD detector type, variations require better understanding the signals before the choice of the appropriate electronics.

8.7 Charge amplifiers

The CSA Charge Sensitive Amplifier (Spieler) depicted in Figure 8-7 converts the charge ΔQ_d produced on the detector capacitance C_{det} into Voltage steps of amplitude U_0 (Fig 7b). Sensitive for charge signals below 1/10 fC, these amplifiers have the acronym CSA for 'charge sensitive amplifier', with the property to discharge the detector capacitance onto the CSA's effective input capacitance, which is physically the feedback capacitor C_f multiplied by the very high open loop

gain A of the amplifier. The effective, very high input capacitance of O(10nF) also makes CSA's largely insensitive to occasional sparking.

Provided the duration of ΔQ_d is less or equal the risetime of the amplifier, the CSA produces a voltage step of opposite polarity to the input charge polarity. State-of-the art amplifiers chips like OPA657 (Texas Instruments), provide output risetimes below O(1 ns). If the ΔQ_d duration is longer than the amplifier risetime, the output signal risetime is dominated by the duration of the detector signal:

$$U_{0out} = -[\ 1/C_f\ ]\ \Delta Q_d$$

This relation defines the CSA charge gain $g = -\ 1/C_f$.

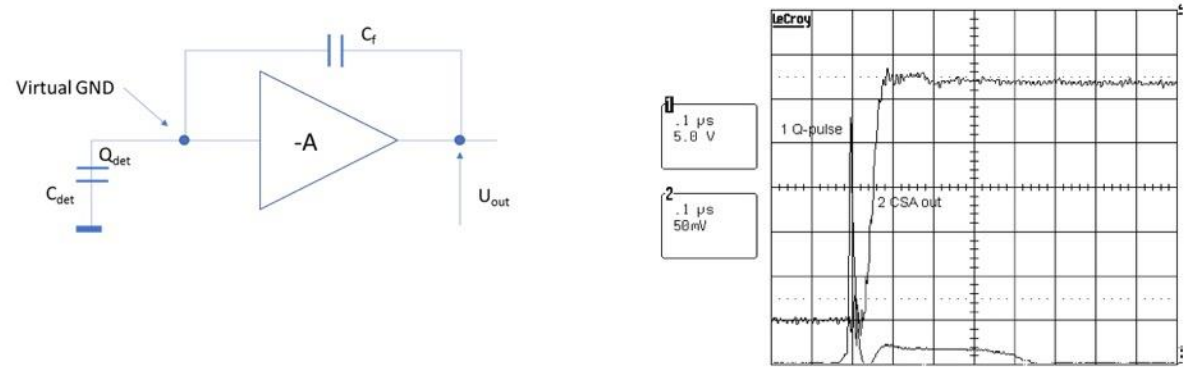

/

Figure 8-7 Left: charge-to-voltage conversion via CSA preamplifier. Right: Voltage step response to a test charge pulse (inverted polarity).

The charge gain *g* is usually measured in mV/fC since the feedback capacitor C_f which defines the gain is of O(1pF). A simple explanation for charge-to-voltage conversion is that the feedback capacitor is virtually grounded at the negative input of the amplifier and, due to an extremely low input bias current, practically 100% of the charge ΔQ_{det} flows onto C_f. With U=Q/C the output Voltage is

$$\Delta U_{out} = -\Delta Q_d / C_f\ .$$

8.8 CSA pileup

The pre-amplifier output voltage step ΔU_{out} is usually transferred to a precisely tuned bandpass filter circuit (shaper) which generates a semi-gaussian and noise-cleaned time envelope signal. In order to discharge the pre-amplifier step output voltage for the next charge measurement, the standard method is to discharge the capacitor C_f via a parallel-connected, high-ohmic discharge resistor R_{dis} (Figure 8-8). As a result, the pre-amplifier is exponentially discharged with a time constant $T_{dis} = R_{dis}\ C_f$:

$$U(t) = U_{out}\,[1-\exp(-t/R_{dis} \cdot C_{dis})$$

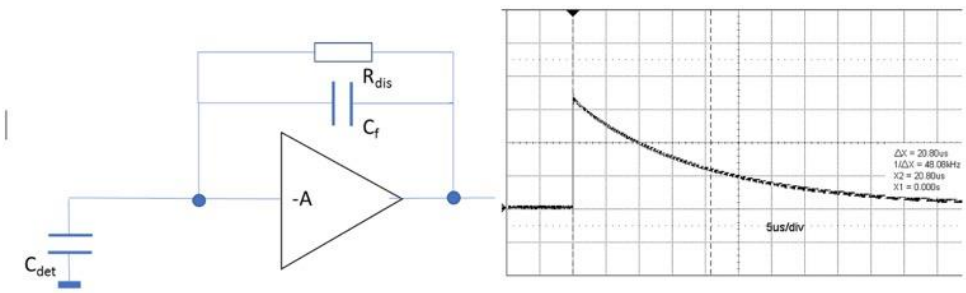

Figure 8-8: Left: charge sensitive preamplifier with discharge resistor R_{dis}. Right: output voltage decay of a charge preamplifier.

Subsequent charge signals can be over-imposed on the previous, generating pileups as shown in Figure 8-9. Pileups beyond the 1/e of time-constant T_{dis} are statistically negligible since the maximum dynamic range limit is normally not overpassed and the shaper circuit after the CSA only

extracts the individual semi-gaussian shapes from each CSA signal step (Statistically, the maximum rate of an RC-discharged charge amplifier is $f_r = 1/ (R_{dis} C_f)$.

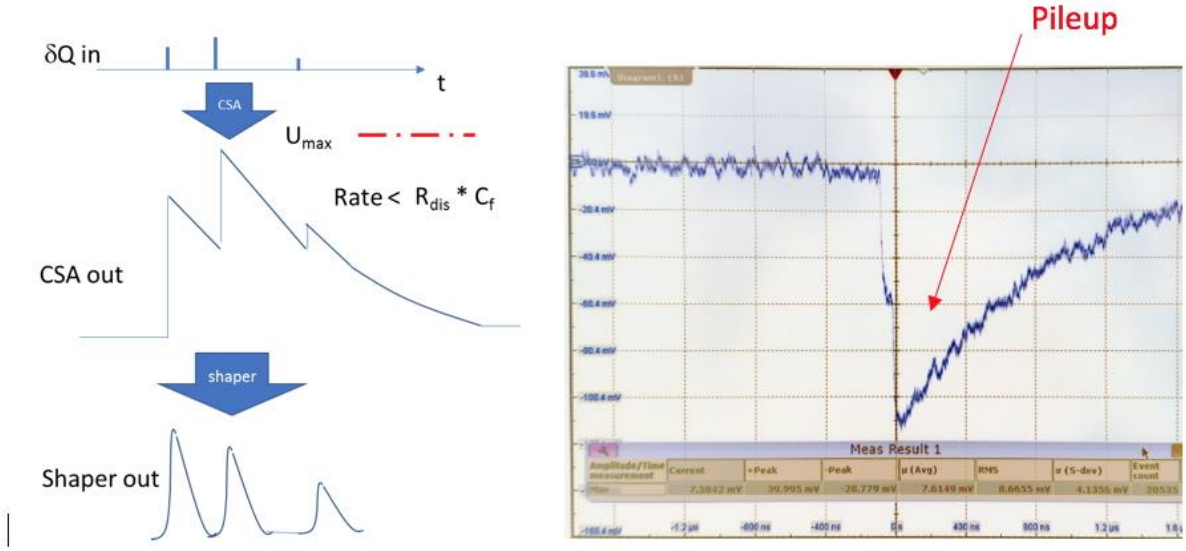

Figure 8-9 *Left: CSA pileup below the dynamic range limit. Right: pileup of 2 successive charge signals.*

8.9 Dynamic range

The dynamic range of an amplifier is given by the charge gain g and maximum linear Voltage U_{max} of the output signal swing. With $g = 1/C_f$ and a maximum linear output signal U_{max}, the dynamic range is

$$Q_{dyn} = U_{max} / g$$

As an example, for a CSA built with a preamplifier having a maximum linear output voltage U_{max} = 4V and with a charge gain set to g= 1mV/fC, the linear dynamic range is Q_{dyn} = 4pC. In practice, U_{max} may also be limited by the maximum voltage of a subsequent shaper circuit if the shaper gain is selected too high.

8.10 AC Coupling

In many practical cases, AC coupling between a DC-biased detector electrode and the 'virtual GND' input of the amplifier is unavoidable, Figure 8-10, in particular to separate DC Bias voltages from the amplifier inputs. AC coupling may not be needed for example for pickup of detector meshes which are grounded with typically a 50 Ω resistor.

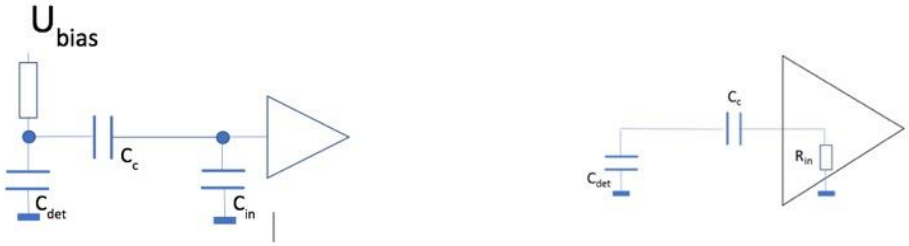

, Figure 8-10 Left: AC-signal coupling for DC-biased detector electrodes. Right: input time constant $C_c * R_{in}$.

The AC coupling capacitor C_c is effectively connected in series with the detector capacitance C_{det} such that the effective detector capacitance $C_{det,eff}$ becomes

$$C_{det,eff} = (C_c C_{det}) / (C_c + C_{det})$$

By choosing $C_c >> C_{det}$ the charge transfer from C_{det} to C_{in} is close to 100%.

8.11 Signal shapers

The signal-over-noise ratio of the preamplifier output can be improved by passing the CSA signal through a bandpass filter (shaper) which retains a narrow passband around a native signal frequency f_s and suppressing all frequencies below and above. Shapers transform the voltage steps generated by a CSA into a semi-gaussian signal shape with a defined peaking time t_p and a peak voltage proportional to the input charge (Figure 8-11).

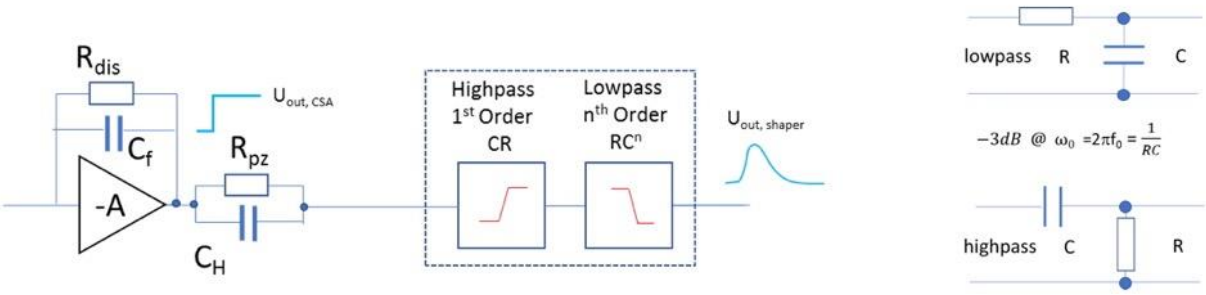

Figure 8-11 Left: charge preamplifier followed by a shaper filter of order n. Right: RC and CR filters.

CR-$(RC)^n$ shapers consist ideally of concatenated RC and CR filters; in practice, each RC or CR element needs to be connected to an high-impedance amplifier to maintain its characteristics. CR filters stand for signal differentiators and RC filters for signal integrators. Their frequency-dependent transfer is characterized by the -3dB point in the logarithmic power transfer diagram and corresponds to a RC time-constant

$$RC = 1/ (2\pi f_s)$$

For a CR $(RC)^n$ shaper the time constant of both filter elements needs to be equal. This constant is called shaping time τ_s and corresponds to the bandpass frequency f_s:

$$\tau_s = 1/(2p f_s)$$

Figure 8-12 shows the shaped output of a combined CSA-shaper signal as response to a very fast input test charge. This circuit is implemented in discrete logic with state-of art chips in the uAPIC (H. Muller, 2022) pickup amplifier box, designed for detector R&D. The CSA has a default charge gain of 4mV/fC and the 2nd order shaper has a default peaking time of 18ns. The superimposed $\Gamma_2(t)$ function in the figure hand-fit demonstrates that shaper signals can be fitted with the underlying mathematical function as a basis for recalculating the input charge from the peak and the signal time from the interpolated peak time.

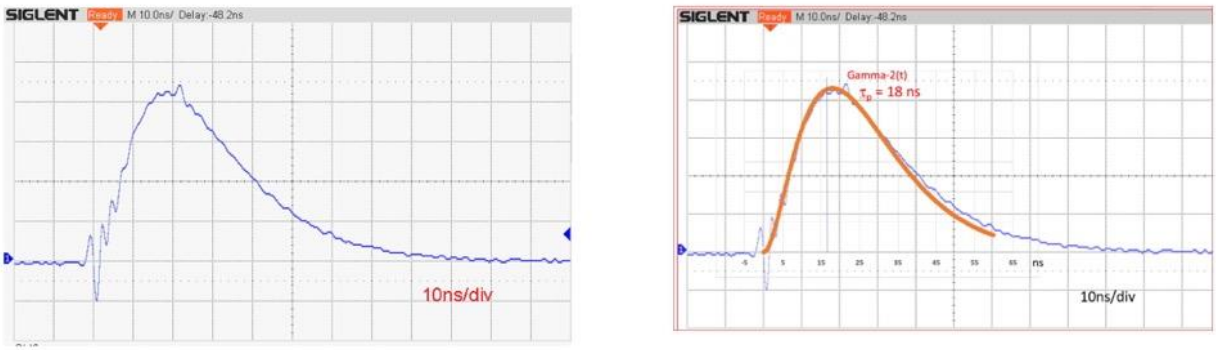

Figure 8-12 Left: shaper output with τ_p =18 ns. Right: Superposition $\Gamma_2(t)$ with τ_p =18ns.

8.12 Shaper implementation

The mathematical formalism that guides the design of a CSA-CR RC^n amplifier can be broken down in a sequence of operators which amplify and shape an ideal delta(t)-like charge input δQ. With this, the electronics from CSA input to shaper output can be represented as a chain of Laplace

operators with variable 's = iωRC' to represent RC filters and 1/s representing an ideal CSA amplifier's property to convert a delta(t) charge into a step(t) function:

$RC \Rightarrow (s\tau_0)/(1+s\tau_s)$

$CR^n \Rightarrow [1/(1+s\tau_s)]^n$

Based on this transformation technique, almost exact equivalents of n-th order CR*RC^n shapers can be implemented also in discrete electronic logic. Shaper implementations in ASICs may be less precise due to compromises required with large chip capacitors and the limited on-chip real-estate.

The implementation of a δQ -> CSA -> CR RC^n signal processing chain with an n-th order filter is represented by the Laplace operator (W.M. Sansen, 1990):

$$H_{shaper}(s) = Q \frac{1}{C_f} \left[\frac{\tau_s}{1+s\tau_s}\right] \left[\frac{A}{1+s\tau_s}\right]^n$$

with the CSA open loop gain A, charge-gain g = 1/C_f and shaping time τ_s .

The re-transformation of H(s) into the time function V(t) returns a Gamma(t) function of order n:

$$V(t) = \frac{n^n Q \cdot A^n}{n!\, C_f} \cdot \left[\frac{t}{\tau_p}\right]^n \cdot e^{-n\frac{t}{\tau p}} \qquad \text{with peaking time } t_p = n\, t_s$$

Electronics built according the above rules was implemented in many experiments.

Figure 8-13 depicts on the top the negative going CSA step voltages produced by varying the detector input charges δQ . The bottom traces are the corresponding, shaped signal outputs of a 2nd order shaper implemented in discrete electronics according the above rules. The timewalk of the peak over the dynamic range is minimal, confirming the mathematics of the Gamma(t) function that the peak is amplitude inependent. On the left, the figure shows a screen picture of a 2nd order shaper of the Alice EMCal Calorimeter (*ALICE Addendum to the technical proposal Electromagnetic Calorimeter*, 2006) with a Γ_2(t) fit over a 2nd order shaper signal to derive the best signal amplitude and time demonstrating how close data and shaper mathematics can be matched.

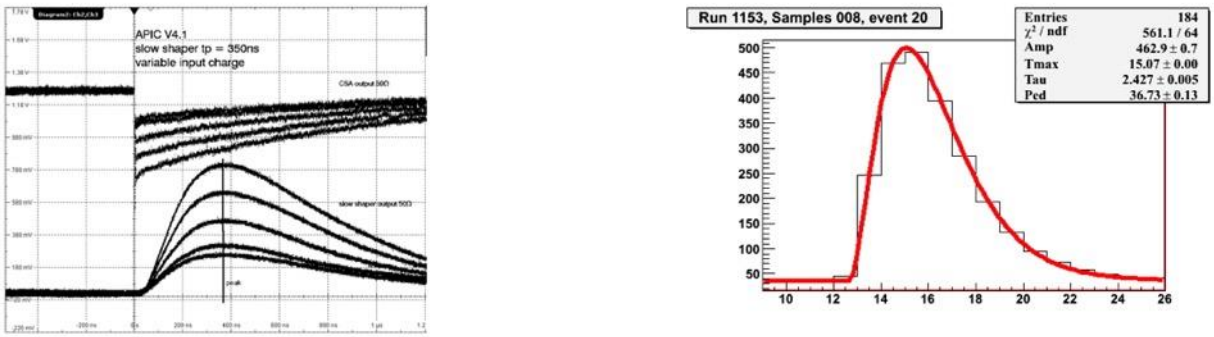

Figure 8-13 Left: CSA and shaper output for different charge inputs. Right: Fit of a 2nd order shaper with Γ_2(t) function.

Shapers of order n=2 can be easily implemented in discrete electronics with a time signal corresponding to

$$\Gamma_2(t) = \frac{2Q\,A^2}{C_f} \left[\frac{t}{\tau_p}\right]^2 e^{-2\frac{t}{\tau p}} \qquad U_{peak,n=2} = Q\, 2g\, A^2$$

The measurement of the peak amplitude requires either a peak finder that keeps the signal peak level long enough to allow for a fast digitization via an ADC, or SCA waveform storage cells which store the analogue samples of the waveform for a subsequent digitization after readout.

8.13 µAPIC preamplifier-shaper

R&D activities in 2021 on MPGDs in the Gaseous Detector Lab at CERN inspired the design of a portable and battery-operated CSA-shaper baptized uAPIC and implemented following the techniques described in the previous chapters for CSA amplifiers and 2nd order shapers. uAPICs will be commercially available in 2022. Built with state-of-art technology the uAPIC was used in the October 2021 test beam exposures at CERN to amplify the signals from a picosec MPGD detector with preamplifier gain of 4mV/fC gain and a 2nd order shaper with 18ns peaking time. Figure 8-14 depicts the uAPIC box with its connection possibilities.

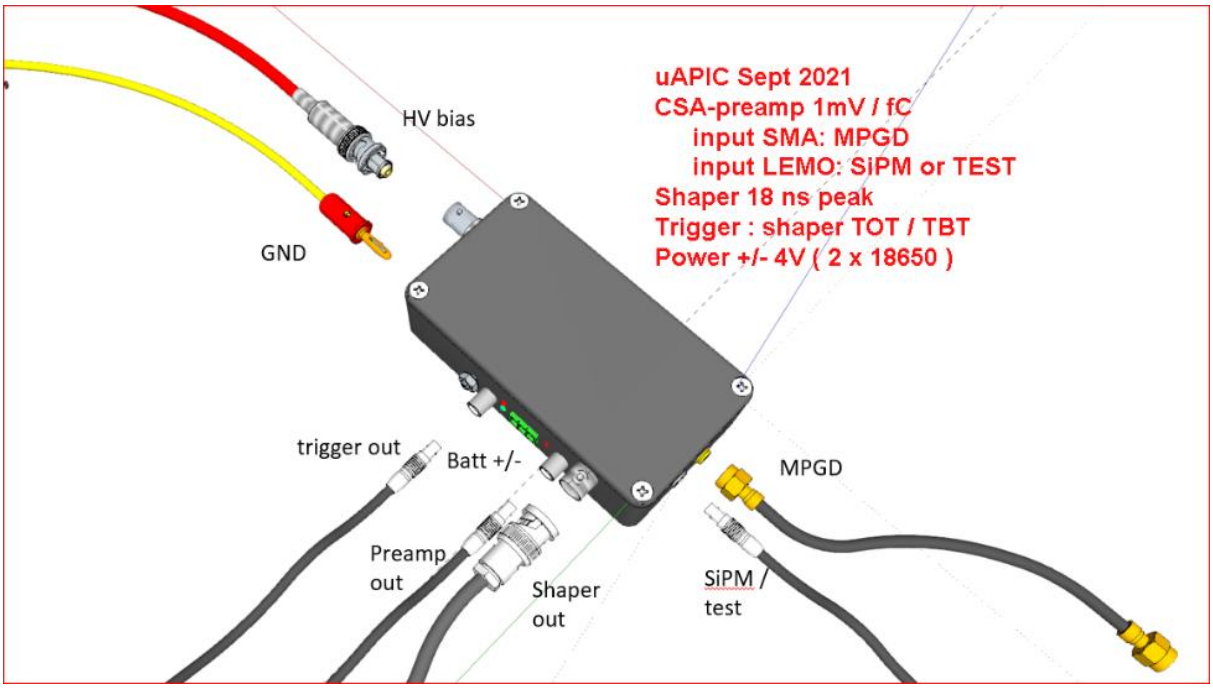

Figure 8-14: uAPIC preamp-shaper box connectivity.

The properties of uAPIC are summarized in Table 8.3. Other values than the default 18 ns peaking time and default gain of 4mV/fC can be implemented. It has separate inputs for charge producing detectors (MPGD) or Voltage producing detectors (SiPM).

Figure 8-15 is a screenshot of the µAPIC preamplifier and shaper output response to a test pulse.

Input polarity	+ / - charge sensitive	Spark protection +/- 50V*10ns
Charge input	SMA AC coupled	Dynamic CSA input impedance nominal 75W for CSA gain 1mV/fC, 300 W for 2mV/fC,, 600W for 4mV/fC
Charge Input coupling	AC coupled 1000V, Cc =10nF / 3 pF	Jumper selectable for charge envelopes from 50 ns to 1 ns respectively
HV bias output for MPGDs	On SMA input after pi- RC filter max 1kV	Jumper selectable 1 or 2 resistors 8.2M with filter capacitors 15nF
Test input	50 W LEMO 0.5pF to CSA	Dynamic 50 W impedance for pos /neg risetimes O(500ps)
Preamplifier CSA	+/- charge, FET input, GPB 2.8 GHz Buffered output driver	50 W output linear max +/- 1.9V 1M output linear max +/- 3.8V
LV Bias output (PIN, SiPM, APD..)	3pin cable connector with 1 Bias 1 GND, 1 enable	Precision Bias Voltage generator 2V -80V limited to 2mA, control via trimmer or I2C, jumper selectable
CSA gain	4mV/fC default	Other Gains between 0.25 … 2 mV/fC can be implemented
Shaper gain	1..10 via trimmer	linear peak max +/- 3.8 V (on 1M) on 50 W +/- 1.8 V

Shaper output	BNC, default peaking time 18 ns , 2nd order filter.	Other peaking times between 15.. 500ns can be implemented on request
Trigger resolution	+/- 0.5ns shaper signal threshold Positive: TOT (red LED) Negative: TBT (green LED)	50 W NIM output threshold via 10-turn trim pot
Size/ weight	135x70 x30 mm incl. connectors	215 g (without batteries)
Power	+/- 3.7V, polarity protected	nominal for two external Lithium cells 18650
Autonomy	12h	(TOT trigger switched off)

Table 8.3: Properties of uAPIC V1.3.

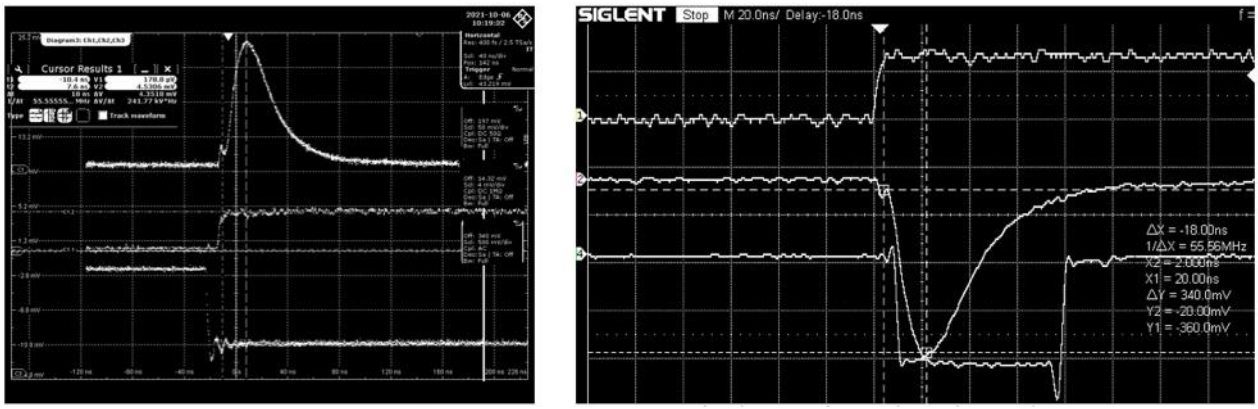

Figure 8-15 Left : uAPIC response to negative test pulse (bottom) ; CSA output (middle) and shaper output (top). Right: signals on the CSA (top), shaper (middle) and TOT (bottom).

The timing cursors show a peaking time of 18 ns. The figure shows also the TOT NIM trigger signal derived from the shaper envelope. The trigger feature is optional and can be disabled to save battery autonomy. A threshold trimmer can be adjusted to intersect the shaper envelope and produce a TOT or TBT timing signal with 50Ω NIM output level.

9 OPTICAL RADIATION IMAGING

Gas molecules, excited by the primary interactions or by collision processes in high electric fields, return to the ground state with the emission of fluorescence photons. Detection of this scintillation before the onset of the dispersions due to the avalanches, permits to reach the statistical limit of energy resolution, as discussed in section 4.6.3.

Excited noble gases emit photons in the far ultraviolet region (see section 5.5) requiring for detection the use of VUV sensors or suitable thin wavelength shifter layers deposited on the windows. A convenient alternative is to add to the main gas mixtures a gas acting as internal wavelength shifter. Several vapors used to detect UV photons, thanks to their low ionization potential, have been found to fluoresce at wavelengths close to or in the visible range: examples are triethyl amine (TEA) and tetrakis dimethyl amino ethylene (TMAE), Table 5.2.

Figure 9-1 is an example of beam tracks recorded with a drift chamber filled with an argon-methane-TEA mixture.

Carbon tetrafluoride (CF_4) is a very efficient scintillator, with emission around 650 nm (2 eV), conveniently in the visible range. The emission matches well the spectral response of modern solid-state sensors, as shown in the example of Figure 9-2 (Brunbauer, 2020). An example of tracks with a long-range delta ray recorded in a muon beam is shown in Figure 9-3.

Used in a variety of applications, optical imaging with MPGD devices and CCD cameras recording is a very convenient tool for laboratory assessment of detectors properties (Brunbauer *et al.*, 2018) (Brunbauer *et al.*, 2020). Figure 9-4 is an example of secondary photons emission map recorded with a GEM foil in two configurations of the sectors separation, part of a study aimed at reducing the dead region; taking into account the hole's standard pitch of 140 µm, the resolution of the image is manifest (Marques *et al.*, 2020).

A large choice of models exists for solid state cameras suitable for radiation imaging recording, depending on requirements: resolution, sensitivity, frame rates. A non-exhaustive compilation of examples is shown in Figure 9-5 (courtesy F. Brunbauer).

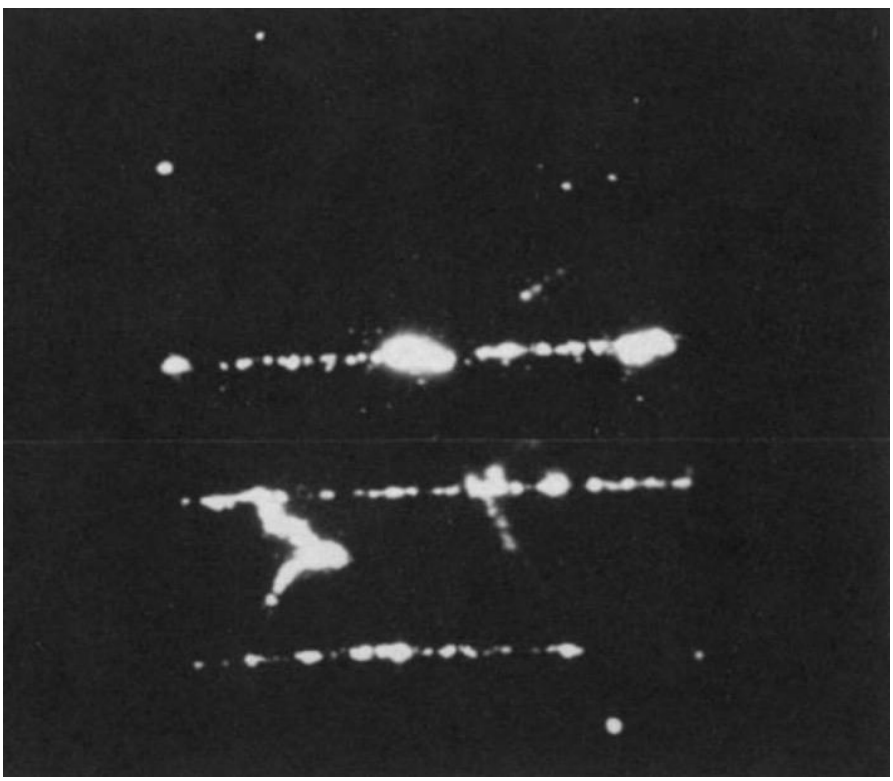

Figure 9-1: Beam tracks recoded with the optical TPC; gas filling A-CH_4-TEA (Charpak *et al.*, 1988).

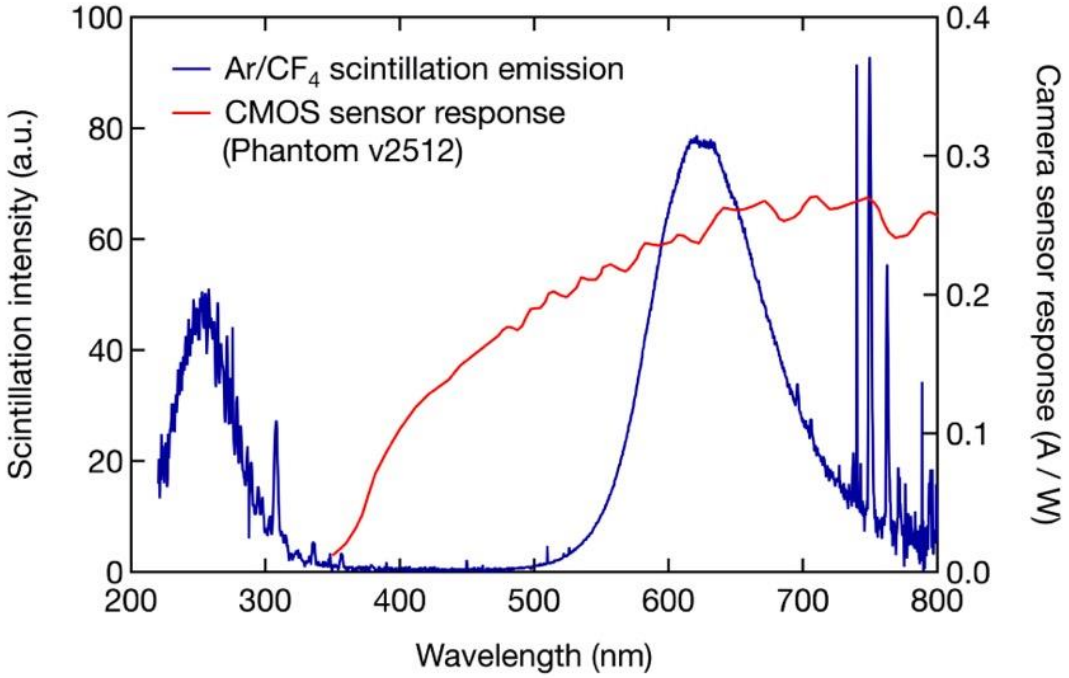

Figure 9-2: Secondary scintillation spectrum of Ar-CF_4 and spectral response of a CMOS camera.

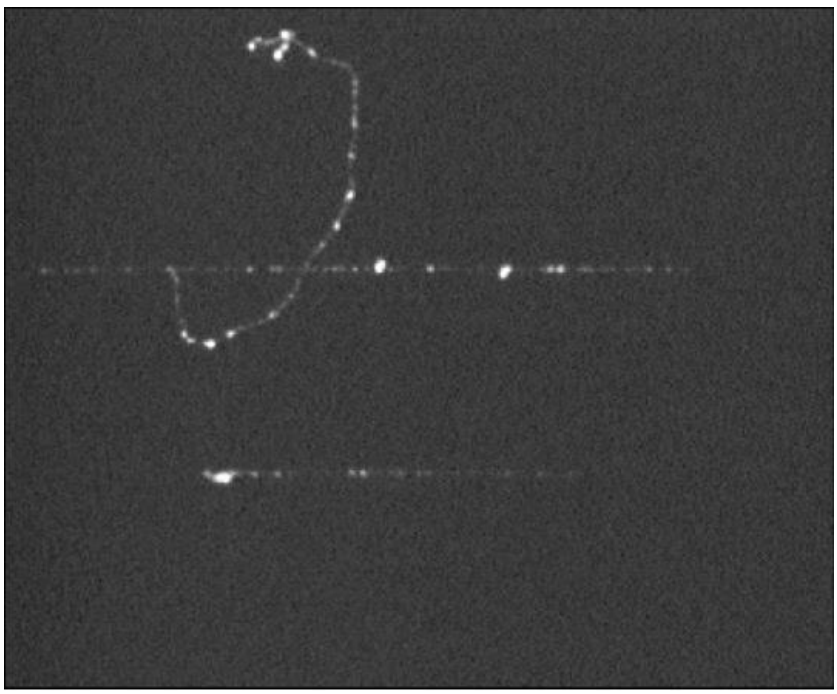

Figure 9-3: Charged particles tracks with a long-range delta electron (Brunbauer *et al.*, 2018).

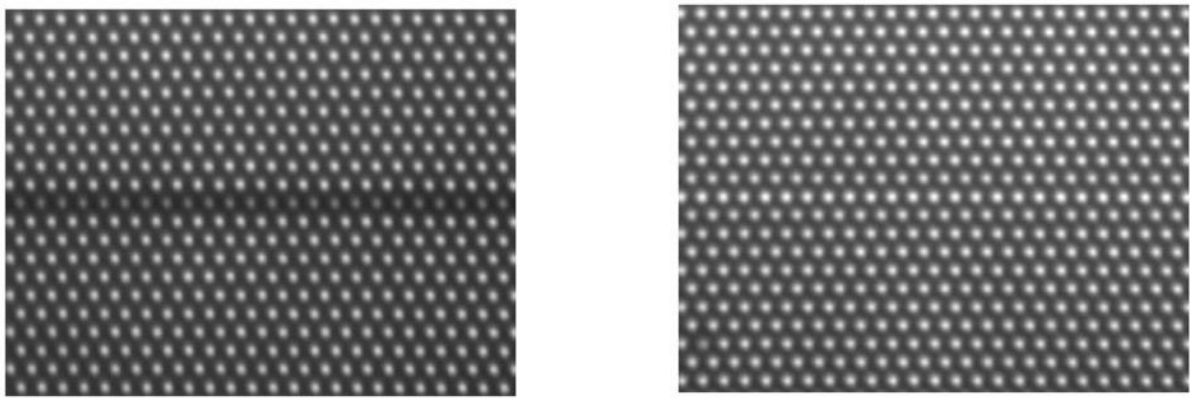

Figure 9-4: Photons emission image recorded with a GEM foil in two configurations of the sectors separation (Marques *et al.*, 2020).

Figure 9-5: Examples of solid-state cameras suitable for optical image recording (courtesy F. Brunbauer).

10 DETECTORS CALIBRATIONS AND MONITORING

Contributed by Florian Brunbauer (CERN)

This chapter provides an overview of common methods for characterizing and calibrating detectors without attempting to comprehensively describe possible approaches. While GEMs and Micromegas are described as examples and indications are given for their testing and operation, these methods are equally applicable for other types of MPGDs.

10.1 Manufacturing and cleaning procedures

MPGD technologies exploit manufacturing techniques developed for PCB fabrication including photolithography. UV illumination through masks or direct laser exposure is used to illuminate photosensitive resists which are subsequently developed and used to control chemical etching processes. Multiple lithography and etching steps are used to create advanced detector build-ups and structure different materials including insulators like polyimide, metallic electrodes or resistive layers. Alternatively, larger MPGD structures like THGEMs can also be manufacturing with mechanical techniques including drilling or sand blasting. Mechanical approaches such as polishing, grinding or lapping can be utilized to achieve high-quality substrates suitable for detector integration.

Before being assembled into operational detector systems, detector components must be thoroughly tested. While this is true for all components ranging from readout structures to gas vessels, it is especially crucial for the amplification structures themselves, such as GEM foils or Micromegas boards. Possible validation steps of MPGDs include visual inspections, electrical testing and operational calibration and characterization. All characterizations and measurements on exposed detector components should take place in a clean environment such as a cleanroom or flow box to minimize the risk of dust or other contaminants accumulating on detector surfaces, which can cause electrical instabilities.

Visual inspection can be by eye, optical microscopy or electron microscopy. The presence of large-scale defects such as chemical residues, incomplete, excessive or non-uniform etching can often be confirmed by eye. Optical microscopy with amplifications of several hundred can be used to inspect photolithographically structured features such as holes, pin electrodes, readout strips, meshes or other structures. This can be used to confirm if the designed pattern was accurately reproduced in the structuring process and to verify if the desired quality such as surface and edge smoothness was achieved. Electron microscopy can be used to examine localized defects or features in higher detail with magnification factors of several thousands. In addition, electron microscopy setups equipped with Focused Ion Beam (FIB) capabilities can be used to cut cross-sections in detectors and subsequently examine their cross-sectional profile.

Electrical inspections of amplification structures are used to verify correct separation of electrodes, detector cleanliness and surface quality. As a first step, simple measurements with multi-meters are useful to identify possible short circuits or broken connections. Continuity measurements with a multi-meter can confirm that electrode contact points are correctly connected to the electrode structures themselves if accessible. Care should be taken to not damage sensitive electrodes during characterization with pin probes. The same measurements can be used to confirm that different electrodes such as the two sides of a GEM foil or the mesh and anode in a bulk Micromegas are electrically insulated from each other.

Once the electrode separation is confirmed, capacitance measurements between parallel electrodes can be used to confirm expected geometrical build-up and connectivity. In many cases, simple calculations of the capacitance of a parallel plate capacitor with the surface area of the detector electrodes and their separation can provide an expected capacitance value which can then be confirmed for the detector under test. As an example, a standard GEM foil (50 µm thick polyimide) with an area of 10 cm x 10 cm and 70 µm diameter holes at a pitch of 140 µm has a capacitance of about 6 nF.

Once continuity of connections and separation of electrodes are confirmed, detectors can be tested under high voltage as shown in Figure 10-1. High voltage supplies as described in Chapter 3 can be used for this and care should be taken to operate detectors in safe conditions during testing. This includes operating them in a clean and dry environment, limiting the energy of potential discharges and gradually increasing the voltage applied between electrodes. Electrical characterization can be done by contacting two electrodes with wires or contact clamps, grounding one of them and applying high voltage on the other one. Before starting these measurements, the connectivity and correct setup of the power supply should be confirmed. Achievable voltages will strongly vary between detector geometries. As an example, standard GEM foils with 50 µm thick polyimide insulators should typically withstand a potential difference of 600 V between top and bottom electrodes while standard non-resistive bulk Micromegas with a 18/45 µm micro-mesh and an amplification gap thickness of 128 µm should withstand up to 980 V between the mesh and anode electrode. The maximum desired voltage for the tests should be set as the voltage limit on the power supply. Similarly, a maximum current setting suitable for the detector under test should be used to limit the current provided by the power supply in case of discharges. Depending on the detector geometry and its capacitance, different parameters can be used. For GEM foils, a current limit of around 4 µA can be used, which provides protection against excessively high current pulses during discharges while at the same time providing sufficient energy in discharges to potentially remove contaminants such as dust. For resistive detectors, such as Micromegas with resistive anode electrodes, discharges do not have enough energy to burn contaminants and lower current limits in the scale of tens to hundreds of nA should be used to protect amplification structures.

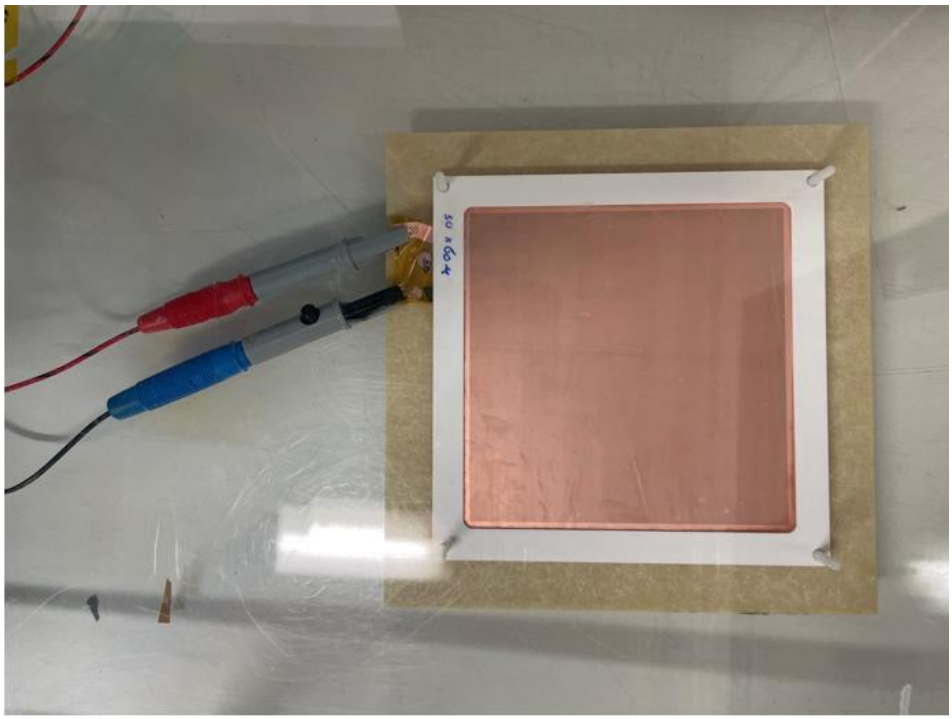

Figure 10-1: GEM foil connected for electrical performance tests. Clamps are used to contact top and bottom electrodes. One electrode of the foil is grounded and high voltage is applied to the other.

Once the high voltage power supply is correctly configured with voltage and current limits, the applied voltage can be gradually increased up to the maximum desired voltage. While increasing the voltage, the current drawn by the structure under test should be monitored. For well-insulated electrodes, low leakage currents less than one nA are expected in dry conditions. When testing detectors in humid ambient air, several nA leakage currents may be observed. In addition to

monitoring possible leakage currents, attention should be given to sparks between the powered electrodes. Depending on applied voltage and detector capacitance, sparks may be clearly visible in ambient light and can also be heard. In low-energy conditions, cameras or testing in dark conditions can be used to observe discharges. Sparks can indicate locations of contaminants such as dust particles or weak points in the detector structures themselves. During testing, the location and frequency of sparks can be used to differentiate between possible origins of discharges. Sparks occurring at random locations across tested detector structures typically indicate distributed contaminants. Localized discharges at the same location hint at weak points in the electrodes such as sharp metal edges, protruding wires from a micro-mesh or other features that result in excessively high electric field values. In non-resistive detectors, multiple discharges in random locations can indicate that dust particles are gradually removed. If discharges occur at a certain voltage, the voltage can be kept constant for some time and the frequency of discharges can be monitored. If only a few discharges occur or if the frequency strongly decreases after initial sparks followed by a period without discharges, the voltage can be increased to the next step. If discharges occur in the same location or if their frequency remains high, the applied voltage should be decreased to avoid damaging the electrodes or deposit conductive contaminants leading to permanent short circuits.

If the voltage can be increased to the nominal voltage, the detector can be kept at high voltage for extended periods of time and its stability can be monitored. Thorough electrical characterizations can include the monitoring of spark rate and leakage current over multiple hours or days. Depending on the intended application, periods without any discharges for several minutes can indicate acceptable quality of the amplification structures.

If excessive leakage current or reoccurring discharges are observed, causes should be investigated and addressed before proceeding with electrical characterizations. This can include additional visual inspections such as microscopy surveillance of areas where repetitive sparking occurred. If defects in structured electrodes are identified, additional chemical etching steps to smooth sharp features may be used. If contaminants such as dust, debris, metallic pieces or similar are suspected as cause for unstable electrical behaviours, detector structures can be cleaned with appropriate methods. Standard cleaning procedures include high-pressure cleaning with deionized water to mechanically remove contaminations. Alternatively, electrostatic cleaning rollers may be used to trap and remove contaminants. Such rollers are available in various sizes and shapes as shown in Figure 10-2 that can be applied to the full active areas of detectors or locally in areas suspected of being contaminated. When using electrostatic cleaning rollers, care should be taken to clean the roller with adhesive sheets before passing it over the active area of detectors and repeat the cleaning before subsequent passes.

Following the cleaning attempts, electrical testing procedures can be repeated to confirm if performance and stability could be improved. In case of failures to withstand the requirements, the electrode has to be discarded.

Systems for optical semi-automatic quality certification and defects localization over large areas, developed in view of serial production of electrodes, are described in Refs. (Kalliokoski *et al.*, 2012) (Hildén *et al.*, 2014) (Brücken *et al.*, 2021).

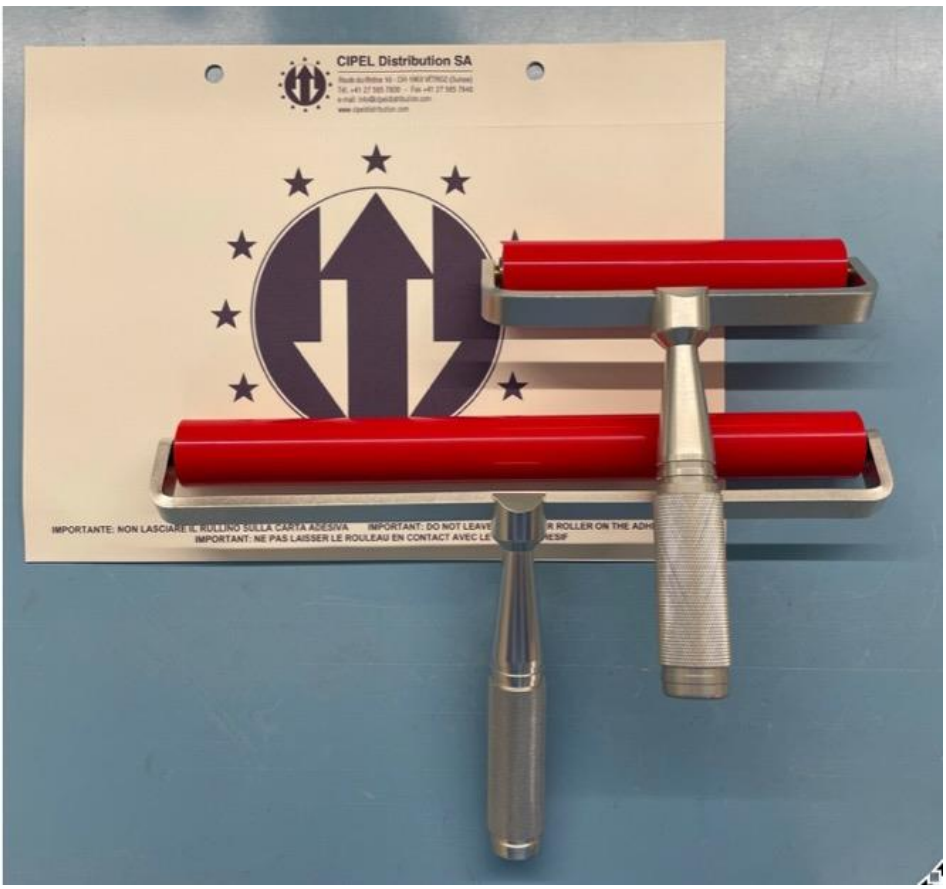

in Figure 10-2: Electrostatic rollers of different sizes can be used to clean amplification structures. Adhesive sheets are used to clean rollers prior to passing over sensitive structures to be cleaned.

10.2 Detector Calibrations

Once optical and electrical characterizations confirm the correct functioning and desired quality of an amplification device, it can be assembled into a detector for a calibration of its response. Calibration measurements of detector parameters can include but are not limited to scans of drift field and induction field strengths to determine charge collection and extraction efficiencies as well as measurements of the gain as a function of applied voltage between electrodes and measurements of the uniformity of response of a detector.

The gain of a detector can be measured with different approaches depending on detector build-up and the range of gain of interest. A schematic detector setup to measure the gain of a single GEM is shown in Figure 10-3.

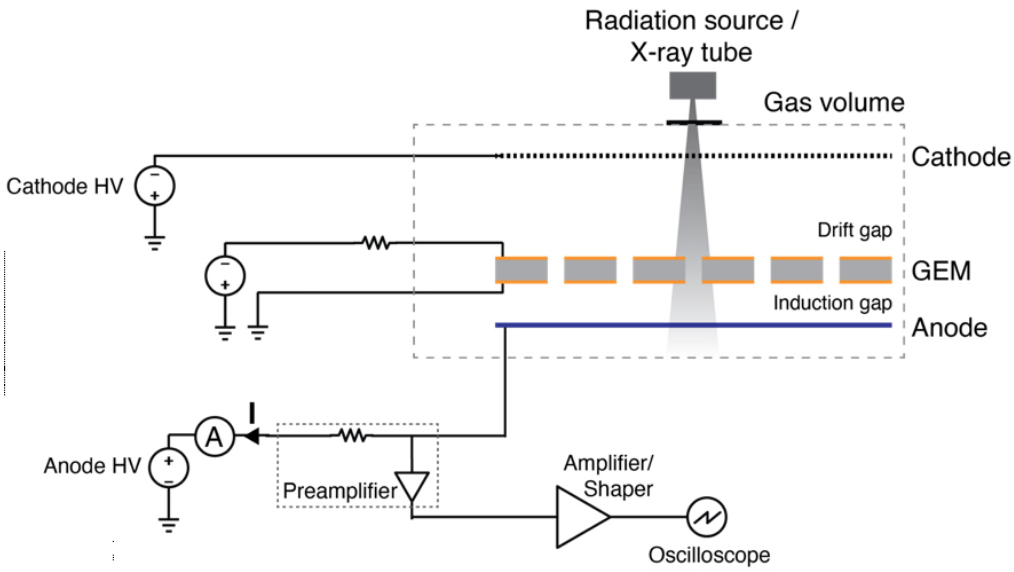

Figure 10-3: Schematic of single GEM for gain measurement. A collimated beam (from radiation source or X-ray tube) illuminates a region of the detectors. Current and signals are measured with an ammeter and an amplifier on the anode.

One way to record gain curves as function of applied voltage is the use of calibrated readout electronics. This can include charge-sensitivity amplifiers (CSAs) described in Chapter 8.2 as well as additional shapers or amplifiers. To calibrate the response of a CSA preamplifier with a subsequent amplifier/shaper, pulses of known charge can be injected and the response of the readout chain can be measured. For this, a known capacitor (e.g. 1 pF) can be pulsed with a pulse generator with short duration pulses of varying voltage to generate different known amounts of charge at the input of the readout chain. The output signal of the CSA and amplifier/shaper can be recorded and its amplitude related to the known input charge. From several data points recorded with different input pulse voltages, a calibration curve relating output amplitude to input charge can be recorded.

As an example, the Ortec 142PC preamplifier connected to an amplifier/shaper can be calibrated as follows: a 1 pF capacitor is connected to the input terminal and is pulsed with square pulses from a pulse generator with voltages of 0.1V, 0.2V or 0.3V, corresponding to charge values of 0.1 pC, 0.2 pC and 0.3 pC, respectively. For these values, output signal amplitudes of 0.53 V, 1.07 V, and 1.588 V, were measured, respectively. This corresponds to a proportionality factor of approximately 5.2 V/pC.

Using a radiation source such as ^{55}Fe, emitting 5.9 keV X-ray photons, the gain of the detector can be measured using one of the methods described above. For this, the number of primary electrons and the number of secondary electrons (after charge multiplication) is determined and the ratio of secondary to primary number of electrons can be used as the gain of the detector. The number of primary electrons can be calculated by dividing the energy deposited by incident events by the w-factor, i.e. the average energy required to create a primary electron-ion pair. For the case of 5.9keV X-ray photons interacting in a commonly used Ar/CO2 gas mixture, this can result in around 220 primary electrons per 5.9 keV X-ray photon.

With a known calibration of the readout chain, signal amplitudes from a detector can be measured for different applied voltages and the charge after multiplication can be extracted from the obtained calibration factor. Relating the charge to the number of electrons, the average number of secondary electrons after multiplication is obtained and can be divided by the number of primary electrons to obtain a gain value. Thus, the gain G can be calculated as $G=A/NeS$, where A is the mean signal amplitude, S the sensitivity in V/C, e the electron charge and N the mean number of primary electrons per event. This measurement is repeated for different voltages applied to the detector to record the gain as a function of applied voltage.

Figure 10-4 is an example of charge spectra recorded with a Triple GEM detector at increasing values of voltage; the position of the 5.9 keV peak provides, after calibration, the gain dependence from voltage, Figure 10-5 (Roy *et al.*, 2019).

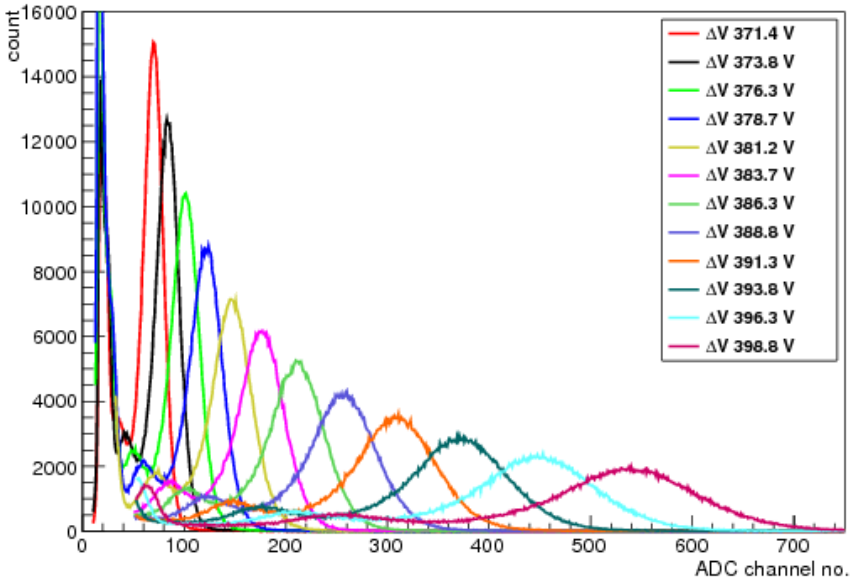

Figure 10-4: ^{55}Fe pulse height spectra recoded with a Triple-GEM at increasing voltages (Roy *et al.*, 2019).

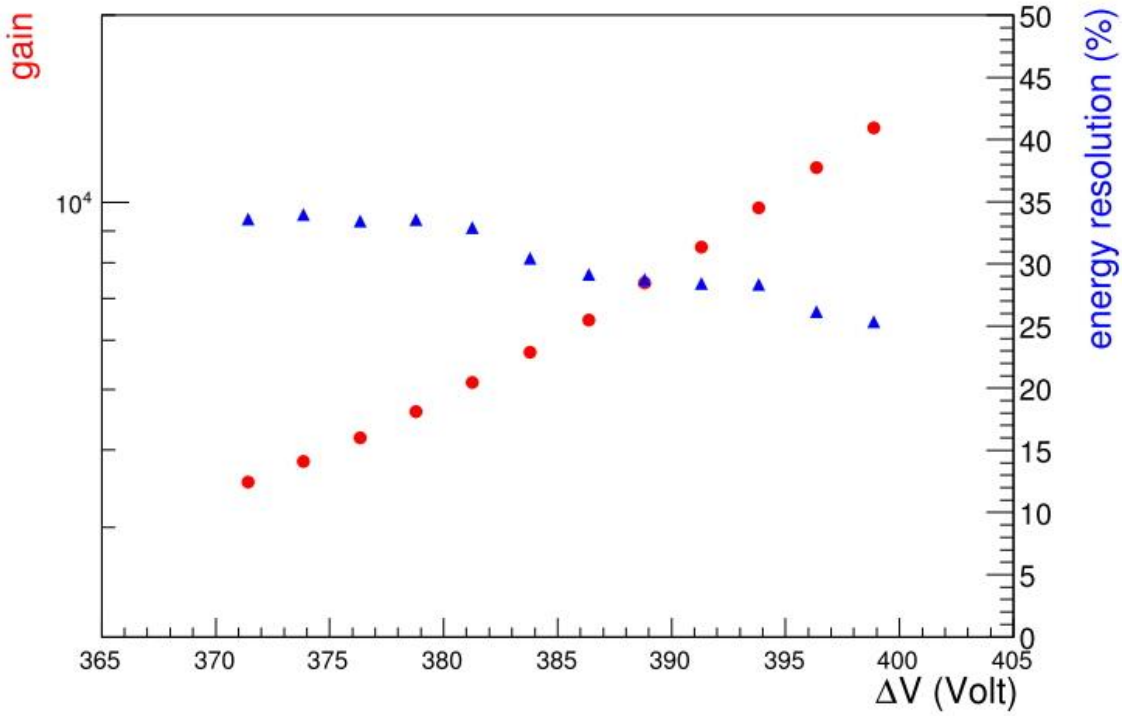

Figure 10-5: Effective gain and energy resolution fwhm for 5.9 keV of a Triple-GEM (Roy *et al.*, 2019).

An alternative approach to measure the gain of an amplification structure as a function of applied voltage is to record event rates and anode current after amplification, as seen in the example of Figure 10-6 (Gola *et al.*, 2020).

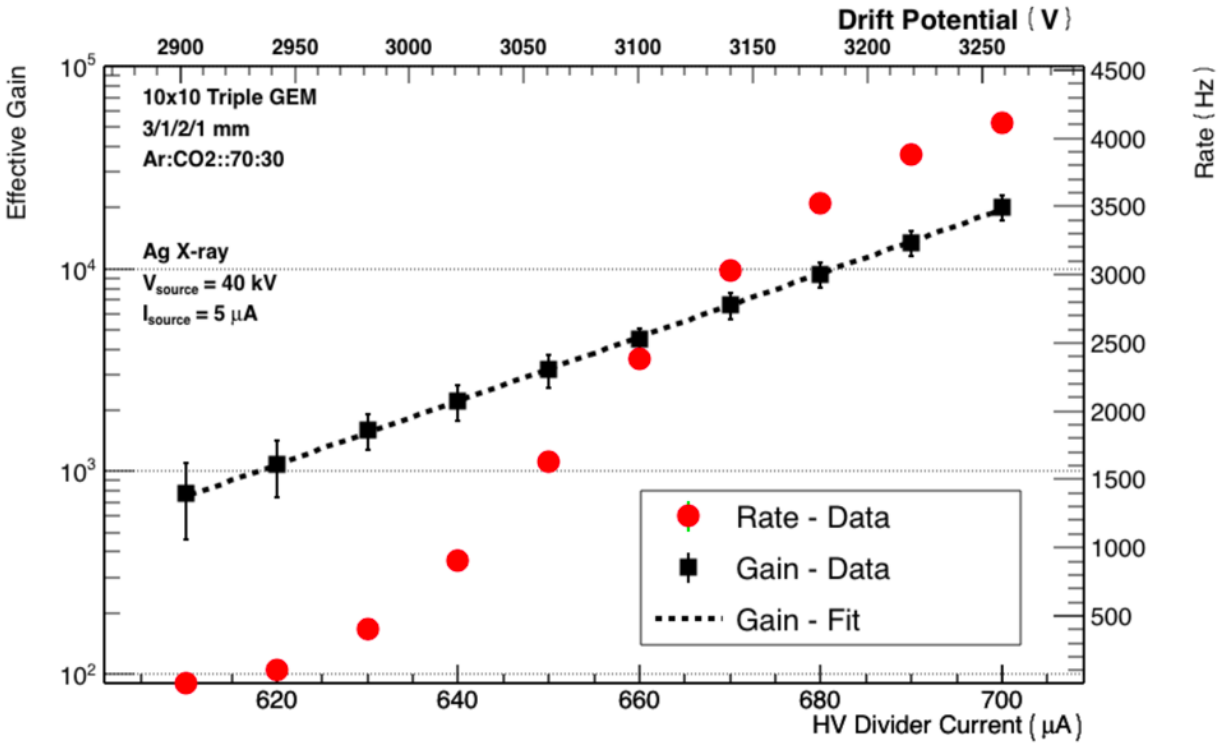

Figure 10-6: Counting rate and gain of a triple GEM detector as a function of divider current and drift voltage (Gola *et al.*, 2020).

This method also requires the knowledge of the amount of primary electron-ion pairs generated by each event interacting in the conversion region. With a known number of primary electrons per event, the gain G of the detector can be calculated as $G=I/NeR$, where I is the current measured at the anode, N the number of primary charges per event, e the electron charge and R the average rate of events. The current after the amplification can be measured with an ammeter connected at the anode as shown in Figure 10-3. The average event rate can be determined with a scaler or an oscilloscope from signals recorded by the electron readout chain including preamplifier and amplifier/shaper.

A third way to measure gain uses higher event rates and does not require the knowledge of the number of primary electrons per event. If the primary current I_0, i.e. the current generated by primary electrons drifting in the conversion region, is measured, the ratio between the secondary current after amplification and the primary current provides a measure for the gain factor of the device under test. Thus, the gain G can be calculated as $G=I/I_0$, where I_0 and I are the primary and secondary currents. This method relies on a good knowledge of the collected primary current, which can be either measured separately (e.g. in a parallel plate configuration) or can be extracted from a measurement of collected current after the amplification structure as a function of applied voltage. For very low voltages across an amplification structure, the primary current will not be collected efficiently and only a fraction of I_0 will be recorded. For moderate voltages, primary current will be collected efficiently but amplification does not yet take place. This is represented as a plateau of the collected current as a function of applied voltage. At higher voltages, amplification will set in and the collected current will increase exponentially. An example of measurement with a single standard GEM in an Ar/CF_4 gas mixture at ambient pressure is shown in Figure 10-7. At low drift fields, a plateau at a value $I_0 \approx 9.2$ nA is reached around 50-100 V. For higher drift fields, the primary current is partly collected by the top electrode before amplification sets in. Fitting an exponential function with an offset this the obtained current values as function of electric field, the offset denotes primary current I_0 and the ratio of measured secondary currents and I_0 corresponds to the gain of the structure.

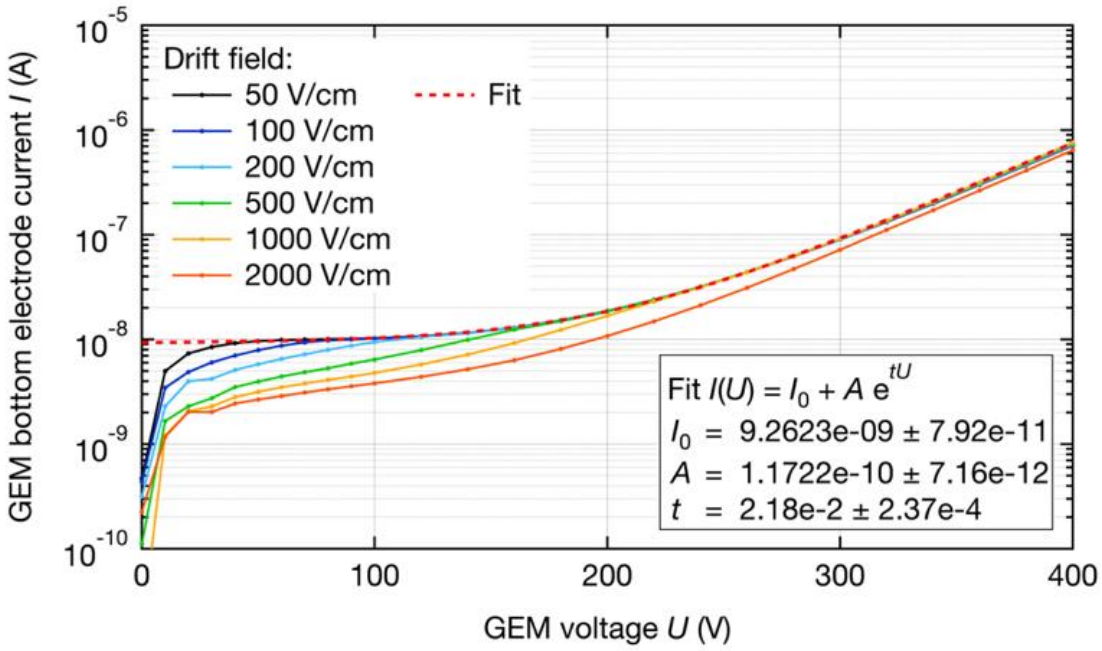

Figure 10-7: Current measured on the bottom electrode of a GEM as function of GEM voltage and for different drift fields from 50 V/cm to 2000 V/cm. An exponential fit with an offset is used to extract primary current $I_0 \approx 9.2$nA for the calculation of gain factors (Brunbauer, 2018).

It should be noted that the above methods present basic estimates of the gain and obtained values should be interpreted as an "effective gain", which accounts for all processes affecting measured currents including collection of charge and extraction from amplification structures if applicable.

In addition to gain measurements as a function of voltage across the amplification structure, the effect of electric fields in the conversion, induction and transfer regions can be measured in a similar fashion. Recording plots of secondary current or signal amplitude when varying drift field, transfer field or induction field strength can be used to identify optimal operating conditions and field ratios. Results of a systematic investigation on charge collection and transfer efficiency for multi-GEM detectors are reported for example in Ref. (Bachmann *et al.*, 1999).

Gain measurements can be carried out globally for a full detector under uniform irradiation or locally when using collimated radiation sources. Localized measurements moving the source across the active area can be used to verify gain uniformity. A simple method is the use of collimated sources and placing them sequentially in different locations across the detector while recording a gain curve for each location. Alternatively, global gain maps can be recorded under uniform irradiation (e.g. with a flat X-ray beam) with position-sensitive readout. Electronic multi-channel readout systems (such as the RD51 Scalable Readout System) can be used to record events across the active area of the detector. Acquired hits can be binned offline into geographic regions and for each region a mean signal amplitude can be used to build a 2D map of detector gain.

While electronic measurements of the signal intensity across the active area will give an indication of the uniformity of the effective gain including collection efficiency, detector gain and induction field uniformity, optical measurements in scintillating gas mixtures can be also be used to record 2D gain maps. Under uniform irradiation, scintillation light images intuitively display uniformities in the effective gain including conversion and collection efficiency as well as detector gain but excluding effects of the induction region as scintillation light is produced during avalanche multiplication.

Figure 10-8 shows a 2D image of a glass Micromegas detector under uniform X-ray irradiation. Dark regions in the corners are attributed to artefacts from the optical system coupling the scintillation light to the image sensor. Brightness variations across the active area indicate differences in the detector response with some global variations visible across the active area as well

as localized bright regions around the pillars. Bright regions correspond to increased collection efficiency or higher gain while darker regions show lower collection efficiency or lower gain.

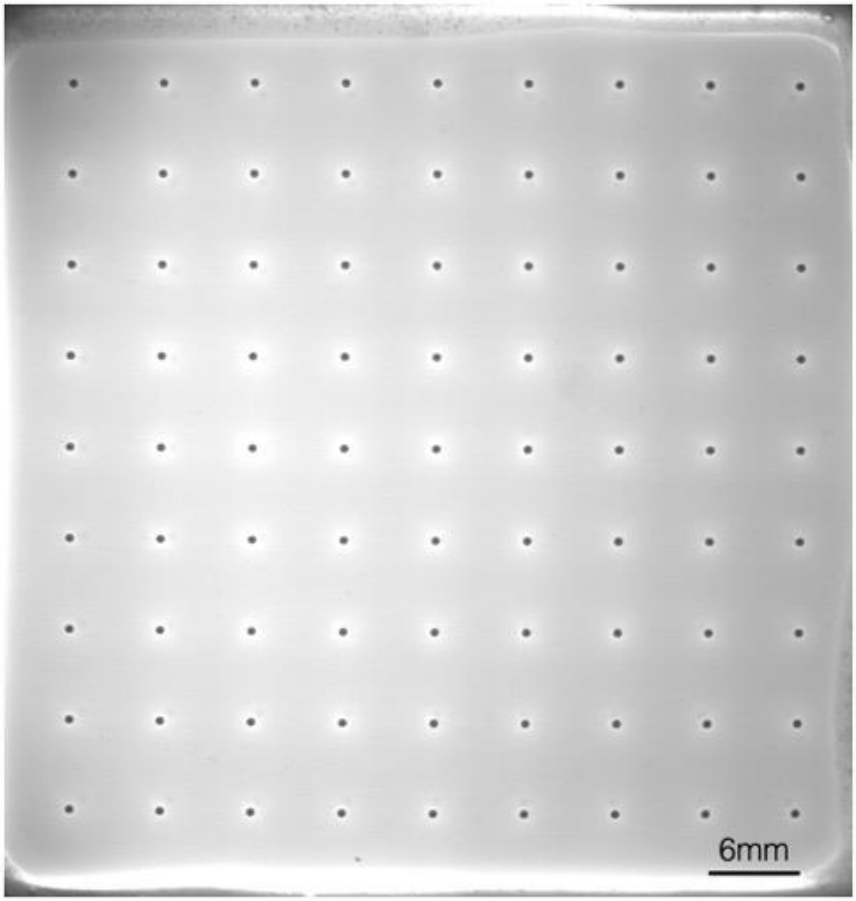

Figure 10-8 : Scintillating light image of glass Micromegas displaying variations of response across the active area (Brunbauer *et al.*, 2020).

10.3 Detection efficiency

Once fully tested and calibrated in the laboratory, detectors can be exposed to radiation sources of various kind to assess their detection efficiency in real operating conditions. Different radiation fields used for experiments are described in Chapter 4. For charged particles, the measurement of efficiency requires an external monitor (usually realised with one or more scintillation counters) to generate a trigger signal; the efficiency is then measured as the ratio of coincidence counts between detector and monitor normalized to the monitor counts, varying the operating conditions in the desired range: gas mixture, operating voltage, coincidence time, electronics gain and detection threshold. Figure 10-9 and Figure 10-10 are examples of efficiencies measured as a function of voltage with a Triple-GEM exposed to cosmic rays and fast electrons from a ^{106}Ru source, and for two gas mixtures (Patra *et al.*, 2017). The length of the plateau depends on electronics threshold and defines the operating range of the detector .

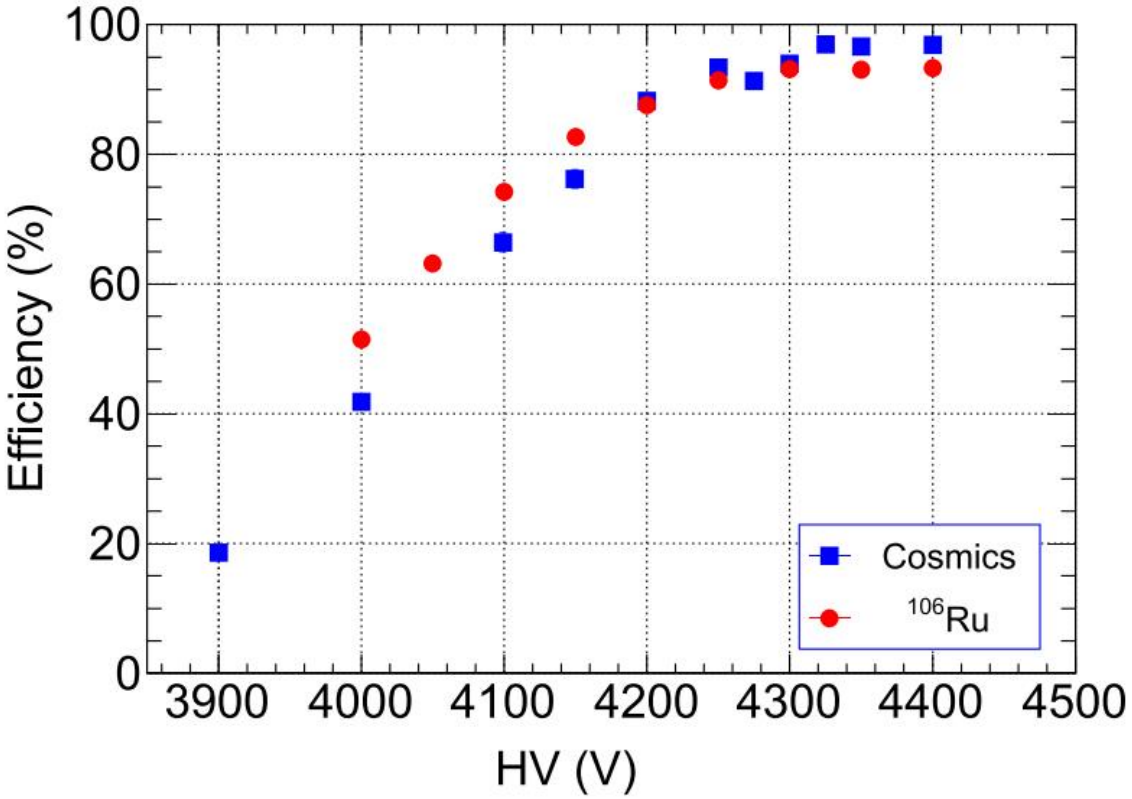

Figure 10-9: Detection efficiency of a Triple-GEM for cosmic rays and fast electrons from a ^{106}Ru source (Patra *et al.*, 2017).

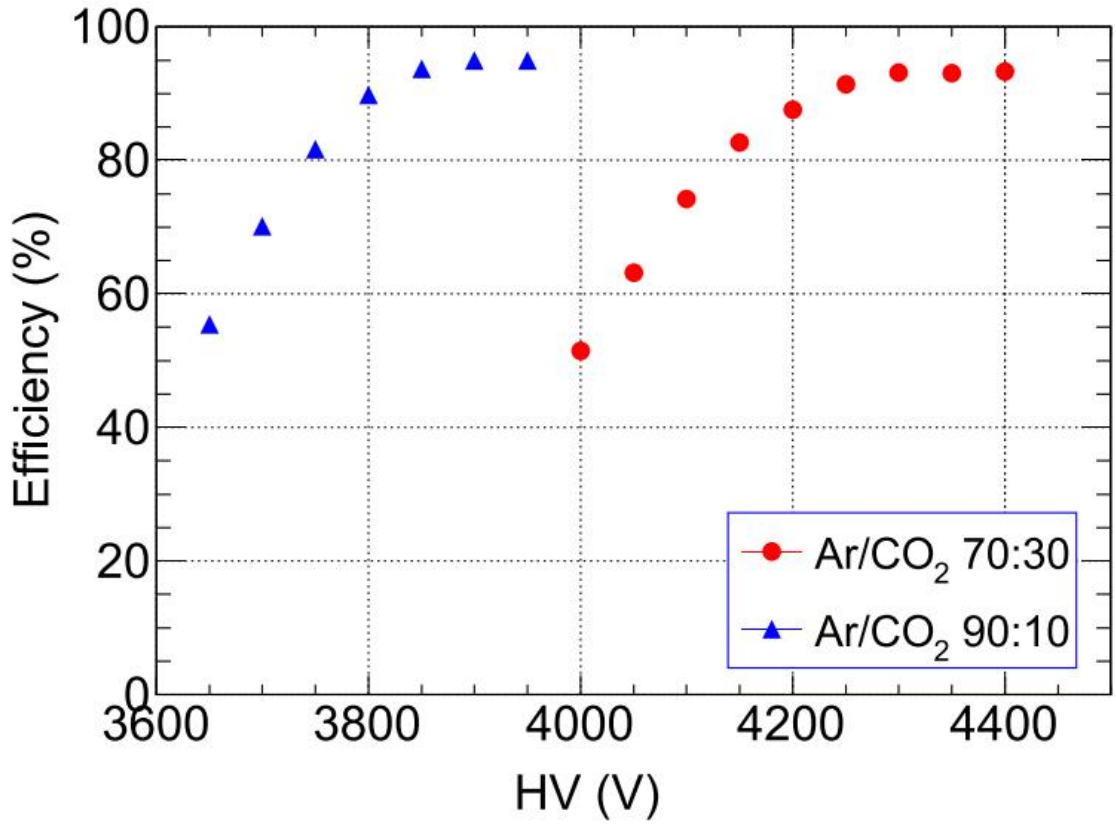

Figure 10-10: Detection efficiency of a Triple-GEM for fast electrons from a ^{106}Ru source and two gas mixtures (Patra *et al.*, 2017).

10.4 Monitoring

The stability of the detector response as a function of environmental parameters as well as over time should be monitored to maintain accurate calibration. Calibration measurements such as gain curves and measurements of the effect of conversion, induction and transfer fields on the detector response should be recorded in comparable conditions to the intended application. If feasible, regular calibration measurements can be recorded to track long term variations and identify correlations of the detector response with varying external or internal parameters.

External factors that can impact a detector's response include gas pressure and temperature. Therefore, monitoring of environmental parameters such as ambient pressure and temperature are useful and can help to understand variations in the detector's performance. Day-and-night variations, gain variations following changes in ambient pressure or temperature should be taken into account when choosing nominal operational points and may also be corrected for. This can include offline corrections of recorded data to account for varying gain or online corrections of applied voltages in response to external factors. Monitoring of environmental parameters can be done with simple temperature and pressure monitoring and logging devices placed in the vicinity of detectors.

Gas quality and contaminations also plays an important role in the stability of the response of detectors. Monitoring contaminations such as water or oxygen can help to understand varying gain behaviour or long-term effects impacting detector performances. Gas monitoring methods are described in detail in Chapter 7.4.

Internal factors affecting the performance of detectors can include deposits during discharges or etching of insulating layers or electrodes by chemical or physical processes as well as charging up effects or polarization of insulating materials. A continuous monitoring of currents on different electrodes can reveal frequency and severeness of discharges as well as variations in leakage currents over time hinting at varying electrical properties of detector components.

11 HIGH RATE, DISCHARGES AND AGING MEASUREMENTS

11.1 Gain modifications due to space charge

Owing to their low mobility in a gas, positive ins created in the process of avalanche multiplication accumulate in the gap between electrodes and induce field modifications, enhanced at high gains and radiation rates. Observed since the early development of gaseous counters, the positive space charge generally induces a reduction gain and a distortion in the coordinate's measurement. For an analysis of these processes see for example Chapter 8 and 13 in (Sauli, 2014) and Chapters 4 and 5 in (Sauli, 2021).

The rate effect is studied experimentally exposing the counters to a controlled rate source of radiation, usually soft X-rays from a source or a generator, and measuring the proportional gain as a function of flux. The gain is obtained from a recording of pulse height for low and moderate rates, while it is deduced from the measurement of currents on electrodes for high rates, when recording of individual events is not doable. In case of cascaded devices, charges may be shared between the electrodes; the "effective gain" is usually deduced from the current recorded on the last electrode in the chain (the anode).

While results are often expressed as a function of flux per unit area, the total irradiated surface of the detector plays a role. Depending on the high-voltage powering scheme adopted, high current values may induce modifications of voltage differences between electrodes, usually a decrease, that should be taken into account (see chapter 3). Other factors play a role on the results:

- Insulating regions in the detector may charge-up, dynamically modifying the fields;
- Electrons un the avalanche may be lost by a field-dependent attachment to molecules;
- Recombination between electrons and ions reduce the collected current.

Of these factors, the more often encountered is the reduction of voltages due to the current in the high-value resistors, mounted between electrodes and power supplies to reduce damages due to accidental discharges.

Figure 11-1 is a representative example of normalized gain dependence from flux in multiwire and microstrip chambers (Breskin *et al.*, 1975)(Bouclier *et al.*, 1995). Figure 11-2 shows the normalized gain dependence from X-ray flux for a GEM detector; the dashed line indicates the transition between the pulse height and the current measurements (Benlloch *et al.*, 1998). Further studies indicated that the gain dependence from flux depends on the value of the low-rate value of the gain, as shown in Figure 11-3, measured with a triple GEM detector. The increase of gain at high fluxes/high gains id well reproduced by a model calculation taking into account the field modifications induced by the positive ions (Franchino *et al.*, 2016).

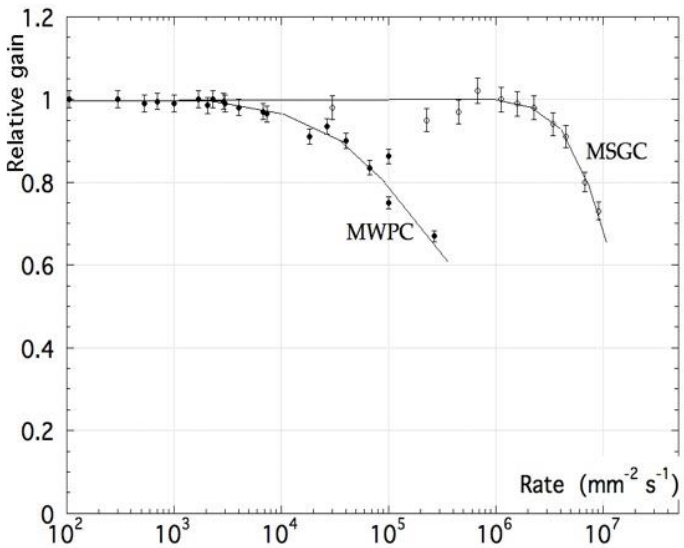

Figure 11-1: Rate dependence of the relative gain for a multiwire (Breskin *et al.*, 1975) and a micro-strips chamber (Bouclier *et al.*, 1995).

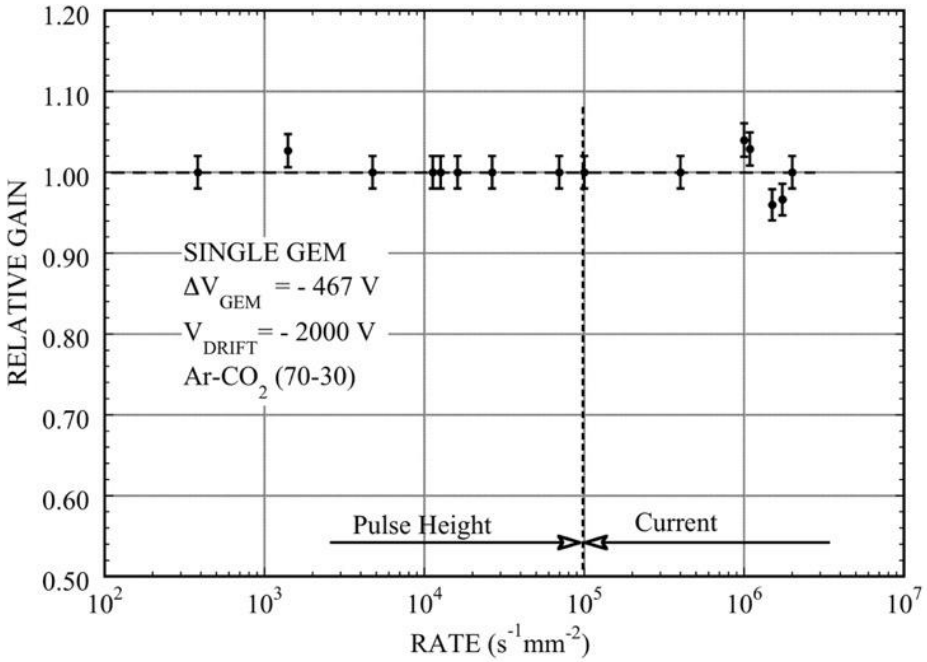

Figure 11-2: Relative gain dependence from flux for a GEM device.

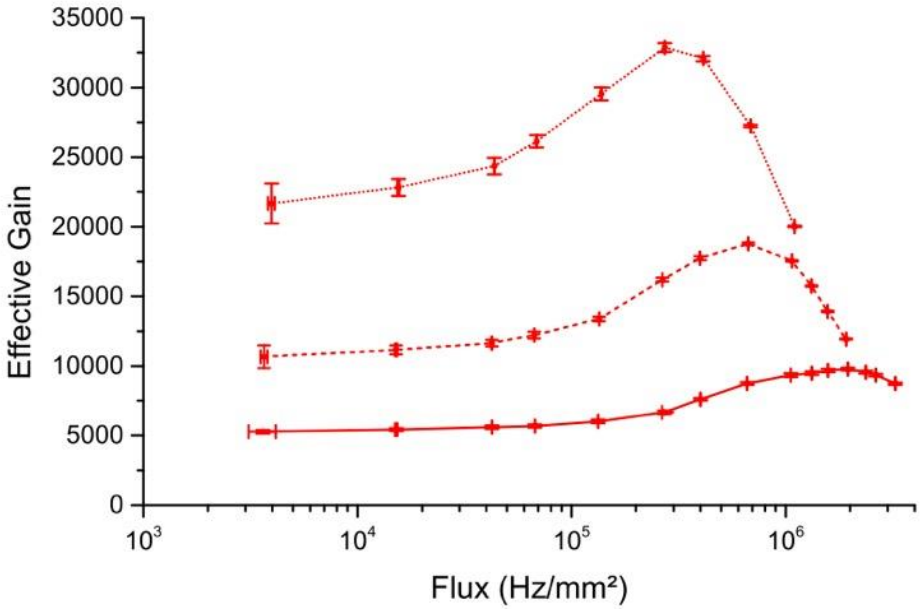

Figure 11-3: Dependence of effective gain from flux measured in a triple-GEM detector.

11.2 Discharges

Gaseous detectors may experience occasional or persistent breakdowns when exceeding a threshold value of voltage. Several factors determine the appearance of discharges:

- Manufacturing imperfections, such as metal smidgens or sharp edges;
- Dust particles or flakes, resulting from inadequate or poor cleaning (see 10.1);
- Improper design: presence of conductive paths between electrodes at different potentials, often on the surface of the frames, or to the pins and bolts used for assembly;
- Exceeding the dielectric rigidity of the gas;
- Dynamic instabilities connected to high rates, positive ions density, surface charging-up.

Of the abovementioned sources of discharge, the last two are basic in the physics of charge multiplication, and are governed by the design, gas choice and operating conditions.

The effect of a discharge on the detector depends on the energy involved, going from a temporary decrease of efficiency to permanent damages. For two electrodes at a difference of potential ΔV, the stored energy depends on the inter-electrode capacitance C, $E=C\ \Delta V^2$. To reduce the available energy, electrodes may be segmented and individually connected to the power supply through high-value protection resistors; depending on the system design, under the effect of a discharge the potentials are temporarily reduced or cut-off until the system is reset.

11.3 Long-term irradiation and aging

Under sustained long-term irradiation, even in absence of discharges, gaseous detectors may suffer a gradual loss of efficiency and an increase of dark current. The detector lifetime, loosely defined as the time lapse before a noticeable degradation of performances, varies by many orders of magnitude depending on the detector design, operating gases and conditions. The major process leading to degradation is the formation under avalanching conditions of deposits on the electrodes of thin insulating layers generated by the polymerization of organic gas molecules used as quenchers or from the outgassing of materials used for manufacturing. Multiwire and microstrip chambers are especially susceptible to this process, due to the small area of the anodes (Va'vra, 2003)(Capeans, 2003); the absence of thin electrodes and a better control of pollutants in modern MPGDs has extended their lifetime by several orders of magnitude, see for example chapter 5.11 in (Sauli, 2021).

Organic gas molecules such as the hydrocarbons are particularly prone to induce fast aging. Addition to the gas mixture of non-polymerizing vapors, such as alcohols and methylal, permitted to extend the early detectors lifetime at the cost of an increased complexity of the gas mixing systems; use of inorganic quenchers such as CO_2 and CF_4, while eliminating direct polymerization, has exposed the dominant role of even very small contaminations due to manufacturing materials, silicone being one of the most obnoxious and ubiquitous compounds found in deposits. Extended tables of outgassing properties of materials and adhesives are given in Ref. (Capeans, 2003).

An example of setup used for aging tests is shown schematically in Figure 11-4 (Bouclier, Capeáns, *et al.*, 1994). It includes a high-intensity collimated radiation source, X-rays or radioactive, the detector under test and one or more single-wire proportional counters for monitoring the incident flux. Various kinds of gas monitors, such as hygrometers and oxygen sensors are added to certify the gas quality before and after the exposed detector; a gas chromatograph, a mass spectrometer and an electron capture device may complement the diagnostic tools. As it has been found that residues of oils used for manufacturing can strongly affect the results, all mechanical parts as well as the connection pipes should be thoroughly degreased, with preference given to metallic or non-hygroscopic plastic pipes, see Chapter 7.

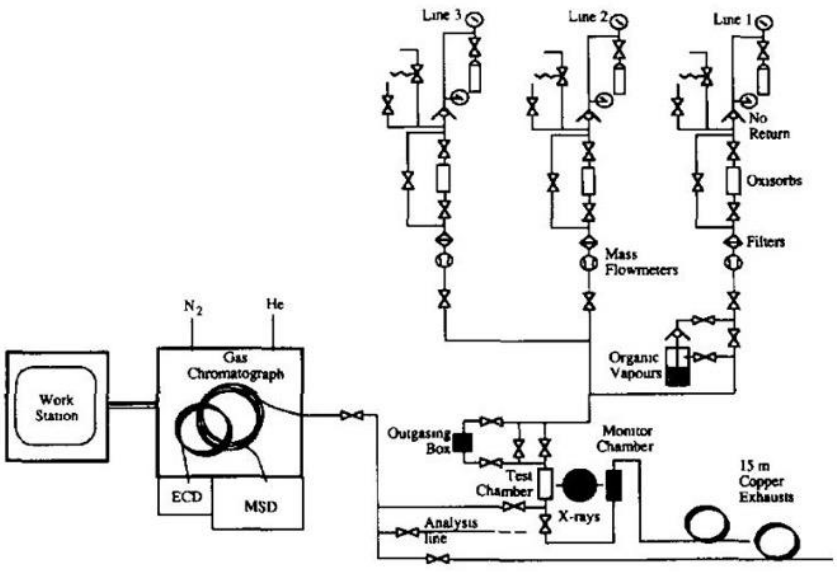

Figure 11-4: Setup for systematic aging tests (Bouclier, Capeáns, *et al.*, 1994).

The aging test procedure consists in irradiating a virgin detector with a constant flux of radiation, recording the gain at regular intervals at a reduced source intensity. As the area of the exposed surface plays a role in the result, it should be as large as possible, compatibly with the maximum value of the current that can be sustained by the detector without affecting the operating voltages. A continuous irradiation at low rate on a separate region of the detector can be used to monitor the stability of gain; the same function is performed by open-flow single-wire counters placed before and after the detector under test.

As the detector's lifetime appears to depend from the charge flow, the gain is usually expressed as a function of collected charge per unit surface and can vary from μC to C/cm^2. For wire chambers, a common unit is the collected charge for unit length of the wire (C/mm); the corresponding flux can be computed taking into account the wire spacing.

Selected from a vast number of results, Figure 11-5 and Figure 11-6 and Figure 11-7 are representative examples of dependence of gain from accumulated charge in various conditions.

It should be stressed that, in order to realize lifetime estimates in reasonable time, the aging tests are performed at radiation fluxes orders of magnitude larger than those met in experiments, raising serious concerns about the applicability of the results in normal operating conditions. Even if all precautions are taken to prevent changes in the operating voltages under extreme conditions, the high space charge density of the avalanches may induce field distortions and modifications of the polymer's formation chemistry. Comparison of aging measurements at different rates generally confirm that high charge densities provide more optimistic results.

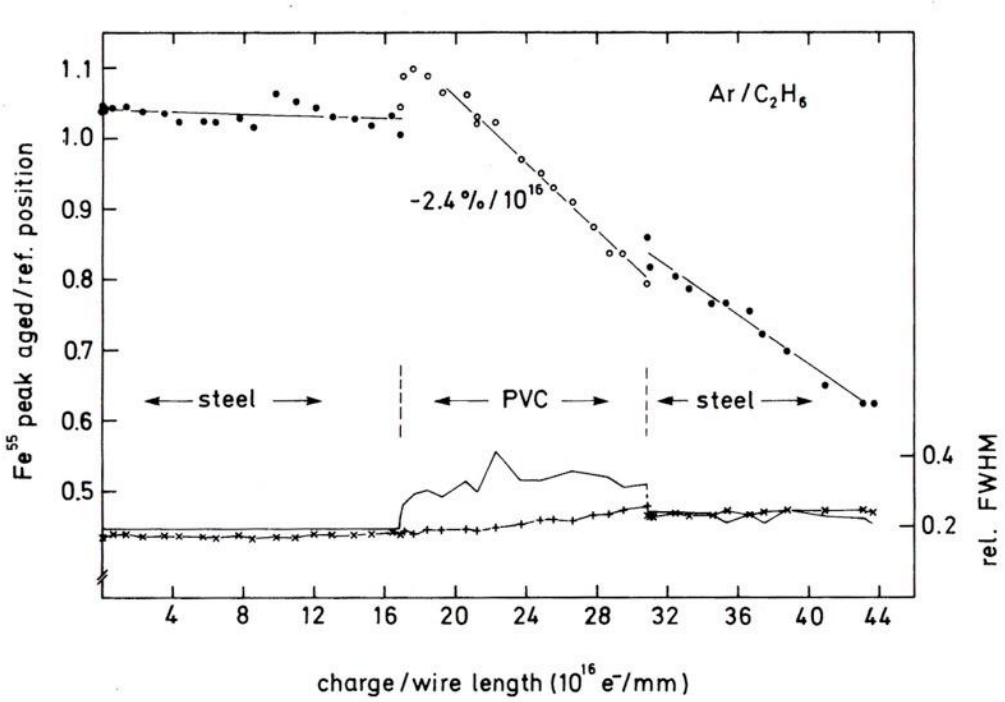

Figure 11-5: Effect of adding a PVC tube segment on aging; the gain drop charge persists after removal of the plastic tube (Kotthaus, 1986).

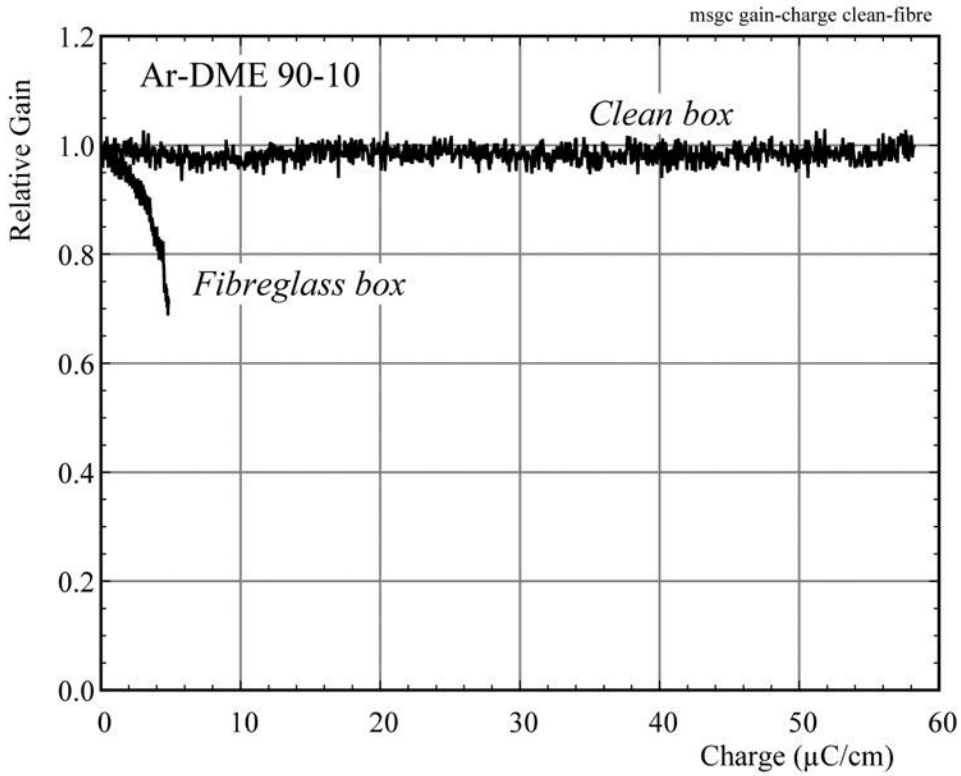

Figure 11-6: Aging of MSGCs in a fiberglass or "clean" assembly (Bouclier, Garabatos, *et al.*, 1994).

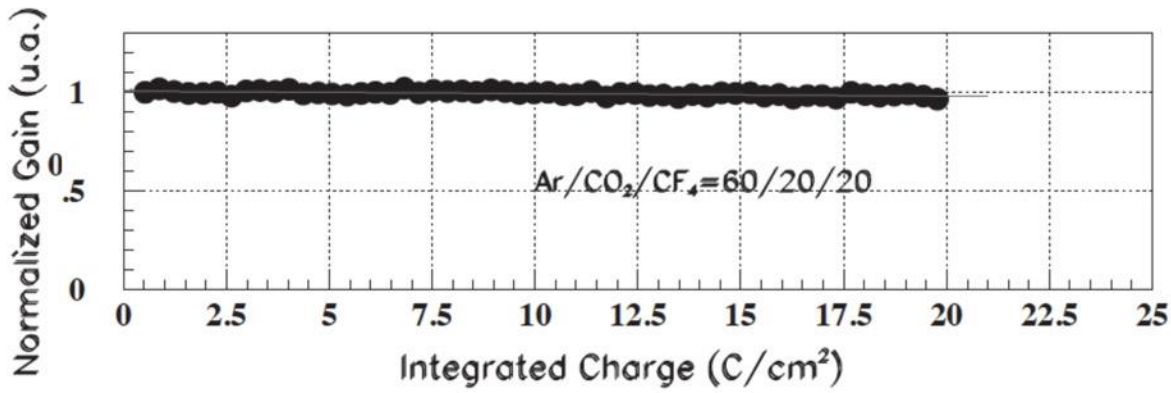

Figure 11-7: Normalized gain as a function of collected charge for a triple-GEM detector (Alfonsi *et al.*, 2004).

11.4 Radiation damage of materials

Structural and morphological changes are induced in materials by strong irradiation; the damages are particularly severe due to neutrons, and for inert materials begin to appear at fluences above ~10^{18} n cm^{-2}. Numerous studies have been published at CERN since the early operation of the accelerators complex, and are included in several reports (CERN-79-04, 1979)(CERN-89-12, 1989)(CERN-98-01, 1998), see Figure 11-8, Figure 11-9 and Figure 11-10. Measured irradiating the materials with mixed neutron and gamma fields at nuclear reactors, the exposures are given in Gy.

Motivated by the increased radiation environment of the high-luminosity LHC upgrade, a recent study extends the studies to extreme conditions, Figure 11-11 (MaxRad, 2020).

It should be noted that the discharge and polymerization processed described in the previous section intervene to degrade the detectors operation much before they suffer from structural material damages.

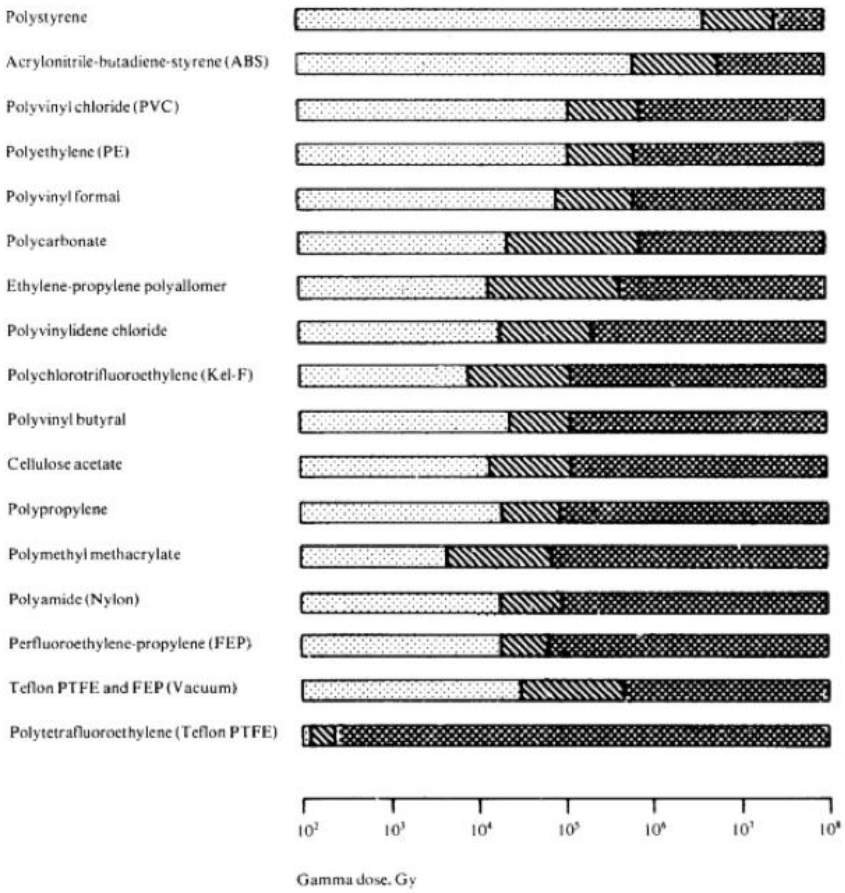

Figure 11-8: Halogen-free cable insulating materials (CERN-79-04, 1979)(CERN-89-12, 1989).

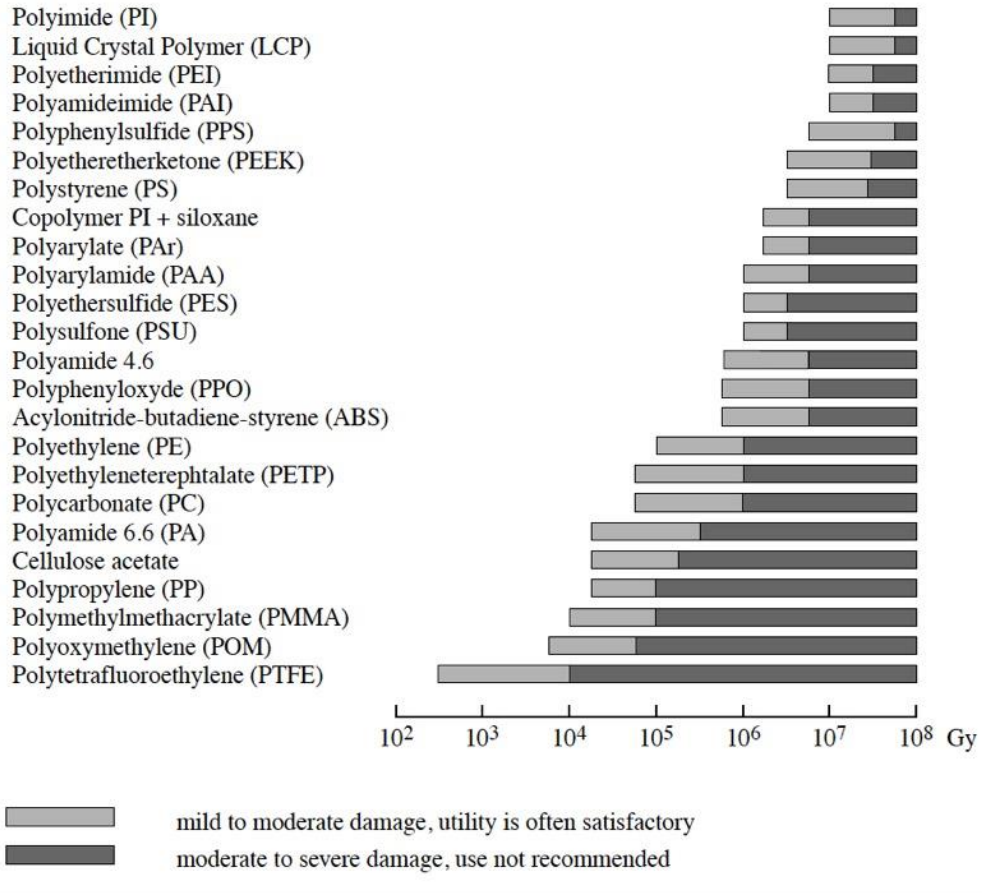

Figure 11-9: Rigid thermoplastic (CERN-98-01, 1998).

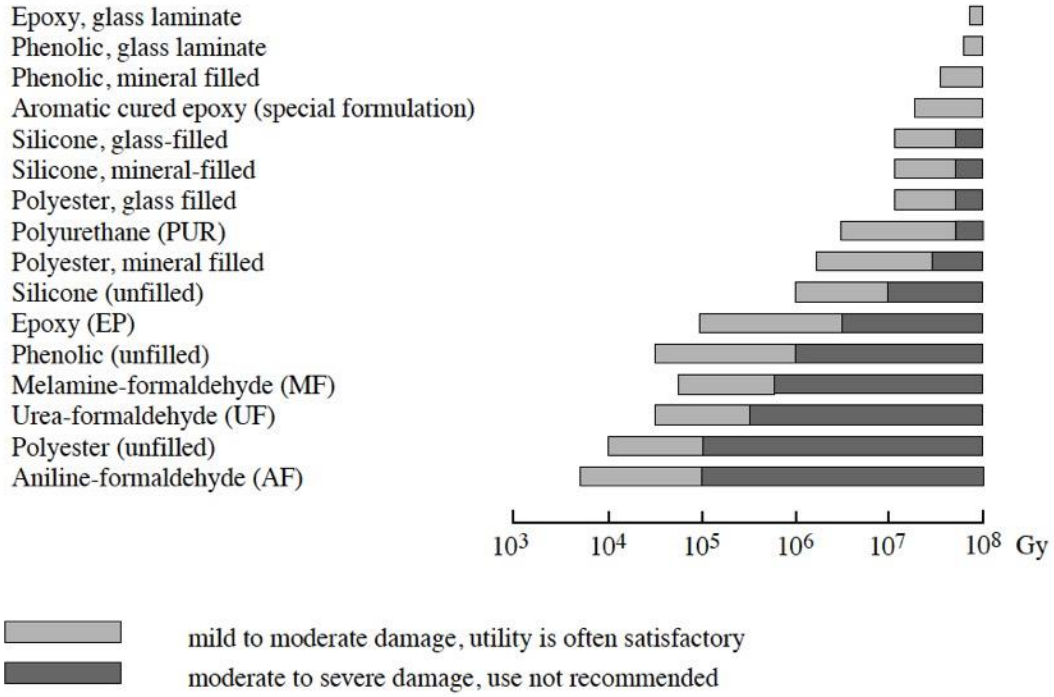

Figure 11-10: Thermoset resins and composites (CERN-98-01, 1998).

Manufacturer	Material	Max dose [MGy]
Dymax	9-20801	7
Huntsman	Araldite 2011	7
Huntsman	Araldite 2020	7
Loctite - Henkel	EA 9396 AERO	7
Al Technology	EG7655	7
Al Technology	EG7655 LV	7
Al Technology	EG7658	7
UHU	Endfest 300	7
Polytec PT	EP 601-LV	0
Carbonwinkel	Epoxyhars L + Verharder W 300	2.5
Loctite - Henkel	F 112 (True Blue)	7
Andover Corporation	FH 5313(Old Epolite)	7
Epoxy-Technology	H20E-100C Cure	5
Epoxy-Technology	H20E-60C Cure	5
Nitto Denko Corporation	No. 5600	5
Scientifica	PCE-FILM-SA80	2.5
Scientifica	PCE-HT 3350/57	2.5
Scientifica	PCE-HTC-1800	2.5
Andover Corporation	PL 7006 (New Epolite)	7
Poly-Service	Poly-Pox THV500 + Harder 355	2.5
Dow Corning	SE4445 (RT cure)	10
Sicomin	SR1126 + Hardener 8202	1
Epoxy-Technology	T7109-19	15
Polytec PT	TC418	15
Polytec PT	TC437	5
Tesa	Tesafix 4962	7
3M	VHB5909	7

Figure 11-11: Materials and adhesives for extreme radiation environments (MaxRad, 2020).

12 SOFTWARE SIMULATION TOOLS

MAGBOLTZ	Charge transport and multiplication
GARFIELD++	Two-and three-Dimensional detector simulation
BOLSIG+	Charge transport and multiplication
MAXWELL	Low frequency Electromagnetic Field Simulation
COMSOL MULTIPHYSICS	Physics-Based Designs and Processes
GEANT4	Toolkit for the simulation of the passage of particles through matter
FLUKA	Particle physics MonteCarlo simulation package
HEED	Modeling of ionization produced by fast charged particles in gases
DEGRAD	Transport of electrons in gas mixtures
GATE	Simulation Toolkit for PET and SPECT (Jan *et al.*, 2004)(Jan *et al.*, 2011)

13 DATA BASES

EVERYTHING:
https://www.wikipedia.org
UNITS CONVERTER
https://www.unitconverters.net/
PERIODIC TABLE OF THE ELEMENTS
https://periodictable.com
TABLES OF RADIOACTIVE ISOTOPES
http://nucleardata.nuclear.lu.se/toi/
CRC HANDBOOK OF CHEMISTRY AND PHYSICS ONLINE
http://hbcponline.com.ezproxy.cern.ch/faces/contents/ContentsResults.xhtml
PLASTIC MATERIALS PROPERTIES
https://omnexus.specialchem.com/selectors
VOLUME RESISTIVITY OF PLASTICS
https://omnexus.specialchem.com/polymer-properties/properties/volume-resistivity#values
REVIEW OF PARTICLE PROPERTIES
https://pdg.lbl.gov/index.html
STOPPING POWER & RANGE FOR ELECTRONS, PROTONS AND HELIUM
https://www.nist.gov/pml/stopping-power-range-tables-electrons-protons-and-helium-ions
X-RAY FORM FACTORS, ATTENUATION AND SCATTERING TABLES
https://physics.nist.gov/PhysRefData/FFast/html/form.html
NIST XCOM: PHOTON CROSS SECTION DATABASE
https://www.nist.gov/pml/xcom-photon-cross-sections-database
NIST X-RAY MASS ATTENUATION COEFFICIENTS
https://www.nist.gov/pml/x-ray-mass-attenuation-coefficients
X-RAY INTERACTIONS TABLES AND PLOTS
https://escholarship.org/content/qt9wh2w9rg/qt9wh2w9rg.pdf
NEUTRON CROSS SECTIONS OF THE ELEMENTS
https://periodictable.com/Properties/A/NeutronCrossSection.html
IRRADIATION FACILITIES DATABASE
https://irradiation-facilities.web.cern.ch/php/database.php
PLASMA DATA EXCHANGE PROJECT LXCat
https://us.lxcat.net/home/

14 AUTHOR'S RECENT BOOKS

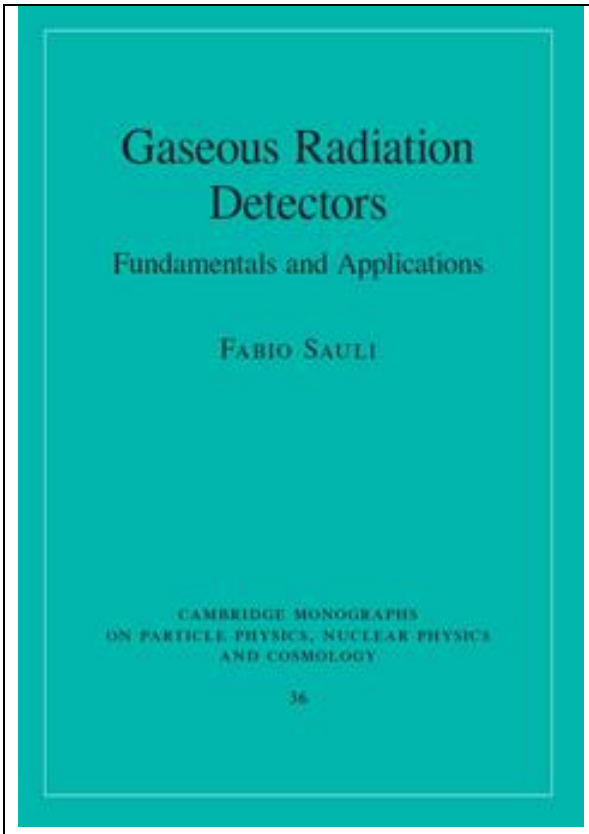

CONTENTS
Introduction
Electromagnetic interactions of charged particles with matter
Interactions of photons and neutrons with matter
Drift and diffusion of charges in gases
Collisional excitations and charge multiplication in uniform fields
Parallel plate counters
Proportional counters
Multiwire proportional chambers
Drift chambers
Time projection chambers
Multitube arrays
Resistive plate chambers
Micro-pattern gas detectors
Cherenkov ring imaging
Miscellaneous detectors and applications
Time degeneracy and aging
Further reading
References
Index

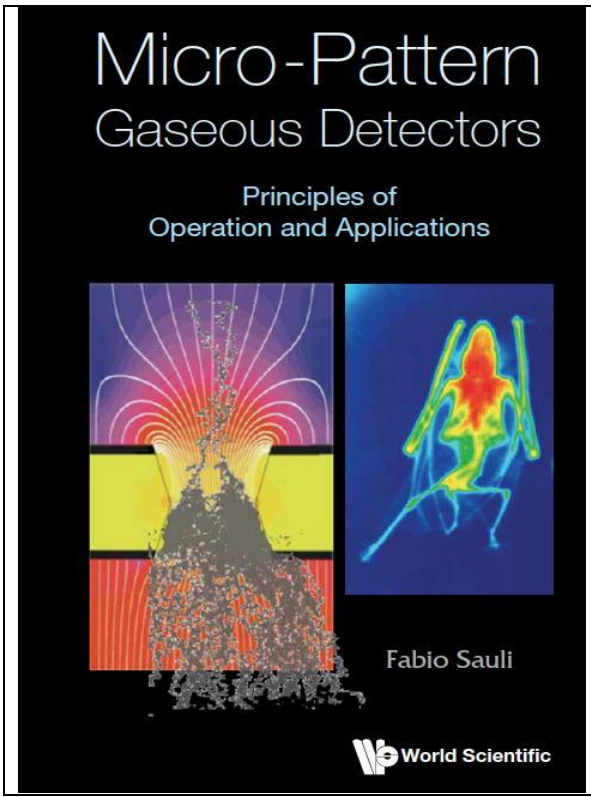

CONTENTS:
One Century of Gaseous Detectors
Micro-Strip Gas Counters
Micro-Pattern Gas Detectors
MICROMEGAS
Gas Electron Multiplier
MPGD Readout of Time Projection Chambers
UV Photons Detection and Localization
Advanced Micro-Pattern Devices
Neutron Detectors
Cryogenic and Dual-Phase Detectors
Optical Imaging Chambers
Future challenges and prospects
Further readings on Gaseous Detectors
References
Index

15 BIBLIOGRAPHY

Abbrescia, M. *et al.* (2005) 'Cosmic ray tests of double-gap resistive plate chambers for the CMS experiment', *Nucl. Instr. and Meth. in Phys. Res. A*, 550, pp. 116–126.

Abdrakhmanov, M. *et al.* (1992) 'Fast UV-luminescence in caesium iodide at high temperatures', *Journal of Luminescence*, 54, pp. 197–201.

Afanasiev, S. *et al.* (1999) 'The NA49 large acceptance hadron detector', *Nucl. Instr. and Meth. in Phys. Res. A*, 430, pp. 210–244.

Al-Rashdi, B. *et al.* (2021) 'Numerical Study of Transport Properties of Ar-based Ternary Gas Mixtures and Their Gain in GEM Detectors', *Applied Mathematical Sciences*, 15(5), pp. 225–237.

Alfonsi, M. *et al.* (2004) 'High-rate particle triggering with triple-GEM detector', *Nucl. Instr. and Meth. in Phys. Res. A*, 518, p. 106.

ALICE Addendum to the technical proposal Electromagnetic Calorimeter (2006) *CERN-LHCC-2006-014*.

Alidra, M. *et al.* (2021) 'The MATHUSLA test stand', *Nucl. Instr. and Meth. in Phys. Res. A*, 985, p. 164661.

Alme, J. *et al.* (2010) 'The ALICE TPC, a large 3-dimensional tracking device with fast readout for ultra-high multiplicity events', *Nucl. Instr. and Meth. in Phys. Res. A*, 622, pp. 316–367.

AMPTEK (2020) 'Mini X-Ray tube', *https://www.amptek.com/products/x-ray-sources/mini-x2-ray-tube*.

Arfaoui, S., Joram, C. and Casella, C. (2015) *Characterisation of a 90Sr based electron monochromator, PH-EP-Tech-Note-2015-003*.

Arnold, R. *et al.* (1988) 'A ring imaging Cherenkov detector, the DELPHI Barrel RICH Prototype. Part A: Experimental studies of the detection efficiency and the spatial resolution', *Nucl. Instr. and Meth. in Phys. Res. A*, 270, pp. 255–288.

ASTAR (2020).

Au, J. W. *et al.* (1993) 'The valence shell photoabsorption of the linear alchanes', *Chem. Phys.*, 173, p. 209.

Bachmann, S. *et al.* (1999) 'Charge amplification and transfer processes in the gas electron multiplier', *Nucl. Instr. and Meth. in Phys. Res. A*, 438, pp. 376–408.

Behling, R. and Grüner, F. (2018) 'Diagnostic X-ray sources-present and future', *Nucl. Instr. and Meth. in Phys. Res. A*, 878, pp. 50–57.

Beingessner, S. P. *et al.* (1988) 'Alaser calibration system for the UA1 central detector at high luminosity (ACL)', *Nucl. Instr. and Meth. in Phys. Res. A*, 263, pp. 26–30.

Bélanger, G., Sauvageau, P. and Sandorfy, C. (1969) ' The far-ultraviolet spectra of perfluoro-normal-paraffin', *Chem. Phys. Lett.*, 3, p. 649.

Bencivenni, G. *et al.* (2002) 'A triple GEM detector with pad readout for high rate charged particle triggering', *Nucl. Instr. and Meth. in Phys. Res. A*, 488, pp. 493–502.

Benlloch, J. *et al.* (1998) 'Development of the Gas Electron Multiplier (GEM)', *IEEE Trans. Nucl. Sci.*, NS-45, pp. 234–243.

Berlman, I. B. (1971) *Handbook of fluorescence spectra of aromatic molecules*. Academic Press.

Berlman, I. B., Steingraber, O. J. and Benson, M. J. (1968) 'Hydrogen flash lamps', *Rev. Sci. Instrum.*, 39, pp. 54–61.

BOLSIG+ (2019) *http://www.bolsig.laplace.univ-tlse.fr*.

Bouclier, R. *et al.* (1983) 'Progress in Cherenkov ring imaging: Part 1. Detection and localization of photons with the multistep proportional chamber', *Nucl. Instr. and Meth.*, 205, pp. 403–423.

Bouclier, R., Garabatos, C., *et al.* (1994) 'Ageing studies with microstrip gas chambers', *Nucl. Instr. and Meth. in Phys. Res. A*, 348, pp. 109–118.

Bouclier, R., Capeáns, M., *et al.* (1994) 'Results of wire chamber ageing tests with CH4− and DME-based gas mixtures', *Nucl. Instr. and Meth. in Phys. Res. A*, 346(1–2), pp. 114–119.

Bouclier, R. *et al.* (1995) 'Development of micro-strip gas chambers for high rate operation', *Nucl. Instr. and Meth. in Phys. Res. A*, 367(1–3), pp. 168–172.

Breskin, A. *et al.* (1975) 'Recent observations and measurements with high-accuracy drift chambers', *Nucl. Instr. and Meth.*, 124, pp. 189–214.
Brücken, E. *et al.* (2021) 'Hole misalignment and gain performance of Gaseous Electron Multipliers', *Nucl. Instr. and Meth. in Phys. Res. A*, 1002, p. 165271.
Brunbauer, F. (2018) *Dissertation Anwendungen von Eigenschaften szintillierender Gase in optisch ausgelesenen GEM-basierten Detektoren, https://repositum.tuwien.at/handle/20.500.12708/1833*.
Brunbauer, F. *et al.* (2018) 'Radiation imaging with optically read out GEM-based detectors', *JINST*, 13, p. T02006.
Brunbauer, F. M. (2020) 'Optical readout for imaging applications', in *GDD Meeting 18.11.20*.
Brunbauer, F. M. *et al.* (2020) 'Radiation imaging with glass Micromegas', *Nucl. Instr. and Meth. in Phys. Res. A*, 955, p. 163320.
Calvert, J. C. and Pitts, J. N. (1966) *Photochemistry*. New York: Wiley.
Capeans, M. (2003) 'Aging and materials: lessons for detectors and gas systems', *Nucl. Instr. and Meth. in Phys. Res. A*, 515, pp. 73–88.
CERN-79-04 (1979) *Compilation of radiation damage test data Cable insulating materials, https://cds.cern.ch/record/133188*.
CERN-89-12 (1989) *Compilation of radiation damage test data Halogen-free cable-insulating materials, https://cds.cern.ch/record/205520?ln=en*.
CERN-98-01 (1998) *Compilation of radiation damage test data Thermoset and thermoplastic resins, composite materials, https://cds.cern.ch/record/357576*.
CERN (2020a) 'Gamma Irradiation Facility GIF++', *https://ep-dep-dt.web.cern.ch/irradiation-facilities/gif*.
CERN (2020b) 'Radioactive Sources Management Service', *https://cern.service-now.com/service-portal?id=service_element&name=radiactive-source*.
CERN (2020c) 'The Isolde facility', *https://isolde.web.cern.ch/isolde-facility*.
CERN (2020d) 'Use of Radioactive Sources', *https://edms.cern.ch/ui/file/856968/LAST_RELEASED/Brochure_EN-ld.pdf*.
'CERN Facilities Data Base' (2020) *https://irradiation-facilities.web.cern.ch/php/database.php*.
Chan, W. F., Cooper, G. and Brion, C. E. (1993) 'The electronic spectrum of carbon dioxide. Discrete and continuum photoabsorption oscillator strengths (6–203 eV) ', *Chem. Phys.*, 178, p. 401.
Charpak, G. *et al.* (1979) 'Detection of far-ultraviolet photons with the multistep avalanche chamber. Application to Cherenkov light imaging and to some problems in high-energy physics', *Nucl. Instr. and Meth.*, 164, pp. 419–433.
Charpak, G. *et al.* (1988) 'Studies of light emission by continuously sensitive avalanche chambers', *Nucl. Instr. and Meth. in Phys. Res. A*, 269, pp. 142–148.
Charpak, G. *et al.* (2002) 'Micromegas, a multipurpose gaseous detector', *Nucl. Instr. and Meth. in Phys. Res. A*, 478, pp. 26–36.
Charpak, G., Rahm, D. and Steinert, H. (1970) 'Some developments in the operation of Multiwire Proportional Chambers', *Nucl. Instr. and Meth.*, 80, pp. 13–34.
Christophorou, L. G. (1971) *Atomic and Molecular Radiation Physics*. London: Wiley.
Corradi, G., Murtas, F. and Tagnani, D. (2007) 'A novel High-Voltage System for a triple GEM detector', *Nucl. Instr. and Meth. in Phys. Res. A*, 572, pp. 96–97.
Cortez, A. F. V. (2017) 'Experimental ion mobility measurements in Xe-CO 2', *JINST*, 12, p. P06012.
Cross, W. G., Ing, H. and Freedman, N. (1983) 'A short atlas of beta-ray spectra', *Phys. Med. Biol.*, 28, p. 1251.
Derré, J. *et al.* (2000) 'Fast signals and single electron detection with a MICROMEGAS photodetector', *Nucl. Instr. and Meth. in Phys. Res. A*, 449, pp. 314–321.
Dion, M. P., Martoff, C. J. and Hosack, M. (2010) 'On the mechanism of Townsend avalanche for negative molecular ions', *Astroparticle Physics*, 33, pp. 216–220.

Druyvesteyn, M. J. and Penning, F. M. (1940) 'The Mechanism of Electrical Discharges in Gases of Low Pressure', *Rev. Mod. Phys.* , 12, p. 87.
Duerdoth, P. *et al.* (1975) 'Measurements of the time resolution and rate capability of Multiwire Proportional Chambers', *Nucl. Instr. and Meth.*, 129, p. 461.
ESTAR (2020) *https://physics.nist.gov/PhysRefData/Star/Text/ESTAR.html*.
European Spallation Source (2020) *https://europeanspallationsource.se*.
Fischle, H., Heintze, J. and Schmidt, B. (1991) 'Experimental determination of ionization cluster size distributions in counting gases', *Nucl. Instr. and Meth. in Phys. Res. A*, 301, pp. 202–214.
Fomin, N. *et al.* (2015) 'Fundamental neutron physics beamline at the spallation neutron source at ORNL', *Nucl. Instr. and Meth. in Phys. Res. A*, 773, pp. 45–51.
Fraga, M. *et al.* (2003) 'The GEM scintillation in He-CF4, Ar-CF4, Ar-TEA and Xe-TEA mixtures', *Nucl. Instr. and Meth. in Phys. Res. A*, 504, pp. 88–92.
Franchino, S. *et al.* (2016) 'Effects of high charge densities in multi-GEM detectors', *IEEE Nuclear Sci. Symp. 2015*. IEEE, pp. 1–5.
Friedman, H. (1960) 'The Sun's Ionizing Radiation', in Ratcliffe, J. (ed.) *Physics of the Upper Atmosphere*. New York: Academic Press.
Gendreau, K. *et al.* (2015) 'MINATURIZED HIGH-SPEED MODULATED X-RAY SOURCE'.
Gkotse, B. and Gorine, G. (2020) 'AIDA-2020 Irradiation Facilities Website and Database User Manual', *https://cds.cern.ch/record/2244674/files/AIDA-2020-NOTE-2017-002.pdf*.
Gola, M. *et al.* (2020) 'Performance of the triple GEM detector built using commercially manufactured GEM foils in India', *Nucl. Instr. and Meth. in Phys. Res. A*, 951, p. 162967.
Gottschalk, B. *et al.* (1993) 'Multiple Coulomb scattering of 160 MeV protons', *Nucl. Instr. and Meth. in Phys. Res. B*, 74, pp. 467–490.
Graybill, J. R. *et al.* (2020) 'Extreme ultraviolet photon conversion efficiency of tetraphenyl butadiene', *Applied Optics*, 59(4), p. 1217.
Grazzi, S. *et al.* (2020) 'AstrO: A portable cosmic ray telescope', *Nucl. Instr. and Meth. in Phys. Res. A*, 976, p. 164275.
Groom, D. E. (2019) 'Commonly Used Radioactive Sources', in *Review of Particle Physics*.
H. Muller (2022) 'uAPIC a fast preamplifier-shaper-trigger box for R&D on detectors', *To be published*.
H.Uhrmann, W.Gaberl and Zimmermann, H. (2008) 'A low-noise current preamplifier in 120 nm CMOS technology', *Adv Radio Sci*, 6, pp. 213–217.
Hallewell, G. (2011) 'Aspects of the use of saturated fluorocarbon fluids in high energy physics', *Nucl. Instr. and Meth. in Phys. Res. A*. Elsevier, 639, pp. 207–210.
Hildén, T. *et al.* (2014) 'Optical quality assurance of GEM foils', *Nucl. Instr. and Meth. in Phys. Res. A*, 770, pp. 113–122.
Hilke, H. J. (1986) 'Detector calibration with lasers -A review', *Nucl. Instr. and Meth. in Phys. Res. A*, 252, pp. 169–179.
Holroyd, R. A. *et al.* (1987) 'Measurement of the Absorption Length and Absolute Quantum Efficiency of TMAE and TEA from Threshold to 120 nm', *Nucl. Instr. and Meth. in Phys. Res. A*, 261, pp. 440–444.
Hubricht, G. *et al.* (1985) 'Ionization of counting gases and ionizable gaseous additives in proportional chambers by UV lasers', *Nucl. Instr. and Meth. in Phys. Res. A*, 228, p. 327.
Jan, S. *et al.* (2004) 'GATE: a simulation toolkit for PET and SPECT', *Phys Med Biol*, 49, pp. 4543–4561.
Jan, S. *et al.* (2011) 'GATE V6: a major enhancement of the GATE simulation platform enabling modelling of CT and radiotherapy', *Phys Med Biol*, 56, pp. 881–901.
Kalliokoski, M. *et al.* (2012) 'Optical scanning system for quality control of GEM-foils', *Nucl. Instr. and Meth. in Phys. Res. A*, 664, pp. 223–230.
Keirim-Markus, I. B. (1972) 'The relative luminescence yield of gas proportional counters', *Instruments and Experimental Techniques*, 15(5), p. 1337.
Ketzer, B. *et al.* (2001) 'GEM Detectors for COMPASS', *IEEE Transactions on Nuclear Science*,

48(4), pp. 1065–1069.
Klein, H. (2020) *Spallation Neutron Sources, Int. Linac Conference*.
Knasel, T. M. (1970) 'Accurate calculation of radiation lengths', *Nucl. Instr. and Meth.*, 83, pp. 217–220.
Kotthaus, R. (1986) 'A laboratory study of radiation damage to drift chambers', *Nucl. Instr. and Meth.*, A252, p. 531.
Kuźniak, M. and Szelc, A. M. (2020) 'Wavelength Shifters for Applications in Liquid Argon Detectors', *Instruments*, 5, p. 4.
Lefeuvre, G. *et al.* (2007) 'Absolute measurement of the nitrogen fluorescence yield in air between 300 and 430 nm', *Nucl. Instr. and Meth. in Phys. Res. A*, 578, pp. 78–87.
Lehraus, I., Matthewson, R. and Tejessy, W. (1982) 'dE/dx MEASUREMENTS IN Ne, Ar, Kr, Xe AND PURE HYDROCARBONS', *Nucl. Instr. and Meth.*, 200, pp. 199–210.
Leidner, J., Murtas, F. and Silari, M. (2021) 'Medical applications of the GEMPix', *Applied Sciences (Switzerland)*, 11(1), pp. 1–20.
Light_Sources (2020) 'Lambda Scientific', *https://lambdasci.com*.
Ligtenberg, C. *et al.* (2021) 'On the properties of a negative-ion TPC prototype with GridPix readout', *Nucl. Instr. and Meth. in Phys. Res. A*, 1014, p. 165706.
LXCat (2020) *https://us.lxcat.net/home/*.
M. Gupta (2010) *Calculation of radiation length in materials, PH-EP-Tech-Note-2010-013*.
Mantel, J. (1972) 'The Beta Ray Spectrum and the Average Beta Energy of Several Isotopes of Interest in Medicine and Biology', *International Journal of Applied Radiation and Isotopes*. Pergamon Press Printed m Northern Ireland, 23, pp. 407–413.
Margato, L. *et al.* (2004) 'Performance of an optical readout GEM-based TPC', *Nucl. Instr. and Meth. in Phys. Res. A*, 535, pp. 231–235.
Marques, A. P. P. *et al.* (2020) 'Minimizing distortions with sectored GEM electrodes', *Nucl. Instr. and Meth. in Phys. Res. A*, 961, p. 163673.
MaxRad (2020) *Materials and Adhesives for Extreme Radiation Environments, https://maxrad.web.cern.ch/maxrad/*.
McDaniel, E. W. and Mason, E. A. (1973) *The mobility and diffusion of ions in gases*. New York: Wiley & Sons.
Meinschad, T., Ropelewski, L. and Sauli, F. (2004) 'GEM-based photon detector for RICH applications', *Nucl. Instr. and Meth. in Phys. Res. A*, 535, pp. 324–329.
Mitsubishi (2020) *PET, https://www.m-petfilm.de/en/hostaphan-polyester-films/*.
Molière, G. (1947) 'Theorie der Streuung schneller geladenen Teilchen I Einzelstreuung am abgeschirmten Coulomb-Field', *Z. Naturforsch. 2a*, pp. 133–145.
Morozov, A. *et al.* (2010) 'Photon yield for ultraviolet and visible emission from CF4 excited with alpha-particles', *Nucl. Instr. and Meth. in Phys. Res. B*, 268, pp. 1456–1459.
Morozov, A. *et al.* (2012) 'Secondary scintillation in CF4: Emission spectra and photon yields for MSGC and GEM', *JINST*, 7(2), p. P02008.
Muraro, A. *et al.* (2021) 'MBGEM: a stack of borated GEM detector for high efficiency thermal neutron detection', *The European Physical Journal Plus*, 136, p. 742.
Muraro, A. and Croci, G. (2019) 'Review of MPGD applications for neutron detection', *JINST*, 14, p. C04005.
Murtas, F. (2020) 'The GEMPix detector', *Radiation Measurements*, 138, p. 106421.
Nitti, M. A. *et al.* (2008) 'Performance analysis of poly-, nano-and single-crystalline diamond-based photocathodes', *Nucl. Instr. and Meth. in Phys. Res. A*, 595, pp. 131–135.
Omnexus (2020) 'Plastic materials properties', *https://omnexus.specialchem.com/selectors*.
P L Policarpo, A. J. *et al.* (1974) 'Detection of soft X-rays with a Xenon Proportional Scintilation Counter', *Nucl. Instr. and Meth.*, 118, pp. 221–226.
Pacella, D. *et al.* (2013) 'GEM gas detectors for soft X-ray imaging in fusion devices with neutron-gamma background', *Nucl. Instr. and Meth. in Phys. Res. A*, 720, pp. 53–57.
Panalytical (2007) 'X-Ray Diffraction Glass Tubes',

http://minerva.union.edu/hollochk/rigaku/docs/X-ray_tube_manual.pdf.
Patra, R. N. *et al.* (2017) 'Measurement of basic characteristics and gain uniformity of a triple GEM detector', *Nucl. Instr. and Meth. in Phys. Res. A*, 862, pp. 25–30.
Peisert, A. and Sauli, F. (1984) 'DRIFT AND DIFFUSION OF ELECTRONS IN GASES: A COMPILATION', *CERN YELLOW REPORT 84-08*.
Petri, A. R. *et al.* (2017) 'Measurement of the first Townsend ionization coefficient in a methane-based tissue-equivalent gas', *Nucl. Instr. and Meth. in Phys. Res. A*. Elsevier, 849, pp. 31–40.
Pfeiffer, D. *et al.* (2017) 'The radiation field in the Gamma Irradiation Facility GIF++ at CERN', *Nucl. Instr. and Meth. in Phys. Res. A*, 866, pp. 91–103.
Policarpo, A. (1977) 'The Gas Scintillation Proportional Counter', *Space Sci. Instr.*, 3, p. 77.
Policarpo, A. J. P. L. (1981) 'Light production and gaseous detectors', *Physica Scripta*, 23(4), pp. 539–549.
Prelas, M. A. *et al.* (2014) 'A review of nuclear batteries', *Progress in Nuclear Energy*, 75, pp. 117–148.
Procureur, S. (2018) 'Muon imaging: Principles, technologies and applications', *Nucl. Instr. and Meth. in Phys. Res. A*, 878, pp. 169–179.
PSTAR (2020) *https://physics.nist.gov/PhysRefData/Star/Text/PSTAR.html*.
Resnati, F. (2016) *Triggerable and time-tagged X-ray generator*.
Roy, S. *et al.* (2019) 'Stability study of gain and energy resolution for GEM detector', *Nucl. Instr. and Meth. in Phys. Res. A*, 936, pp. 485–487.
Said, K. I. and Green, G. W. (1977) 'Optical properties of caesium iodide in the vacuum ultraviolet', *Solid State Physics*, (10), pp. 179–188.
Saito, K. *et al.* (2002) 'Absolute number of scintillation photons emitted by alpha particles in rare gases', *IEEE Trans. Nucl. Sci.*, 49 I(4), pp. 1674–1680.
Sauli, F. (1977) 'Principles of Operation of Multiwire Proportional and Drift Chambers', *CERN 77-09*.
Sauli, F. (1986) 'Ultraviolet photon detection and localization with Multiwire Chambers', *Nucl. Instr. and Meth. in Phys. Res. A*, 248(1), pp. 143–149.
Sauli, F. (2014) *Gaseous Radiation Detectors: Fundamentals and Applications*. Cambridge University Press.
Sauli, F. (2016) 'The gas electron multiplier (GEM): Operating principles and applications', *Nucl. Instr. and Meth. in Phys. Res. A*, 805, pp. 2–24.
Sauli, F. (2018) 'Radiation imaging with gaseous detectors', *Nucl. Instr. and Meth. in Phys. Res. A*, 878, pp. 1–9.
Sauli, F. (2021) *Micro-Pattern Gaseous Detectors: Principles of Operation and Applications*. Singapore: World Scientific Publishing.
Schilly, P. *et al.* (1970) 'Construction and performance of large multiwire proportional chambers', *Nucl. Instr. and Meth.*, 91, p. 221.
Schultz, G., Charpak, G. and Sauli, F. (1977) 'Mobilities of positive ions in some gas mixtures used in proportional and dtift chambers', *Revue de Physique Appliquee*, (12), p. 67.
Séguinot, J. *et al.* (1990) 'Reflective UV photocathodes with gas-phase electron extraction: solid, liquid, and adsorbed thin films', *Nucl. Instr. and Meth. in Phys. Res. A*, 297, pp. 133–147.
Sellers, B., Papadopoulos, J. and Wilson, H. (1967) *Generation and Practical Use of Monoenergetic X-Rays from Alpha Emittinh Isotopes*, *NYO-3491-2*.
Sharma, A. and Sauli, F. (1993) 'First Townsend coefficient measured in argon based mixtures at high fields', *Nucl. Instr. and Meth. in Phys. Res. A*, 334(2–3), pp. 420–424.
Simons, D. G. and De Korte, P. A. J. (1989) 'Soft X-Ray Energy Resolution and Background Rejection in a Driftless Gas Scintillation Proportional Counter', *Nucl. Instr. and Meth. in Phys. Res. A*, 277, pp. 642–656.
Smirnov, I. B. (2005) 'Modeling of ionization produced by fast charged particles in gases', *Nucl. Instr. and Meth. in Phys. Res. A*, 554, pp. 474–493.
Stapelmann, K. *et al.* (2014) 'A H2 very high frequency capacitively coupled plasma inactivates

glyceraldehyde 3-phosphate dehydrogenase(GapDH) more efficiently than UV photons and heat combined', *Journal of Physics D: Applied Physics*, 47(8).
Stewart, T. E. *et al.* (1970) 'Proton Excitation of Continuous Emission in the Noble Gases*', *Journal of the Optical Society of America*, 60(10), p. 1290.
Suzuki, M. *et al.* (1987) 'The emission spectra of Ar, Kr and Xe + TEA', *Nucl. Instr. and Meth. in Phys. Res. A*, 254, pp. 556–560.
Tanaka, Y., Inn, E. C. and Watanabe, W. (1953) 'Absorption Coefficients of Gases in the Vacuum Ultraviolet. Part IV. Ozone', *J. Chem. Phys.*, 21, p. 1651.
Thompson, A. C. and et al (2009) *X-Ray Data Booklet, http://xdb.lbl.gov*. LBL.
Ullaland, O. (2005) 'Fluid systems for RICH detectors', *Nucl. Instr. and Meth. in Phys. Res. A*, 553, p. 107.
Va'vra, J. (2003) 'Physics and chemistry of aging-early developments', *Nucl. Instr. and Meth. in Phys. Res. A*, 515, pp. 1–14.
Veenhof, R. (2019) *MAGBOLTZ, https://magboltz.web.cern.ch/magboltz/*.
W.M. Sansen (1990) 'Limits of low noise performance of detector readout frontends in CMOS technology', *IEEE Trans on Circuits ans Systems*, 37(11).
Watanabe, K. and Zelikoff, M. (1953) 'Absorption Coefficients of Water Vapor in the Vacuum Ultraviolet', *J. Opt. Soc. Am.*, 43(9), p. 753.
Wikipedia (2020a) 'Arc Light Sources', *https://en.wikipedia.org/wiki/Deuterium_arc_lamp*.
Wikipedia (2020b) 'Common Beta Emitters', *https://en.wikipedia.org/wiki/Common_beta_emitters*.
Wikipedia (2020c) *Commonly used gamma-emitting isotopes, https://en.wikipedia.org/wiki/Commonly_used_gamma-emitting_isotopes*.
Workman, R. L. and et al. (2022) 'PDG Reviews, Tables & PLots', *Prog.Theor. Exp. Phys. 2022(2022)083C01*.
Yamashita, T. *et al.* (1989) 'Measurement of the electron drift velocity and positive-ion mobility for gases containing CF4', *Nucl. Instr. and Meth. in Phys. Res. A*, 283, pp. 709–715.
Zerguerras, T. *et al.* (2009) 'Single-electron response and energy resolution of a Micromegas detector', *Nucl. Instr. and Meth. in Phys. Res. A*, 608, pp. 397–402.
Zhang, W. *et al.* (1989) 'Excitation and Ionization of freon molecules 1', *Chem. Phys.*, 137, p. 391.
Zyla, P. A. (2020) *Review of Particle Physics, Prog. Theor. Exp. Phys.*